DEVELOPMENT AND IMPROVEMENT OF SPECTROSCOPIC TECHNIQUES FOR ATMOSPHERIC COMPOSITION MEASUREMENTS FROM GROUND AND SPACE

ZAHRA VAZIRI ZANJANI

A DISSERTATION SUBMITTED TO
THE FACULTY OF GRADUATE STUDIES
IN PARTIAL FULFILLMENT OF THE REQUIREMENTS
FOR THE DEGREE OF

DOCTOR OF PHILOSOPHY

GRADUATE PROGRAM IN EARTH AND SPACE SCIENCE AND ENGINEERING
YORK UNIVERSITY
TORONTO, ONTARIO
DECEMBER 2018

Abstract

Investigating the role of the atmosphere in climate change requires a large body of observations and measurements of atmospheric composition. This requires the development of observational techniques and instrumentation, as well as modeling and methods for the correction of past measurements. Some of the more important atmospheric components that contribute significantly to climate change are ozone (O_3), methane (CH_4), carbon dioxide (CO_2) and water vapour (H_2O). The effect of the changes in these elements is more prominent in the Arctic region. In the Arctic, changes in greenhouse gas amounts can have amplified effects through their indirect impact on surface albedo, humidity, ocean currents and temperature. This thesis focuses on investigating improvements of O_3 measurements and the development of spectroscopic techniques and instrumentation to measure CO_2, CH_4 and the O_2 A-band in the arctic atmosphere.

The first section of this thesis focuses on retrieval methods and analyzing data produced by the Brewer Spectrophotometer. Stray light in the Brewer instrument causes an underestimation of daily ozone values especially in the northern latitudes where, at certain times of the year, measurements must be made at large solar zenith angles. This section focuses on a practical method to correct for stray light effects that includes a mathematical model of the instrument response and a non-linear retrieval approach that calculates the best values for the model parameters.

In the second section, new instrumentation designed and developed to measure atmospheric mixing ratios of CH_4, CO_2 and the O_2 A-band is reported. This instrument, an imaging Fourier Transform Spectrometer (IFTS), is one of the first of its kind to be built. It is a next-generation, atmospheric measurement instrument that can provide high spatial resolution and continuous observations of the Arctic. This thesis will describe the optical and mechanical design of the

payload, including the fore-optics that includes an image stabilizer. The system design is also described, which involves instrument characterization, electronic interfaces, software interfaces, data storage and handling, testing the payload in a lab setting and data analysis methods.

Dedication

I would like to dedicate this thesis to my father,

Mohammad Ali Vaziri Zanjani.

Acknowledgments

First and foremost, I would like to thank my supervisor, Charles Thomas McElroy, for his outstanding help and support. The work reported in this thesis would not have been possible without his dedicated guidance and feedback. I am very grateful to have had the opportunity to be part of the amazing and exciting projects presented in this thesis.

Thank you to David Barton for his technical support in electronics and software and for his friendly advice. I would like to thank my other committee members, Jim Whiteway and Regina Lee, for their continued encouragement and support. Thank you to my examiners Doug Degenstein, Michael De Robertis and Peter Taylor.

I would like to acknowledge the support of the Canadian Space Agency for providing funding for this research. Special thanks to ABB Bomem for supplying instrumentation and to Frederic Grandmont for his support and guidance in developing the instrumentation presented in this thesis.

I am very grateful to my lab members, Gurpreet Singh and Omid Moeini for their friendship and encouragement. Thank you to the post-doctoral members of the group, Chen Zheng and Rehan Seddiqui, for their support, without which this work would not have been complete.

Thank you to York University for giving me the opportunity to work and do research in this interesting field and for letting me become acquainted with my amazing supervisor and friends who stood by me through all the hard work.

Many thanks to my father, Mohammad Ali Vaziri Zanjani, and sister, Leila Vaziri Zanjani, for helping me proof read my thesis and to my mother, Maryam Abdollahian, for her emotional support.

Lastly, I would like to thank my husband, William Dennis, who encouraged me and had faith in me to complete this work. He has been an amazing partner and wonderful friend.

Table of Contents

Contents

List of Figures

List of Tables

List of Abbreviations

ABB	ABB Measurements and Analytics Division
A/W	Amp per Watt
ACE	Atmospheric Chemistry Experiment
AMF	Airmass Factor
CFC	Chlorofluorocarbons
CNES	Centre national d'Etudes spatiales
CSA	Canadian Space Agency
DAS	Differential Absorption Spectroscopy
DB	Double Brewer
DFT	Discrete Fourier Transform
ECCC	Environment and Climate Change Canada
EM	Electromagnetic
FFT	Fast Fourier Transform
FR	Fringe
FR90	De-phase Fringe
FT	Fourier Transform
FTS	Fourier Transform Spectrometer
FWHM	Full Width at Half Maximum
GEO	Geostationary Orbit
GHG	Greenhouse Gas
HCFC	Hydrochlorofluorocarbons
HeNe	Helium-Neon
HEO	Highly Elliptical Orbit
IASI	Infrared Atmospheric Sounding Interferometer
IFTS	Imaging Fourier Transform Spectrometer
InGaAs	Indium Gallium Arsenide
IR	Infrared
ISPS	Image Stabilizer Pointing System
K	Kelvin
LARSS	Laboratory for Atmospheric Remote Sounding from Space
LEO	Low Earth Orbit
MAESTRO	Measurement of Aerosol Extinction in the Stratosphere and Troposphere Retrieved by Occultation
MI	Michelson Interferometer
OPD	Optical Path Difference
PARABLE	Payload for Remote sounding of the Atmosphere using Balloon Limb Experiments
PARIS	Portable Atmospheric Research Interferometric Spectrometer

PCW	Polar Weather and Communication
PHEOS	Polar Highly Elliptical Orbital Science
PSC	Polar Stratospheric Clouds
PSD	Position Sensitive Device
RCD	Reference Column Density
RTM	Radiative Transfer Model
SB	Single Brewer
SCD	Slant Column Density
SD	Scan Direction
SF	Setup File
SNR	Signal to Noise Ratio
SPS	Sun-Photo-Spectrometer
SW	Scan Window
TAP	Three Apogee
TOA	Top Of the Atmosphere
TRL	Technology Readiness Level
UV	Ultraviolet
VCD	Vertical Column Density
VCM	Voice Coil Motor
VMR	Volume Mixing Ratio
ZnSe	Zinc Selenide
ZPD	Zero Path Difference

1. Introduction

The Earth's atmosphere has been an important subject of study for many years. Different instrumentation has been developed to make observations from ground-, aircraft-, balloon- and space-based platforms. It is essential to understand the atmosphere and data retrieval techniques in order to improve measurements from current instruments and to design and develop new instrumentation to measure atmospheric composition.

Observing and quantifying the atmosphere has become more and more important as the effects of climate change are reaching critical levels. There is an additional need to further improve the historical data of current instrumentation as well as to develop new instruments with higher accuracy, resolution and long-term coverage.

This thesis will have two main sections, one deals with correcting ozone data for the Brewer instrument and the other will focus on instrument development for the high-latitude regions. This chapter will present the motivation for this work, the objectives of the project, the scientific contributions and an outline of the thesis.

1.1. Motivation

Climate change is the main motivation for the work presented in this thesis. Climate change has several indicators such as surface temperature change, atmospheric water vapour content, sea level rise, receding glaciers and land and sea ice extent and thickness (Cubasch et al., 2013). The increased surface temperature causes the land and sea ice to melt faster and thus, increases the water vapour content of the atmosphere. Water is one of the main greenhouse gases (GHG). GHGs cause the Earth to warm up and, therefore, an increase in these gases causes a positive feedback

loop to climate change. Other anthropogenic GHGs that contribute to this cycle are Carbon dioxide (CO_2), Methane (CH_4) and Nitrous Oxide (N_2O) (Cubasch et al., 2013).

Climate change will have amplified effects at northern latitudes according to general circulation models. This amplification is due to feedback provided by the reduction of sea ice extent, decreased stability in the lower troposphere and the thawing of permafrost (perennially frozen ground) (Serreze et al., 2000).

It is predicted that climate change will also delay the recovery of stratospheric ozone especially in the Polar regions (Hassol, 2004). Ozone depletion is highly sensitive to temperature in the stratosphere which is affected by the increase in GHGs (Shindell et al., 1998). It is therefore crucial to monitor the ozone layer and ultraviolet radiation. Atmospheric Ozone has been studied for over 100 years. Since the 1920s, the Dobson Spectrophotometer (Dobson, 1931) and since the 1980s, the Brewer Spectrophotometer (Brewer, 1973), have been observing total column ozone. Per the WOUDC website, more than 160 Brewers, single and double are being used in more than 40 countries and 100 stations to measure ozone (WOUDC, 2016). The Brewer Instrument is one of the primary global standard instruments for the ground-based measurements of ozone. It is now known that Single-Monochromator Brewer Spectrophotometer ozone and sulphur dioxide (SO_2) measurements suffer from non-linearity due to the presence of instrumental stray light caused by scattering within the optics of the instrument (Bais et al., 1996). Stray light in the Brewer instrument was found to cause errors in photometry and calculated absorptivity which, therefore, leads to an underestimation of the ozone column amount for large ozone slant column amounts (Slavin, 1963). This effect is more apparent when the solar zenith angle is large, for example in the polar regions. The measurements can be on the order of 10% low for an ozone column of 600 D.U at an airmass factor of 3 (1800 D.U. slant column amount). The first section of this thesis will

focus on a practical method to correct for stray light effects. The method includes a mathematical model of the instrument response and a non-linear retrieval approach that calculates the best values for the model parameters. The parameterization used was validated using an instrument physical model simulation. The parameterization can then be used in reverse to retrieve accurate total ozone values.

As mentioned earlier in this section, monitoring GHGs is essential in the Arctic region. Ground-based instruments in the Arctic do not provide coverage of the whole region. As the Arctic is an ocean covered in ice, installing instruments on the surface is challenging. In this case, satellite-based instruments come to the aid of scientists. Currently, satellites that monitor the Arctic region are in polar, sun-synchronous orbits which make short passes over the Arctic approximately every 100 minutes. The frequency of visits to the high-latitude regions by these Low Earth Orbit (LEO) satellites is restricted to the observation latitude and the refresh rate on measurements depend on the satellite ground track width and the orbital period (Trishchenko et al., 2016). On the other hand, geostationary orbits (GEO) do not provide useful observations of the Arctic because of the shallow viewing angle. Thus, current instrumentation does not provide long-term and high temporal resolution in the Arctic.

The second section of the thesis is focused on the design and development of a demonstrator Imaging Fourier Transform Spectrometer (IFTS) to be flown on a high-altitude balloon to demonstrate the capacity to measure atmospheric mixing ratios of CH_4, CO_2 and the O_2 under near-space conditions. The spectrometer has two separate channels centred at 762 nm for the O_2 A-band and 1650 nm for CO_2 and CH_4. The author and other group members in the Laboratory for Atmospheric Remote Sounding from Space (LARSS) at York University are developing the IFTS payload. ABB Measurements and Analytics Division (ABB) of Quebec City constructed the core

of the interferometer. The novelty in this instrument is that it uses a 320 × 256 pixels, infrared array detector which provides high spatial resolution (Design goal: 8 km from 40,000 km from space). The challenge faced is to track a surface element of interest for the duration of the scan of the interferometer, especially in the Arctic region, which is covered in snow and ice much of the year and may make it difficult to provide accurate image tracking. However, the primary goal is the detection of the evolution of CH_4 and CO_2 from melting permafrost, which will take place during the summer months as the snow melts. The future objective of this project is to fly a similar instrument on a three-apogee, highly elliptical orbit (HEO) satellite (e.g.: Trishchenko et al., 2011) to achieve long-term quasi-geostationary observations of the Arctic by using two satellites in complementary orbits with apogees above the Arctic (McElroy et al., 2012; McConnell et al., 2012). This thesis will cover the optical and mechanical design of the payload, including the fore-optics and detectors. The system design is also described, as well as instrument characterization, electronic interfaces, software interfaces, data storage and handling, testing the payload in a laboratory setting and data analysis methods.

1.2. Objectives

The objectives of this thesis are to:

- Characterize stray light effects on the single Brewer Spectrophotometer
- Design a mathematical model to quantify the effects of stray light
- Provide a correction algorithm for stray light effects
- Demonstrate design elements of a next-generation space-based instrument (IFTS) to measure CO_2, CH_4 and O_2
- Design and develop an image stabilizer pointing system to serve as fore-optics for the IFTS

instrument to track an image on the ground for the duration of the measurements

1.3. Scientific Contributions

To achieve the objectives of work presented in this thesis, the work has been designed in the following three sections:

1. Stray light analysis of the Brewer spectrophotometer
2. Design and development of a lab demonstrator IFTS Instrument to provide proof of concept for Nadir observations of CO_2, CH_4 and O_2
3. Design, construction and testing of an image stabilizer pointing system component for the fore-optics of the IFTS

A mathematical model for the response of the single and double Brewer spectrophotometers was developed in MATLAB to account for the effects of stray light on total column ozone amounts measured by the Brewer. The model can be applied in reverse to provide corrections to the ozone observations. A manuscript of this work has been submitted to the journal of Atmospheric Measurements and Techniques (AMT) and has been published.

The mechanical, electrical and optical aspects of an IFTS instrument were designed and developed. The core of the instrument was supplied by ABB Measurements and Analytics Division. (ABB Inc., 2018). CATIA was used to design the mechanical parts of the IFTS as well as assemble the payload with all the optics. The work reported in this thesis includes the design and development of the optics, electronics and software, however, most of the software was developed by other LARSS group members (Gurpreet Singh and Greg Blair).

The fore-optics of the IFTS is an image stabilizer pointing system. This component of the project

was designed in CATIA by the author and a prototype was constructed in the York University machine shop. The electronics and software aspect of it was designed and constructed with input from the author by other LARSS group members (David Barton and Bobby Ngo)

1.4. Outline

This thesis has 6 chapters. The first chapter introduces the work done by stating the motivation, objectives and scientific contributions. The second chapter covers some basic atmospheric physics needed to understand the work presented. Chapter three demonstrates the stray light problem in the Brewer spectrophotometer and the mathematical model developed is described that is used to assess these effects and correct for them. The corrections have been applied to observational data to prove the practicality and importance of correcting for stray light effects. The fourth chapter presents the design and development of the optics, mechanics and electronics of a lab demonstrator IFTS instrument. The data analysis method is described, and experimental data are presented. Chapter five presents the design and development of an image stabilizer for use with the IFTS instrument. The mechanics and optics are described as well as the software and electronics. In chapter six a summary and conclusions based on the work presented in this thesis are provided.

2. Atmospheric Physics

As an introduction to the work presented in this thesis, this chapter summarizes the nature of the atmosphere, its composition and vertical thermal structure. The nature of electromagnetic radiation and its interaction with the atmosphere is also discussed. At the end of the chapter, information about the remote sounding of the atmosphere, retrieval theory and stratospheric ozone are presented.

2.1. Atmospheric Structure and Composition

The Earth's atmosphere is mainly composed of nitrogen, oxygen and argon. These gases are the permanent constituents and compose 99.96% of the atmosphere (Refer to Table 1). Other permanent gases in order of percentage by volume are listed in Table 1. Other trace constituents of the atmosphere are given in the second column of the table. In recent years greenhouse gases (GHGs) such as methane (CH_4) and carbon dioxide (CO_2) have been increasing due to the combustion of fossil fuels as well as emissions from industry, agriculture and the surplus energy required for the support of the increasing human population. The ozone layer, which resides in the stratosphere in an altitude range of approximately 15 to 30 km, depending on latitude, is quite variable. The largest source of variability over a particular location is the effect of weather systems on transport. Some of this variation is due to photo-chemical reactions driven by solar radiation. Reactions involving chlorine and bromine released from chlorofluorocarbons (CFCs) and hydrochlorofluorocarbons (HCFCs) cause ozone depletion (Liou, 2002).

The atmosphere is commonly divided into four layers. These layers are the troposphere, stratosphere, mesosphere and thermosphere. In the troposphere, the temperature decreases with altitude up to ~12 km (down to 220 Kelvin (K)). The reason for that is, the gases in the troposphere

absorb very little of the solar radiation and the main source of heating is the Earth's surface. The troposphere heats up by convection and therefore the layer of the troposphere closest to the surface will be warmer. The boundary between the troposphere and stratosphere is called the tropopause. In the stratosphere, the temperature stays constant up to an altitude of ~20 km. From this altitude up to the stratopause (~50 km) the temperature increases from ~220 K to ~270 K. The mesosphere begins at ~50 km and ends at ~85 km. In the mesosphere, the temperature decreases down to about 190 K. Above the mesopause, the boundary between the mesosphere and thermosphere, the temperature starts to increase again. These variations are plotted in Figure 2-1, using data from the US standard atmospheric model of 1976 (NOAA and NASA, 1976).

Table 1: The composition of Earth's Atmosphere. (Reproduced from Liou, 2002)

Permanent constituents		Variable constituents	
Constituent	% by volume	Constituent	% by volume
Nitrogen (N_2)	78.084	Water vapor (H_2O)	0–0.04
Oxygen (O_2)	20.948	Ozone (O_3)	$0–12 \times 10^{-4}$
Argon (Ar)	0.934	Sulfur dioxide (SO_2)[b]	0.001×10^{-4}
Carbon dioxide (CO_2)	0.036	Nitrogen dioxide (NO_2)[b]	0.001×10^{-4}
Neon (Ne)	18.18×10^{-4}	Ammonia (NH_3)[b]	0.004×10^{-4}
Helium (He)	5.24×10^{-4}	Nitric oxide (NO)[b]	0.0005×10^{-4}
Krypton (Kr)	1.14×10^{-4}	Hydrogen sulfide (H_2S)[b]	0.00005×10^{-4}
Xenon (Xe)	0.089×10^{-4}	Nitric acid vapor (HNO_3)	Trace
Hydrogen (H_2)	0.5×10^{-4}	Chlorofluorocarbons	Trace
Methane (CH_4)	1.7×10^{-4}	($CFCl_3$, CF_2Cl_2	
Nitrous oxide (N_2O)[b]	0.3×10^{-4}	CH_3CCl_3, CCl_4, etc.)	
Carbon monoxide (CO)[b]	0.08×10^{-4}		

[a] After the U.S. Standard Atmosphere (1976) with modifications.
[b] Concentration near the earth's surface.

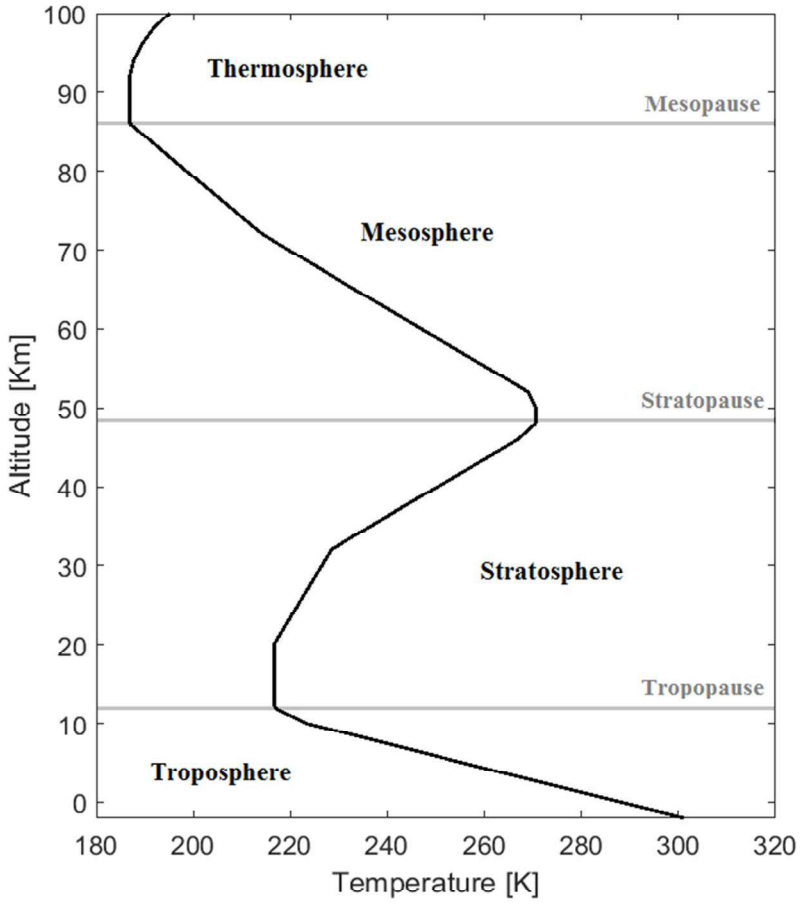

Figure 2-1: An atmospheric temperature vertical profile plotted using data from the U.S. standard atmosphere model, 1976 (NOAA and NASA, 1976)**.**

2.2. Electromagnetic Radiation

The radiation emitted by the sun travels in the form of electromagnetic (EM) waves that travel at the speed of light ($c = 2.99 \times 10^8$ m/s in vacuum). Wavelength (λ), measured in metres can be expressed in terms of the speed of light (c) and frequency (f), measured in Hz as given in equation (2-1). Wavenumber (ν) is the inverse of wavelength usually measured in cm^{-1} as seen in equation (2-2) (Liou, 2002). The conventional symbol used for wavenumber is $\bar{\nu}$ but throughout this thesis ν is used.

$$\lambda = \frac{c}{f} \quad \textbf{(2-1)}$$

$$\nu = \frac{1}{\lambda} \quad \textbf{(2-2)}$$

The EM spectrum ranges from short wave gamma rays, at 10^{-5} μm, to long-wavelength radio waves, at 10^{12} μm, as illustrated in Table 2. The visible part of the spectrum that our eyes can detect ranges from 0.4 μm to 0.7 μm. Different types of detectors and filters are used to detect radiation in other parts of the EM spectrum.

Table 2: Electromagnetic radiation spectrum.

Region	Wavelength (μm)	Wavenumber (cm^{-1})	Frequency (Hz)
Gamma Rays	10^{-5}	10^{9}	10^{18}
X rays	10^{-2}	10^{6}	3×10^{16}
Ultraviolet (UV)	3×10^{-1}	0.33×10^{5}	10^{15}
Visible (Vis)	0.4 — 0.7	1.43×10^{4} - 2.5×10^{4}	5×10^{15}
Infrared (IR)	1 10^{3}	10^{4} 10	3×10^{11}
Microwaves	10^{4}	1	3×10^{10}
Radio waves	10^{9}	10^{-5}	3×10^{5}
Long radio waves	10^{12}	10^{-8}	3×10^{2}

The energy transported by EM radiation per unit time (power) per unit area is called Irradiance (E) with units of $W.m^{-2}$. Irradiance per unit wavelength interval at a particular wavelength is denoted by E_λ. Irradiance per unit solid angle is the definition of radiance or intensity and is denoted by L_λ. Solid angle (Ω) is defined as A/R^2 where, R is the distance from the observing point to the emitting area, A. A differential element of solid angle can be written as:

$$d\Omega = \sin\theta d\theta d\emptyset \quad \textbf{(2-3)}$$

Where θ and ϕ are the angles in a polar coordinate system. Hence, irradiance is given by:

$$\mathbf{E} = \int_{0}^{\infty} \int_{\theta_0}^{\theta} \int_{\emptyset_0}^{\emptyset} \mathbf{L_\lambda \cos\theta \sin\theta \, d\theta \, d\emptyset \, d\lambda} \qquad \textbf{(2-4)}$$

Where cos(θ) is multiplied to find the component of L_λ perpendicular to the illuminated surface area. EM radiation is not only emitted by the sun, but by any object that has a temperature above 0 Kelvin. The spectrum of an object depends on its temperature and its ability to emit or absorb radiation at different wavelengths. A black body is an ideal object that can emit and absorb at all wavelengths. Planck's law describes the relationship between the intensity of emitted monochromatic radiation to the frequency or wavelength and the temperature of the emitting object. This relation is as follows (Liou, 2002):

$$\mathbf{B_f(T) = \frac{2hf^3}{c^2\left(e^{\frac{hf}{kT}} - 1\right)}} \quad \textbf{or} \quad \mathbf{B_\lambda(T) = \frac{2hc^2}{\lambda^5\left(e^{\frac{hc}{k\lambda T}} - 1\right)}} \qquad \textbf{(2-5)}$$

Where h = 6.626 x 10^{-34} J.s is the Planck constant and k = 1.3806 x 10^{-23} $J.K^{-1}$ is the Boltzmann constant. The Planck function for different emitting temperatures as a function of wavelength is plotted in Figure 2-2.

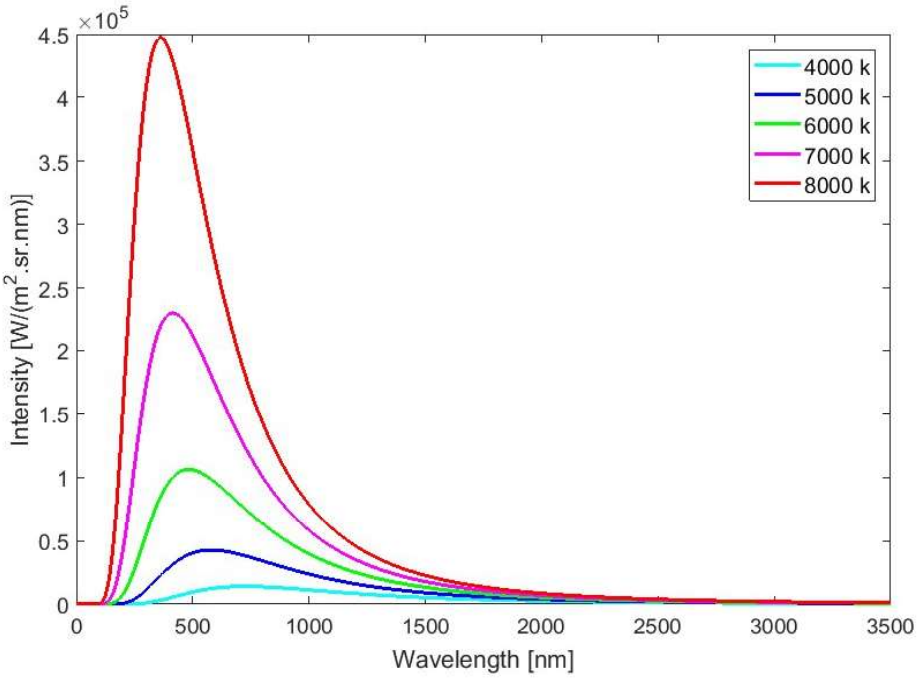

Figure 2-2: Planck function (intensity) of a black body as a function of wavelength for different emitting temperatures.

The radiance of a black body is obtained by integrating the Planck function over all frequencies. This integration results in:

$$\boldsymbol{E = \sigma T^4} \qquad \textbf{(2-6)}$$

Where $\sigma = 5.67 \times 10^{-8}$ W.m^{-2}.K^{-4} is the Stefan-Boltzmann constant. To find the temperature of a black body, the derivative of the Planck function with respect to wavelength is put equal to zero. The relation between the maximum wavelength and temperature of a black body which is obtained from this differentiation is called Wien's displacement law:

$$\boldsymbol{\lambda_{max} = \frac{a}{T}} \qquad \textbf{(2-7)}$$

where λ_{max} is the maximum wavelength, T is temperature and $a = 2.897 \times 10^{-3}$ m.K is a constant. A black body not only emits energy but also absorbs it. Under thermodynamic equilibrium,

Kirchhoff's law states that the emissivity, ε_λ, which is unitless and determines the energy emitted, is equal to the absorptivity, A_λ. For a black body object $\varepsilon_\lambda = A_\lambda = 1$. Below an altitude of 60-70 km, the atmosphere can be considered in local thermodynamic equilibrium and thus Kirchhoff's law can be applied (Liou, 2002).

2.3. Atmospheric Interaction with Radiation

Radiation interacts with constituent gaseous molecules as it passes through the atmosphere in the form of scattering, absorption and emission. Figure 2-3 shows the solar radiation at the top of the atmosphere (TOA) as a solid line. For reference, the Planck function at 6000 °K is shown as a dashed line. The solar radiation after crossing the atmosphere at sea level is shown as a thick solid line with the absorption of different gasses blacked out (Lacis and Hansen, 1974).

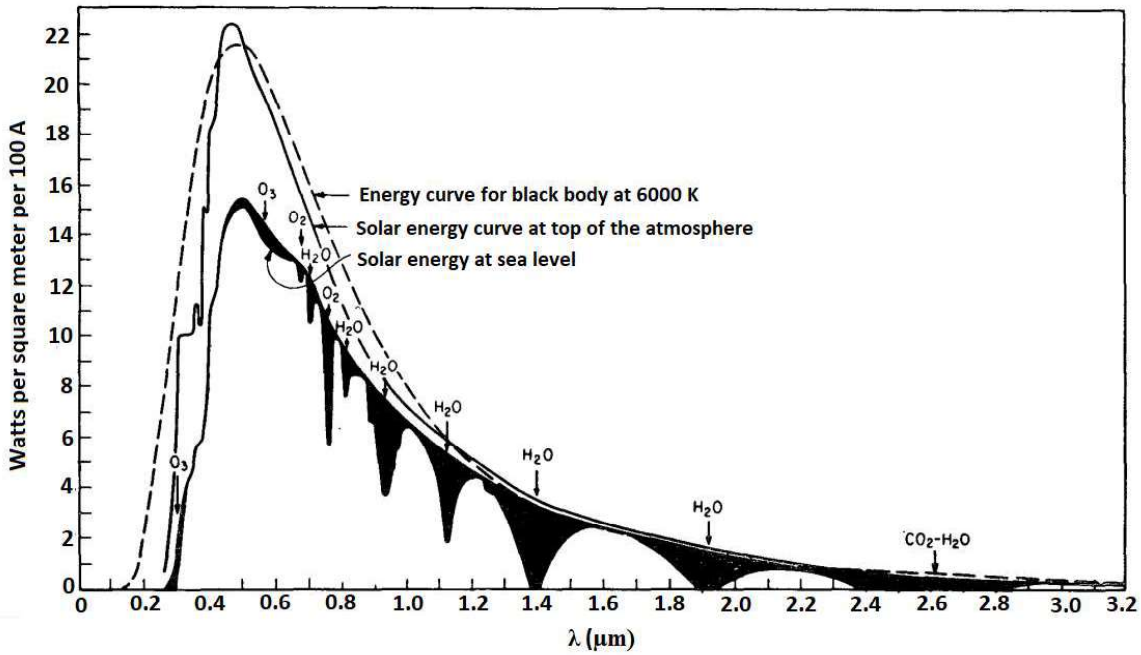

Figure 2-3: The solar energy curve at the top of the atmosphere compared with the energy curve of a black body object at 6000 °K and the solar energy curve at sea level. Absorption by gases in the atmosphere have been blacked out in this figure. (Lacis and Hansen, 1974)

The differential change in intensity of solar radiation, denoted by dI, over an infinitesimally small path length is dependent on the differential changes in intensity due to absorption, dI_{abs}, emission, dI_{emit} and scattering, dI_{scat}:

$$\mathbf{dI = dI_{abs} + dI_{emit} + dI_{scat}} \quad \textbf{(2-8)}$$

2.3.1. Atmospheric Absorption

Some of the radiation going through an absorbing medium will undergo extinction. For a thin column of absorbing material of thickness ds (Figure 2-4) the change in intensity, dI_λ, is given by the equation below, where I_λ is the incident intensity, α is the absorption coefficient and X is the slant column amount of the absorbing material. The Slant column is defined in equation (2-10) as the vertical column amount of the absorbing material multiplied by the airmass factor (AMF). The definition and derivation of the airmass factor is given in section 2.4.1.

$$\mathbf{dI_\lambda = -\alpha_\lambda I_\lambda dX} \quad \textbf{(2-9)}$$

$$\mathbf{X = x\mu} \quad \textbf{(2-10)}$$

Integrating both sides of the equation gives:

$$\mathbf{I_\lambda = I_\lambda(0)exp(-\alpha_\lambda \mu x)} \quad \textbf{(2-11)}$$

Where, $I_\lambda(0)$ is the intensity before entering the column of absorbing material and I_λ is the intensity after exiting the column of absorbing material. The exponential term is defined as the optical depth, τ, given in equation (2-12):

$$\mathbf{\tau(\lambda) = -\alpha_\lambda \mu x} \quad \textbf{(2-12)}$$

By replacing τ in equation (2-11) the Beer-Bouguer-Lambert Law (Beer's Law) is derived:

$$\mathbf{I_\lambda = I_\lambda(0)exp(-\tau(\lambda))} \quad \textbf{(2-13)}$$

Beer's law states that the intensity of radiation passing through a uniformly absorbing medium

decreases exponentially with respect to optical depth which is a function of the absorption coefficient of that medium and the amount of absorbing material in that medium.

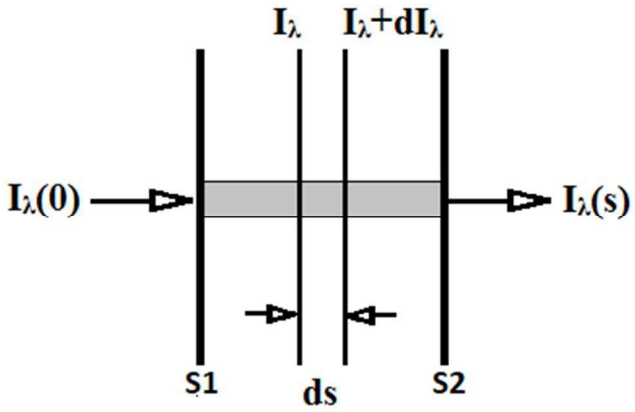

Figure 2-4: Solar radiation, when travelling through a medium, changes due to absorption. $I_\lambda(0)$ is intensity before entering the medium and $I_\lambda(s)$ is the intensity after crossing the medium.

2.3.2. Atmospheric Emission

In a medium where there is no scattering present, the absorption coefficient, α, is equal to the emission coefficient, β_e ($\alpha = \beta_e = \beta_a$). In this case the change in intensity due to emission will be:

$$dI_{emit} = \beta_a B_\lambda(T)\rho ds \quad \textbf{(2-14)}$$

Where $B_\lambda(T)$ is the Planck function. By substituting equation (2-9) and (2-14) into (2-8) the change in intensity becomes:

$$dI = dI_{abs} + dI_{emit} = \beta_a(B_\lambda(T) - I_\lambda)\rho ds \quad \textbf{(2-15)}$$

2.3.3. Atmospheric Scattering

Atmospheric particles, depending on their size, scatter solar radiation in different forms. To characterize scattering a dimensionless parameter is defined as below:

$$x = \frac{2\pi r}{\lambda} \qquad (2\text{-}16)$$

Where r is the effective radius of the molecule or particle. Rayleigh scattering happens when particles are very small ($x \leq 1$). Gas molecules have an approximate effective radius of ~10^{-4} μm and when illuminated by visible light, $x << 1$, therefore, Rayleigh scattering occurs. Mie scattering occurs when particles are larger ($x \geq 1$) such as aerosols in the atmosphere (effective radius ~1 μm). In Rayleigh scattering, the forward and backward scattering is equal, whereas, in Mie scattering the forward scattering is stronger than the backward scattering (Liou, 2002).

Raman scattering by molecules results in a shift in frequency between the incident and scattered radiation (e.g. water vapour molecules). Referring to Figure 2-5, when the molecule is excited from the ground vibrational state (m) and returns to a higher vibrational state (n), it is called Stokes scattering and when the molecule is already at a higher vibrational state (n) and gets excited and returns to the ground vibrational state (m), it is called anti-Stokes scattering.

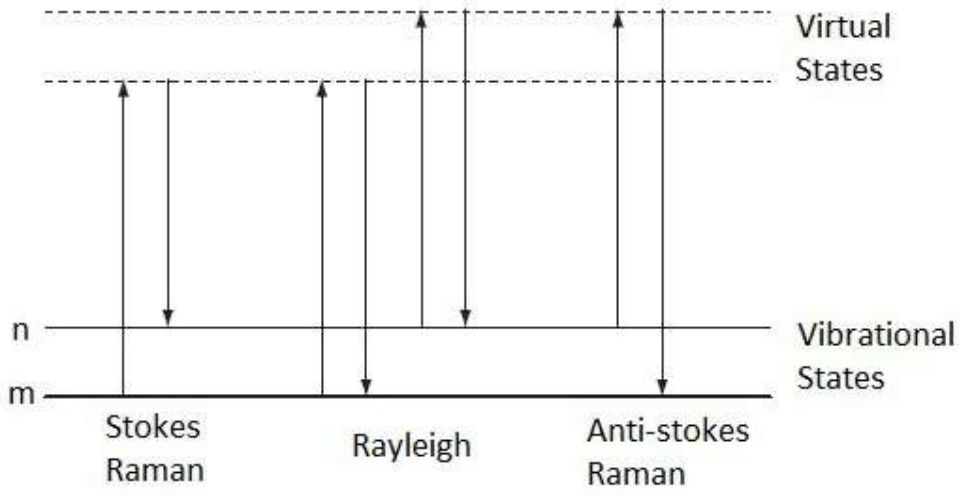

Figure 2-5: Diagram of Rayleigh and Raman scattering of a molecule. (Smith and Dent, 2005)

If the size of the atmospheric particle matches the incident wavelength then resonant scattering

happens, In other words the particle becomes a resonator of the incident light (Lagendijk and van Tiggelen, 1996).

2.4. Remote Sensing of the Atmosphere

Remote sensing is the measurement of EM radiation that has passed through the atmosphere, or has been scattered by atmospheric particles, or reflected from the Earth's surface, used to indirectly determine information about the composition and state of the atmosphere. These measurements can be made from the ground with ground-based instruments which observe the direct sunlight or sunlight scattered by atmospheric molecules and aerosol particles. Measurements can also be made by airborne and spaceborne instruments. Examples of airborne platforms are aircraft, weather balloons and high-altitude, stratospheric balloons. A spaceborne instrument is mounted on a satellite platform and can observe the atmosphere in the nadir, limb or occultation mode. These viewing geometries are illustrated in Figure 2-6.

Remote sensing instruments can be passive or active. Passive instruments are those that measure naturally occurring EM radiation, for example, spectrometers which measure the intensity of sunlight passing through the atmosphere or radiometers which detect thermal emission. Active instruments include a source of EM radiation and then measure the reflected or scattered radiation such as lidars which produce a laser beam and then measure the reflected or scattered light from atmospheric molecules and particles.

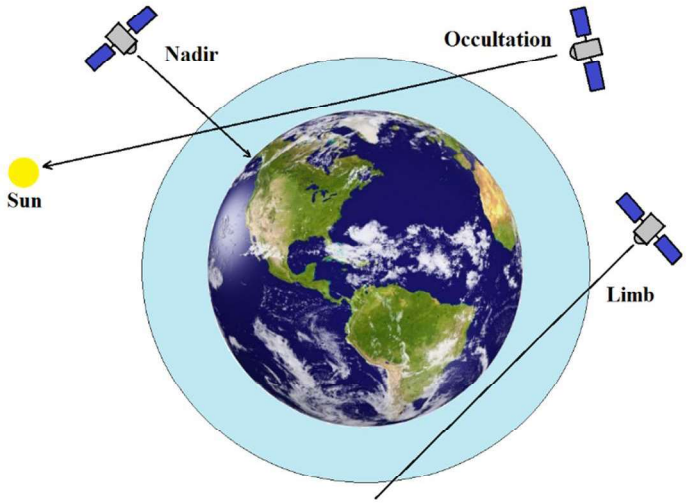

Figure 2-6: Different viewing geometries of spaceborne atmospheric remote sounding instruments.

Remote sensing has many advantages. It is often difficult or impossible to measure a quantity such as the composition of the atmospheric directly. Remote sensing makes such measurements possible. Spaceborne instruments allow the sounding of the atmosphere to be done globally in a short time.

Spaceborne instruments used for atmospheric measurements can be in different orbits, such as low-Earth orbits (LEO). LEO orbits are usually nearly circular with an altitude of 300 km to 1500 km. Sun-synchronous orbits refer to LEO orbits that are nearly polar orbits and pass over the same place at the same local solar time (Montenbruck and Gill, 2000). Geostationary (GEO) orbits are also used in atmospheric remote sounding. Satellites in GEO orbit are placed at an altitude of 35,800 km above the equator. At this altitude, the satellite revolves around Earth with the same angular speed as the Earth rotates about its axis. This allows the satellite to observe the same location on the Earth continuously. This orbit is ideal for communication satellites but is also used for remote sounding of the atmosphere as it allows continuous observations. The limitation of a GEO orbit is that it only covers the globe from approximately 60°N to 60°S and does not allow

coverage of the polar regions. To make continuous measurements near the poles, highly elliptical orbits (HEO) can be used. These orbits can reach an altitude of approximately 40,000 km at apogee and 1,000 km at perigee. A satellite in this type of orbit can spend ± 4 to 8 hours near apogee. By using two or three satellites in such orbits a quasi-geosynchronous view of the Arctic or Antarctic can be achieved (Montenbruck and Gill, 2000; Trishchenko et al., 2011).

2.4.1. Airmass Factor

A concept that is widely used in remote sounding of the atmosphere is that of the Airmass Factor (AMF). The airmass factor is the ratio of the effective optical path length to the vertical optical path length and depends on the solar zenith angle (SZA). The solar zenith angle is the angle the sun rays make with the zenith. In an ideal flat Earth situation, approximated in the atmosphere for small SZA, the airmass factor can be approximated as equal to the secant of the solar zenith angle (SZA). For large SZA ($\theta > 60°$), the spherical nature of Earth and atmospheric refraction cause a large error in approximating airmass to be sec (θ). In this case, the atmosphere is considered to be composed of many thin layers, each layer being considered a flat layer. The AMF for the j^{th} attenuating species as a function of SZA, θ, and wavelength, λ, is described in equation (2-17) where $\alpha(\lambda,z)$ is the absorption extinction coefficient as a function of altitude at wavelength λ, $n(z)$ is the index of refraction of air at altitude z, θ_0, n_0 and z_0 are the values of these variables at the Earth's surface (Thomason et al., 1983).

With the following three approximations, equation (2-17) simplifies to (2-18) (Bernhard et al., 2005; Antón et al., 2009):

- The ozone layer is at a fixed height above sea level
- The change in the refractive index with altitude is considered minimal and $n(z) = n_0 = 1$

- The apparent SZA is equal to the true SZA

The curved Earth scenario is portrayed in Figure 2-7, the airmass factor as a function of SZA, θ, is calculated by equation (2-18), where, R_e is the mean radius of Earth, h is the height of the observing station, and z is the thickness of the layer in the atmosphere being observed, which in the case of ozone measurements, is the height of the ozone layer (Solomon and Sanders, 1987).

$$\mathbf{AMF_j(\theta,\lambda) = \frac{1}{\int_{z_0}^{\infty} \alpha(\lambda,z)dz} \int_{z_0}^{\infty} \frac{\alpha(\lambda,z)dz}{\left[1-\frac{n_0}{n_z}\left(\frac{z_0}{z}\right)^2 \sin^2(\theta_0)\right]^{1/2}}} \quad \textbf{(2-17)}$$

$$\mathbf{AMF(\theta) = \frac{R_e + z + h}{[(R_e + z + h)^2 - (R_e + h)^2 Sin^2(\theta)]^{1/2}}} \quad \textbf{(2-18)}$$

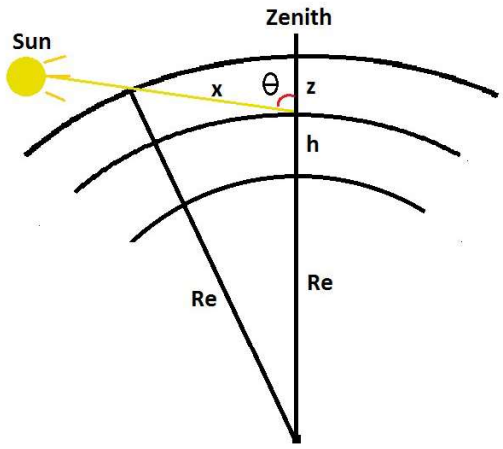

Figure 2-7: Curved Earth viewing geometry of an instrument at height h from the surface of Earth where, R_e is the mean radius of Earth, z is the layer of atmosphere that is of interest and x is the optical path length of light within the atmospheric layer.

2.5. Retrieval Theory

In the case of remote sensing of the atmosphere, the quantity measured is the EM radiation and the parameters that are to be retrieved have a complicated relationship to the EM radiation measured.

The retrieval of atmospheric parameters such as temperature and atmospheric composition requires solving an inversion of these complicated functions (Rodgers, 2000). One example of the inversion problem is to retrieve ozone amounts by measuring the intensity of solar radiation on the ground. Systematic measurements of ozone started with Dobson in the 1920s where he retrieved ozone values using a UV spectrometer (Dobson, 1968). Referring to Beer's law (equation (2-13)), a spectrometer measures the intensity of light received at the altitude of the instrument. This intensity is a function of the amount of absorbing gas present in the path length of the light. The objective is to derive the amount of absorbing gas and this can be achieved by inverting the Beer's law function.

2.6. Stratospheric Ozone

Ozone plays an important role in the Earth's climate. The Ozone layer present in the stratosphere absorbs harmful wavelengths of UV radiation from the sun, thereby preventing it from reaching the Earth's surface. The absorption of UV energy by the ozone layer causes heat deposition in the stratosphere which reverses the atmospheric temperature profile and causes the tropopause (National Research Council, 1994). Ozone absorbs in several spectral bands. The strongest absorption band is the Hartley band with wavelengths between 200 nm and 300 nm. The weaker absorption bands are the Huggins bands between 300 nm and 360 nm and the Chappuis bands between 440 nm and 1180 nm. These bands as well as the oxygen absorption bands can be seen in Figure 2-8, where the absorption cross-sections of ozone and oxygen have been plotted against wavelength (Liou, 2002).

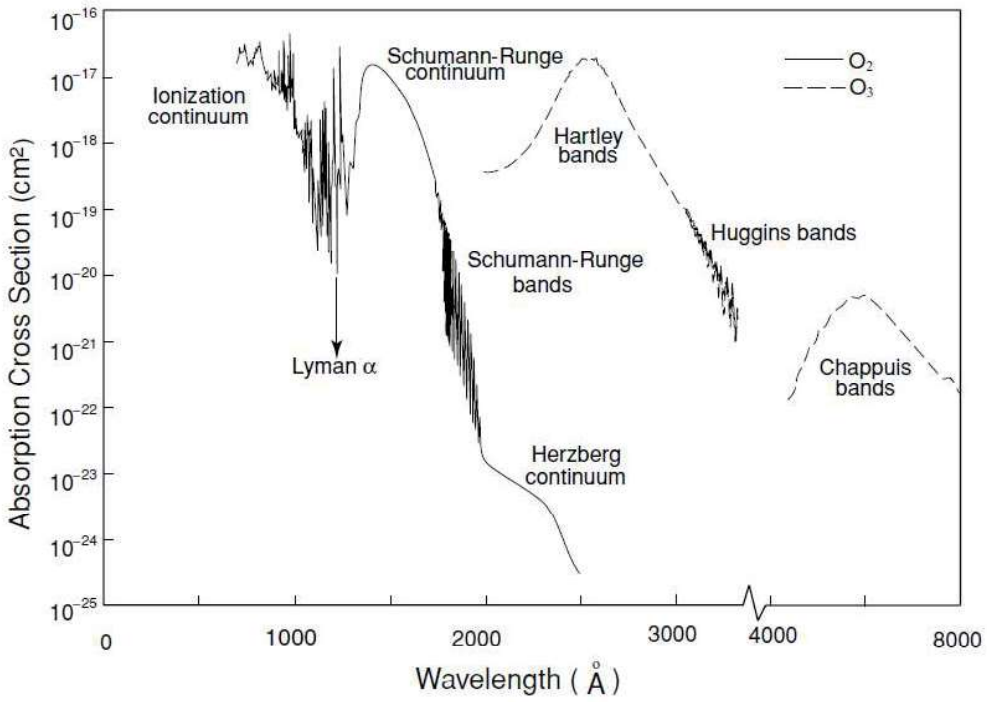

Figure 2-8: Absorption cross sections of oxygen (O_2) and ozone (O_3) marked as the Hartley, Huggins and Chappuis bands. (Liou, 2002)

Systematic measurements of total column ozone in various locations near the poles have shown that since about 1980 ozone has decreased (Solomon, 1999), causing concern in the scientific community. Data from the Total Ozone Mapping Spectrometer (TOMS) on the Nimbus 7 satellite show that this decrease is not exclusively a polar phenomenon and is observed globally (Bowman, 1988). This decrease is due to anthropogenic, ozone-depleting substances (ODS) such as CFCs, HCFCs and halons (Solomon, 1999). Ozone is constantly produced and destroyed in the stratosphere, as explained by Chapman (Chapman, 1930). The Chapman mechanism is given below:

$$O_2 + h\nu \longrightarrow O + O \qquad \lambda < 242\ nm \tag{2-19}$$

$$O + O_2 + M \longrightarrow O_3 + M \quad (2\text{-}20)$$

$$O_3 + h\nu \longrightarrow O_2 + O \quad 200 < \lambda < 1100\ nm \text{ (Grebenshchikov et al., 2007)} \quad (2\text{-}21)$$

$$O + O + M \longrightarrow O_2 + M \quad (2\text{-}22)$$

$$O_3 + O \longrightarrow 2O_2 \quad (2\text{-}23)$$

Where M is the molecules of air, and hν is the energy of the solar radiation. The role of air molecules is to stabilize O_3 by removing some of the energy from it and to put it precisely, it is to simultaneously achieve energy and momentum balance (McConnell and Jin, 2008). The production of ozone is balanced by its destruction in these reactions (equations (2-19) to (2-23)). The Chapman cycle is much too slow to account for, the amount of ozone and atomic oxygen in the atmosphere. In other words, the Chapman cycle produces too high an equilibrium amount of ozone. Therefore, other reactions are needed. Catalytic cycles are also important in destroying ozone. These reactions are as below:

$$XO + O \longrightarrow X + O_2 \quad (2\text{-}24)$$

$$X + O_3 \longrightarrow XO + O_2 \quad (2\text{-}25)$$

$$\text{Net: } O + O_3 \longrightarrow 2O_2 \quad (2\text{-}26)$$

Where X can be NO, OH, H, Cl or Br. The cycle above is important in the upper stratosphere, but in the lower stratosphere, due to lower concentrations of atomic oxygen, other reactions are important (McConnell and Jin, 2008). The following are examples of such reaction chains (McElroy et al., 1986):

$$Cl + O_3 \longrightarrow ClO + O_2 \quad (2\text{-}27)$$

$$\mathbf{Br + O_3 \longrightarrow BrO + O_2} \quad \textbf{(2-28)}$$

$$\mathbf{BrO + ClO \longrightarrow Br + ClO_2} \quad \textbf{(2-29)}$$

$$\mathbf{ClO_2 + M \longrightarrow Cl + O_2 + M} \quad \textbf{(2-30)}$$

$$\mathbf{Net: 2O_3 \longrightarrow 3O_2} \quad \textbf{(2-31)}$$

and,

$$\mathbf{ClO + ClO + M \longrightarrow Cl_2O_2 + M} \quad \textbf{(2-32)}$$

$$\mathbf{Cl_2O_2 + h\nu \longrightarrow Cl + ClO_2} \quad \textbf{(2-33)}$$

$$\mathbf{ClO_2 + M \longrightarrow Cl + O_2 + M} \quad \textbf{(2-34)}$$

$$\mathbf{2(Cl + O_3 \longrightarrow ClO + O_2)} \quad \textbf{(2-35)}$$

$$\mathbf{Net: 2O_3 \longrightarrow 3O_2} \quad \textbf{(2-36)}$$

The presence of CFCs has a catalytic effect in destroying ozone. The release of Cl from CFCs by photolysis causes the catalytic reactions. As an example of CFCs, Trichlorofluoromethane ($CFCl_3$) is used in the reactions below:

$$\mathbf{O_2 + h\nu \longrightarrow O + O} \quad \textbf{(2-37)}$$

$$\mathbf{ClO + O \longrightarrow Cl + O_2} \quad \textbf{(2-38)}$$

$$\mathbf{CFCl_3 + h\nu \longrightarrow CFCl_2 + Cl} \quad \textbf{(2-39)}$$

$$\mathbf{Cl + O_3 \longrightarrow ClO + O_2} \quad \textbf{(2-40)}$$

In the arctic stratosphere, when the temperature drops during the polar night, polar stratospheric clouds (PSCs) can form. The reactions that deplete ozone (reaction A 1 to A 7 in Appendix A)

happen heterogeneously on the particles of these clouds. These reactions produce active chlorine in the forms of HOCl, ClO_x and Cl_2 from inactive species (Solomon, 1999). Due to these reactions, the concentration of chlorine increases during the polar night, and in the spring when the sun rises, massive ozone depletion happens until the stratosphere becomes warm enough to prevent the PSCs from forming.

Other catalytic agents that effect ozone loss in the stratosphere are the nitrogen oxide radicals (NO_x). Nitric oxide, which is formed by the oxidization of N_2 at high temperatures (e.g. aircraft exhaust in the ozone layer) reacts with ozone and produces NO_2 (reaction (2-41)). The reactions described in reactions (2-41) to (2-43) have no effect on ozone loss but it creates a rapid exchange between NO and NO_2. A portion of the NO_2 molecules react with atomic oxygen from the reaction in (2-19) and create NO and O_2 as described in reaction (2-44). Reactions (2-41) and (2-44) form a catalytic cycle for ozone loss with a net effect described in reaction (2-45) (Jacob, 1999).

$$\mathbf{NO + O_3 \longrightarrow NO_2 + O_2} \qquad \textbf{(2-41)}$$

$$\mathbf{NO_2 + h\nu \longrightarrow NO + O} \qquad \textbf{(2-42)}$$

$$\mathbf{O + O_2 + M \longrightarrow O_3 + M} \qquad \textbf{(2-43)}$$

$$\mathbf{NO_2 + O \longrightarrow NO + O_2} \qquad \textbf{(2-44)}$$

$$\mathbf{Net: O_3 + O \longrightarrow 2O_2} \qquad \textbf{(2-45)}$$

The loss of NO_x radicals ends this catalytic cycle. In the daytime NO_x oxidizes by OH and produces nitric acid (HNO_3) described in reaction (2-46). In the night time, due to the absence of OH, NO_x is oxidized by O_3 and produces dinitrogen pentoxide (N_2O_5) as described in reactions (2-47) and (2-48).

$$NO_2 + OH + M \longrightarrow HNO_3 + M \quad (2\text{-}46)$$

$$NO_2 + O_3 \longrightarrow NO_3 + O_2 \quad (2\text{-}47)$$

$$NO_3 + NO_2 + M \longrightarrow N_2O_5 + M \quad (2\text{-}48)$$

The products of the above reactions, HNO_3 and N_2O_5 are non-radical and have long lifetimes of weeks for HNO_3 and hours for N_2O_5. These species are eventually converted back to NO_x.

2.7. Brewer-Dobson Circulation

Most of the ozone in the stratosphere is produced in the tropics where the sun is overhead by the reactions described in (2-19) and (2-20). But, most of the ozone is observed at higher latitudes. This displacement of ozone in the stratosphere is explained by the Brewer-Dobson circulation published by Brewer in 1949 (Brewer, 1949) and by Dobson in 1929 and 1956 (Dobson et al., 1929; Dobson, 1956).

Brewer observed the distribution of water vapour and helium in the troposphere and stratosphere and concluded that there must exist a circulation in which air over the equator enters the stratosphere where it cools and condensates and becomes very dry. Then it is transported to the temperate and polar regions where it sinks into the troposphere (Brewer, 1949). Dobson Observed that the distribution of ozone across latitude and altitude followed the same circulation pattern and described it as a slow poleward drift in the stratosphere with a descent of air in the polar region (Dobson et al., 1929).

The cause of the Brewer-Dobson circulation can be attributed to the dissipation of Rossby and gravity waves in the stratosphere (Holton et al., 1995). There are several models that describe the Brewer-Dobson circulation such as the Eulerian mean or Lagrangian mean circulation models

(Butchart, 2014). A study done by Butchart et al. in 2006 concluded that with anthropogenic climate change the Brewer-Dobson circulation will strengthen (Butchart et al., 2006). One of the most important impacts of a strengthening Brewer-Dobson circulation is its effect on the concentration and loss of ozone in the stratosphere (Bekki et al., 2011).

3. Stray Light Analysis of the Brewer Spectrophotometer

Measurements techniques of Ozone in the high latitudes received greater attention after ozone decline was observed in the Antarctic in the 1980s. The total column amount of ozone is lower in the tropical areas and becomes higher at high and mid-latitudes due to the Brewer-Dobson circulation. There is an annual variation in the ozone layer in the Arctic which is due to the changes in the Brewer-Dobson circulation as well as anthropogenic emissions and the presence of Chlorine, Bromine and NO_x in the atmosphere (Fioletov, 2008). During the polar night, PSC clouds form and during the spring the perturbed chemistry causes strong ozone depletion in the Arctic. The countries in the Arctic region such as Canada, have put an emphasis on ozone measurements in this region (Fioletov, 2008). Several spectrometers have been developed for monitoring the ozone layer. One of the spectrometers to make routine total column ozone measurements was the Dobson spectrometer developed by G.M.B. Dobson in the 1930s (Dobson, 1931). After that came the Brewer spectrometer in the 1970s (Brewer, 1973). This chapter discusses the Brewer spectrophotometer and includes a description of the development of a new algorithm for accounting for non-linearity in ozone measurements caused by instrument internal stray light.

3.1. Brewer Spectrophotometer

The Brewer spectrophotometer is a diffraction-grating, polychromator that produces monochromatic light at a set of 6 exit slits. It is a modified Ebert-Fastie spectrometer (Fastie, 1952) which measures total column amounts of ozone and sulphur dioxide as well as aerosol optical depth (Silva and Kirchhoff, 2004). There are two types of Brewers in use today; single Brewers (MarkII, Mark IV, Mark V) and Double Brewers (Mark III). The double Brewer (DB) spectrophotometer is the combination of two single Brewer (SB) optical frames where the exit slits

of the first spectrometer are the entrance slits of the second one. The first spectrometer disperses the light while the second one recombines it giving the polychromator a much greater capability for stray light rejection (Gröbner et al., 1998).

The history of the Brewer instrument starts with David Wardle producing a grating spectrometer to make stellar ozone measurements in the high Arctic. A more compact, multiwavelength instrument was designed by Wardle while a lecturer at the University of Toronto, in cooperation with Alan Brewer, Jim Kerr and Tom McElroy. The Brewer spectrophotometer was designed as a replacement for the Dobson instrument in the late 1970s (Brewer, 1973) and was made commercially available in 1982 (Redondas et al., 2014).

3.1.1. Instrument Description

The Brewer instrument consists of fore-optics, the spectrometer itself and a photomultiplier detector. The instrument is mounted on an azimuth tracking box that can point to the sun with a resolution of 0.02° and an accuracy of 0.2° (Kipp and Zonen, 2009).

The flow chart of the optics of a double Brewer spectrophotometer is presented in Figure 3-2. The fore-optics of the instrument starts with light entering the instrument through the UV-B port (item #1), angled window (item #2) or the calibration lamps (items #3 and #4). The zenith prism (item #5) is a prism rotated via a stepping motor and accommodates the four different inputs to the instrument. There are two test lamps. The first one, a mercury lamp, is used for calibrating the wavelength setting. The second one is a quartz-iodine lamp. Measurements of light from this lamp are used to track the relative sensitivity of the instrument as a function of wavelength. Light entering the instrument passes through a focusing lens (item #6) which projects an image from infinity onto an iris (item #7). A viewing port (item #7a) is provided which is used during direct

sun and moon measurements to check for pointing accuracy. The iris is closed to five solar diameters to reject scattered sky radiation. After passing through a second lens which collimates the light, it passes through two filter wheels (items #9 and #10). The first filter wheel has an open position and five neutral density filters that progressively scales the radiation by a factor of $1/\sqrt{10}$. The second filter wheel with six positions includes a ground-quartz filter and polarization filters. The ground-quartz filter is used when doing direct sun measurements and its purpose is to diffuse the solar radiation to decrease the measurement sensitivity to possible solar pointing errors. After the filter wheels, the light goes through an aperture (item #11) and a focusing lens (item #12) which produces an image of infinity (e.g.: the sun) on the spectrometer entrance slit (item #13). Another viewing port (item #13a) is provided at this point to provide a high sensitivity check of pointing (Kerr, 2010).

The core of the spectrometer starts at the entrance slit. The light is directed through a lens (item #14) which provides a correction for optical aberrations to a spherical mirror (item #15) which collimates the light before sending it to a holographic grating surface (item #16). The grating disperses the light and the spherical mirror focuses the spectrum onto a set of six exit slits (item #19).

The single Brewers Mark II and Mark IV use a 1800 line/mm grating in the second order and a 1200 line/mm grating in the third order respectively. The double Brewer Mark III uses two 3600 line/mm gratings in the first order (Kerr, 2010). The six exit slits (item #18) are spaced out to match the centre of six wavelength bands centred nominally at 302.1 nm, 306.4 nm, 310.1 nm, 313.5 nm, 316.8 nm and 320.0 nm. The 302.1 nm slit is used for wavelength calibration and the other slits are used for ozone and sulphur dioxide measurements (Kerr et al., 1984). A 45° mirror (item #17a) directs the light from the spherical mirror toward the exit slits. The six slits are covered

by a slit mask (item #18) which can be moved by a stepper motor to rapidly open and close the individual slits.

After the exit slits, in the case of the double Brewer, light is directed by a lens that images the gratings in the two halves of the instrument on each other into an identical spectrometer via a second 45º mirror. Light of all wavelengths is recombined at the second grating and focused onto the final exit slit by the spherical mirror. The detector is a photomultiplier which receives the output of the instrument and counts the number of received photons (Kerr, 2010).

In the case of a single Brewer, a Fabry lens is placed after the exit slits which images the diffraction grating on the photomultiplier cathode. A filter placed after the exit slits is included to reject light from other orders of the grating and to reduce stray light.

The optical layout of the instrument is shown in Figure 3-1. The optics fit in a weatherproof container as shown in Figure 3-3 with dimensions 70 by 46 by 34 cm with a weight of 34 kg. With a complete insulating jacket, it operates at temperatures of -80° to +40° centigrade (Kipp and Zonen, 2009).

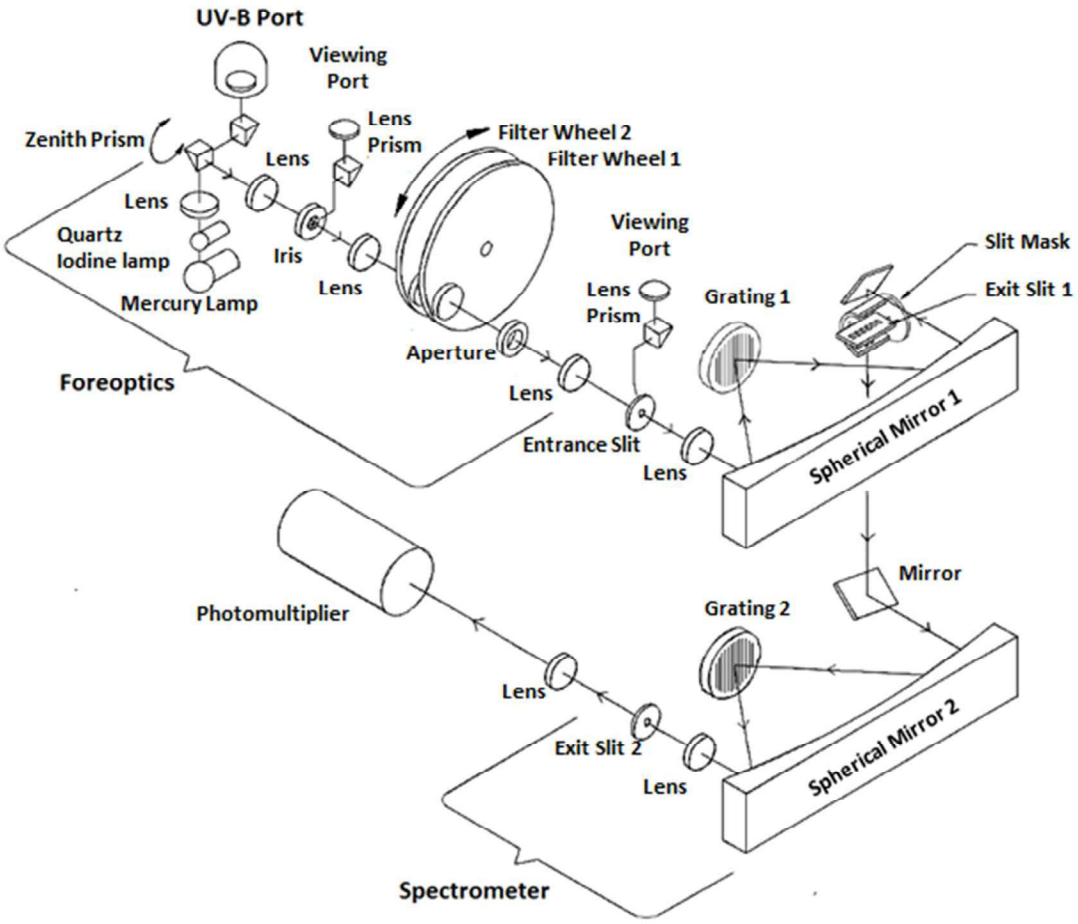

Figure 3-1: Optical layout of a double monochromator Brewer spectrophotometer. (Kipp and Zonen, 2009)

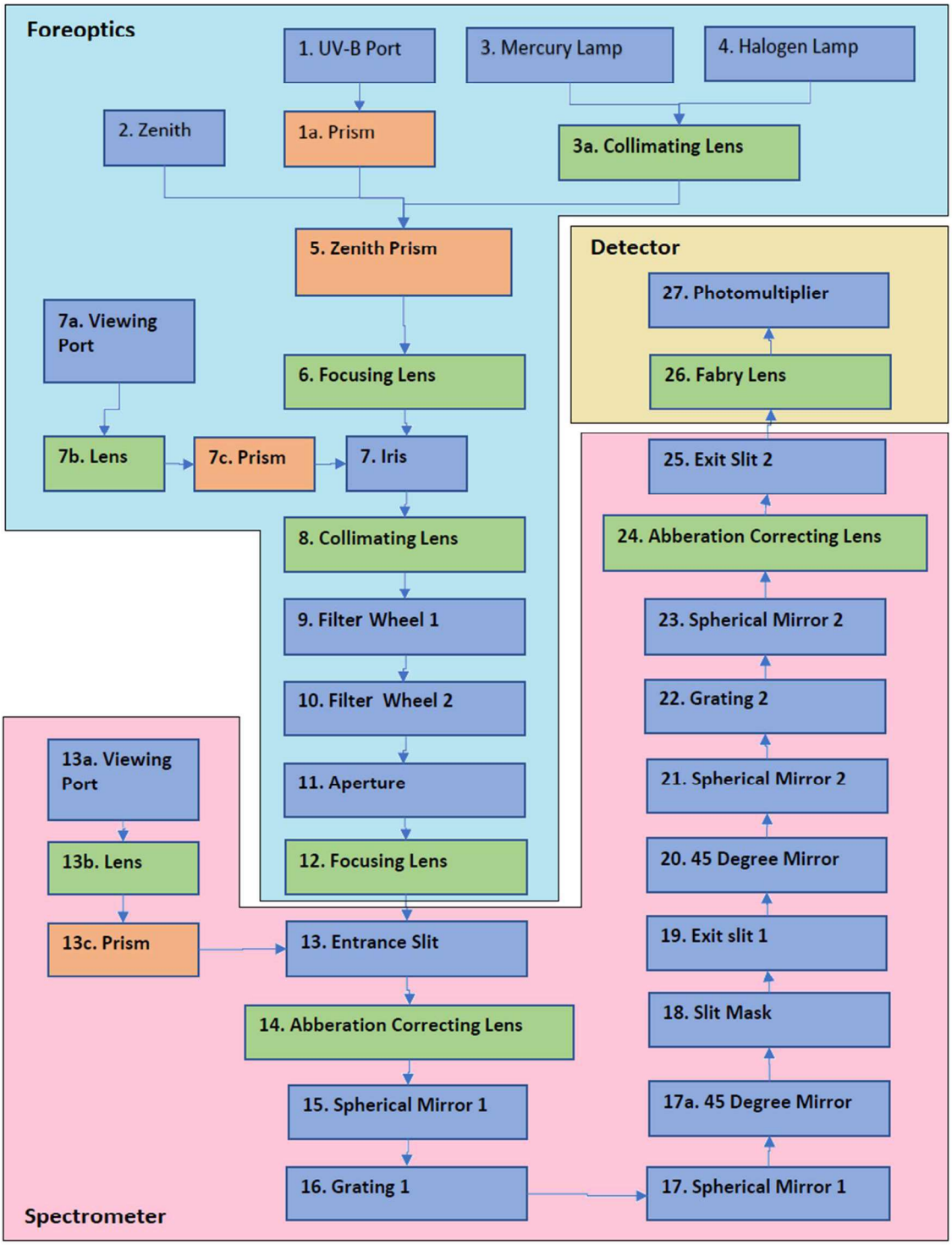

Figure 3-2: Flow chart of the optical layout of the double Brewer Spectrometer.

Figure 3-3: Double Brewer MKIII exterior configuration. (Kipp and Zonen, 2009)

3.1.2. Retrieval Algorithm for the Brewer Spectrophotometer

Beer's law which previously was derived in section 2.3.1, states that the absorbance of a material increases linearly with an increase in path length of light in a uniformly absorbing medium. Taking the logarithm in base e (ln) of equation (2-11) results in equation (3-1) which shows this relation where, $I_{\lambda 0}$ is the signal measured by the instrument with no atmosphere in the path and I_{λ} is the signal measured at the ground. In the Brewer instrument, ratios of the intensity of a short (I_S) and long (I_L) wavelength are measured. Equation (3-2) shows the Beer's law relation for a short and long wavelength pair where I_{S0} and I_{L0} are the intensity in the short and long wavelength respectively, before entering the column of absorbing material named the extraterrestrial or ETC value. Subtracting the two equations results in equation (3-3). The logarithm in base e (ln) of the ratio of the two intensities is named absorption function and is denoted with F for the value at ground and F_0 for the extraterrestrial value. The difference in the short and long wavelength absorption coefficient (α_S-α_L) is denoted by $\Delta\alpha$. This form of the Beer's law is shown in equation (3-4). In this form, the absorption function (F) has a linear relationship with the ozone airmass

(μ). Since the instrument does not directly measure F_0, by plotting F against μ and interpolating to zero airmass (μ=0) the value for F_0 can be calculated. This method is known as the Langley method. This method of using relative measurement is better, especially with ozone since the wavelengths in which ozone absorbs are close together and the differential absorption is rather large (refer to Figure 2-3 and Figure 2-8)

$$\ln(I_\lambda) = -\alpha_\lambda x\mu + \ln(I_{\lambda 0}) \quad (3\text{-}1)$$

$$\begin{cases} \ln(I_S) = -\alpha_S x\mu + \ln(I_{S0}) \\ \ln(I_L) = -\alpha_L x\mu + \ln(I_{L0}) \end{cases} \quad (3\text{-}2)$$

$$\ln\left(\frac{I_s}{I_L}\right) = -(\alpha_S - \alpha_L)x\mu + \ln\left(\frac{I_{s0}}{I_{L0}}\right) \quad (3\text{-}3)$$

$$F = -\Delta\alpha \cdot x \cdot \mu + F_0 \quad (3\text{-}4)$$

In the Brewer measurement, five wavelengths are used instead of just two. These wavelengths are 306.3, 310.1, 313.5, 316.8, and 320.0 nm. At each wavelength the instrument measures the photon counts, C_λ, where λ refers to the specific wavelength. In order to find the absorption function the logarithm of the photon counts multiplied by 10^4 is used which is denoted by L and is shown in equation (3-6). In the next step a weighting is applied to the logarithm of the photon counts. This weighting is denoted by w and is shown in equation (3-5). This weighting eliminates the absolute dependence on intensity and suppresses anything that is linear with respect to wavelength. It will also produce measurements that are more sensitive to ozone. A study done by Savastiouk et al. in 2005 shows the calculations for deriving the weighting vector (Savastiouk and McElroy, 2005).

The absorption function, F, is calculated by the product of the weighing vector, w, by L which is shown in equation (3-7).

$$\mathbf{w} = [\mathbf{0.0} \quad \mathbf{-1.0} \quad \mathbf{0.5} \quad \mathbf{2.2} \quad \mathbf{-1.7}] \tag{3-5}$$

$$\mathbf{L} = \mathbf{log}(\mathbf{C_\lambda}) \cdot \mathbf{10^4} \tag{3-6}$$

$$\mathbf{F} = \mathbf{w} \cdot \mathbf{L} = [\mathbf{0.0} \quad \mathbf{-1.0} \quad \mathbf{0.5} \quad \mathbf{2.2} \quad \mathbf{-1.7}] \cdot \mathbf{log}(\mathbf{C_\lambda}) \cdot \mathbf{10^4} \tag{3-7}$$

For observations made at the Earth's surface, Beer's law can be written as:

$$\mathbf{log}(\mathbf{I_\lambda}) = \mathbf{log}(\mathbf{I_{0\lambda}}) - \boldsymbol{\beta_\lambda}\mathbf{m} \times \frac{\mathbf{P}}{\mathbf{P_0}} - \boldsymbol{\tau_\lambda}\,\mathbf{sec}(\mathbf{SZA}) - \boldsymbol{\alpha_\lambda}\mathbf{X}\boldsymbol{\mu} \tag{3-8}$$

Where I_λ is the measured intensity at Earth's surface at wavelength λ.

$I_{0\lambda}$ is the extraterrestrial intensity at wavelength λ.

β_λ is the Rayleigh scattering coefficient at λ.

m is the effective radiation path length of light through the atmosphere.

P is the pressure at the height the measurement is taken.

P_0 is the standard pressure at sea level.

τ_λ is the aerosol optical depth at λ.

sec(SZA) is the secant of the solar zenith angle (SZA).

α_λ is the ozone absorption coefficient at λ.

X is the column amount of Ozone.

μ is the ratio of direct pathlength to vertical path length in the atmosphere (Kerr, 2010).

If the ratio of wavelength pairs is considered and the weighting discussed in equation (3-7) is applied, the following equation is derived:

$$\mathbf{F} + \Delta\boldsymbol{\beta}\mathbf{m} = \mathbf{F_0} - \Delta\boldsymbol{\tau}\,\mathbf{sec}(\mathbf{SZA}) - \Delta\boldsymbol{\alpha}\mathbf{x}\boldsymbol{\mu} \tag{3-9}$$

Where Δα is the difference in the ozone absorption coefficients of the two wavelengths and Δβm is the difference between the Rayleigh scattering coefficients of the two wavelengths. The aerosol

scattering term, $\Delta\tau$ sec(SZA), is negligible because it is linear with respect to wavelength over a short range of wavelengths and becomes negligible. The Rayleigh scattering term, $\Delta\beta m$, is calculated via the tabulated Rayleigh scattering coefficients of Bates 1984 (Kerr, 2010). Therefore, the total column amount of ozone is calculated as follows:

$$\mathbf{x = (F_0 - F - \Delta\beta m)/\Delta\alpha\mu} \qquad \textbf{(3-10)}$$

Each instrument must be calibrated to obtain values for the extraterrestrial absorption function (F_0) and the effective ozone absorption coefficient ($\Delta\alpha$). One of the ways to find these calibration constants is to take many side-by-side measurements with a calibrated instrument. The calibrated instrument, which is the reference, measures the total column ozone amount (X in equation (3-9)) with an accuracy of 0.5%. The un-calibrated instrument measures F values. When $F+\Delta\beta m$ is plotted against ozone slant column amount, $X\mu$, where, X comes from the calibrated instrument, the plot should be linear where the slope of the plot is $\Delta\alpha$ and the y-intercept is F_0. To find the y-intercept, the plot is extrapolated to zero. This method is called the Langley method (Kerr et al., 1985).

Another way to find these calibration constants is to use the Langley method when a reference instrument is not present. In this case the instrument slit function is convolved with the absorption coefficients of Bass and Paur (1985) to calculate the effective ozone absorption coefficient for each slit. F_0 is calculated by extrapolating the plot of the absorption function versus ozone airmass, to zero (Kerr et al., 1985).

It is assumed that daily ozone values do not vary when using the above methods. That is why primary calibrations are done at sites like Mauna Loa, Hawaii in the tropics or subtropics where the ozone column tends to be very stable over the day and from day to day. To avoid errors arising from this assumption, measurements for several days are taken and the calibration constants are

averaged over the number of days (Kerr, 2010).

3.2. Stray Light in the Brewer Spectrophotometer

It is now known that Single-monochromator Brewer Spectrophotometer ozone and sulphur dioxide measurements suffer from non-linearity at large ozone slant column amounts due to the presence of instrumental stray light caused by scattering within the optics of the instrument. Because of the large gradient in the ozone absorption spectrum in the near-ultraviolet, the atmospheric spectrum measured by the instrument possess a very large gradient in intensity in the 300 to 325 nm wavelength region. This results in a significant sensitivity to stray light when there is more than 1000 Dobson Units (DU) of ozone in the light path. As the light path (airmass) through ozone increases, the stray light effect on the measurements also increases. The measurements can be on the order of 10% low for an ozone column of 600 DU and an airmass factor of 3 (1800 DU slant column amount) which is one example of conditions that produce large, slant-column amounts.

As in all optical instruments, stray light is also present in Brewer spectrophotometers. The source of stray light in a monochromator is light scattering from the various optical surfaces and walls of the instrument. In the Brewer instrument the main source appears to be imperfect dispersion from the dispersing element, in this case a holographic diffraction grating (Silva and Kirchhoff, 2004).

Instrumental stray light becomes much more significant when the source of energy (e.g. the sun), or detector sensitivity changes rapidly as a function of wavelength. When measuring ozone, as the solar zenith angle increases the importance of instrumental stray light increases due to the increasing gradient in intensity towards the longer wavelengths. One way to quantify the effect of stray light is to observe how the measurements deviate from linearity according to Beer's Law at large ozone slant paths. (Slavin, 1963).

Comparisons between measurements of SB and DB have been made by Bais et al. which show a much lower effect of stray light in measurements from the DB. At wavelengths below 300 nm the SB shows a 10% underestimation in ozone column amounts when there is more than 1000 DU of ozone present (Bais et al., 1996). At wavelengths above 300 nm this difference may also be significant.

According to the WOUDC website over 200 Brewers, single and double, are being used in more than 40 countries and 100 stations to measure ozone column amounts (WOUDC, 2016; Savastiouk, 2006). Many single Brewers are being replaced by double Brewers and, therefore, new measurements may show a false increase in ozone column amounts due to the effect of lower stray light in the DB, particularly for measurements made at large solar zenith angles (and ozone slant paths). In this chapter a new method is introduced that corrects for the effect of stray light in the data from the SB to provide more accurate reprocessed SB data.

Primary calibrations for the Brewer instrument are carried out at Mauna Loa Observatory in Hawaii and Izana Observatory in Tenerife. They are done using the Langley plot method to extrapolate a set of measurements made under a constant ozone vertical column to an extraterrestrial calibration constant. Since the effects of a small non-linearity at moderate ozone paths may still be important, a better calibration procedure should account for the non-linearity of the instrument response. Studies involving the scanning of a laser source have been used to characterize the stray light response of the Brewer, but until recently these data have not been used to elucidate the relationship between the stray light response and the ozone measurement non-linearity.

In a study done by Karppinen et al. (2015), a method for correcting stray light has been presented that uses an additive correction which is determined via instrument slit characterization and a

radiative transfer model simulation and is then applied to the single Brewer data (Karppinen et al., 2015). The European Brewer Network is also applying stray light corrections which include an iterative process that results in correcting the single Brewer data to agree with double Brewer data (Rimmer et al., 2018; Alberto Redondas et al., 2018). Both these methods rely on a calibrated instrument such as a double Brewer to characterize the instrument and to provide a correction for stray light.

This thesis presents a simple and practical method of correcting for the effects of stray light that includes a non-linear mathematical model of the instrument response and a retrieval approach that calculates the best values for the model parameters. This non-linear approach is based on the Langley method. The parameterization used in the non-linear model was validated using an instrument physical model simulation discussed in section 3.3. The non-linear model can then be used in reverse to provide more accurate ozone values up to a defined maximum ozone slant path. This method can be applied independently to any Brewer instrument and correct for the effects of stray light.

3.3. Physical Model of the Brewer Spectrophotometer

In the physical model the slit function of the instrument as measured is used to characterize the stray light. For this purpose, a Helium Cadmium (HeCd) laser at 325 nm is used as a source and all wavelengths starting at 290 nm for the SB and DB are measured. The photon count rate measured by the Brewer is the integral of the spectral intensities on all wavelengths weighted by the slit function. These measurements were performed by Omid Moeini and published in a paper co-authored by the writer of this thesis in the journal of Atmospheric Measurement Techniques (Moeini et al., 2018). Figure 3-4 shows the measured slit function of a SB No. 009 and DB No. 119. The dots show the measurements made by the HeCd laser and the solid lines show the best

fit to the measurements. Under ideal conditions, without the effect of stray light, the fit to the slit function would be a trapezoid with its wings extending to zero. But in reality, as seen in the figure, the fit is trapezoidal from FWHM to the peak, but, the wings follow a Lorentzian function and extend to a horizontal line which is not at zero. The difference between the wings of the SB and DB slit functions shows the presence of stray light. The horizontal fit line is approximately 10^{-4} for SB and 10^{-6} for DB which shows that the effect of stray light is more pronounced in the SB measurements than the DB (Moeini et al., 2018). The slit function as measured this way must be reversed when it is applied to a source in wavelength space to predict the instrument response. This is to account for the instrument output being the inverse of the wavelength of the line source.

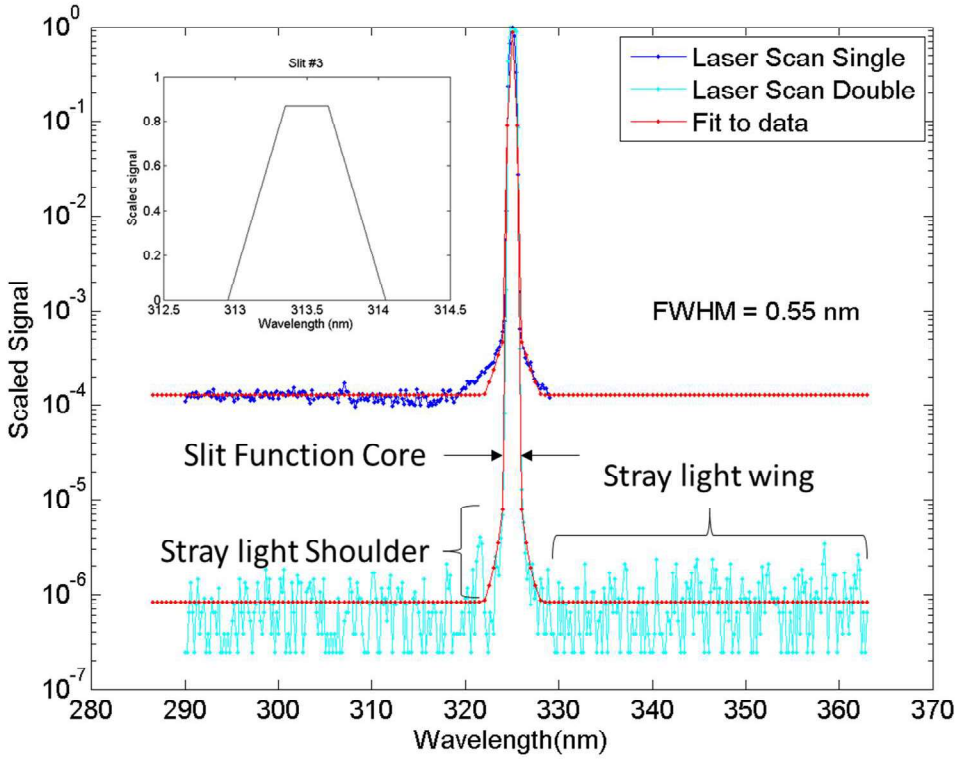

Figure 3-4: Slit function measurements made with a HeCd-laser for single Brewer No. 009 and double Brewer No. 119 and their fitted slit functions. The ideal slit function is shown within the graph titled Slit#3. (Moeini et al., 2018)

3.4. Mathematical Model of the Brewer Spectrophotometer

This thesis describes a new technique to compensate for the effects of stray light on the measured ozone column amount. A sensitive method for measuring the effect of instrumental stray light is by using the deviation of the measurements from Beer's law linearity at large ozone slant paths (Slavin, 1963).

Under realistic conditions, equation (3-4) deviates from its linear form at large airmass values in the presence of instrumental stray light. To account for this non-linearity, a mathematical model for the absorption function measured by the instrument is defined. This non-linear model incorporates a correction to the absorption function which includes a non-linearity factor. It is also dependent on ozone in a cubic form.

This new model accounts for the non-linearity in measuring ozone column amount. It also accounts for filter changes and deadtime in the instrument. This instrument model is presented in equation (3-11) where, F_m is the model absorption function, α is the absorption coefficient of ozone, μ is ozone airmass, X is ozone column amount, F_0 is the absorption function at zero airmass, γ is the non-linearity factor, b_j is the filter change factor and ND_j is the filter vector. Different powers for the ozone term in the non-linear model have been experimented with and it was found that the model described in equation (3-11) agreed best with the observations collected in Mauna Loa in summer and fall of 2010. The power term can only be determined numerically. The reason for that will be explained further on in the chapter when the mathematics is being developed.

$$\mathbf{F_m = F_0 + \alpha \cdot \mu \cdot X - \gamma \cdot (\alpha \cdot \mu \cdot X)^3 + \sum_j b_j \cdot ND_j} \qquad \mathbf{(3\text{-}11)}$$

The components of the model (equation (3-11)) to be determined are $v_k = (X, \gamma, b_j, F_0)$, where k indicates the number of components of v that are to be retrieved. The non-linear model is used to

determine the k components of vector v by finding suitable values for v that minimize the square error between the model and the observations. This method is described in the following.

In the first step, initial values for v_k are estimated. To predict an initial value for F_0 a conventional Langley (linear) plot is used, where the absorption function versus airmass is plotted. As an example, the absorption function versus airmass of the single Brewer #009 is plotted in Figure 3-5, where the dots show the instrument measurements and the line represents the Langley regression. The measured values tend to deviate from the linear model as the airmass increases. The plot is quite linear at airmass values smaller than 2, therefore, this part of the data is used to apply the least-squares method using the linear model (equation (3-4)) to find the slope ($-\Delta\alpha.x$) and the intercept at zero airmass (F_0). The initial value of γ and b_j should be very small, therefore an initial value close to zero (0.0001) is chosen.

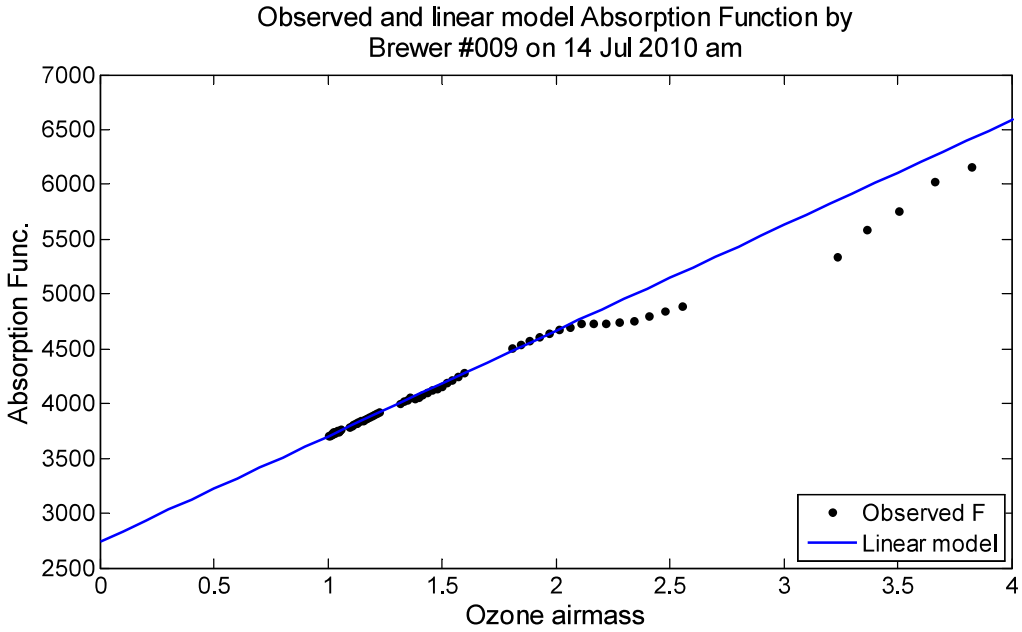

Figure 3-5: Absorption function versus ozone airmass for the single Brewer #009. The fitted linear model is presented as the blue line and the black dots represent the observations.

The non-linear model also uses the least-squares method to determine v_k. In this process the square error, SE, between the absorption function measured by the instrument, F_i, and the modelled absorption function, F_{mi}, for all the N observations will be minimized. The square error is shown in equation (3-12). The index i denotes the observation number from 1 to N. Therefore, the derivative of the difference of the observations and the modeled absorption function with respect to all the components of vector v_k should be zero as shown in equation (3-14).

$$\mathbf{SE} = \sum_{\mathbf{i=1}}^{\mathbf{N}} (\mathbf{F_i} - \mathbf{F_{mi}})^{\mathbf{2}} \qquad \textbf{(3-12)}$$

Because the model is non-linear in ozone, several iterations of the solution are made to arrive at an accurate result. equation (3-13) to equation (3-24) show the solution cycle. This cycle is repeated until SE becomes minimized. The solution will be the final values determined for vector v_k. (equation (3-24)).

$$\frac{\partial}{\partial \mathbf{v_k}}(\mathbf{SE}) = \frac{\partial}{\partial \mathbf{v_k}}\left[\sum_{\mathbf{i=1}}^{\mathbf{N}} (\mathbf{F_i} - \mathbf{F_{mi}})^{\mathbf{2}}\right] = \mathbf{0} \qquad \textbf{(3-13)}$$

Substituting $\mathbf{\Delta F_i = F_i - F_{mi}}$

$$\frac{\partial}{\partial \mathbf{v_k}}(\mathbf{SE}) = \mathbf{2}\sum_{\mathbf{i=1}}^{\mathbf{N}} [\mathbf{\Delta F_i}] \frac{\partial(\mathbf{F_{mi}})}{\partial \mathbf{v_k}} = \mathbf{0} \qquad \textbf{(3-14)}$$

A better solution can be found with a step, Δv away :

$$\Longrightarrow \frac{\partial}{\partial \mathbf{v_k}}(\mathbf{SE}) = \mathbf{2}\sum_{\mathbf{i=1}}^{\mathbf{N}} \left[\mathbf{\Delta F_i} - \frac{\partial(\mathbf{F_{mi}})}{\partial \mathbf{v_n}} \mathbf{\Delta v_n}\right] \cdot \frac{\partial(\mathbf{F_{mi}})}{\partial \mathbf{v_k}} = \mathbf{0} \qquad \textbf{(3-15)}$$

$$\Rightarrow \sum_{i=1}^{N}\left[\Delta F_i \frac{\partial(F_{mi})}{\partial v_k}\right] - \Delta v_n \sum_{i=1}^{N}\left[\frac{\partial(F_{mi})}{\partial v_n}\frac{\partial(F_{mi})}{\partial v_k}\right] = 0 \quad \textbf{(3-16)}$$

The derivative of the non-linear model (equation (3-11)) with respect to the k^{th} or n^{th} components of v_k at each measurement point, i, is substituted with the Jacobian matrices M_{ik} and M_{in} respectively. The equations used to calculate these Jacobian matrices can be found in Appendix B.

$$M_{ik} = \frac{\partial(F_{mi})}{\partial v_k} \quad \textbf{(3-17)}$$

$$M_{in} = \frac{\partial(F_{mi})}{\partial v_n} \quad \textbf{(3-18)}$$

Substituting these matrixes in equation (3-16) gives:

$$\sum_{i=1}^{N}[\Delta F_i M_{ik}] - \Delta v_n \sum_{i=1}^{N}[M_{in} M_{ik}] = 0 \quad \textbf{(3-19)}$$

$$H = \sum_{i=1}^{N}[\Delta F_i \cdot M_{ik}] \quad \textbf{(3-20)}$$

$$K = \sum_{i=1}^{N}[M_{in} \cdot M_{ik}] \quad \textbf{(3-21)}$$

H and K are matrices with dimensions N and k. Substituting them into equation (3-19) gives:

$$H - \Delta v_n K = 0 \quad \textbf{(3-22)}$$

$$\Rightarrow \Delta v_n = K^{-1}.H \quad \textbf{(3-23)}$$

And the solution becomes:

$$v_{k_{n+1}} = v_{k_n} + \Delta v_n \quad \textbf{(3-24)}$$

To improve accuracy, a weighting of the observations is needed. From Figure 3-5, it can be seen that the measurements are denser at smaller airmass than at larger airmass. Therefore, the model will put more emphasis on these points and estimate the components of v_k accordingly. To reduce this problem, before applying the model, the data are multiplied by airmass and the uncertainty ($\frac{1}{\sigma^2}$) associated with the counts as shown in equation (3-25). j is the number of wavelengths which in this case is 1 to 5, $Counts_j$ is the photon count for each of the 5 wavelengths and w_j is the weighting for each wavelength. With this weighting the difference between the model and measurements is exaggerated at large airmass and, therefore, carry more weight.

$$\sigma_i = \frac{1}{\sqrt{N_i}} = \frac{1}{\sqrt{\sum_{j=1}^{5}(Counts_{i,j} \cdot w_j)}} \quad \textbf{(3-25)}$$

Dead Time

The dead-time of an instrument is important to account for. In a Brewer instrument the detector photomultiplier output pulses have a finite width of ~30 ns. If two or more photons arrive at the detector within that time they will be counted as one count. This will cause an error in counting the photons. This error associated with the dead-time increases with count rate. The dead-time is modelled in equation (3-26) where C is the measured photon count, C_0 is the true photon count and τ is the dead-time (Kerr, 2010).

$$C = C_0 \, e^{-C_0 \tau} \quad \textbf{(3-26)}$$

To calculate the dead-time, measurements are done with the Brewer through two exit slits simultaneously and separately through each exit slit. Measurements are made with exit slits 2 and 4 resulting in C_2 and C_4 and measurements are done with both exit slits open resulting in C_{2+4}. If equation (3-26) is written for each case, there will be 3 equations with 4 unknowns which are C_{02},

C_{04}, C_{02+4} and τ. A forth equation, $C_{02+4} = C_{02} + C_{04}$, makes it possible to find the dead-time (Kerr, 2010). The deadtime varies from instrument to instrument and can also change with time. For low ozone slant columns and high intensity solar radiation, a small change of 10 ns in the deadtime can cause an error of up to 5% in the measured total ozone column amount (Fountoulakis et al., 2016). This procedure is not done on a regular basis and the dead-time of an instrument may change over time, therefore, a correction for the dead-time must be performed in the non-linear model.

To account for the dead-time prediction, when calculating the derivative of the square error, SE, the derivative of F_i with respect to dead-time must also be considered. In this case, v_k is τ and thus equation (3-17) becomes equation (3-27).

$$\mathbf{M_{ik}} = \frac{\partial(\mathbf{F_{mi}})}{\partial \boldsymbol{\tau}} \qquad \textbf{(3-27)}$$

Adding a deadtime correction term (τ') to equation (3-26) gives:

$$\mathbf{C' = C\, e^{C_0 \cdot}} = \mathbf{C_0\, e^{-C_0\, \tau}\, e^{C_0\, \tau'} = C_0\, e^{-C_0(\tau - \tau')} = C_0\, e^{-C_0(\Delta \tau)}} \qquad \textbf{(3-28)}$$

As discussed in section 3.1.2, the absorption function for the Brewer instrument is calculated via equation (3-7). To include deadtime correction in the non-linear absorption function model, equation (3-28) is incorporated into equation (3-7):

$$\begin{aligned} \mathbf{F_m} &= \mathbf{w.\,(10^4 \log(C'_\lambda)) = 10^4\, w. \log\left(C_{\lambda 0}\, e^{-C_{\lambda 0}(\Delta \tau)}\right)} \\ &= \mathbf{10^4\, w.\,(\log\left(C_{\lambda 0}\right) - C_{\lambda 0}(\Delta \tau))} \end{aligned} \qquad \textbf{(3-29)}$$

Where the subscript $\boldsymbol{\lambda}$ is used to denote the 5 wavelengths the Brewer records measurements in. Substituting equation (3-29) in to equation (3-27) to find the derivative of F_m with respect to deadtime gives:

$$\mathbf{M_{ik}} = \frac{\partial \mathbf{F_m}}{\partial \boldsymbol{\tau}} = \mathbf{10^4\ w.}\left(\frac{\partial}{\partial \boldsymbol{\tau}}\left(\mathbf{log}(\mathbf{C_{\lambda 0}})\right) - \frac{\partial}{\partial \boldsymbol{\tau}}(\mathbf{C_{\lambda 0}}(\Delta\boldsymbol{\tau}))\right) = \mathbf{-10^4\ w.\, C_{\lambda 0}} \quad \textbf{(3-30)}$$

3.5. Model Application and Results

The non-linear model was applied to the data collected by two Brewer instruments #009 (single Brewer) and #119 (Double Brewer) stationed at Mauna Loa at -155.5° longitude and 19.5° latitude and as an example the results for 14th July 2010 and 25th October 2010 are presented. The non-linear mathematical model (equation (3-3)) was applied to the data and model parameters were retrieved. The non-linearity term, filter change term and dead-time term were applied in reverse to the data to calculate corrected values for the absorption function and ozone values in Dobson units.

The observed, modelled and corrected absorption function (F) values for single Brewer #009 for 14th July 2010 are plotted in Figure 3-6. In the observed and modelled F, the filter change is clearly visible, causing a jump in the intensity of light received by the detector. This sudden fluctuation in intensity is modelled using the non-linear model and is corrected to give a more linear F with respect to ozone slant column. The same has been plotted for the Double Brewer #119 in Figure 3-7 where the observed, modelled and corrected values are very close to linear with respect to airmass and thus the correction is less than 1%.

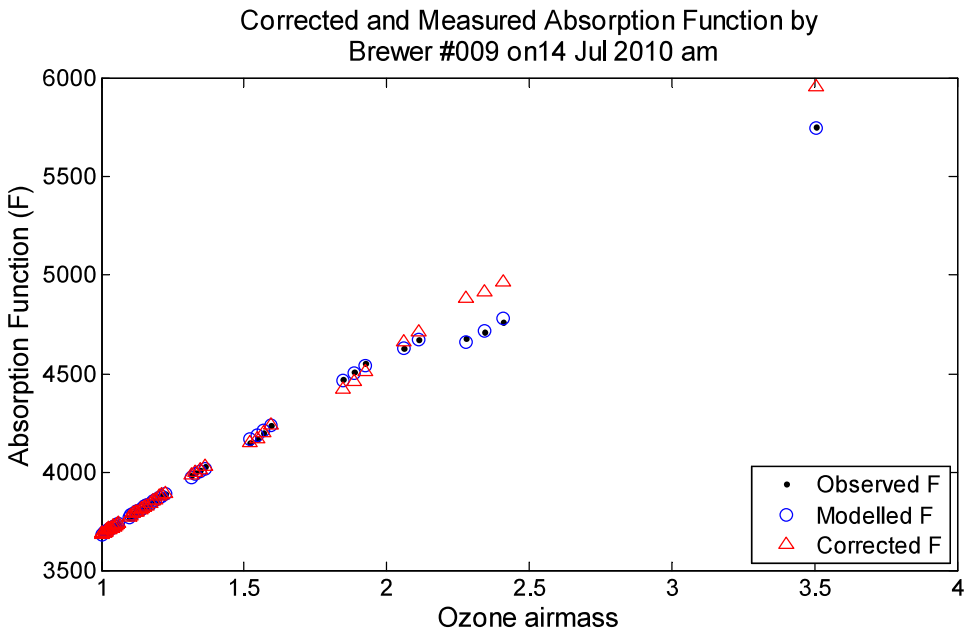

Figure 3-6: Observed, Modelled and Corrected absorption function (F) for single Brewer #009. The step change in observed F shows the filter change and the non-linear model corrects for the sudden drop in F.

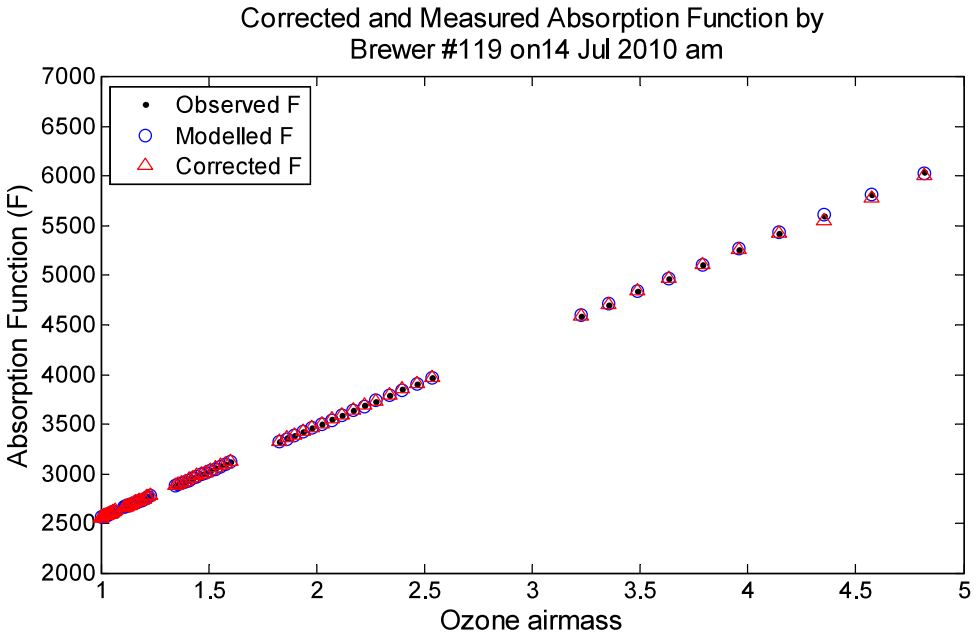

Figure 3-7: Observed, Modelled and Corrected absorption function (F) for Double Brewer #119. The corrected values are very close to observed due to the Double Brewer's ability to reject stray light better than the single Brewer.

Using the corrected absorption function the corrected ozone values were calculated. The measured and corrected ozone column amount in Dobson units versus ozone airmass for both the single (#009) and double (#119) Brewers for 14th July 2010 and 25th October 2010 are illustrated in Figure 3-8 and Figure 3-10 respectively. There is some nonlinearity observed for the single Brewer at low airmass which is corrected to an amount slightly higher than the double Brewer corrected amounts. The ratios of single to double Brewer measurements before and after applying corrections for 14th July 2010 and 25th October 2010 are plotted in Figure 3-9 and Figure 3-11 respectively. The corrected ratio in red is closer to linearity than the uncorrected ratio in black.

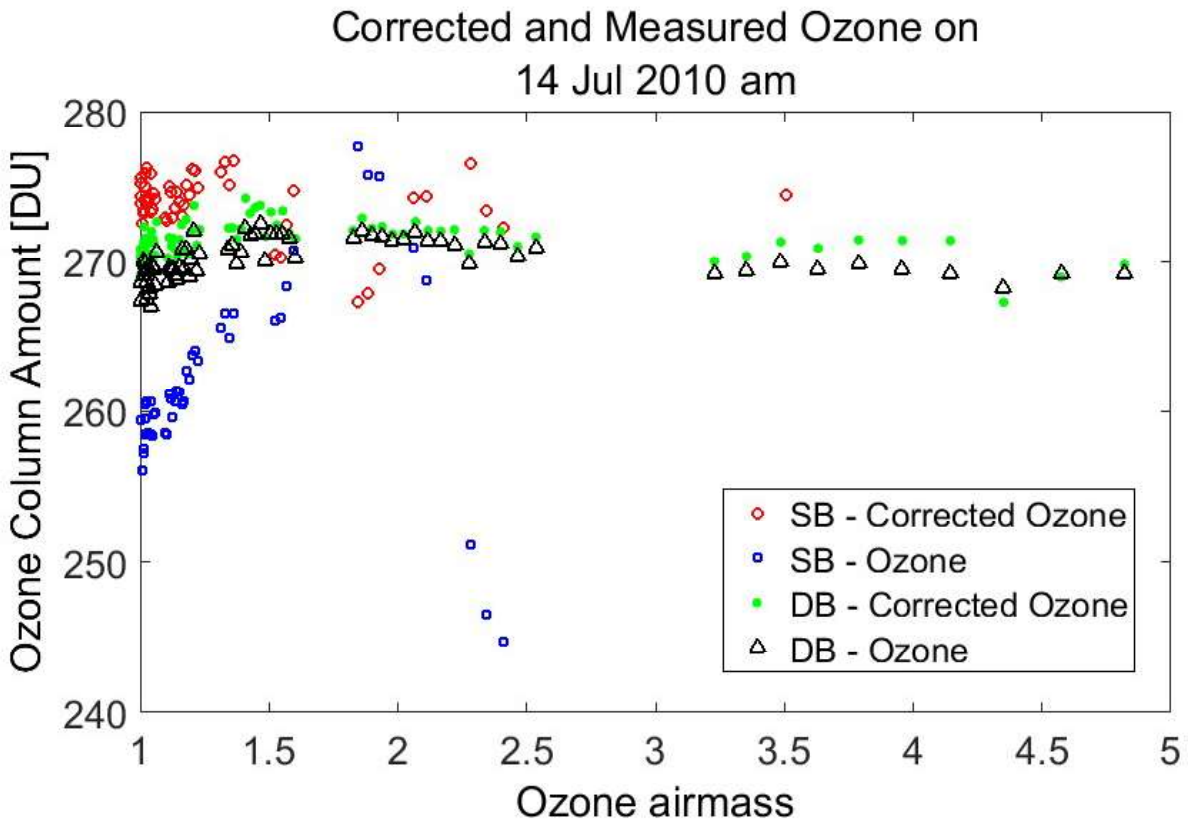

Figure 3-8: Corrected and Measured Ozone by Single (#009) and Double (#119) Brewer on 14th July 2010.

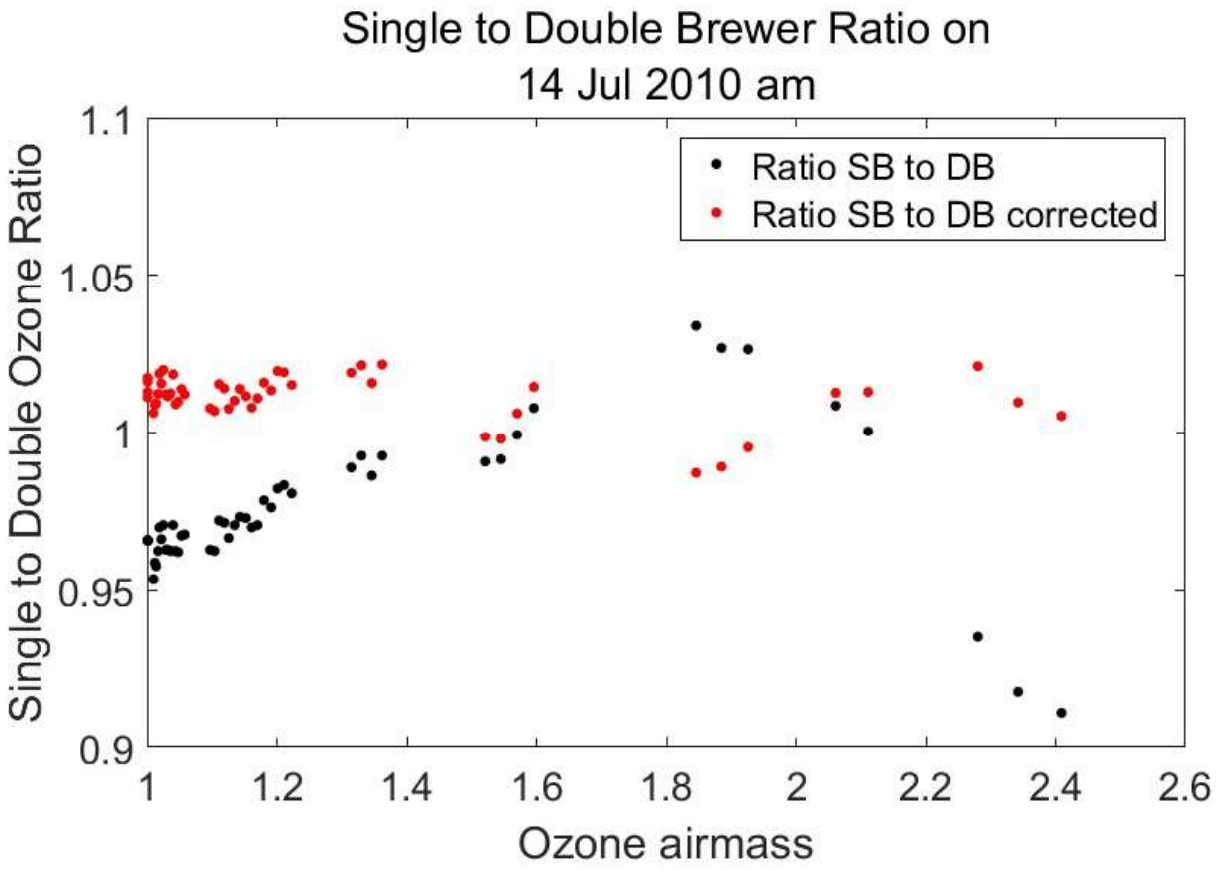

Figure 3-9: Ratio of measured and corrected Single to Double Brewer Ozone values for data points measured within 5 minutes of each other on 14th July 2010.

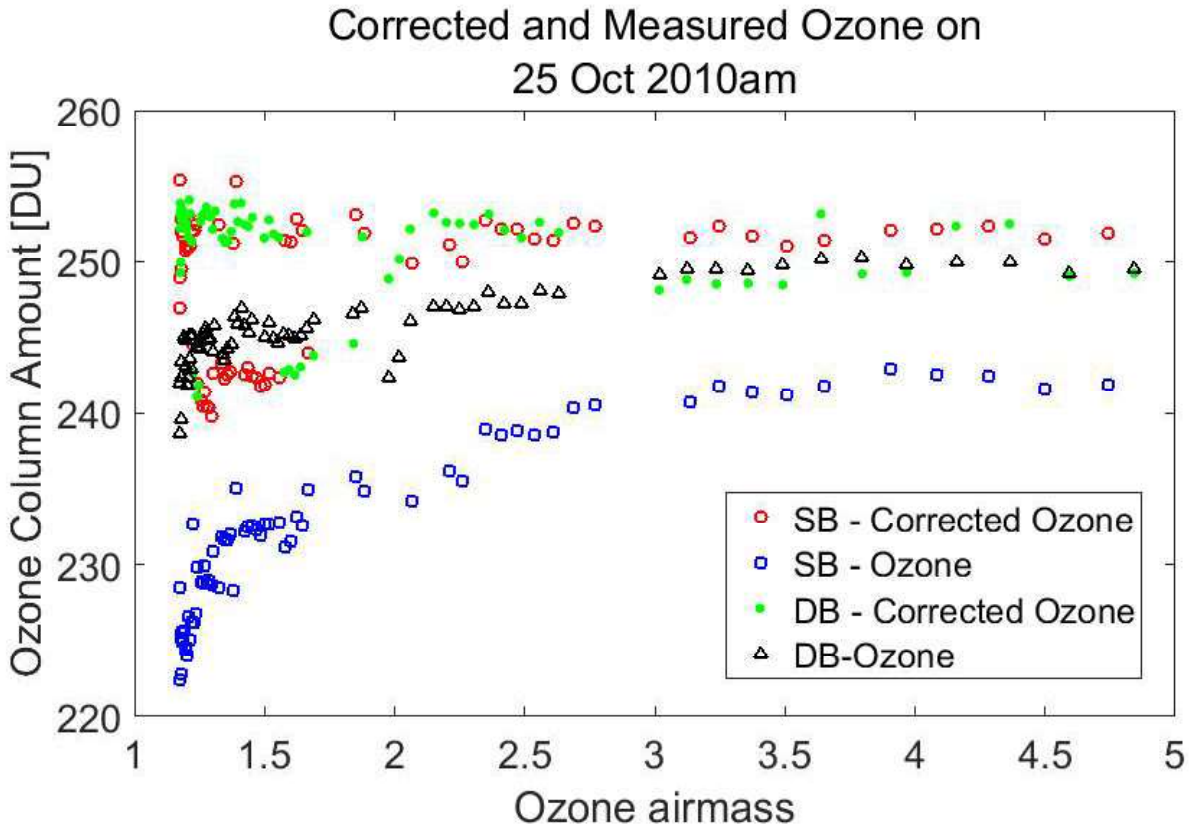

Figure 3-10: Corrected and Measured Ozone by Single (#009) and Double (#119) Brewer on 25th October 2010.

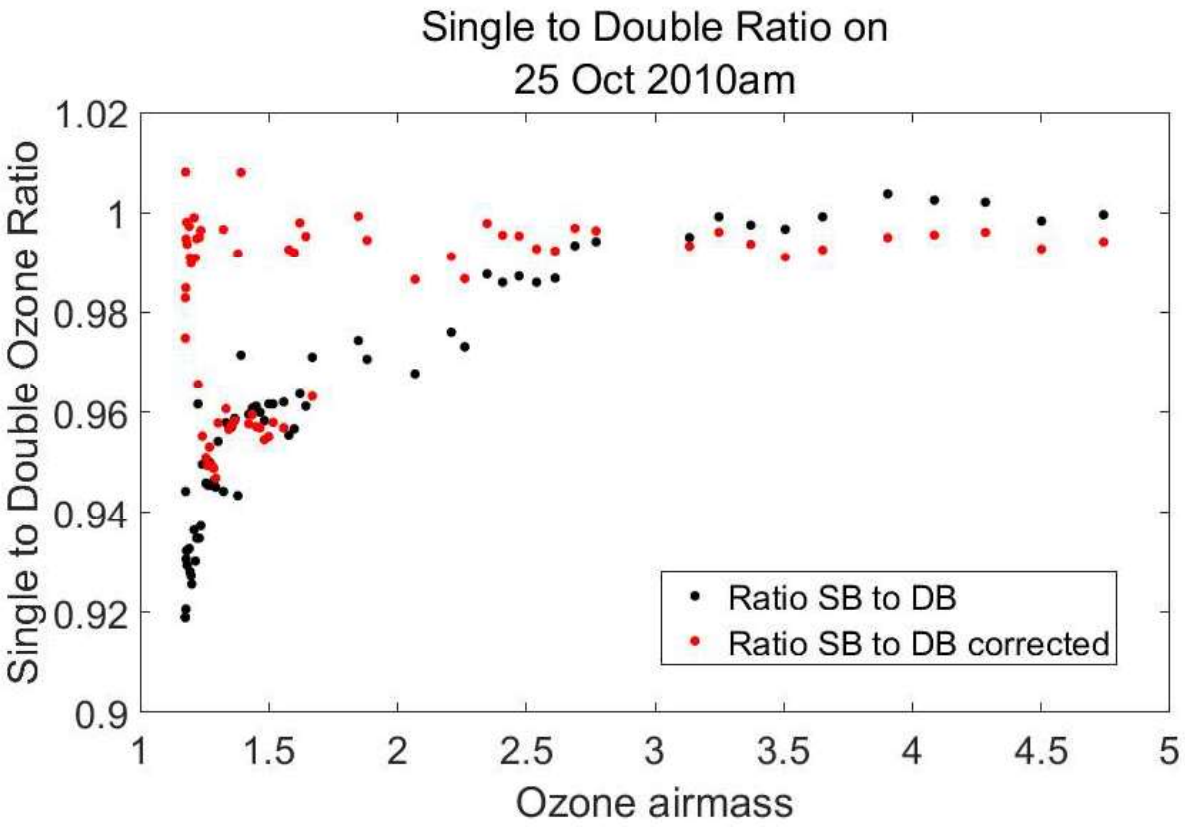

Figure 3-11: Ratio of measured and corrected Single to Double Brewer Ozone values for data points measured within 5 minutes of each other on 25th October 2010.

3.6. Discussion

There is a difference of up to 10% in the ozone column amount measured by the single and double Brewers (single lower than double) as observed at large ozone slant paths and illustrated in Figure 3-8 for 14th July 2010 and in Figure 3-10 for 25th October 2010. The mathematical model presented in this chapter accounts for this non-linearity in the data collected by single Brewers. Applying corrections to the historical data of single Brewers is essential, as it will eliminate errors due to, the effect of stray light on the ozone measurements.

The double Brewer is relatively unaffected by stray light (Gröbner et al., 1998), and as the single Brewers in ozone measurement stations around the world are being replaced by the more advanced

double Brewer, a slight increase in ozone amounts may be observed, particularly in those months in which observations must necessarily be made at large solar zenith angles. This may lead to a false assumption that the total ozone column amounts are showing an increase where this may not be the case.

The departure from linearity is more prominent in large ozone slant paths as is seen in Figure 3-6, Figure 3-8 and Figure 3-10. The non-linearity related to large airmass values becomes more prominent in the high-latitude regions, such as the Arctic, where the sun is at large solar zenith angles most of the year. It is also difficult to take reference Brewer instruments to the Arctic for calibration purposes. To provide an accurate onsite method to correct the ozone data for non-linearity, the process described in this chapter is recommended.

Future steps for this research would be to apply this method to historical data. Data processed using the new methodology leads to a more accurate absolute calibration of single Brewers and an improved method to properly transfer calibration constants among single and double Brewers.

4. Instrument development for Nadir Observations

This chapter discusses the design and development of a new atmospheric measurement instrument intended to demonstrate a number of technologies that would lead to the design of a satellite instrument. This instrument which is named an Imaging Fourier Transform Spectrometer (IFTS) will be the first of its kind to make continuous, diurnal measurements of carbon dioxide (CO_2), methane (CH_4) and air column (oxygen; via the A-band) utilizing a Fourier Transform Spectrometer (FTS) with imaging detectors. The use of imaging detectors allows for higher spatial resolution with a higher coverage. This type of instrument is particularly important to observe greenhouse gases (GHGs) in the Arctic.

The Arctic is a sensitive world were small changes in greenhouse gas amounts can have amplified effects through feedbacks from surface albedo, humidity, and ocean current changes. With an increase in temperature, the sea ice extent recedes which in turn decreases the albedo resulting in a feedback loop causing more and more sea ice to melt each year. These changes will result in new sources of air pollution and an increase in the release of CO_2 and CH_4. It is important to monitor these greenhouse gases (GHGs) in the atmosphere to understand and quantify their sources and sinks and this is no less important in the Arctic and high latitudes where making quasi-continuous measurements with high spatial resolution is a problem.

In the following sections, the objectives of the project are discussed as well as the principles underlying this type of instrumentation. The scientific requirements, mechanical and optical design, electronics, software and optical bench tests will be presented.

4.1. Literature Review

As already stated, the site to be observed by the instrument to be developed by this project is the

high latitudes. The boreal forest situated above 50°N latitude is the most important driver of the carbon cycle in this region. These forests include 25% to 30% of the world's total forest ecosystems. Climate change has several effects on them such as lengthening the growth season and increasing the number of wildfires. These changes impact CO_2 exchange with the atmosphere and can alter the carbon cycle (Nassar et al., 2014).

Another effect that climate change inflicts on the Arctic is the melting of sea ice and the exposure of more ocean to the atmosphere. The CO_2 exchange between the ocean and atmosphere is not well understood and monitoring any changes is essential. The melting sea ice also increases shipping traffic and exploration activities for natural resources. These new sources of pollution also add to the CO_2 emissions at northern latitudes (Nassar et al., 2014).

One of the largest reserves of organic carbon is permafrost, perennially frozen ground. Global climate change predictions suggest that the average temperature change in the future will be highest at northern latitudes. Some models predict that the temperature increase in this region will be on the order of 7° to 8° over land (Schuur et al., 2008). A study done by Tarnocai et al. shows that the CO_2 amount stored in northern permafrost is approximately 1672 Pg. Around 88% or 1466 Pg of this amount is stored in perennially frozen soil. As the permafrost melts some of the carbon from the top layer of soil will be released into the atmosphere. This carbon, depending on whether the soil is wet or dry, is released in the form of CH_4 or CO_2 respectively. The release of these greenhouse gases can have severe impacts on the global CO_2 amount and can produce a positive feedback to global warming (Tarnocai et al., 2009).

Current instrumentation onboard satellites have limitations on both coverage and spatial resolution in observing northern latitudes. Most greenhouse gas monitoring satellites, such as TANSO-FTS, OCO-2 and CarbonSpec are in sun-synchronous, low-Earth orbits (LEO). LEO orbits provide

short passes over each location and do not provide a long-term, quasi-geostationary view of the Arctic. On the other hand, instruments that are in a GEO orbit such as GeoCarb, aiming to launch in 2021, do not provide good coverage of northern latitudes and can only resolve data over latitudes from 60°[S] to 60°[N] at most. To provide long-term monitoring of the Arctic with high spatial resolution, a Highly Elliptical Orbit (HEO) is required, with its apogee above the north pole. Such an orbit is described by Trishchenko (Trishchenko et al., 2011). The orbit proposed by Trishchenko is a three-apogee (TAP), highly elliptical orbit with its apogees over the Arctic. Two satellites in opposing orbits, as shown in Figure 4-1, can give continuous coverage over the Arctic. While one satellite is at apogee the other is at perigee. This orbit has a 16-hour period with ± 4 to ± 6 hours spent near apogee. The apogee and perigee are at approximately 43,000 km and 8,000 km which reduces the satellite's exposure to the radiation belts of Earth.

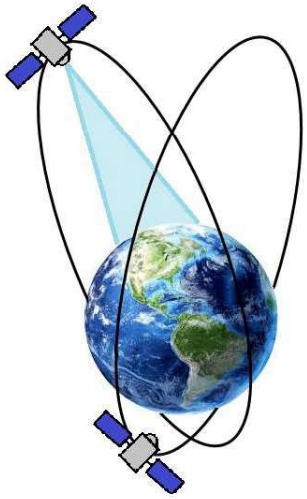

Figure 4-1: HEO setup for a northern latitudes quasi-geostationary satellite. (Trishchenko et al., 2011)

4.2. Objectives

The objectives of this project are:

1. The development and testing of a new Imaging Fourier Transform Spectrometer (IFTS) to demonstrate the possibility of atmospheric sounding;
2. Demonstrate the capacity to make measurements of spectra with a spectral resolution of approximately 0.5 cm^{-1};
3. Demonstrate the capability of making measurements with a higher spatial resolution (~10 km) and a larger coverage (~2000 by 2500 km^2) in a shorter time (Length of one scan ~65 s);
4. Design calibration tests and carry out these tests in a lab setting;
5. Develop data analysis software.

4.3. Principles of IFTS spectrometry

An IFTS (Imaging Fourier Transform Spectrometer) is a Fourier transform spectrometer (FTS) with an imaging array detector at the focal plane of the instrument. This section of the thesis focuses on the methods used in developing an IFTS instrument for atmospheric sounding. It includes the principles of making measurements with an IFTS where the data analysis methods of an FTS must be implemented on the data retrieved from each pixel of the IFTS separately. At first, the operational characteristics of the Michelson interferometer are discussed which also apply to the IFTS instrument. The IFTS design is based on the Michelson Interferometer (MI) which is described in section 4.3.1. The advantages of using an IFTS over other types of instruments are described in section 4.3.2., and methods for transforming the output of an IFTS to spectra are presented in section 4.3.3.

4.3.1. Michelson Interferometer

A standard Michelson interferometer (MI) is comprised of two mirrors, one moving and one stationary, a beam-splitter and a detector. Figure 4-2 shows the optical setup of a simple MI instrument. It shows the relative positions of the mirrors, beam-splitter, source and detector. Light enters through the aperture and is split into two beams at the beam-splitter. The transmitted light goes to the moving mirror while the reflected light goes to the fixed mirror. After reflection the two beams of light recombine at the beam-splitter and approximately half of the light is transmitted to the detector. The moving mirror provides an optical path difference (OPD) between the two beams which results in an interference pattern. The detector records this interference pattern as changes in the intensity of light as a function of path difference. This results in an interferogram which contains the spectral information of the incoming light. (Griffiths and Haseth, 2006)

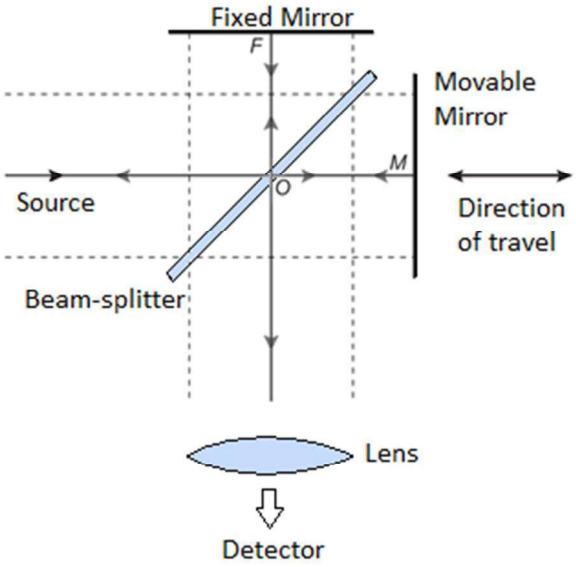

Figure 4-2: Optical diagram of the Michelson interferometer. Light from the source is split at the beam-splitter and recombined after reflection from two mirrors. The resulting interferogram provided by the scanning of the moving mirror is recorded by the detector. (Griffiths and Haseth, 2006)

In a MI, the source is usually an extended light source. If the mechanical path difference of the fixed mirror with respect to the moving mirror is d, for a light source on the optical axis, the OPD is 2d. For rays that are off axis with an angle of θ with respect to the optical axis such as in Figure 4-3, the OPD will be 2dcosθ.

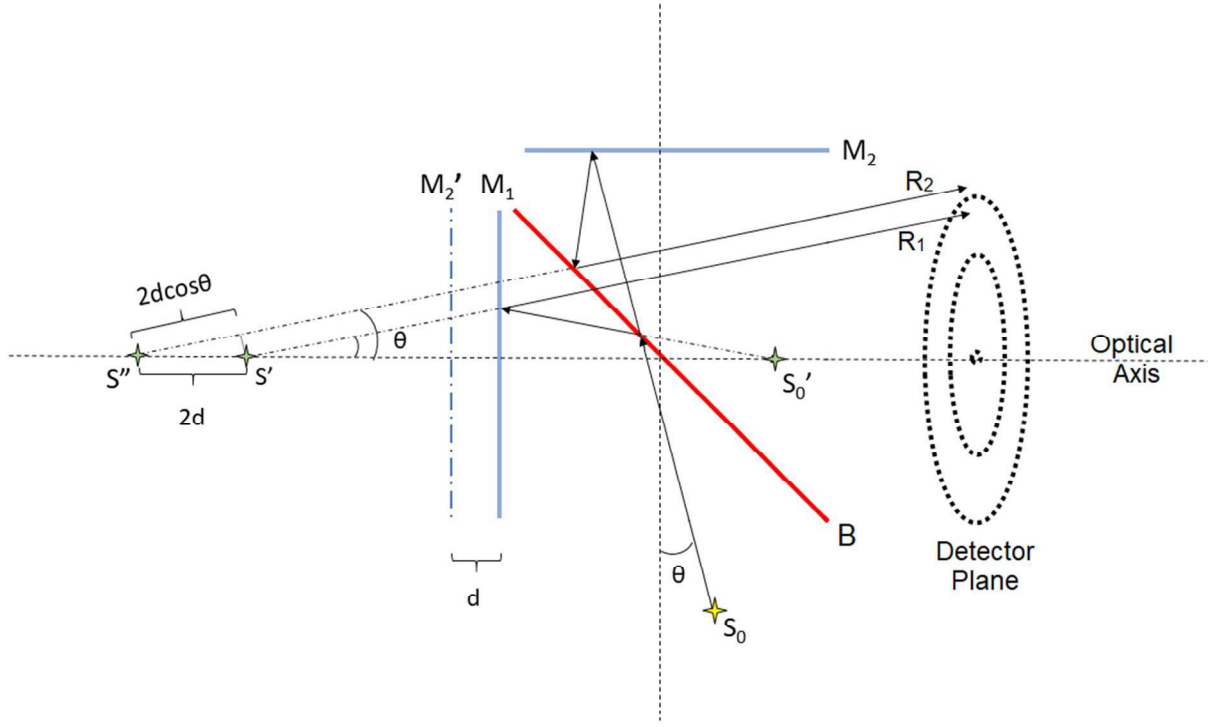

Figure 4-3: Off-axis light propagation showing the interference pattern formed by a MI. S_0 is the light source at an angle θ from the optical axis. M_1 is the fixed mirror and M_2 is the moving mirror. M_2' is the image of M_2 and S0' is the image of S_0 formed by the beam splitter (B). S' is the image of S_0' formed by M_1 and S" is the image of S_0' formed by M_2'. The path difference of the two rays R_1 and R_2 which are reflected from M_1 and M_2 becomes 2dcosθ where d is the mechanical path difference of the two mirrors M_1 and M_2.

Assuming a monochromatic waveform entering the MI, the electric field strength (E) is defined as (Kauppinen and Partanen, 2001):

$$\mathbf{E} = \boldsymbol{A}\mathbf{e}^{\mathbf{i}(\vec{\mathbf{k}}.\vec{\mathbf{r}}-\omega\mathbf{t})} \quad \textbf{(4-1)}$$

$$\vec{\mathbf{k}} = |\mathbf{k}| = \frac{\mathbf{2\pi}}{\boldsymbol{\lambda}} = \mathbf{2\pi}\nu \quad \textbf{(4-2)}$$

where A is the amplitude of the wave, **k** is the wave vector defined in equation (4-2), **r** is the position vector, ω is the angular frequency, t is time and ν is the wavenumber. The beam-splitter splits the beam into two parts (E_1 and E_2) with amplitudes A_1 and A_2 and phase difference of δ. The phase difference between E_1 and E_2 is a result of the path difference between the fixed and the moving mirror. In practice, the intensity (I) or the power of the electromagnetic wave per area is measured. Knowing that the intensity (I) is proportional to A^2, the resulting intensity will be:

$$\mathbf{I} = \mathbf{I_1} + \mathbf{I_2} + \mathbf{2}\sqrt{\mathbf{I_1 I_2}}\mathbf{cos\delta} \quad \textbf{(4-3)}$$

If the MI beam-splitter is perfect, $I_1 = I_2 = I_0$ then:

$$\mathbf{I} = \mathbf{2I_0}(\mathbf{1} + \mathbf{cos\delta}) \quad \textbf{(4-4)}$$

and,

$$\boldsymbol{\delta} = \frac{\mathbf{2\pi x}}{\boldsymbol{\lambda}} = \frac{\mathbf{2\pi}}{\boldsymbol{\lambda}}\mathbf{2ndcos\theta} \quad \textbf{(4-5)}$$

where θ is the angle between the waveforms and the optical axis of the MI and n is the refractive index of the medium which in case of vacuum is 1. In an MI instrument with a single point input source, emphasis is on the input EM radiation to be in the same axis as the optical axis, therefore, θ is assumed to be zero. If the source is a monochromatic point source, then the output intensity in the optical axis of the interferometer (interference record) becomes:

$$\mathbf{F} = \mathbf{2I_0}[\mathbf{1} + \mathbf{cos}(\mathbf{2\pi\nu x})] \quad \textbf{(4-6)}$$

where x = 2d is the optical path difference (OPD). Depending on how x relates to λ the interference

pattern can be constructive or deconstructive. Assume $x = n\lambda$, if $n = 0, \pm 1, \pm 2, \ldots$ then the interference is constructive and if $n = \pm (1/2), \pm (3/2), \pm (5/2), \ldots$ then the interference is destructive. As an example, the output intensity (F) versus optical path difference (x) of part of the output of a MI with an input source with an amplitude of 10 arbitrary units and a wavelength of $\lambda = 632$ nm has been plotted using MATLAB in Figure 4-4. After removing the constant term of the output signal from it, the remaining signal is called an interferogram (Figure 4-5). If the source is monochromatic the interferogram will look like a cosine wave.

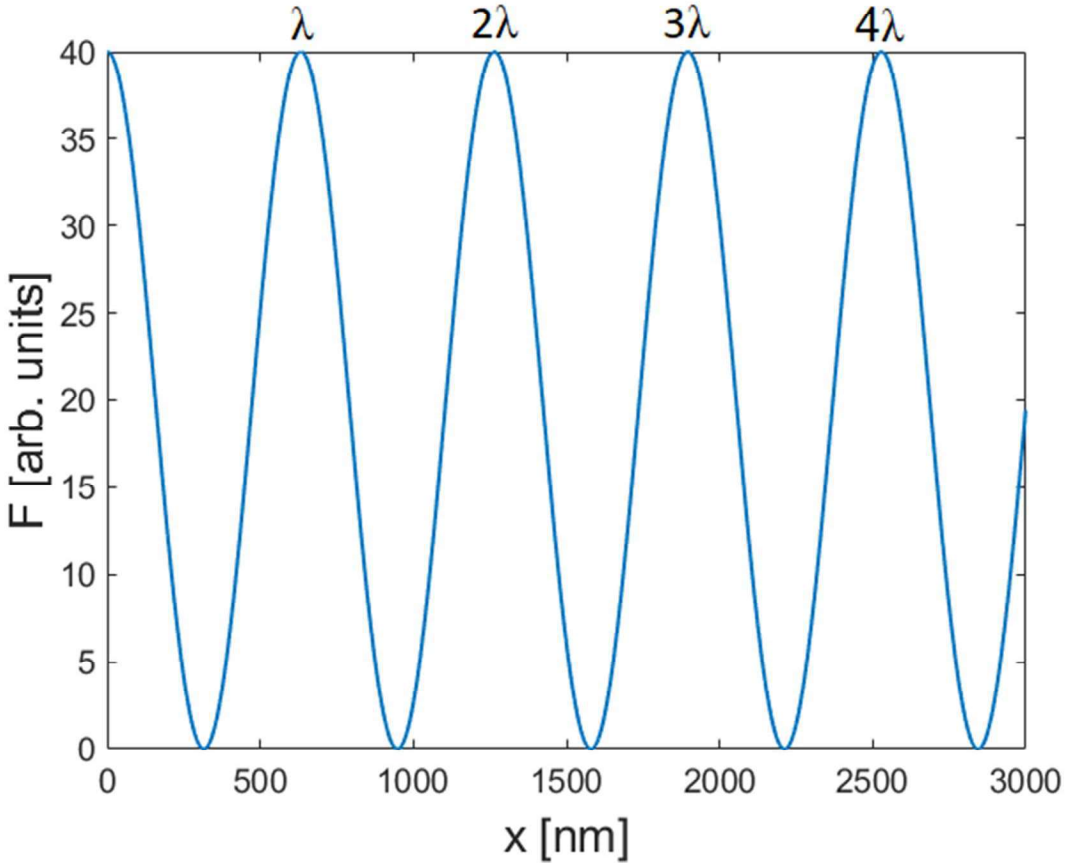

Figure 4-4: Simulated output intensity (F) versus OPD (x) of the interference pattern of a MI with an input source of wavelength of $\lambda = 632$ nm. (Calculated by a MATLAB program)

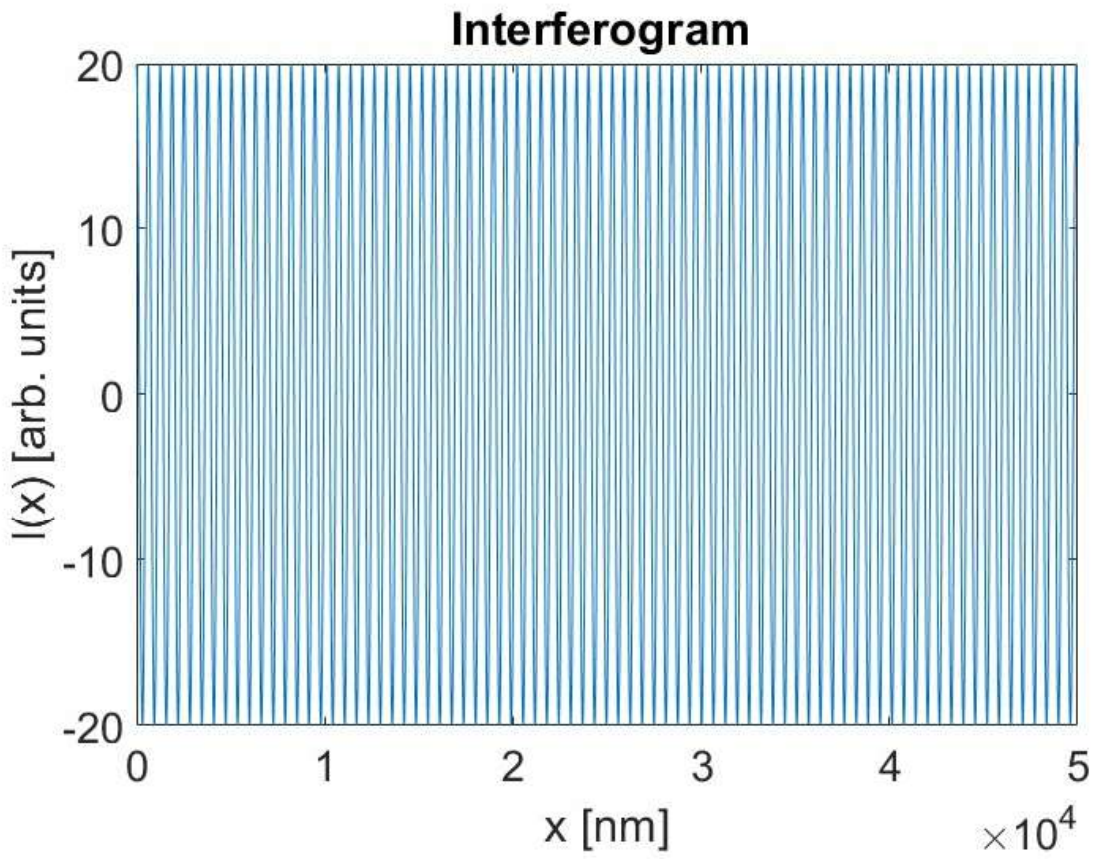

Figure 4-5: Simulated interferogram output of a MI with an input source of wavelength of λ = 632 nm. (Calculated by a MATLAB program)

In practical interferometry the source is polychromatic and continuous denoted as E(ν). In this case the output intensity of a spectral element between υ and dυ from equation (4-6) becomes:

$$\mathbf{dF(x,\nu) = 2E(\nu)[1 + \cos(2\pi\nu x)]d\nu} \qquad \textbf{(4-7)}$$

and to find the output intensity over the total spectral band equation (4-7) is integrated over all wavenumbers:

$$\mathbf{F(x) = 2\int_0^{\infty} E(\nu)[1 + \cos(2\pi\nu x)]d\nu} \qquad \textbf{(4-8)}$$

In the above equation, F(x) is the interference signal (output intensity). If the constant term, which is $\frac{1}{2}F(0) = 2\int_0^{\infty} E(\nu)d\nu$, is subtracted from the interference signal, the result will be the

interferogram (I(x)) given below:

$$\boldsymbol{I(x) = 2\int_0^{\infty} E(\nu)\cos(2\pi\nu x)\,d\nu} \quad \textbf{(4-9)}$$

If the interferogram is symmetrical and E(-ν) = E(ν), the interferogram becomes:

$$\boldsymbol{I(x) = \int_{-\infty}^{\infty} E(\nu)\left(e^{i2\pi\nu x}\right)\,d\nu = \mathcal{F}\{E(\nu)\}} \quad \textbf{(4-10)}$$

where $\mathcal{F}$ is the Fourier transform (FT) of E(ν) and forms a Fourier transform pair with I(x):

$$\boldsymbol{E(\nu) = \int_{-\infty}^{\infty} I(x)\left(e^{-i2\pi\nu x}\right)\,dx = \mathcal{F}^{-1}\{I(x)\}} \quad \textbf{(4-11)}$$

Therefore, by recording the interferogram, I(x), and applying an inverse Fourier transform on it, the spectrum, E(ν) is obtained.

To continue the example of a monochromatic wave input to the MI presented in Figure 4-4, the Fourier transform of such an output is presented in Figure 4-6, where the peak shows the wavenumber (~15,8222 cm^{-1}) of a 632 nm monochromatic light source. In theory, the interferogram is infinite and continuous but in practice, it is truncated and discrete, therefore, the FFT will result in a peak with wings rather than a delta function. More on the effects of these characteristics of an interferogram will be presented in section 4.3.3.

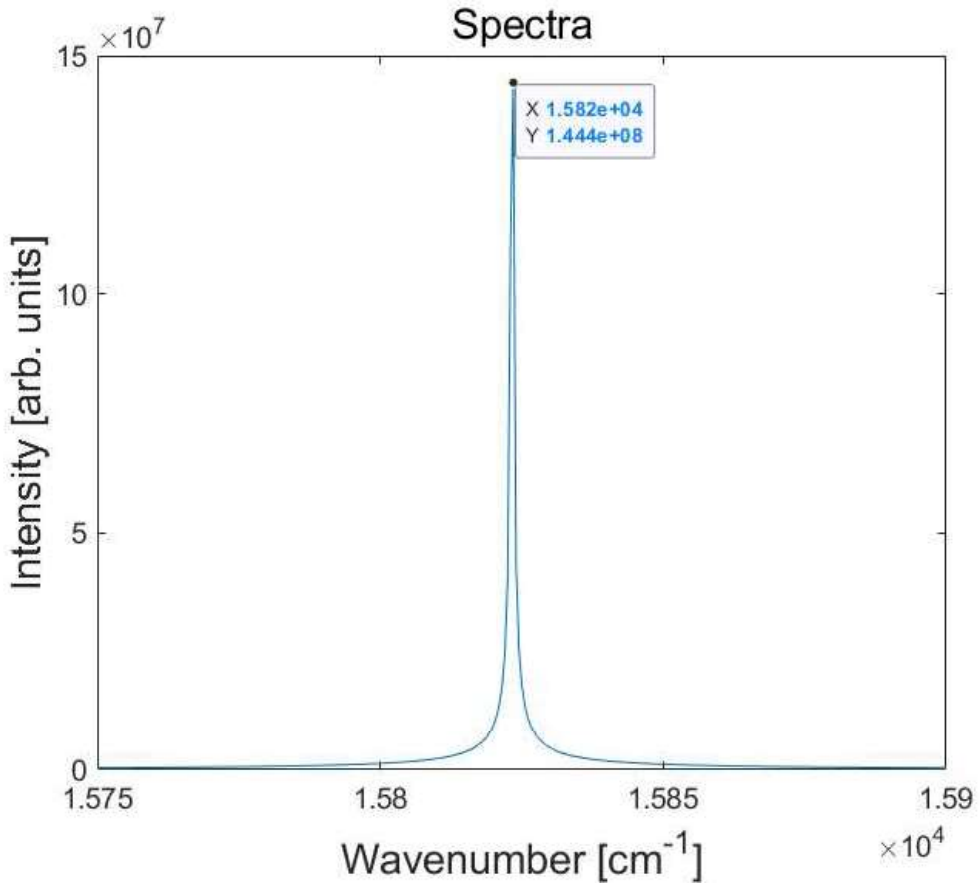

Figure 4-6: Spectrum obtained by taking the Fourier transform of the simulated interferogram in Figure 4-5 of a 632 nm wavelength (15,822.8 cm^{-1} wavenumber) monochromatic laser. The peak shows a wavenumber of ~15,820 cm^{-1}. (Calculated by a MATLAB program)

4.3.2. Advantages of using an IFTS

Imaging Fourier transform spectrometers (IFTS) have several advantages over dispersive atmospheric remote sounding instruments. The IFTS instrument's optical throughput is not limited by its fore-optics whereas a dispersive instrument is limited by an entrance slit which limits the light and therefore decreases Signal to Noise Ratio (SNR) (Griffiths and Haseth, 2006). The optical throughput depends on the area of the entrance aperture. In an IFTS the aperture is large (on the order of 25-50 mm) and therefore the optical throughput is larger than a dispersive spectrometer

(Davis et al., 2001). Another advantage of an IFTS is its high wavelength accuracy which is called the Connes advantage. The accuracy of the wavelength calibration of the instrument depends on the relation between modulation frequency and wavelength. This relationship is determined by the scanning velocity of the mirrors. A monochromatic laser also known as the metrology laser in a MI helps control the scanning velocity of the mirrors and therefore the frequency of the sampling of the interferogram. In ideal conditions where vibration is not present, sampling the interferogram at every zero crossing of the fringe signal of the metrology laser provides the high wavelength accuracy (Buijs and McKinnon, 2009).

One of the valuable advantages of an IFTS is that while measuring a broad spectral band in a single scan the dispersion and instrument line shape do not change and stay constant for every spectral line in the wavelength range. Dispersive spectrometers may have a line shape that changes as a function of wavelength. The spectral resolution of an IFTS depends on the maximum optical path difference (OPD). This value can be adjusted easily in an IFTS by reducing or increasing the mechanical path difference of the moving mirror with respect to the fixed mirror, within its maximum range (Davis et al., 2001).

One disadvantage of an IFTS instrument is its sensitivity to vibrations and temperature change. The source of vibrations may stem from the scanning mechanism or the environment of the instrument. Most of these vibrations are eliminated by using precise, low vibration scanning motors such as a voice coil motor (VCM) and a low vibration mechanical design for the scanning pivot. Voice coil motors, when running on high power induce very little vibration. The details of the operations of a VCM are provided in Appendix E. In a lab environment, the instrument can be placed on a vibration isolation table. On a balloon or space platform, most of the low frequency vibrations are eliminated and the high frequency vibrations are limited by the use of voice coil

motors as mentioned before (Buijs and McKinnon, 2009).

The advantage in using an imaging detector in the IFTS is in its spatial resolution and ground coverage. If the interferometer has a single detector pixel, therefore, considering the pixel size and imaging lens focal length, the spatial resolution will be large when observing the atmosphere from a GEO or HEO orbit, unless, a large telescope is used as its fore-optics. Considering a single pixel size of 1 mm and an imaging lens with focal length of f_1=10 cm at an orbital altitude of 650 km (Figure 4-7, red), the spatial resolution will be ~ 6.5 km. If the same optical setup where to be placed at an orbital altitude of 36,000 km (Figure 4-7, blue), the spatial resolution will become ~ 360 km. In order to reduce the spatial resolution to the same 6.5 km, a focal length of f_2 ~ 5.5 km would be required for the imaging lens (Figure 4-7, green).

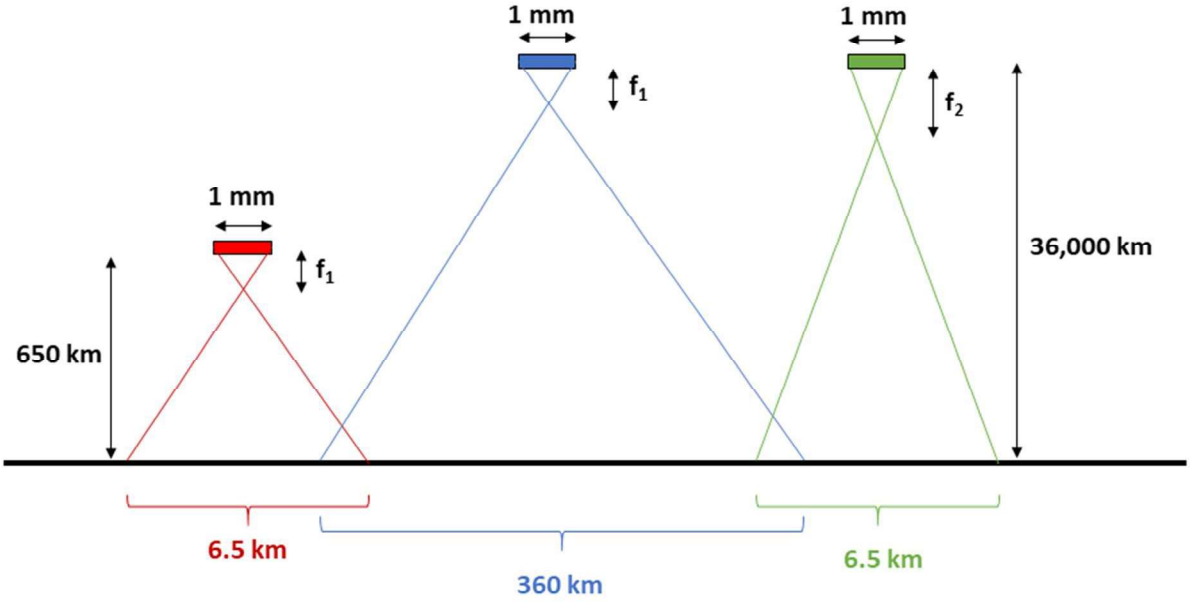

Figure 4-7: The effect of imaging lens focal length on spatial resolution for a single-pixel detector.

An IFTS instrument utilizes multiple pixels with the use of a focal plane array (FPA) as a detector. This allows the IFTS to have a much finer spatial resolution without the use of a heavy and large telescope. This also allows it to observe a large field of view (FOV) with a fine spatial resolution

in a single scan. This concept is shown in Figure 4-8.

An example of an FTS instrument making measurements of atmospheric CO_2 and CH_4 from space in the nadir direction is The Thermal and Near Infrared Sensor for Carbon Observation Fourier-Transform Spectrometer (TANSO-FTS) onboard the Greenhouse Gases Observing Satellite (GOSAT). This instrument is a single-pixel detector with an instantaneous field of view (IFOV) of 10.5 km when projected on the Earth's surface in the nadir direction from an orbital altitude of 666 km (LEO) (Kuze et al., 2009).

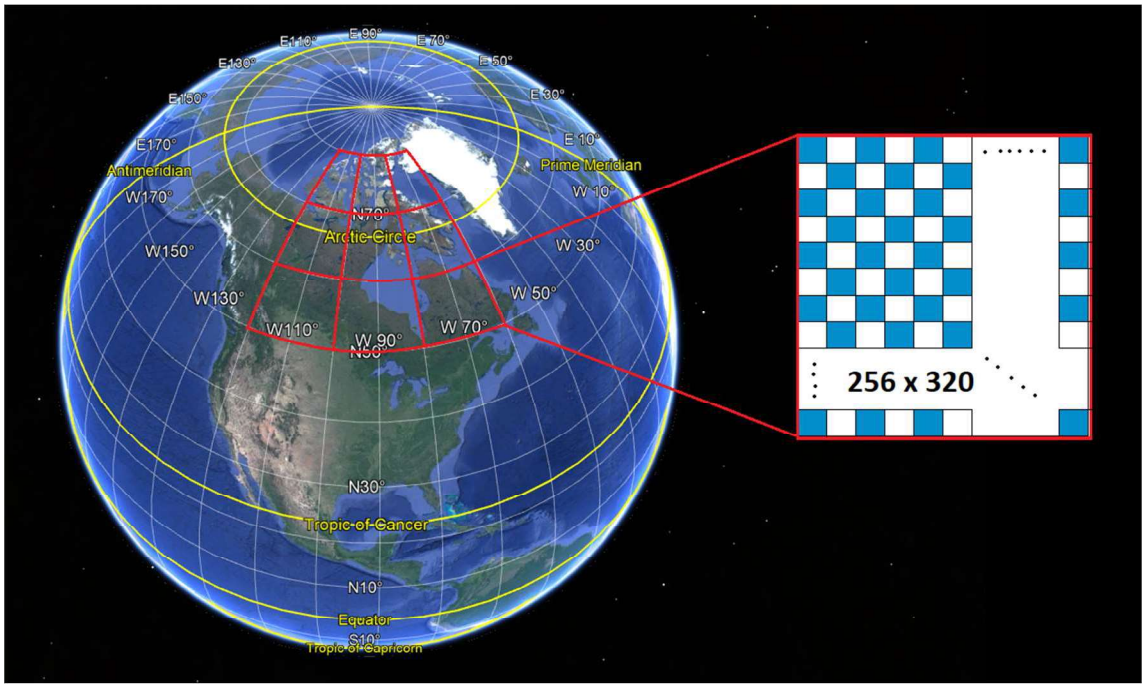

Figure 4-8: Field of view of an IFTS instrument in a HEO orbit in red and the spatial resolution of each red panel on the right in blue.

As mentioned earlier, TANSO-FTS has a single-pixel detector whereas the IFTS has a multi-pixel detector. Multi-pixel detectors have not been used widely on this type of instrument. The Infrared Atmospheric Sounder Interferometer (IASI) was one of the first instruments to use a multi-pixel imaging detector. The detector is a 2 x 2 element array with a pixel size of 0.9 x 0.9 mm^2. This

instrument was first launched on board the MetOp-A satellite in 2006 in a LEO orbit with an average altitude of 817 km. Each pixel of the detector corresponds to a 12 km spatial element (spatial resolution) on the ground in the nadir direction (Royer et al., 1994).

The Cross-track Infrared Sounder (CrIs) is another one of this type of instruments. It used a 3 x 3 array detector. This instrument was launched on board the National Polar-orbiting Operational Environmental Satelite System (NPOESS) in 2011 in a polar LEO orbit at an altitude of 833 km. Each pixel of the detector corresponds to a 14 km spatial element (spatial resolution) on the ground in the nadir direction. (Bloom, 2001).

The Infrared Sounder (IRS) onboard the Meteosat Third Generation (MTG) will be one of the first imaging Fourier transform spectrometer instruments utilising a 160 x 160 pixel detector. It will take measurements in the 4 μm to 8.3 μm spectral region with a spatial resolution of 3 km and the 8.3 μm to 15 μm spectral region with a spatial resolution of 6 km from a geostationary orbit (Aminou et al., 2004). The launch of this satellite is scheduled for 2021.

The IFTS instrument was originally proposed for flight on the Polar Communication and Weather-Polar Highly Elliptical Orbital Science (PCW-PHEOS) Fourier Transform Spectrometer (FTS) instrument. This instrument was to have a spatial resolution of 10 by 10 km from a viewing altitude of ~40,000 km (McConnell et al., 2012). This mission was put on hold by Canadian Space Agency after the design phase (phase 0 and phase A studies) in early 2012.

Table 3 provides a summary of different instruments on board different satellites which measure greenhouse gases from space. The orbit, instrument type, detector type and spatial resolution is given for each instrument. The IFTS instrument which will be described in the following sections is also included.

Table 3: Summary of satellite instrumentation measuring greenhouse gases.

Instrument	Satellite	Orbit (km)	Launch	Instrument Type	Detector	Spatial Resolution [km]
MOPITT	Terra	710	1999	Gas correlation spectrometer	4 x 1 array	22 × 22
SCIAMACHY	Envisat	790	2002	Imaging Spectrometer	1024 Pixel array	32 × 215
IASI	MetOp-A	817	2006	FTS	2 x 2	12
TANSO-FTS	GOSAT	666	2009	FTS	Single Pixel	10.5
CrIs	Suomi NPP (JPSS)	824	2011	FTS	3x3 array	14
OCO-2	OCO-2	705	2014	Grating Spectrometer	1024 Pixel Array	1.29 × 2.25
CarbonSpec	Tansat	700	2016	Grating Spectrometer	Imaging	2 × 2
TROPOMI	Sentinel-5P	824	2017	Grating Spectrometer	1000 x 256	7 × 7
MicroCarb	MicroCarb	650	2020	Grating Spectrometer	1024 x 1024	4.5 × 9
MTG IRS	Meteosat 3rd Generation	36000	2021	IFTS	160 x 160 pixel CCD	3 - 6
GeoCarb	GeoCarb	36000	2021	Grating Spectrometer	Focal Plane Array (FPA)	3 × 6
PHEOS	PCW	36000	cancelled	IFTS	Multiple pixel Array	10 × 10
GIFTS	GIFTS-IOMI	36000	cancelled	IFTS	FPA	4 × 4
AIM North	N/A	36000 (HEO)	proposal	IFTS	N/A	3 × 3
IFTS	Balloon	40	N/A	IFTS	320 x 256 pixel Array	0.012 × 0.012
	Satellite	40000 (HEO)				12 × 12

4.3.3. Interferometer Data Transformation

In section 4.2.1 the basic data analysis of a MI instrument in the case of a continuous interferogram was discussed. Here the focus is on analyzing a discreet Fourier transform (DFT). When recording an interferogram, time sampling or spatial sampling is applied that results in a discrete interferogram. Assuming the sampling interval is Δx, the sample location in the interferogram becomes, $x_j = j\Delta x$, where, j = -N, -N+1, …, -1, 0, 1, …, N-1. As well as discrete sampling, the interferogram is truncated and can only be obtained in a finite range of -L to L where, $L = N\Delta x$. The integral in equation (4-11) becomes a sum from -N to N-1:

$$\mathbf{E_L^{\Delta x}(\nu) = \Delta x \sum_{j=-N}^{N-1} I_j e^{-i2\pi\nu j\Delta x}} \qquad \textbf{(4-12)}$$

The use of equation (4-12) includes numerous sin and cos function calculations. With the use of different algorithms, the Fast Fourier Transform (FFT) is introduced that significantly reduces the complexity and time required to do the FT calculations. The most common algorithm used is the Cooley-Tukey algorithm which requires that the number of samples in the interferogram to be a power of 2. The Cooley-Tukey algorithm has been explained with detail in many different textbooks and will not be elaborated upon here.

There are several artifacts introduced in the spectrum due to applying the DFT. These artifacts include aliasing, picket-fence effect and leakage.

Aliasing

The DFT of an interferogram with 2N real sample points produces an output of 2N complex points. But when observing the output spectrum, only the first N points are the spectrum and the other N points are the mirror image of the spectrum. This mirror image is the alias of the spectrum.

In the case of a wide-band spectrum, where the maximum wavenumber in the spectrum is υ_{max},

the spectrum and its alias will overlap if υ_{max} is bigger than the folding (mirror position) wavenumber. The folding wavenumber is defined as:

$$\boldsymbol{\nu_f = N\Delta\nu = N\frac{1}{2N\Delta x} = \frac{1}{2\Delta x}} \quad \textbf{(4-13)}$$

If the sampling period is short, then the period of the discretized spectrum is larger than the spectral band, $2\,\upsilon_{max} \leq 1/(\Delta t)$. In this case, the spectrum is distinguished, and aliasing does not occur. If the sampling period is large, then the period of the discretized spectrum will be smaller than the spectral band, $2\,\upsilon_{max} > 1/(\Delta t)$. In this case, the spectrum becomes distorted due to aliasing, meaning that the period of the spectrum is smaller than the width of the spectrum and overlap with each other (Kauppinen and Partanen, 2001). Therefore, the Nyquist frequency is defined (equation (4-14)) which determines the critical sampling frequency. In this equation, f_{max} is the maximum frequency of the true spectrum being measured.

$$\mathbf{f_N = \frac{1}{\Delta t} = 2f_{max}} \quad \textbf{(4-14)}$$

This translates to the sampling interval of an interferogram being:

$$\mathbf{(\Delta x)_{Nyquist} = \frac{1}{2\nu_{max}}} \quad \textbf{(4-15)}$$

Picket-Fence Effect

Before applying the Discrete Fourier transform (DFT) on the data, some corrections must be made to the interferogram. One of these corrections is called zero-padding, defined as adding zeros to the end of the interferogram to make the number of samples a power of 2. As mentioned before, the number of samples being a power of 2 is the requirement of performing an FFT. For example, if the interferogram has 16,000 points, zeros are added until the number of points become 2^{14} or 16,384 points. The effect of adding zeros to the end of the interferogram, is an interpolation of the

spectrum because more sample points are added per wavenumber in the spectrum. Therefore, if there are spectral frequencies that don't coincide with the interferogram sample points, the error that arises from this may be reduced by zero-padding. This is known as the "picket-fence" phenomenon. This means that the spectrum is being observed through a picket-fence and the spectral features that don't coincide with the interferogram sample points are behind the pickets (Herres and Gronholz, 1984).

Leakage

The truncation of the interferogram has the effect of convolving it with a boxcar function. The FT of a boxcar function is a sinc function. Therefore, if recording the interferogram of a monochromatic spectrum discreetly and with a finite length, the DFT of the interferogram will show a sinc function instead of a delta function with the main peak at the wavelength measured (see Figure 4-9).

The box car function and its Fourier transform, the sinc function, cause large oscillations in the side lobes of the spectrum. These side lobes are leakage of the spectral intensity from the main peak and are not desired. To reduce these side lobes, instead of using the box car function, for example, a triangular function can be used. This function is called the apodization function (Kauppinen and Partanen, 2001).

The range of the apodization function is determined by the number of points in the interferogram before zero-padding. There is a tradeoff between the apodization and resolution of the spectrum. For example, the best apodization function to reduce oscillations in side lobes of the spectrum is the Blackmann-Harris function with three or four terms but, this function increases the FWHM of the spectral lines and thus, reduces spectral resolution.

This function, which is given in equation (4-16) has a FWHM of 0.9/L. If a higher resolution is

required, then, using the boxcar function is ideal which has a FWHM of 0.61/L (Herres and Gronholz, 1984).

$$\mathbf{BH(x) = A_0 + A_1 cos\left(\frac{\pi n}{L}\right) + A_2 cos\left(\frac{\pi 2n}{L}\right) + A_3 cos\left(\frac{\pi 3n}{L}\right)} \qquad \textbf{(4-16)}$$

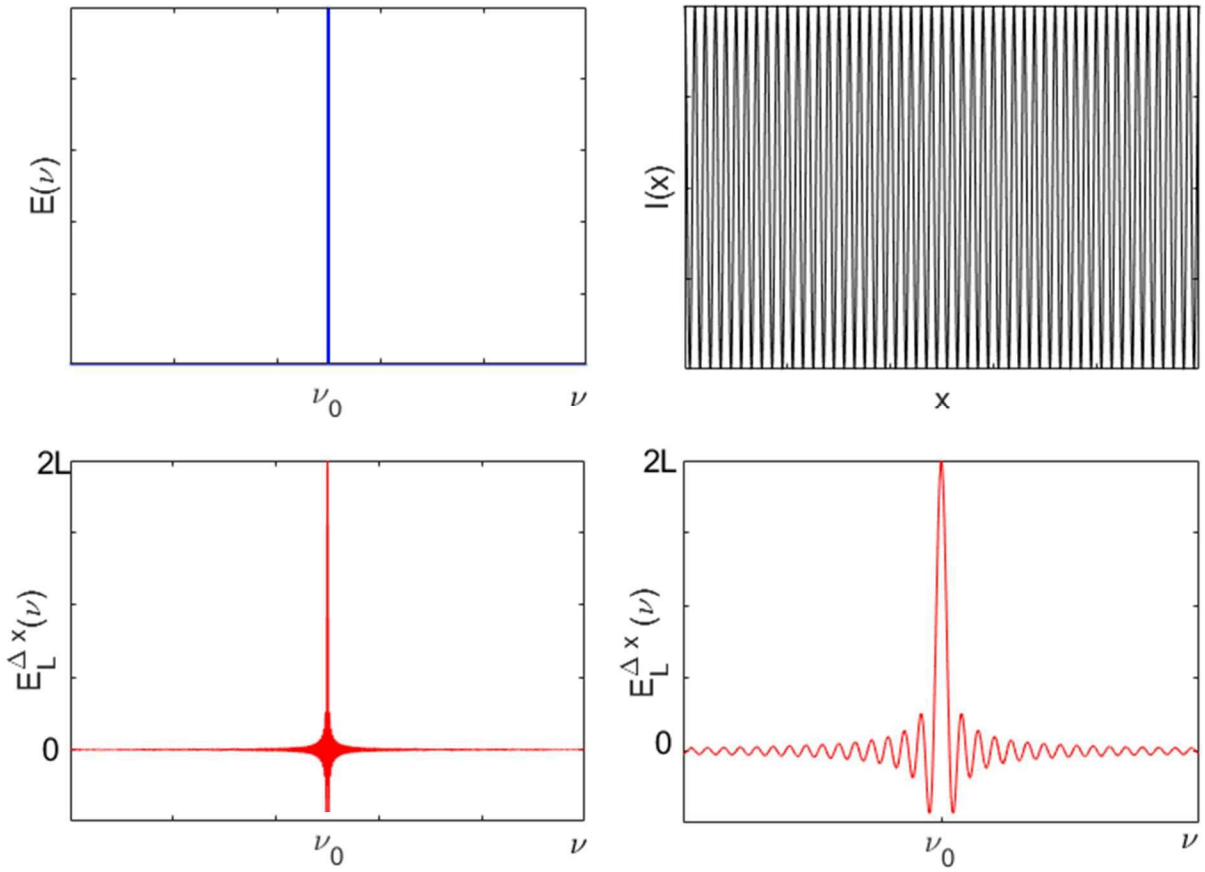

Figure 4-9: Top left: spectrum of a perfect monochromatic source (Delta function at ν_0). Top right: discrete truncated interferogram of the monochromatic source. Bottom left: DFT of the interferogram giving the spectrum. Bottom right: the spectrum zoomed in showing the sinc function. (Data plotted are simulated with a MATLAB program)

In analyzing the data of an FTS instrument, it is important to apply phase corrections. The phase

shift is due to the FT or DFT of an interferogram producing a complex spectrum (C(υ)). The complexity of the spectrum arises from the sample points of the interferogram not being in phase to sample ZPD precisely and, therefore, results in the interferogram being un-symmetrical about ZPD. If sample zero is not exactly at ZPD then the resulting data series will have cosine and sine components that can be represented by a complex vector. Another reason for the non-zero phase is that a double-sided (both sides of the ZPD was recorded) interferogram is recorded but is asymmetric because of delays in sampling which can be due to electronics and vibrations in the optics, it can also create a non-zero phase. By applying a phase correction, more of the signal appears in the cosine transform of the FFT and results in a slight advantage of a higher SNR.

This complex spectrum can be represented by equation (4-17), where, R(υ) is the real part and I(υ) is the imaginary part, or by equation (4-18), where S(υ) is the amplitude spectrum and contains a complex exponential part where, Φ(υ) is the phase of the complex spectrum (Herres and Gronholz, 1984).

$$\mathbf{C(\nu) = R(\nu) + iI(\nu)} \qquad \textbf{(4-17)}$$

$$\mathbf{C(\nu) = S(\nu)exp(i\phi(\nu))} \qquad \textbf{(4-18)}$$

Phase correction on the FT of the interferogram isolates the amplitude spectrum which, is what is desired. Without the phase correction the noise is somewhat higher. The Mertz method describes how to correct the phase shift in a double-sided interferogram. In this method, C(υ) is multiplied by the inverse of the phase exponential and the real part is extracted as in equation (4-19) and the phase is calculated from equation (4-20).

$$\mathbf{S(\nu) = Re[C(\nu)exp\left(-i\phi(\nu)\right)]} \qquad \textbf{(4-19)}$$

$$\phi(\nu) = \arctan\left[\frac{I(\nu)}{R(\nu)}\right] \quad (4\text{-}20)$$

The steps in correcting and analyzing a discrete interferogram have been described in this section and are listed below:

- The first step is the apodization of the interferogram;
- The second step is zero-padding the interferogram to complete the number of points in the series to at least the next larger power of two to improve the transform,
- The third step is to apply the FFT on the interferogram, to produce a complex spectrum.
- The final step is to apply a phase correction to the complex spectrum, resulting in a real spectrum.

4.4. IFTS Instrument

The newly developed Imaging Fourier Transform Spectrometer (IFTS) is composed of a core interferometer along with a camera detector which images the interferogram on an Indium Gallium Arsenide (InGAs) array detector. The core of the instrument, which is provided by ABB, is shown in Figure 4-10. The core design is based on a classical Michelson interferometer except that instead of one stationary mirror and one moving mirror it utilizes corner cube mirrors that both move. The corner cubes are mounted on a double-pivot scanning mechanism operated by a linear voice coil motor (VCM). Provided in the core are a HeNe laser and a detector which are used to control the scanning motor and to measure the Optical Path Difference (OPD). For calibration purposes, a white light source with its detector is also provided which detects the Zero Path Difference (ZPD) 'centre burst'. The HeNe laser, white light source and their associated detectors are labelled in Figure 4-11. The dimensions of the core are 36 cm by 25 cm by 12 cm.

The aft-optics of the instrument were designed at the Laboratory for Atmospheric Remote

Sounding from Space (LARSS) at York University. The aft-optics includes a dichroic mirror, mirror, lenses and detectors.

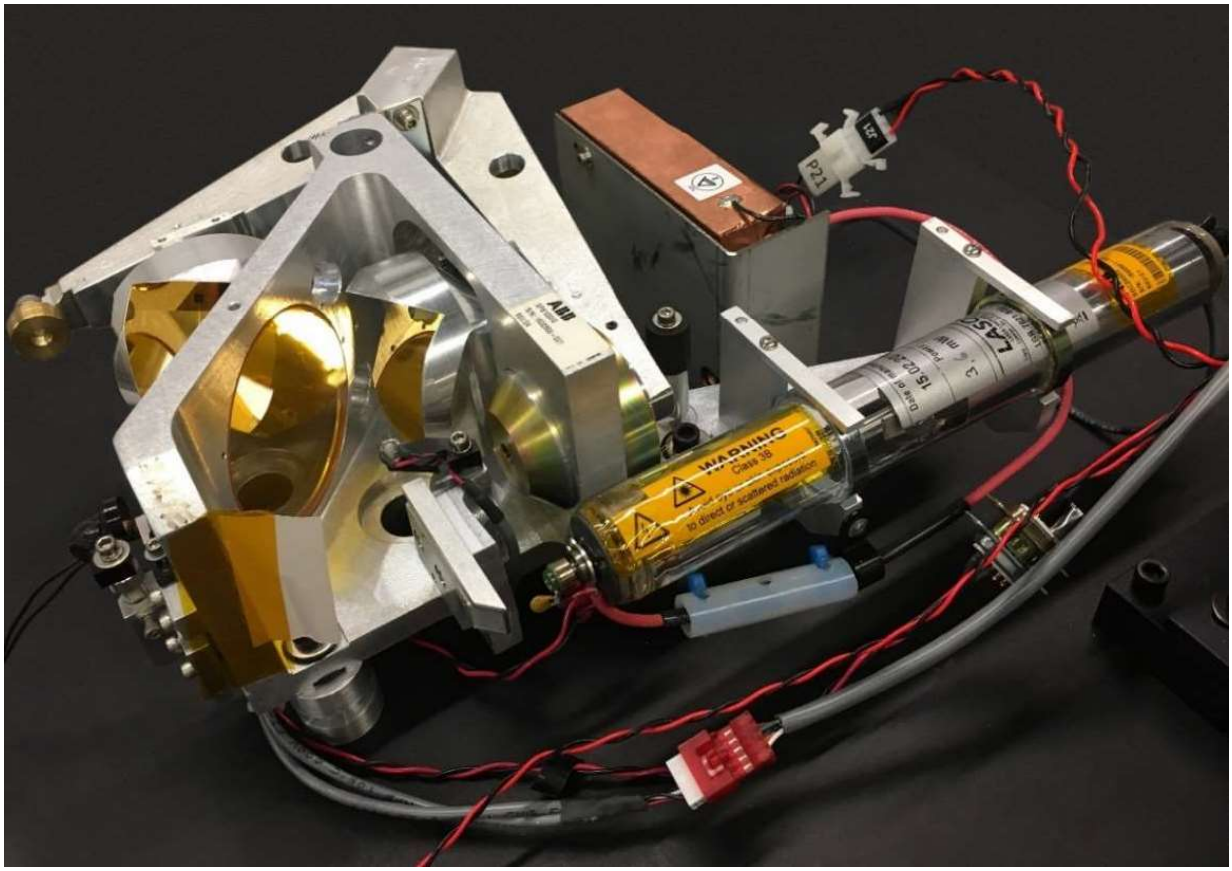

Figure 4-10: IFTS core provided by ABB Measurements and Analytics Division (ABB).

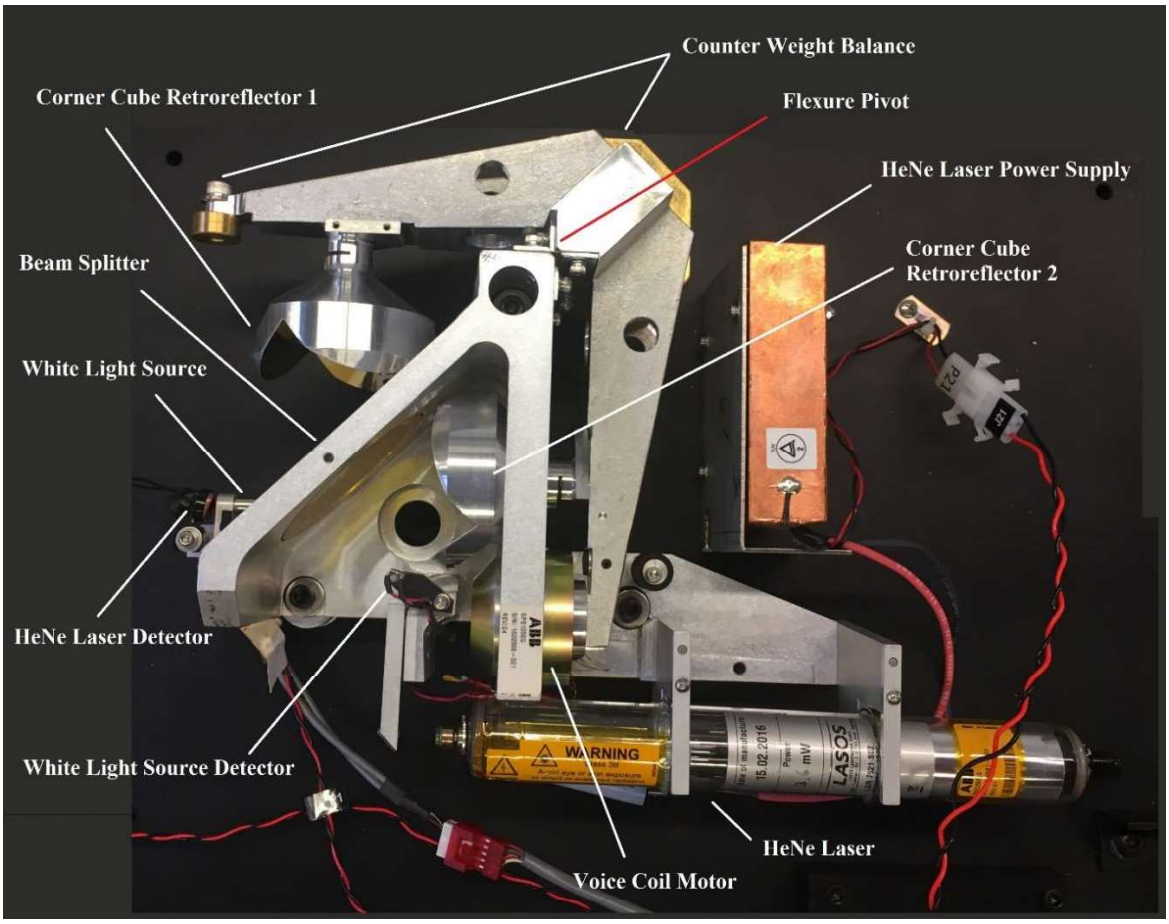

Figure 4-11: Core of the IFTS with all components labelled.

4.4.1. Scientific Requirements

The instrument is designed to measure in two spectral bands. One is the 1.6 μm band for measuring absorption by CO_2 and CH_4. This channel has a range of 5950 cm^{-1} to 6450 cm^{-1}. The second spectral band is at 762 nm for measuring absorption in the O_2 A-band with a range of 13,060 cm^{-1} to 13168 cm^{-1}. The simulated spectrum of CO_2 and CH_4 are plotted in Figure 4-12 and of the O_2 A-band spectrum is plotted in Figure 4-13. For these simulations a Gaussian instrument line shape and a spectral resolution of 0.5 cm^{-1} was chosen. The simulations were made for an observing altitude of 40 km.

The instrument has a 50 mm diameter aperture and a maximum mechanical path difference of

L = 1 cm, thus the ideal un-apodized spectral resolution of the instrument is:

$$\Delta\nu = \frac{1}{OPD} = \frac{1}{2L} = 0.5\ \mathbf{cm^{-1}} \qquad \textbf{(4-21)}$$

But in reality, as explained in section 4.3.3, the interferogram is truncated and therfore the FFT of the truncated interferogram yields a sinc function with Full Width at Half Maximum (FWHM) of approximately $\frac{1.207}{2L}$ (Kauppinen and Partanen, 2001), which transelates to a resolution of:

$$\Delta\nu = \frac{1.207}{2L} = 0.6\ \mathbf{cm^{-1}} \qquad \textbf{(4-22)}$$

The goal for the IFTS instrument is to achieve a spatial resolution of 12 km square from a 40,000 km orbit which is similar to a geostationary orbit (the inscribed circle of a 12 km square is approximately 8 km). This number depends on the pitch of the detector pixels and telescope used.

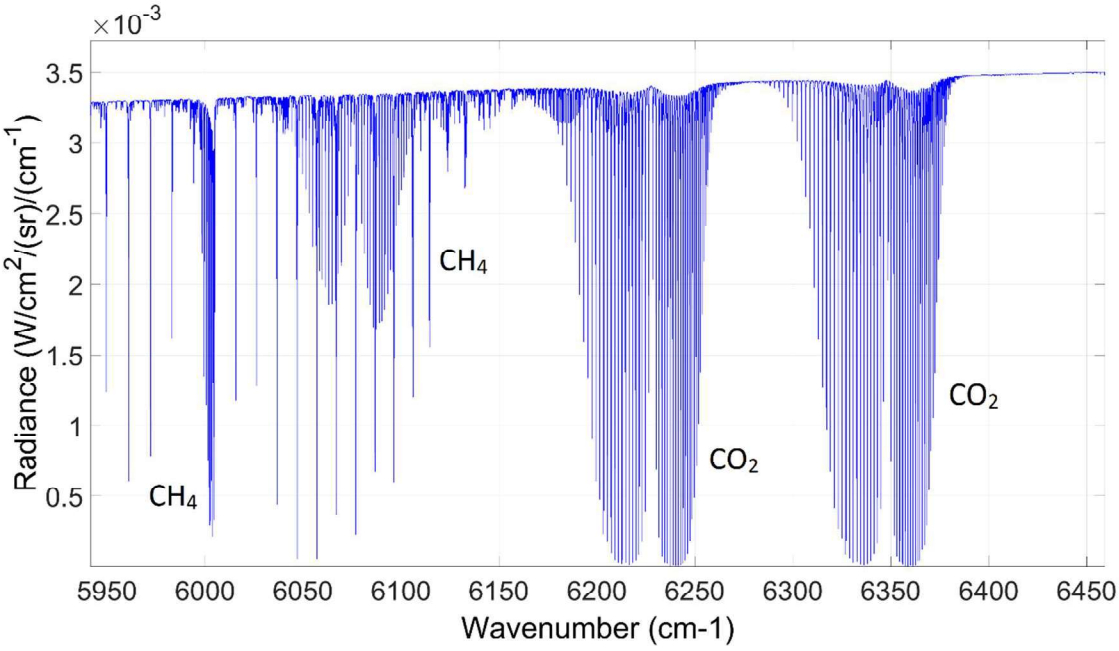

Figure 4-12: Simulated spectrum of CO_2 and CH_4. (Siddiqui, 2018, Personal Communications)

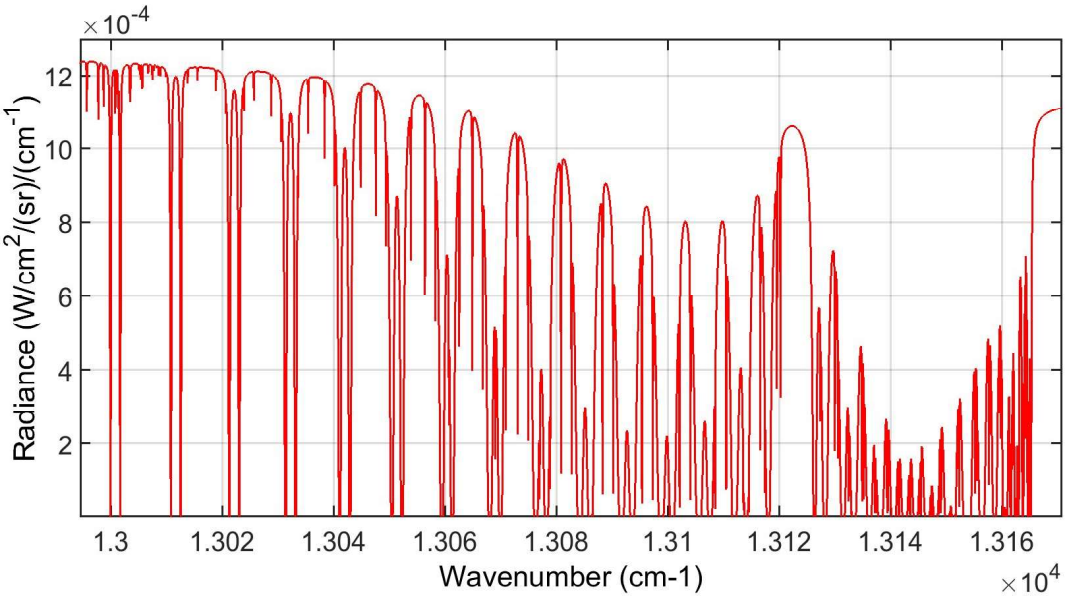

Figure 4-13: A simulated spectrum of the O_2 A-band. (Siddiqui, 2018, Personal Communications)

4.4.2. Optical-Mechanical Design

As mentioned before, the design of the core of the IFTS instrument is based on a Michelson interferometer with the use of corner cubes for reflectors. A corner cube retro-reflector is made up of three perpendicular flat mirrors. These corner cubes are mounted on a double flexure pivot scanning mechanism operated by a linear VCM. To achieve efficient modulation, the combining wave fronts from the interferometer need to be precisely aligned optically with respect to tilt and shear. Tilt and shear refers to the alignment of the wave-fronts angularly and transversely respectively. The alignment with respect to shear depends on how well the wave-fronts are situated in one plane. The corner cubes eliminate the need to align with respect to shear due to the light triple passing the retro-reflectors (Buijs and McKinnon, 2009). The angular sensitivity is eliminated because the reflected ray is precisely parallel to the incoming ray. So if the two cubes are in the same vertical plane the wavefronts will exactly align even though the angles are changing as the scanning arm moves.

The optical flowchart of the instrument is shown in Figure 4-14. The light enters the instrument through an aperture (item #1). The first optical element in the core of the interferometer that the light passes through is a Zinc Selenide (ZnSe) beam-splitter (item #2) placed at 45° with respect to the beam. It reflects part of the beam to the first corner cube (item #3) and transmits the rest to the second corner cube (item #4). The percentage of light reflected and transmitted by the beam-splitter determines the modulation efficiency. The corner cubes are mounted on the scanning arm which rotates back and forth from ZPD driven by the voice coil motor. The scanning arms are mounted on the frame of the interferometer via a flexure pivot which provides frictionless movement for the arms. The scanning arms of the IFTS provide an optical path difference between the two beams of light divided by a zinc selenide beam-splitter. The two beams recombine at the beam-splitter (item #5) and exit the IFTS core. A long-pass dichroic mirror (item #6) reflects the 762 nm wavelength band to the first detector (item #10) and transmits the 1600 nm wavelength band to a 45° mirror (item #7) and the second detector (item #11) respectively.

The optical layout of the IFTS payload is shown in Figure 4-15. The core of the instrument, which is the Michelson interferometer from ABB, is in green. The HeNe laser that provides information to control the modulation speed and the reference for sampling the interferogram, is shown in pink. The laser power supply is in burgundy. The O_2 A-band channel detector is in purple and the CO_2 and CH_4 channel detector is in blue. The detectors used are Xenics 320 x 256 pixels, Visible Near Infrared (VisNIR) array detector cameras equipped with a USB 2.0 interface for control and image readout. The maximum frame rate for these detectors is 100 Hz but, with windowing, the detectors can achieve a higher frame rate. A different version of the same camera can be operated up to 200 Hz, full frame, using the Cameralink interface from Xenics.

For an optical bench setup, the instrument is mounted onto a Minus K passive vibration isolation

platform which, weighs approximately 32 kg and has dimensions of 42.7 cm x 42.7 cm x 21.6 cm. The vibration transmission curves for the minus k model 100BM-4 are provided in appendix D, Figure D-1. The complete instrument has dimensions of 60 cm x 45 cm x 15 cm and weighs approximately 25 kg. Figure 4-16 shows the optical bench setup of the instrument. The mechanical CAD drawings of the IFTS can be found in appendix N.

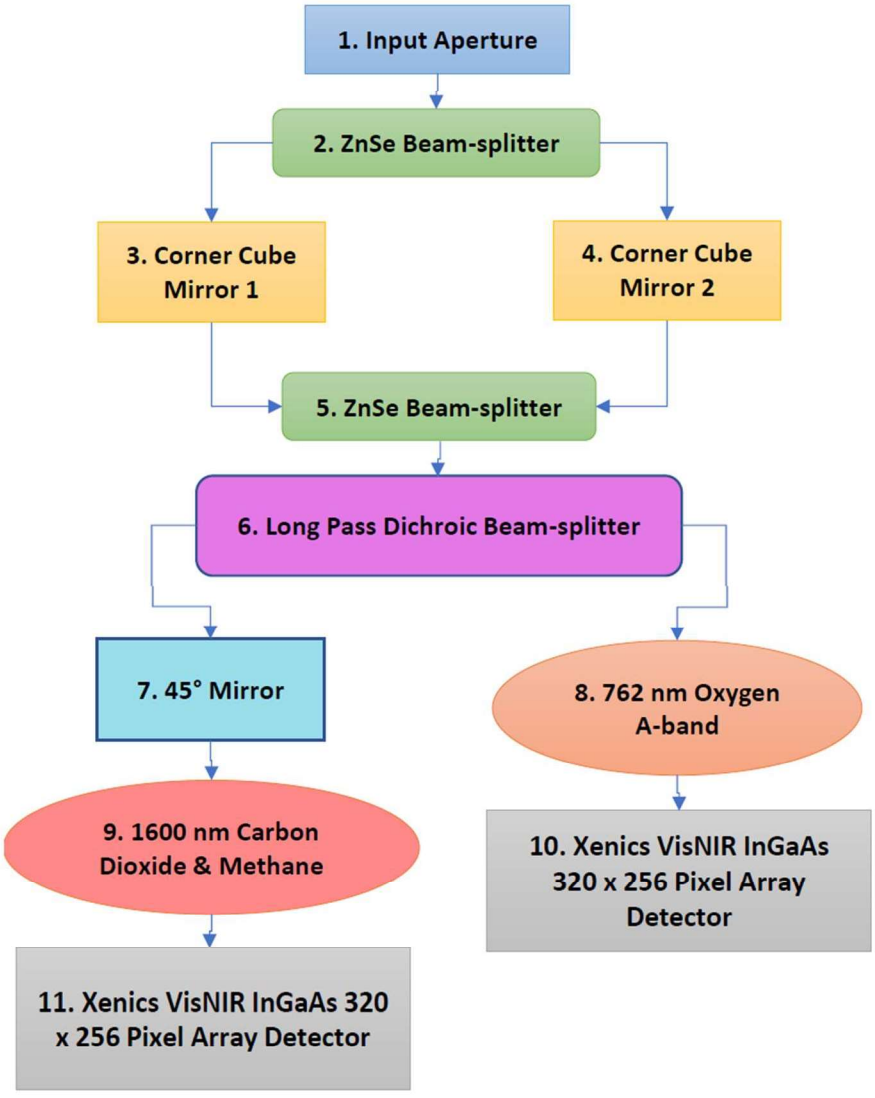

Figure 4-14: IFTS optical flow chart.

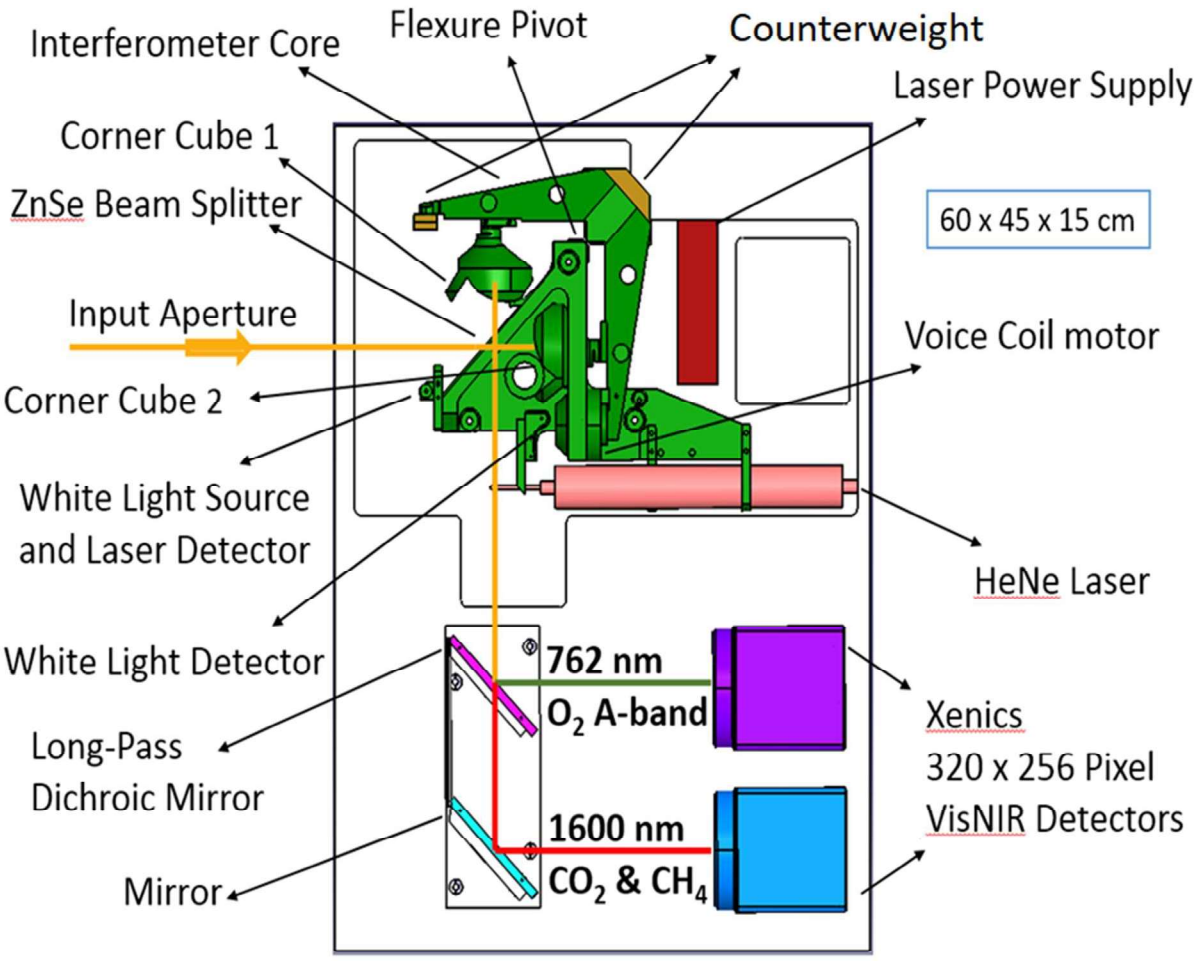

Figure 4-15: IFTS payload optical layout.

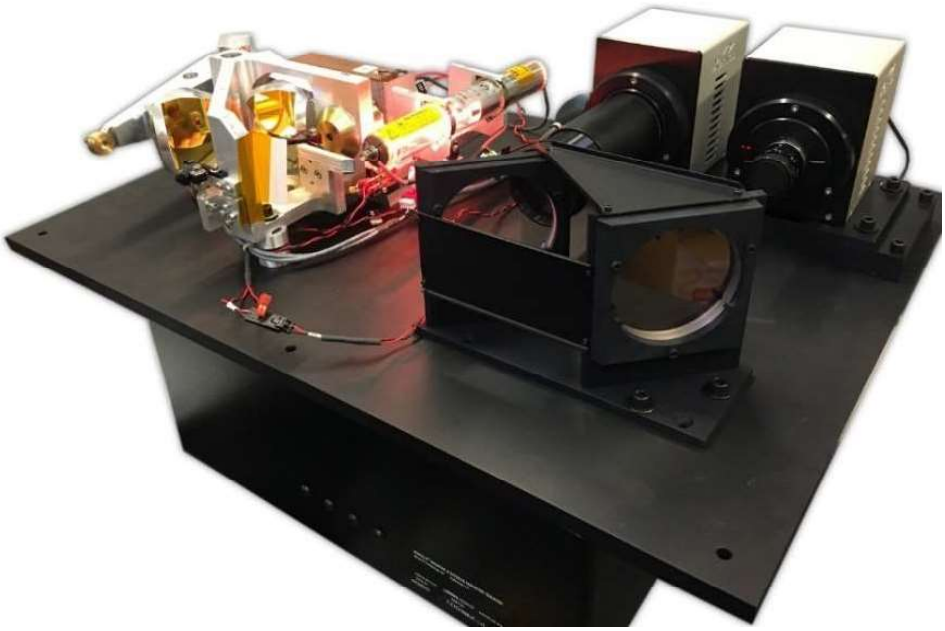

Figure 4-16: Optical bench setup of the IFTS instrument payload mounted on the vibration isolation platform.

As mentioned before, the spatial resolution of the IFTS depends on the pitch of the detector pixels and the imaging lens used. The IFTS is equipped with an IR camera with a range of 0.4 to 1.7 μm and a pixel pitch of 30 μm. The imaging lenses have a focal length of ~100 mm. The angle subtended by the pixel is projected by the focal length of the imaging lens used, which results in a spatial resolution of 12 m from a 40-km altitude and 12 km from a 40,000-km altitude.

4.4.3. Signal to Noise Ratio (SNR)

The detectors used are Xeva-1.7-320 VisNIR digital array detector cameras. The photo-response of this camera at 1.6 μm is about 1 Amp per Watt (A/W) and at 762 nm is about 0.4 A/W. These numbers were obtained from the graph in Figure 4-17 from the data sheet of the cameras.

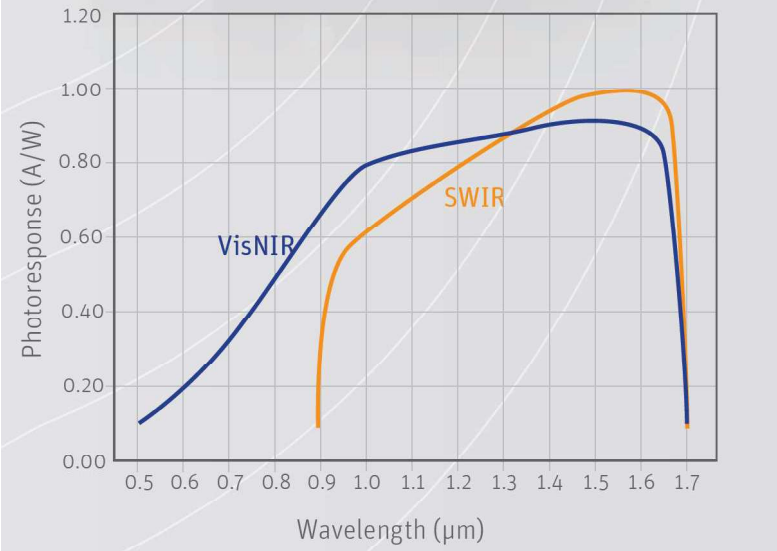

Figure 4-17: Photo-response versus wavelength of the Xenics camera detectors. (Xenics, 2018)

CO_2 and CH_4 channel:

The first step in calculating the SNR is to calculate the incident intensity at the Earth's surface. The solar irradiance (I_s) at 1.6 µm is 250 $W.m^{-2}.\ \mu m^{-1}$ obtained from Figure 2-3. For a Lambertian surface with an assumed albedo (ρ_d) of 1 and a solar incident angle of 0:

$$\mathbf{I = \frac{\rho_d}{\pi} \cdot I_s \cdot \cos(\theta)} = \frac{1}{\pi} \cdot (250) \cdot \cos(0) = \ 80\ [\mathrm{W.m^{-2}.\mu m^{-1}.sr^{-1}}] \qquad \textbf{(4-23)}$$

In the 1.6 µm band the energy of one photon is:

$$E = \frac{h \cdot c}{\lambda} = \frac{6.626 \times 10^{-3} \ \times 3 \times 10^{8}}{1.6 \times 10^{-6}} = 1.24 \times 10^{-19}\ [\mathrm{J/Ph}]$$

Therefore $1\ \left[\frac{J}{s}\right] = \frac{1}{1.24 \times 10^{-1}} = 8.05\ \times\ 10^{18}\ [\frac{Ph}{s.W}]$ photons, and the surface radiance will be:

$$I = 80\ [\mathrm{W.m^{-2}.\mu m^{-1}.sr^{-1}}] \times 8.05\ \times\ 10^{18}\ \left[\frac{Ph}{s.W}\right] = 6.44 \times 10^{20} [\mathrm{Ph.m^{-2}.\mu m^{-1}.sr^{-1}.s^{-1}}]$$

The radiance will be attenuated by many factors within the instrument. The combination of the ZnSe beam-splitter and corner cubes attenuate the signal by 33%. The calculation of this number

can be found in Appendix G. The second beam-splitter has a transmission efficiency of 92% for 1600 nm wavelength and 0% for the 762 nm wavelength (100% reflectance). The transmission curve for this beam-splitter is given in appendix D, Figure D-4. The 45° mirror has an efficiency of 98% and each of the lenses in front of the detectors have an efficiency of 98%. The 762 nm channel filter has an efficiency of 55% (appendix D, Figure D-3) and the 1600 nm channel filter has an efficiency of 90% (appendix D, Figure D-2). The optical efficiency diagram of the IFTS is shown in Figure 4-18. For the 1600 nm channel the accumulated attenuation will be 26.24% and for the 762 nm channel is 16.36%. Therefore, the apparent surface irradiance for the 1600 nm channel becomes:

$$I = 6.44 \times 10^{20}[\mathrm{Ph.\,m^{-2}.\,\mu m^{-1}.\,sr^{-1}.\,s^{-1}}] \times 0.2624 = 1.7 \times 10^{20}[\mathrm{Ph.\,m^{-2}.\,\mu m^{-1}.\,sr^{-1}.\,s^{-1}}]$$

To find the signal-to-noise ratio the equation below is used:

$$\mathbf{SNR} = \frac{\mathbf{1}}{\mathbf{2}}\,\Delta\boldsymbol{\lambda}\sqrt{\frac{\boldsymbol{\pi}\,\mathbf{I}\,\mathbf{A}\,\boldsymbol{\Omega}\,\mathbf{t}\,\mathbf{Q}}{\mathbf{2}\,\Delta\boldsymbol{\lambda}_{\mathbf{f}}}} \qquad \textbf{(4-24)}$$

Where,

I is the surface radiance [photons/m^2/µm/sr/s],

A is the detection area of the instrument [m^2],

Ω is the solid angle subtended by the instrument optics of the instrument [sr],

$\Delta\lambda$ is the instrument resolution in wavelength space [µm],

$\Delta\lambda_f$ is the bandpass of the filter in wavelength space [µm],

Q is the quantum efficiency of the detector [e/photons].

The development of this model is discussed in Appendix F.

Instrument Detection Area, A

The corner-cube mirror diameter is 50 mm, therefore, the instrument detection area (A) will be:

$$A = \pi r^2 = \pi(25\text{mm} \times 10^{-3})^2 = 1.9 \times 10^{-3}[\text{m}^2]$$

Instrument Solid Angle, Ω

The IFTS input lens has a focal length of 100 mm and the detector has a 30 μm square pixel. Therefore, the solid angle subtended by the instrument optics for one pixel will be:

$$\Omega = \frac{A}{f^2} = \frac{30 \times 30 \times 10^{-12}\ \text{m}^2}{(0.1\ \text{m})^2} = 9 \times 10^{-8}[\text{sr}]$$

Instrument Resolution, Δλ

The instrument resolution (Δν) is 0.5 cm^{-1} which in the wavelength space is:

$$\Delta\lambda = \frac{\Delta\nu \cdot \lambda}{\nu} = \frac{0.5 \times 1.6}{6250} = 1.3 \times 10^{-4}[\mu\text{m}]$$

Total Integration Time, t

The total integration time, t, is calculated by multiplying the number of samples by the integration time of each sample. The interferogram is sampled at the zero-crossing points of the metrology laser fringes at a rate of once per fringe in the 1.6 μm band and twice per fringe at 762 nm. If the 1600 nm channel is considered, for a physical path difference scan of x, there will be $N_L = 2x/\lambda_L$ samples collected where λ_L is the laser wavelength. If each sample is integrated for Δt = 500 μs, then the total integration time will be $t = N_L\ \Delta t = 31{,}645 \times 500 \times 10^{-6} = 15.8$ s.

Filter Bandpass, $\Delta\lambda_f$

If the band is limited to 6190 cm^{-1} to 6500 cm^{-1} by means of an optical filter (transmission curve provided in appendix D, Figure D-2) meaning $\Delta\lambda_f$ = 77.05 nm = 0.077 μm.

Quantum Efficiency, Q

In the 1.6 μm band the energy of one photon is:

$$E = \frac{h \cdot c}{\lambda} = \frac{6.626 \times 10^{-34} \times 3 \times 10^{8}}{1.6 \times 10^{-6}} = 1.24 \times 10^{-1} \ \ [\mathrm{J/Ph}]$$

Therefore 1 joule = $\frac{1}{1.24 \times 10^{-19}} = 8.05 \times 10^{18}$ [Ph] photons. Dividing both sides by 1 s results in 1 W = 8.05×10^{18} [Ph/s]. The sensitivity of the detector in this spectral region is 1 A/W where 1 A is 6.24 x 10^{18} electrons per second. Considering the above, the quantum efficiency will be:

$$Q = \frac{6.24 \times 10^{18}\ \mathrm{e/s}}{8.05 \times 10^{18}\ \mathrm{Ph/s}} = 0.78\ [\frac{\mathrm{e}}{\mathrm{ph}}]\ .$$

The signal to noise ratio calculated from equation (4-24) for the 1600 nm band will be:

$$\mathrm{SNR} = (0.5)(1.3 \times 10^{-4})\sqrt{\frac{\pi \times 1.7 \times 10^{20} \times 1.9 \times 10^{-3} \times 9 \times 10^{-8} \times 15.8 \times 0.78}{2 \times 0.07}} = 184$$

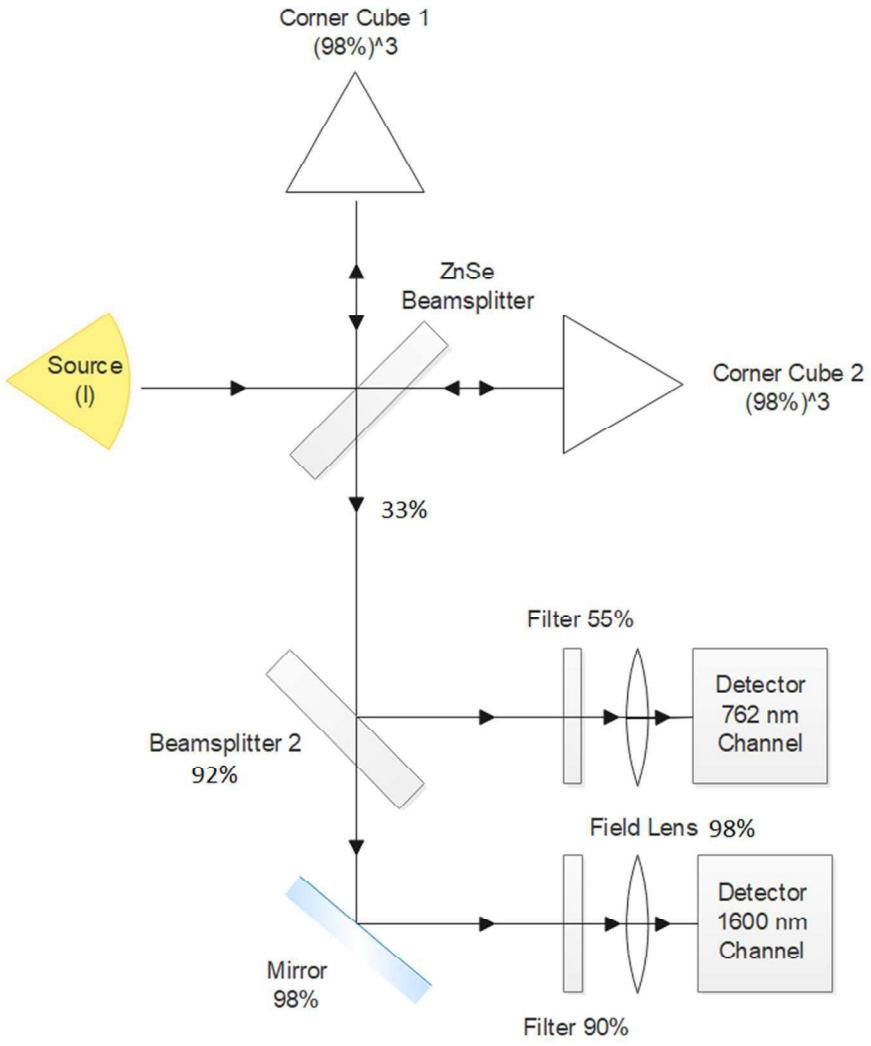

Figure 4-18: Optical efficiency diagram of the IFTS.

O_2 A-band channel:

The solar irradiance at 762 nm is 1100 $W.m^{-2}.\ \mu m^{-1}$ obtained from Figure 2-3. For a Lambertian surface with an assumed albedo (ρ_d) of 1 and a solar incident angle of 0, the surface radiance from equation (4-23) will be 350 $W.m^{-2}.\ \mu m^{-1}.sr^{-1}$.

In the 762 nm band the energy of one photon is:

$$E = \frac{h \cdot c}{\lambda} = \frac{6.626 \times 10^{-3} \ \times 3 \times 10^{8}}{762 \times 10^{-9}} = 2.6 \times 10^{-19}\ [J/ph]$$

Which results in $1\left[\frac{J}{s}\right] = \frac{1}{2.6\times10^{-1}} = 3.8 \times 10^{18}\ [\frac{Ph}{s.W}]$, and the surface radiance will be:

$$I = 350\ [W.m^{-2}.\mu m^{-1}.sr^{-1}] \times 3.8\ \times\ 10^{18}\ \left[\frac{Ph}{s.W}\right] = 13.3 \times 10^{20}[Ph.m^{-2}.\mu m^{-1}.sr^{-1}.s^{-1}]$$

The radiance for this channel will be attenuated by a factor of 16.36%. Therefore, the apparent surface irradiance for the 762 nm channel becomes:

$$I = 13.3 \times 10^{20}[Ph.m^{-2}.\mu m^{-1}.sr^{-1}.s^{-1}] \times 0.1636 = 2.17 \times 10^{20}[Ph.m^{-2}.\mu m^{-1}.sr^{-1}.s^{-1}]$$

The instrument detection area (A) and solid angle (Ω) are the same as the 1600 nm channel.

Instrument Resolution, $\Delta\lambda$

The instrument resolution ($\Delta\nu$) is 0.5 cm^{-1} which in the wavelength space is:

$$\Delta\lambda = \frac{\Delta\nu\cdot\lambda}{\nu} = \frac{0.5\times0.762}{13123.36} = 2.9 \times 10^{-5}\ [\mu m]$$

Total Integration Time, t

The interferogram is sampled at the zero-crossing points of the metrology laser fringes at a rate of twice per fringe at 762 nm. In this channel, for a physical path difference scan of x, there will be $N_L = 4x/\lambda_L$ samples collected where λ_L is the laser wavelength. If each sample is integrated for Δt = 500 μs, then the total integration time will be $t = N_L\ \Delta t = 63291 \times 500 \times 10^{-6} = 31.64$ s.

Filter Bandpass, $\Delta\lambda_f$

If the band is limited to 755 nm to 766 nm by means of an optical filter (transmission curve provided in appendix D, Figure D-3), meaning $\Delta\lambda_f$ = 11 nm = 0.01 μm.

Quantum Efficiency, Q

In the 762 nm band the energy of one photon is:

$$E = \frac{h \cdot c}{\lambda} = \frac{6.626 \times 10^{-3} \times 3 \times 10^{8}}{762 \times 10^{-9}} = 2.6 \times 10^{-19} \text{ [J/ph]}$$

Therefore 1 joule = $\frac{1}{2.6 \times 10^{-1}} = 3.8 \times 10^{18}$ [Ph] photons. Dividing both sides by 1 s results in 1 W = 3.8×10^{18} [Ph/s]. The sensitivity of the detector in this spectral region is 0.4 A/W where 1 A is 6.24E18 electrons per second. Considering this, the quantum efficiency will be:

$$Q = \frac{0.4 \times 6.24 \times 10^{18} \text{ e/s}}{3.8 \times 10^{18} \text{ Ph/s}} = 0.65 \left[\frac{e}{ph}\right].$$

The signal to noise ratio calculated from equation (4-24) for the 762 nm band will be:

$$SNR = (0.5)(2.9 \times 10^{-5}) \sqrt{\frac{\pi \times 2.17 \times 10^{20} \times 1.9 \times 10^{-3} \times 9 \times 10^{-8} \times 31.64 \times 0.65}{2 \times 0.01}} = 158$$

A more realistic SNR would be to assume an albedo of 0.25 and therefore the SNR for the 1600 nm channel would be 92 and for the 762 nm channel would be 80.

4.4.4. Electronics

The electronics of the payload controls the instrument scan speed, its spectral resolution and the triggering of the detectors. The control electronics unit of the instrument core were provided by ABB. The inputs for the ABB control box are the HeNe laser detector output and the white-light source detector output. As mentioned before, the white-light signal identifies the location of ZPD, which serves as a means to centre the mechanical scan and the interferogram in the data acquisition window. The HeNe laser is used as the metrology laser to control the instrument scan speed and interferogram sampling. The ABB control electronics unit outputs are listed below and are shown in Figure 4-19 with respect to an arbitrary OPD position:

- The fringe signal (FR) in digital and analog form:
    - This signal is the output of the metrology HeNe laser detector and has a cosine waveform.
- The de-phase fringe signal (FR90) in digital and analog form:
    - This signal is phase shifted by 90° relative to the FR signal to determine the direction of the scan depending on whether it is leading the FR signal or is preceding it.
- The ZPD in digital form:
    - This signal is at zero volts except when the scanning mirror crosses ZPD and shows the ZPD location within the scan.
- The scan direction (SD) in digital form:
    - This signal uses the FR and FR90 signals to determine in which direction the scanning arms are moving. It has the shape of a step function and has values of 0 V and 5 V.
- The scan window (SW) in digital form.
    - This signal has the shape of a step function and has a value of 0V when the scan data are useful. When the scanning arms hit their end stop in each direction this signal goes to 5 V momentarily to indicate the arms would be vibrating and an accurate FR signal will not be produced.

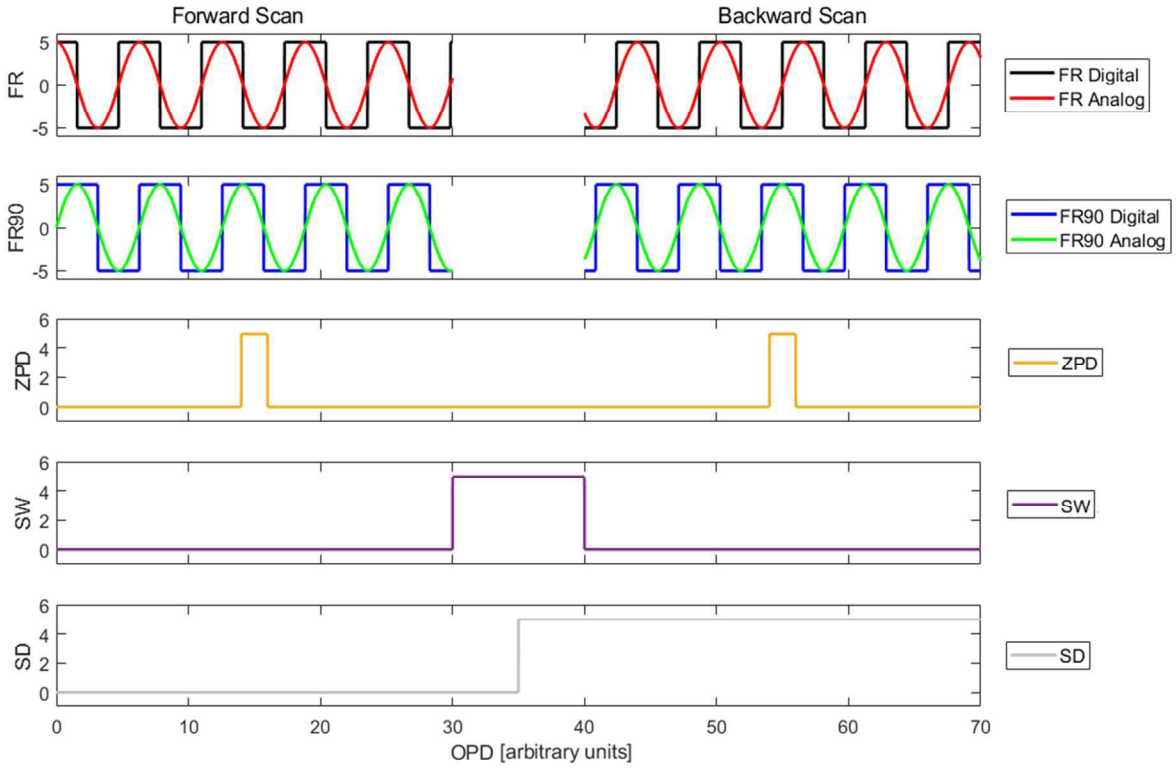

Figure 4-19: ABB control electronics unit output signals with respect to arbitrary OPD positions.

These outputs are inputs to the instrument control electronics that were designed as part of the work reported in this thesis and built at the LARSS laboratory at York by the author. The schematics of the instrument control electronics are shown in Figure 4-20 and the protocol of operation is described below:

- The output signals of the ABB control box are all 5-volt signals that are connected to the control electronics via BNC connectors.
- The signals are led through Schmitt triggers that acts as a line conditioner and removes unwanted noise from the signals.
- The signals are then put through a level shifter that brings the voltage down to 3.3 volts for use by the Freescale microcontroller.

- The Freescale is the payload master controller. It analyses the signals received and sends triggers to the detectors via two level shifters that generate 5-volt signals.

There are three computers that are part of the system:

- The control computer connects to the Freescale via an RS232 interface. It also connects to the IFTS control box via an RJ45 ethernet connection.
- Computer1 connects to the camera1 detector via a USB 2.0 which records the 762 nm channel and saves the data on this computer. It also connects to the Freescale via RS232. This computer has a Linux (Ubuntu 16.04) operating system.
- Computer2 connects to the camera2 detector via USB 2.0 which records the 1600 nm channel and saves the data on this computer. It also connects to the Freescale via RS232. This computer also has a Linux (Ubuntu 16.04) operating system.

The electronics were made meticulously by hand and tested several times. This process was necessary to determine the most suitable configuration to achieve the goals of the project. Several configurations of capacitors were used on the power supply lines to each component to reduce noise throughout the electronics. The final configuration can be seen in the circuit diagram in Figure 4-21.

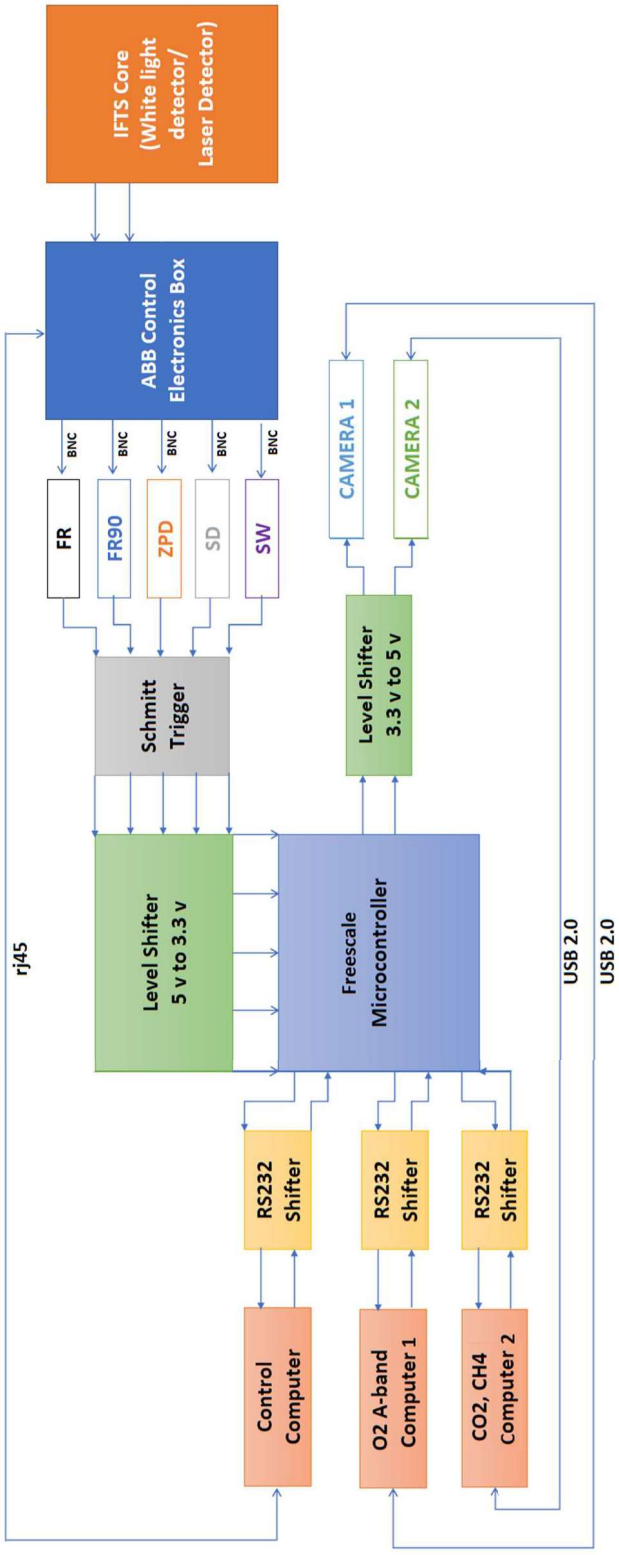

Figure 4-20: Electronics flowchart of the IFTS instrument control electronics

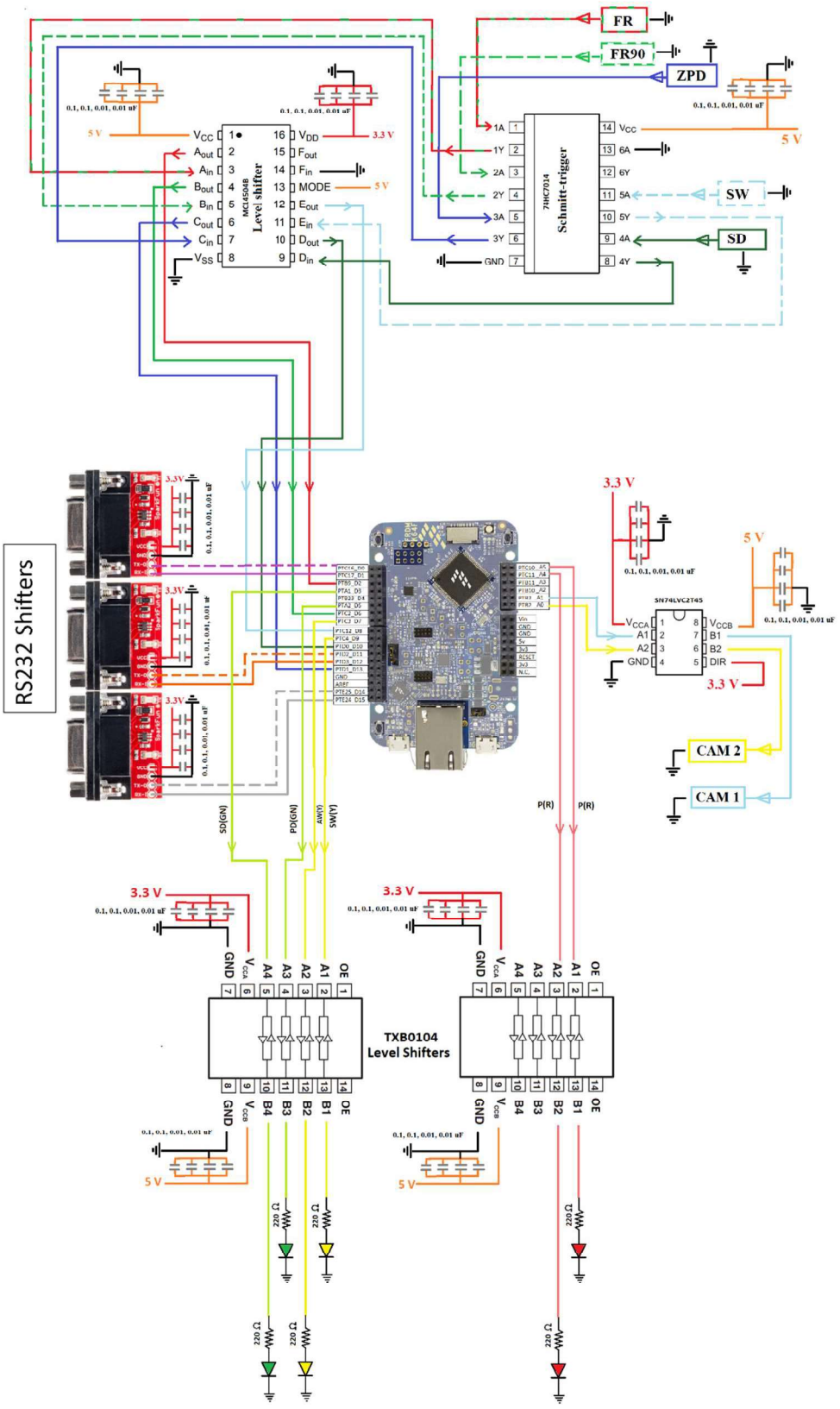

Figure 4-21: Circuit diagram of the IFTS control electronics.

4.4.5. Software

The control and acquisition software for the payload was developed by group members working on the project, Gurpreet Singh, David Barton and Greg Blair with recommendations from the author. The software controls when the camera detectors are triggered and how the data are recorded and stored.

The Freescale microcontroller reads four signal outputs from the ABB control box. These signals are the FR signal in digital form, the ZPD, the SD and SW. the FR90 signal is not used because it simply shows the scan direction and that is already provided by the SD signal (Personal communications: Singh, 2018).

Four setup files (SF) are used:

- SF1 contains the arm speed of the IFTS core and the spectral resolution in cm^{-1} which is loaded on to the ABB control software from the control computer.
- SF2 contains the trigger width which is loaded in to the Freescale microcontroller.
- SF3 contains the trigger width, integration time, starting pixel in the X-direction, ending pixel in the X-direction, starting pixel in the Y-direction, ending pixel in the Y-direction and the cooler set temperature. This file is loaded into the camera1 software on computer1.
- SF4 contains the same variables as SF3 but for camera2 which is loaded into the camera software on computer 2.

The protocol of operation of the control software is as follows:

- The first step in starting up the instrument is to activate the power-on switch. This switch supplies power to the control computer, computer1, computer2, Freescale microcontroller, ABB control box, IFTS core, camera1 and camera 2.

- After the switch is turned on, the Freescale waits for 5 min to allow for the IFTS core power-up routine and the cool-down of the cameras.
- The control computer autonomously starts the IFTS core software and reads SF1. At this time, SF2, SF3 and SF4 are read by the Freescale, computer1 and computer2 respectively. The Freescale now waits for 5 min for the IFTS core to reach the required scan speed and resolution.
- In the next step, the Freescale sends queries to computer1, computer2, camera1 and camera2 respectively to verify that they are alive and responding. After receiving the OK from the computers and cameras, the Freescale reads the SW signal.
- Once the SW signal goes from high to low, the Freescale sends a "Get ready" command to computer1 and computer2. At this time, computer1 and computer2 create data files and folders.
- The Freescale starts saving the SW, ZPD and SD signals in its memory and reads the FR signal. The Freescale sends trigger signals 1 and 2 to cameras 1 and 2 at every positive (and possibly negative) transition of the FR signal and keeps a count of trigger 1 and trigger 2 signals.
- At each external trigger, camera1 and camera2 take an image with the settings specified in SF3 and SF4. When the counts for triggers 1 and 2 reach a maximum number decided by the length of the scan window, the Freescale sends a "Done" command to computer 1 and computer 2 and data recording stops.
- While the IFTS core is in turn-around mode (one scan has ended, and the arms are reversing direction for a new scan), the FR signal data are downloaded from the Freescale memory to computer1 and computer2.

- When the SW signal goes from high to low again the procedure explained in this paragraph repeats itself (Personal communications: Singh, 2018).

4.4.6. Testing

In this section the results of tests conducted to determine the experimental spectral resolution of the instrument, the wavelength distribution over the width of the detector and the SNR of the instrument are reported. For this purpose, different light sources were measured such as a HeNe and an IR laser as well as a broad-spectrum white light source reflected from a diffuser.

Spectral Resolution

The first experiment was to measure the spectral resolution of the instrument and to determine how well it matches the theoretical numbers. For this purpose, two different monochromatic lasers were used. A 632 nm HeNe laser with an approximately 2 mm beam diameter and a 1550 nm IR laser with an approximately 2.8 mm beam diameter was used. The optical setup is shown in Figure 4-22. The laser beam is expanded via the beam expander and reflected from two 45° mirrors to the aperture of the IFTS. The beam goes through the interferometer section and is then reflected from another 45° mirror to the detector. For the 632 nm laser, no filter was used and for the 1550 nm laser, a bandpass filter centered at 1595 nm with a bandwidth of 100 nm was used.

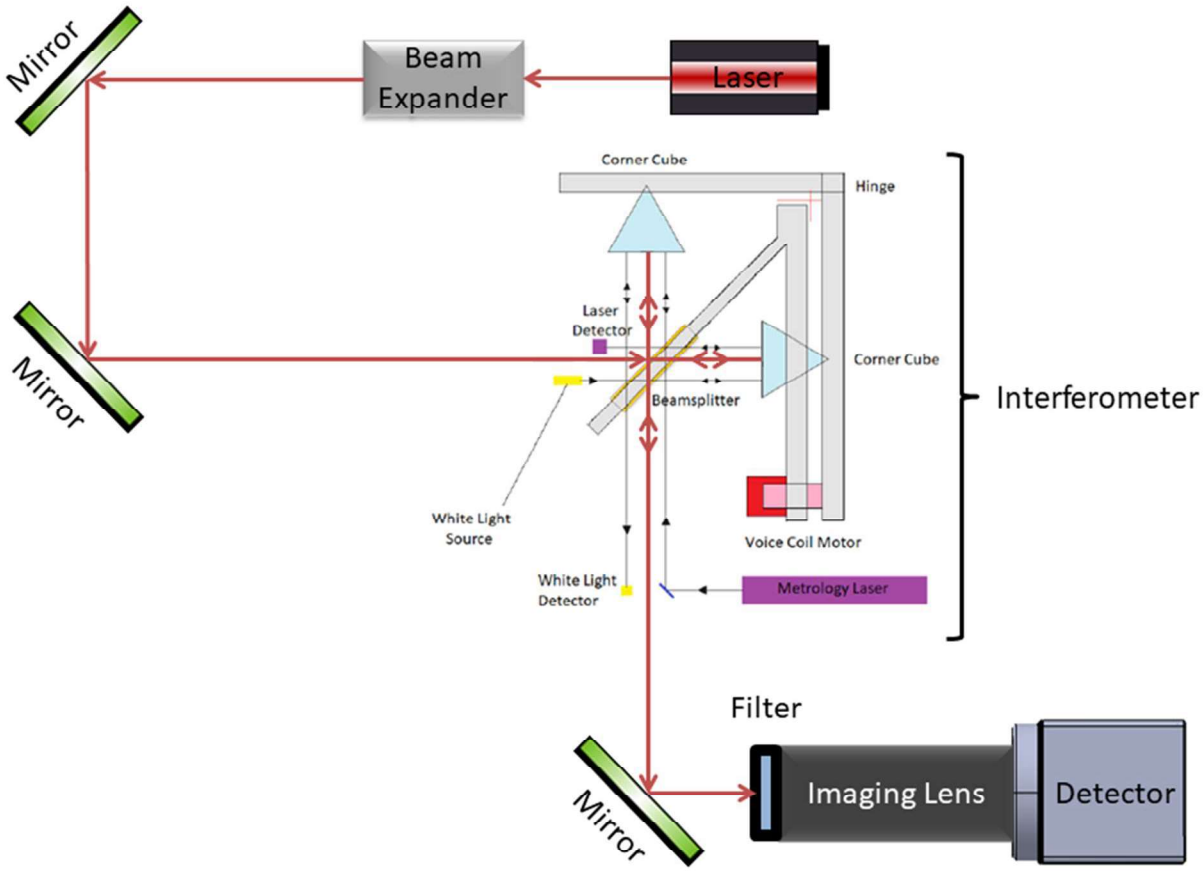

Figure 4-22: Optical setup used to test the IFTS spectral resolution and the distribution of wavelength across the detector.

632 nm HeNe Laser

The interferogram recorded for the 632 nm laser can be seen in Figure 4-23. The detector settings for this measurement were: 150 µs integration time, 50 µs trigger width and pixel number (318, 135). The IFTS was running with a scan speed of 500 Hz of the metrology laser fringe signal and the detectors were sampling at each zero crossing of the metrology signal (double-sampling). An FFT was applied to the interferogram and the resulting spectrum can be seen in Figure 4-24 with the peak at 15,789.3 cm^{-1} which corresponds to 633.34 nm. There was no apodization function applied to the interferogram in this case. The wavelength assumed for the metrology laser is

632.816 nm. A magnification of the un-apodized spectrum is shown in Figure 4-25 where the FWHM of the peak is 0.64 cm^{-1} which shows the spectral resolution of the instrument.

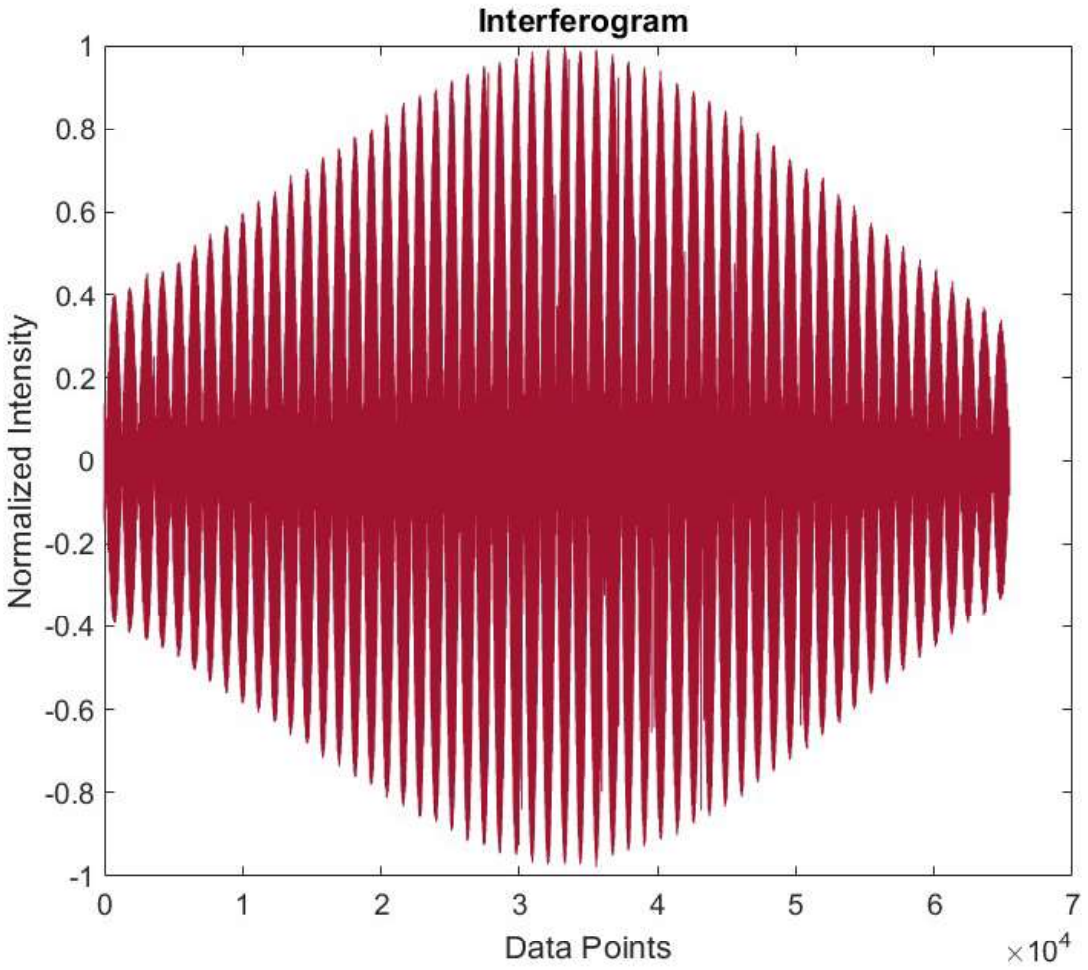

Figure 4-23: Interferogram of a 632 nm HeNe laser recorded by the IFTS.

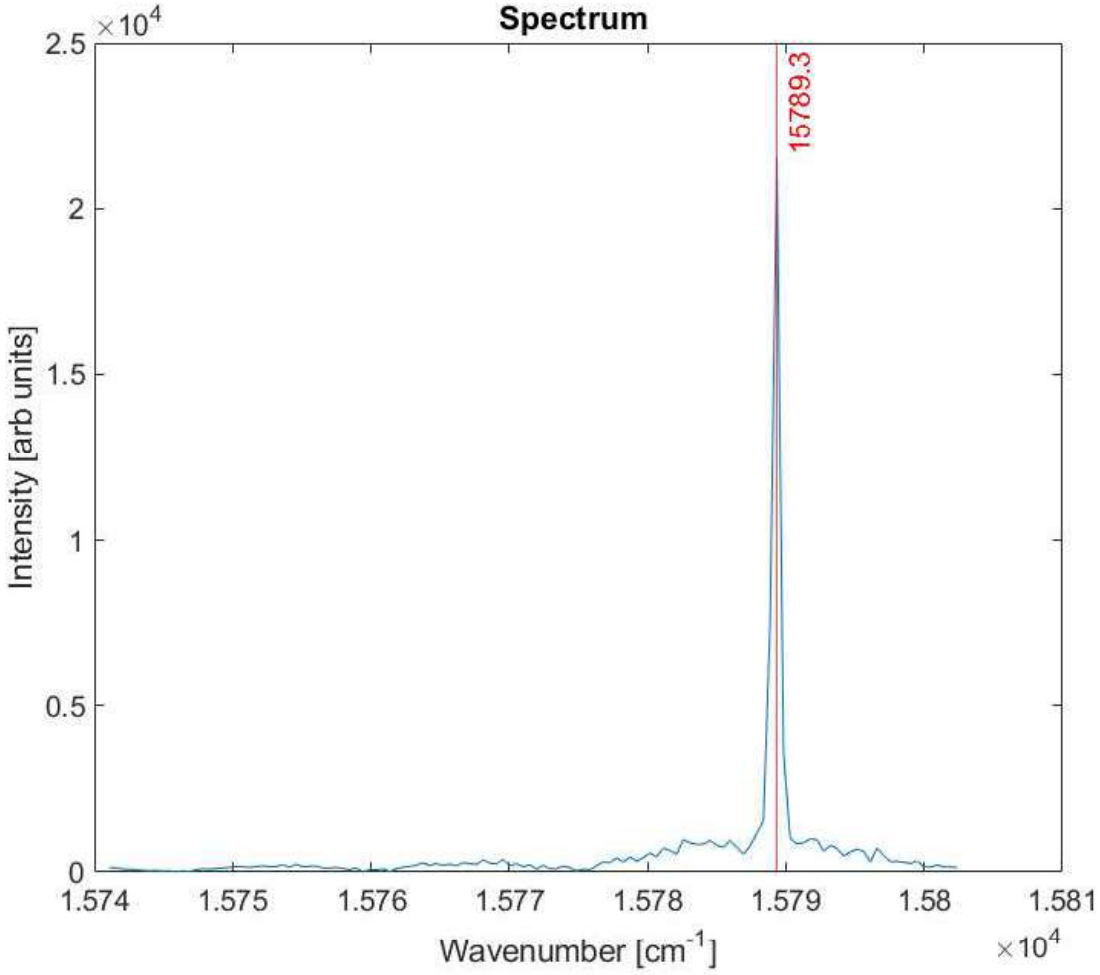

Figure 4-24: FFT of the interferogram in Figure 4-23 resulting in the un-apodized spectrum of the 632 nm laser. The peak is at 15789.3 cm^{-1} which corresponds to 633.34 nm.

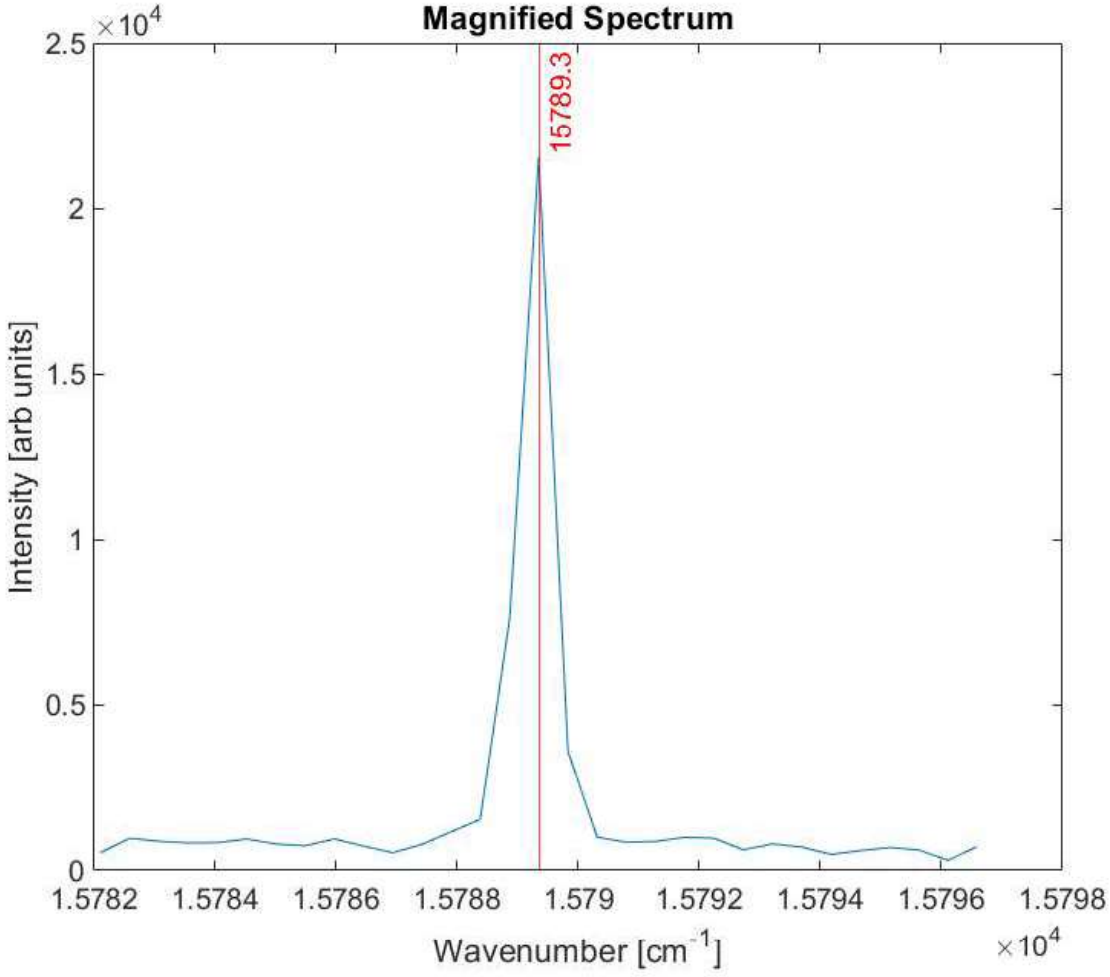

Figure 4-25: The magnification of the un-apodized spectrum shown in Figure 4-24. The FWHM of the peak is 0.64 cm^{-1} which shows the spectral resolution of the instrument.

1550 nm IR Laser

The interferogram recorded for the 1550 nm laser can be seen in Figure 4-26. The detector settings for this measurement were: 350 µs integration time, 100 µs trigger width and pixel number (214, 58). The IFTS was running with a scan speed of 300 Hz of the metrology laser fringe signal and the detectors were sampling at each zero crossing of the metrology signal (double-sampling). An FFT was applied to the un-apodized interferogram and the resulting spectrum can be seen in Figure

4-27 with the peak at 6440 cm^{-1} which corresponds to 1552.8 nm. The multiple peaks observed in the spectrum are due to the multiple modes of the laser used. A magnification of the un-apodized spectrum is shown in Figure 4-28 where the FWHM of the peak is 0.58 cm^{-1} which shows the spectral resolution of the instrument.

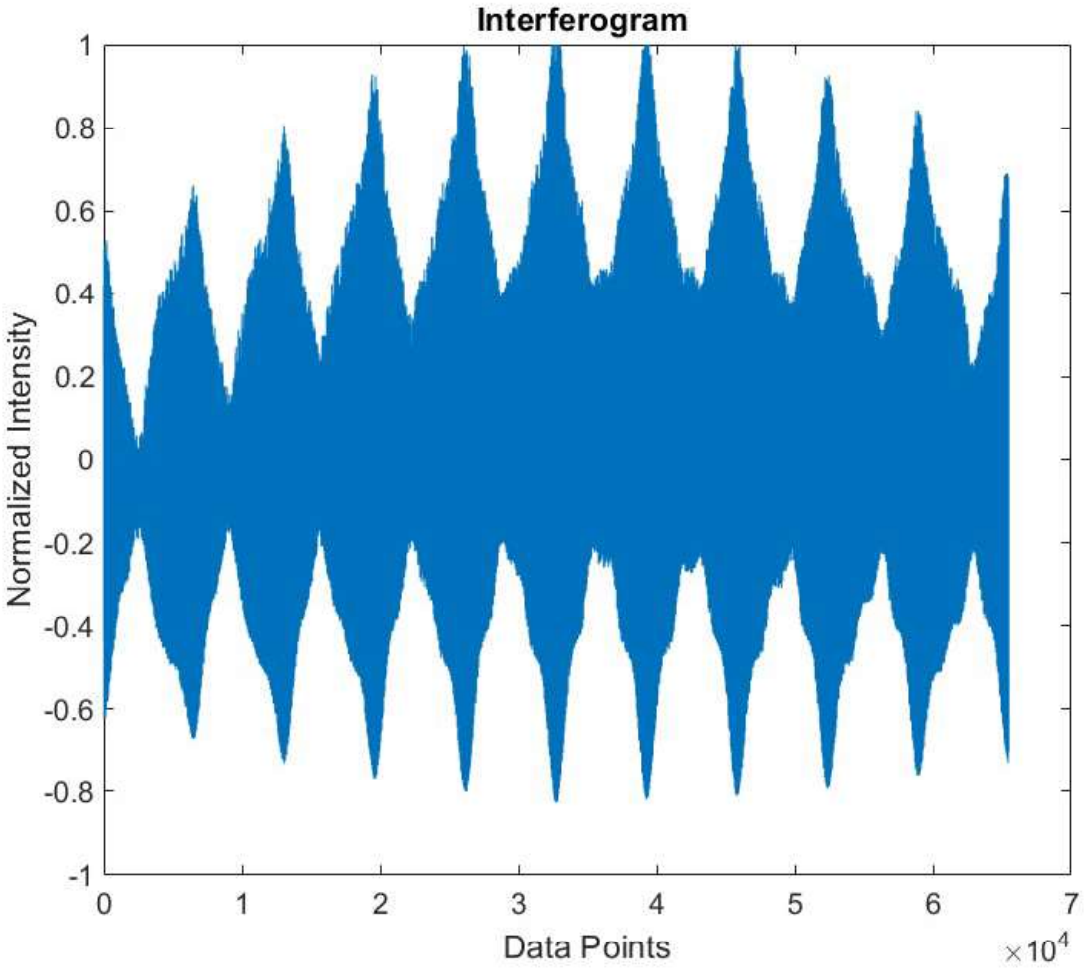

Figure 4-26: Interferogram of a 1550 nm IR laser recorded by the IFTS.

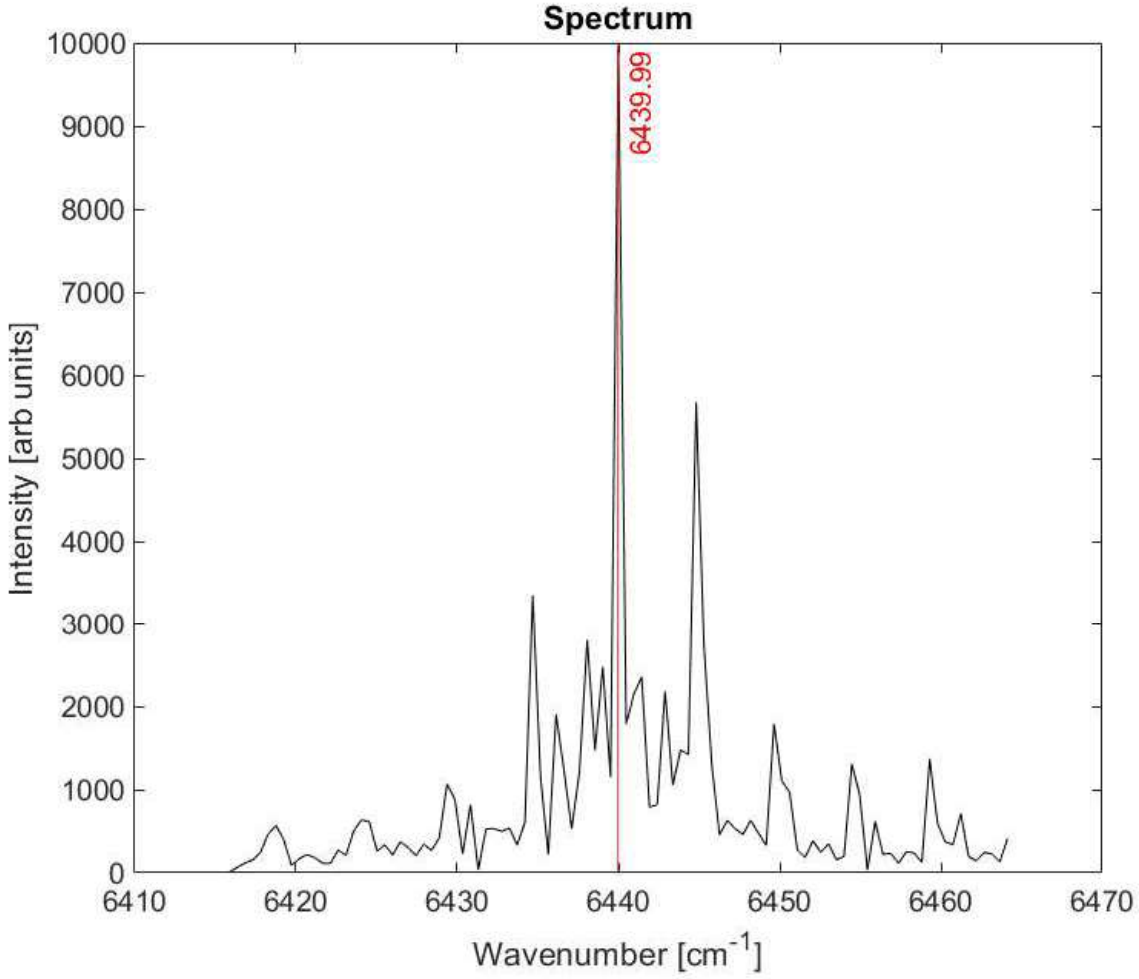

Figure 4-27: FFT of the interferogram in Figure 4-26 resulting in the un-apodized spectrum of the 1550 nm laser. The peak is at 6440 cm^{-1} which corresponds to 1552.8 nm.

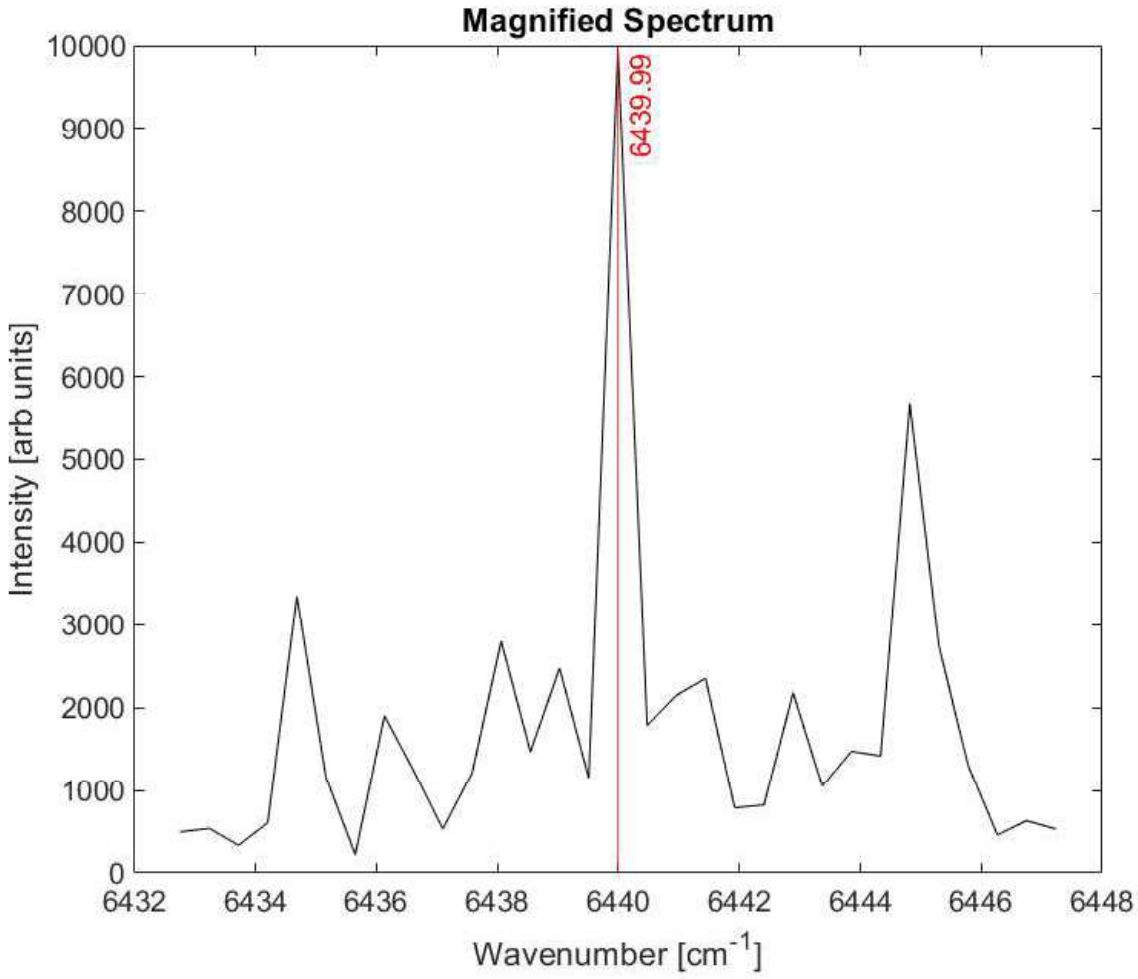

Figure 4-28: The magnification of the un-apodized spectrum shown in Figure 4-27. The FWHM of the peak is 0.58 cm^{-1} which shows the spectral resolution of the instrument.

Wavelength Distribution Over the Detector

As discussed in section 4.3.1, when light from the source being measured is propagating parallel to the optical axis of the interferometer, the optical path difference is $X_0 = 2d$ where d is the mechanical path difference of the two mirrors. As observed in Figure 4-3, the off-axis light source has an optical path difference of $2d\cos\theta = X_0\cos\theta$. As a result, equation (4-11) becomes:

$$\boldsymbol{E(\nu) = \int_{-\infty}^{\infty} I(x)\left(e^{-i2\pi X_0(\nu cos\theta)}\right) dx} \qquad \textbf{(4-25)}$$

Which shows that the wavenumber of the spectrum obtained at an optical path difference of X_0 for an on-axis pixel is ν and for an off-axis pixel is νcosθ.

The 632 nm HeNe laser was used to test this phenomenon. The same optical setup as described in Figure 4-22 was used. The laser was adjusted to focus on the left, centre and right side of the detector. The IFTS scan speed was 500 Hz and the interferogram was double-sampled. The results are presented in Figure 4-29. From the left edge of the detector pixel number (64,70) was measured and the spectrum peaks at 15,758.7 cm^{-1}. From the centre of the detector, pixel number (144,58) was measured and the spectrum peaks at 15,784.8 cm^{-1}. From the right edge of the detector, pixel number (298,80) was measured and the spectrum peaks at 15,758.9 cm^{-1}. The wavenumber distribution is consistent between the left and right edge of the detector and show an off-axis angle of approximately 3.3°:

$$\nu = \nu_0 cos\theta \quad \rightarrow \quad \theta = cos^{-1}\left(\frac{\nu}{\nu_0}\right) = cos^{-1}\left(\frac{15758.9}{15784.8}\right) = 3.28$$

Where, ν is the wavenumber at the edge of the detector and ν_0 is the wavenumber at the centre of the detector.

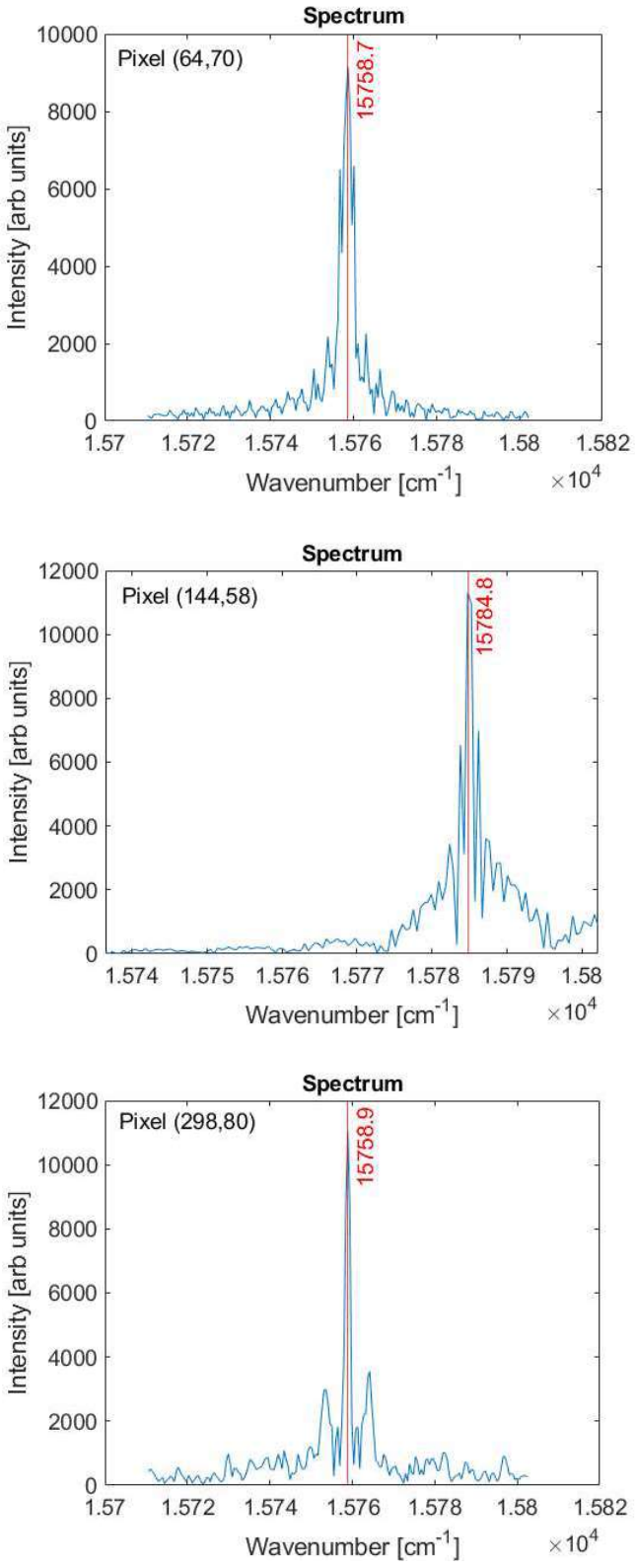

Figure 4-29: Spectrum of the 632 nm HeNe laser focused on the left (top), centre (middle) and right (bottom) of the detector.

SNR

To test for the SNR of the IFTS instrument, the 1595 nm bandpass filter was measured. The source used was a 200 W tungsten-iodine lamp, dispersed from a Lambertian diffuser surface. The optical setup for this test can be seen in Figure 4-30. The IFTS was running at a scan speed of 500 Hz. The detector was windowed and only data from one pixel are used. The detector parameters used are an integration time of 200 μs and a trigger width of 50 μs. The interferogram was apodized using a $\cos^2$ function and an FFT was applied to it. The recorded interferogram by the IFTS can be seen in Figure 4-31. The interferogram of a broad-band source has a very large signal at ZPD and lower signal as it moves away from ZPD. The un-apodized spectrum of the IR filter can be seen in Figure 4-32 and the $\cos^2$ apodized spectrum can be seen in Figure 4-33. The blue curve shows the IFTS spectrum and the red curve shows the manufacturer's spectrum. The manufacturer's spectrum peaks at about 6333.12 cm^{-1} and has a FWHM of 306.1 cm^{-1}. The IFTS spectrum peaks at about 6335.44 cm^{-1} and has a FWHM of 306.46 cm^{-1}. The difference in FWHM is about 0.34 cm^{-1} which may indicate that the resolution of the spectrometer the manufacturer used was less than the IFTS. The difference in peak wavenumber between the IFTS and the manufacturer is 2.32 cm^{-1}. The spectrum the manufacturer has provided is for measurements made in vacuum. Since the measurements presented here were taken in air, the difference in the refractive index of air (1.000293) will push the spectrum into higher wavenumbers as described in equation (4-26). Based on the equation the IFTS wavenumber should be at 6334.97 cm^{-1}.

$$\frac{\nu}{\nu_0} = \frac{\lambda_0}{\lambda} = \frac{c/f}{v/f} = \frac{c}{v} = n \qquad \textbf{(4-26)}$$

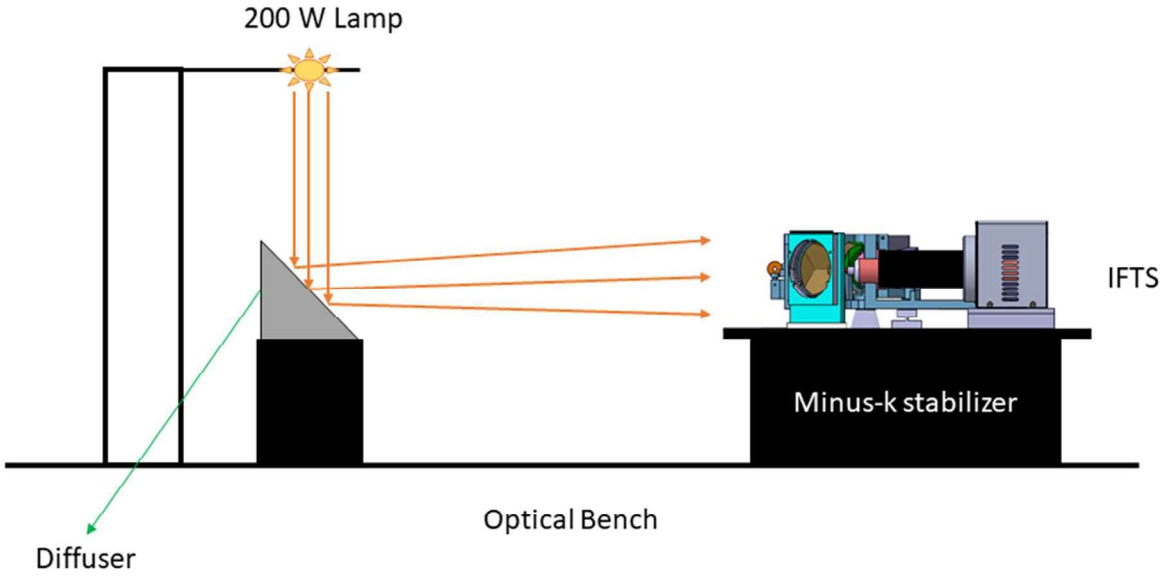

Figure 4-30: Optical setup used to scan the 1595 nm bandpass filter.

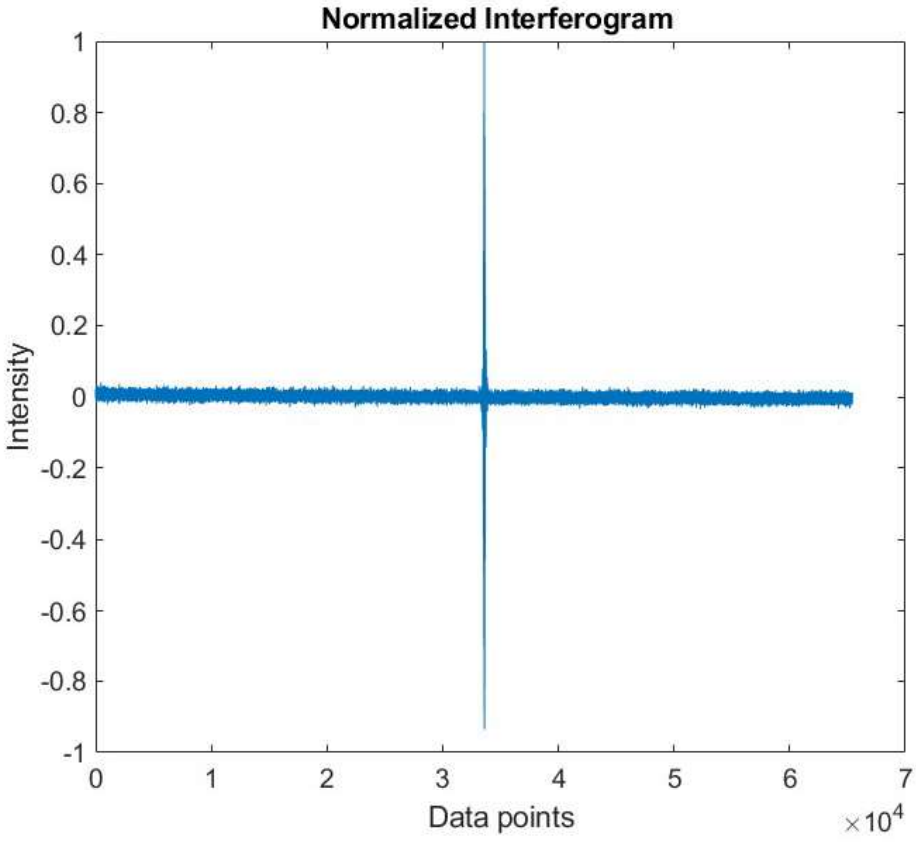

Figure 4-31: The normalized interferogram of the 1595 nm IR filter as recorded by the IFTS.

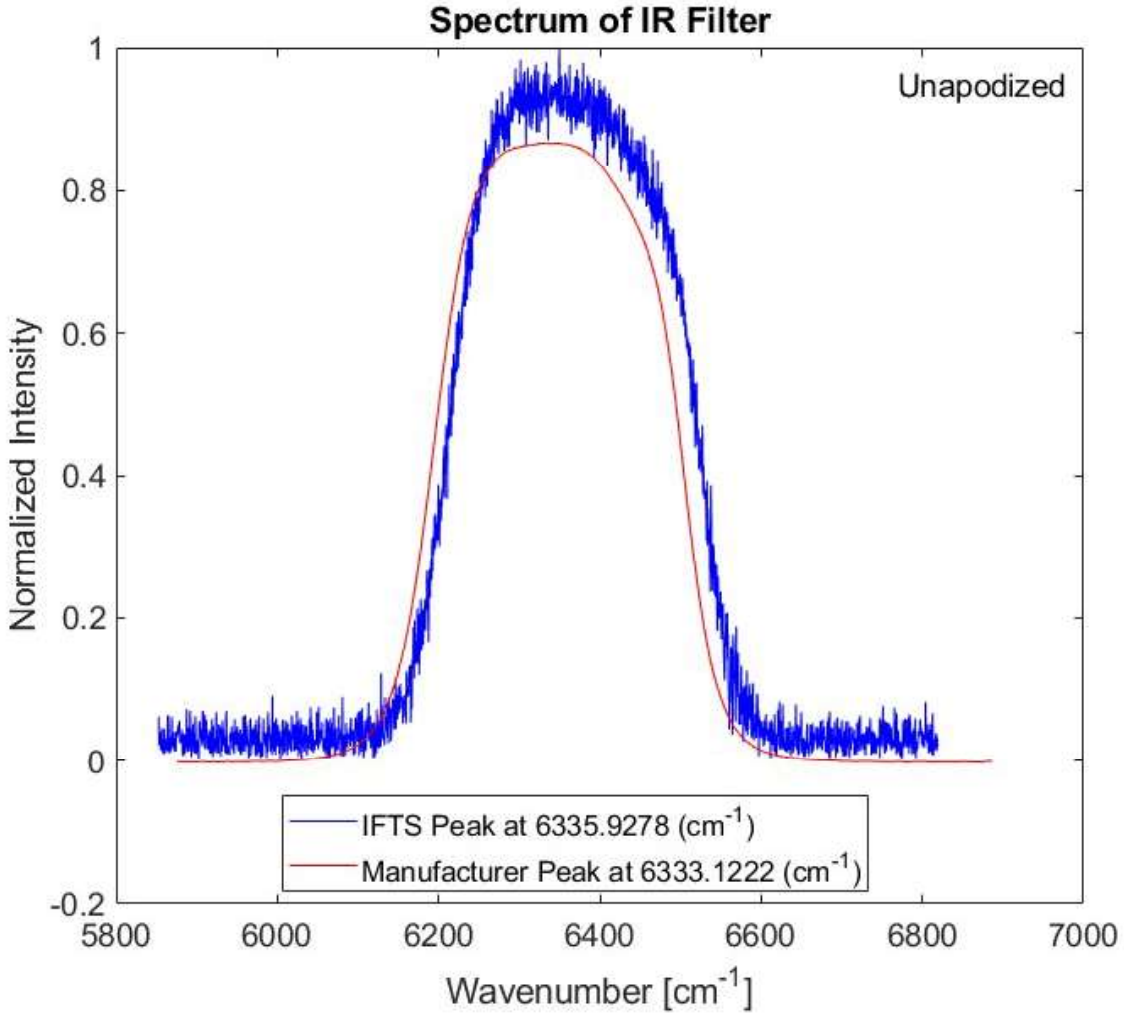

Figure 4-32: The un-apodized spectrum of the IR filter (blue) and the filter manufacturer's given spectrum (red).

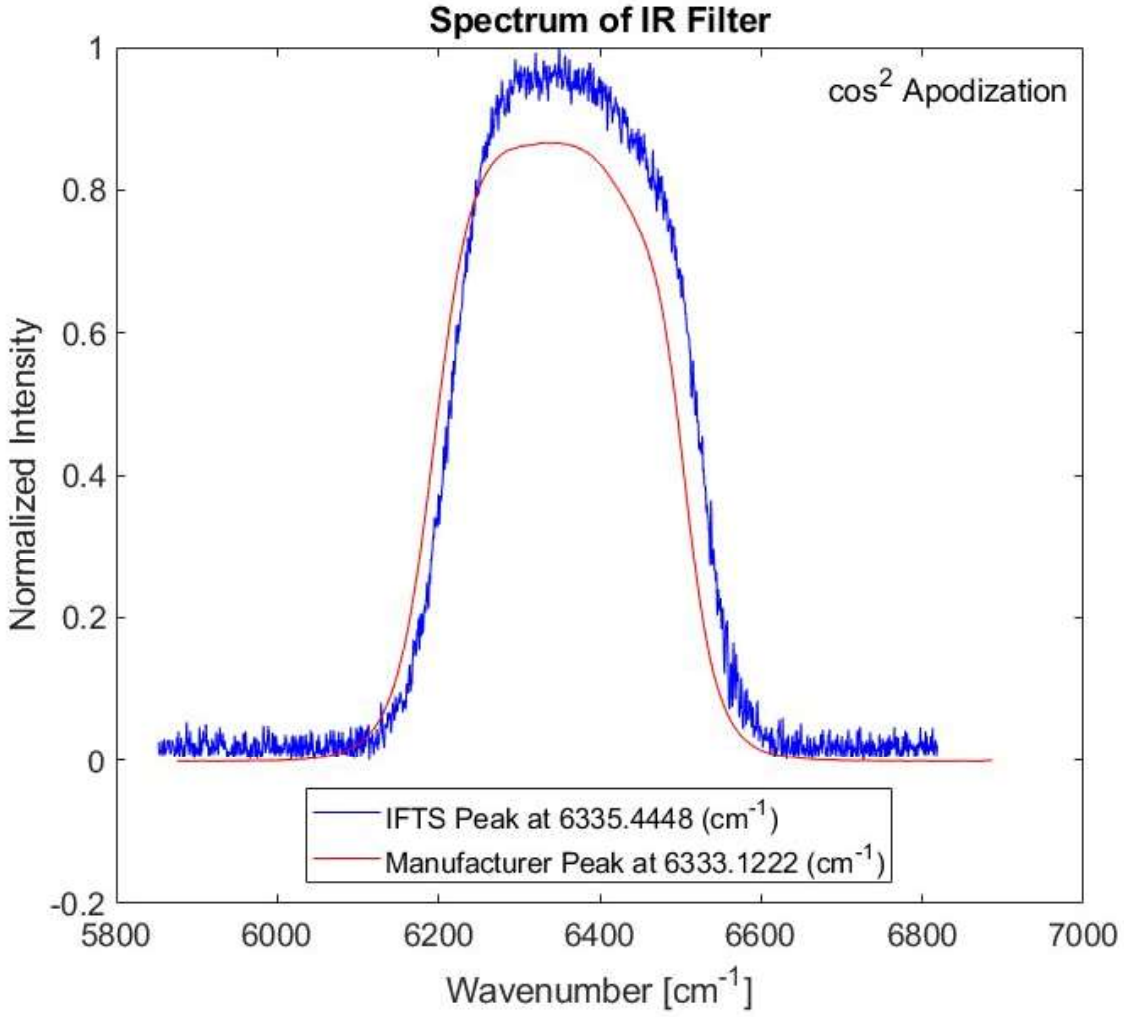

Figure 4-33: The apodized ($\cos^2$) spectrum of the IR filter (blue) and the manufacturer's given spectrum (red).

A 6-degree polynomial was fit to the apodized spectrum shown in Figure 4-34. The line of best fit (red) is the base of the signal and the noise is the scatter about the model (blue). The mean of the summed squared magnitude of the signal to that of the noise (SNR) is ~ 47.7.

Using equation (4-24), the theoretical SNR of the 200 W lamp should be 46. The lamp SNR calculations can be found in appendix H.

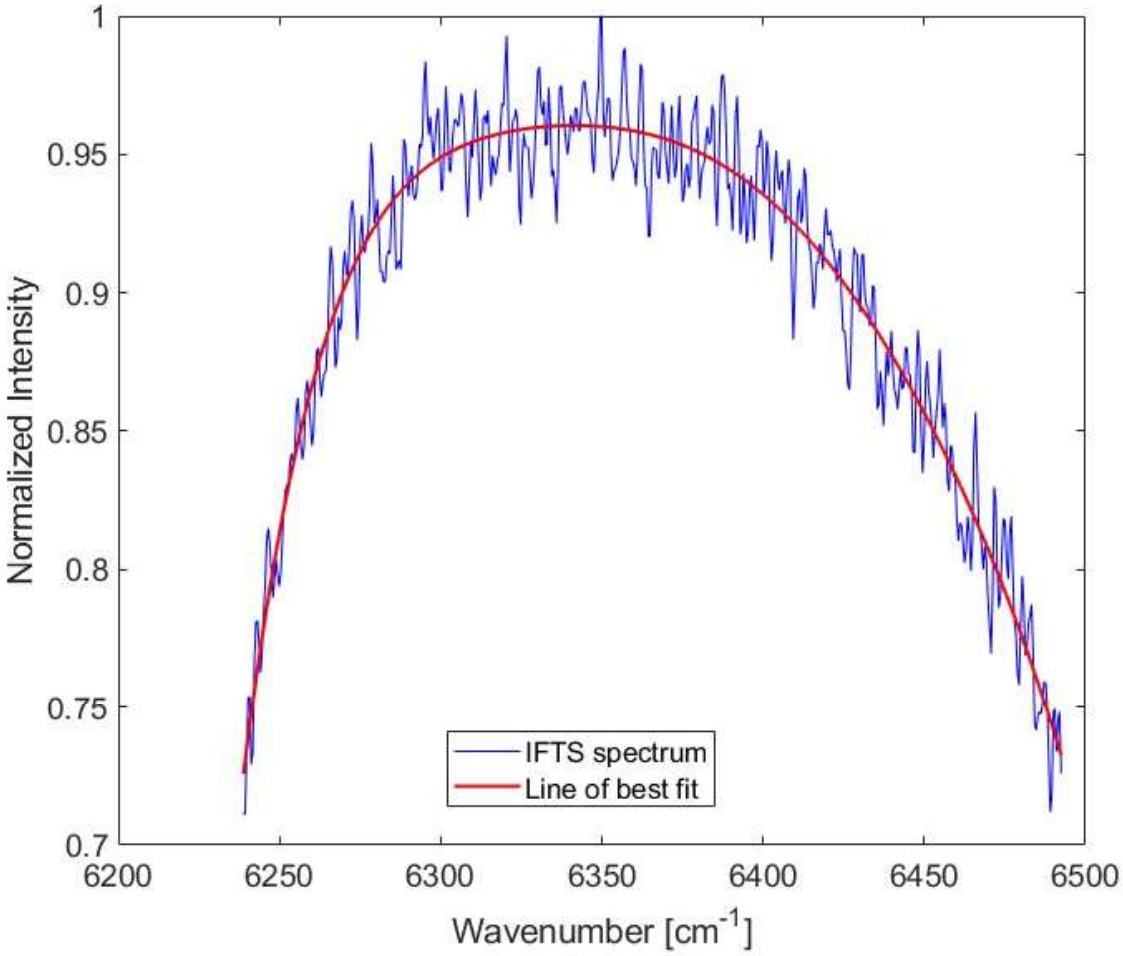

Figure 4-34: Line of best fit to the IFTS IR filter spectrum.

4.5. Discussion

The IFTS instrument design and development presented in this chapter, with focus on the Arctic regions, will provide a 12 x 12 m spatial resolution from a balloon platform at 40 km altitude and a 12 x 12 km spatial resolution from a satellite platform at 40,000 km altitude. The spatial resolution can easily be adjusted by changing the detector pixel spacing or changing the focal length of the imaging lens but, there is a tradeoff between SNR and these factors. The smaller the pixels are, the lower the SNR becomes.

In the case of the IFTS, a 100 mm imaging lens was chosen because it provided a representative resolution appropriate to the eventual application of the technology in space.

The IFTS is a demonstrator instrument and therefore it was decided that it should only measure in two spectral channels. One is centred at 762 nm for the O_2 A-band, and the other is centred at 1600 nm for CO_2 and CH_4 which are the second and third most important GHGs present in the atmosphere after water vapour.

The detectors used in the IFTS instrument are Xenics digital array detector cameras with model number Xeva-1.7-320. They are visible near infrared cameras with a range of 0.4 to 1.7 μm and, with the USB 2.0 interface, have an image acquisition speed of 100 Hz (frames per second). The image acquisition speed for the O_2 A-band should be 200 Hz to fulfill the Nyquist frequency requirement. In order to achieve 200 Hz, the detector needs to be windowed.

The data acquisition software for the IFTS is being designed and developed by group members of LARSS. This software as described in section 4.4.5 of this chapter is still under development at the time of the completion of this thesis.

4.6. Satellite Instrument Recommendations

The IFTS instrument whose design and construction is investigated and reported in this thesis is designed with consideration to be installed on a balloon payload and provide evaluation data for a proposed space-based instrument. One of the main issues that arises with this instrument for space applications is data handling. The IFTS instrument produces a large amount of data which may make the downlink to Earth, challenging. The rough calculations for data volume can be found in appendix I.

One way to overcome this challenge is to do the level 1 data processing onboard and downlink

relevant parts of the spectrum. Level 1 data processing refers to converting interferograms to spectra. This method requires more powerful computers onboard for the data processing.

Another issue for a space-based instrument is its mass and volume. In a space mission the mass and volume budget assigned to each payload must be followed precisely. Therefore, the lower the mass and the smaller the volume the more likely it is for the IFTS instrument to win a spot on a space mission. For an optical bench setup, the IFTS instrument is mounted on a vibration isolation platform which weighs approximately 32 kg. The complete setup along with the payload weighs approximately 57 kg and has dimensions of 60 cm x 45 cm x 37 cm. It is anticipated that on a space platform the IFTS instrument will not experience low frequency vibrations when in orbit and therefore, vibration isolation platform is not needed which, in turn, will reduce the mass and volume significantly.

The instrument at its current stage is not designed to withstand the vibrations and shocks during launch. Additional mechanical design is required to lock the scanning arms of the core of the IFTS to prevent motion during launch. This mechanism should automatically disengage when the instrument is ready to turn on.

5. Image Stabilizer Pointing System

The fore-optics of the IFTS instrument includes an Image Stabilizer Pointing System (ISPS). Its purpose is to track an image on the ground in the nadir direction for the duration of a single scan of the interferometer. During each scan, which is equivalent to one measurement, the image on the ground should stay fixed with respect to the instrument to avoid intensity variations on the detector pixels. Intensity variation on the pixels during the scan introduces noise on the interferogram and also results in the loss of resolution and geolocation of the pixel images on the ground.

This chapter discusses the design, development and testing of the ISPS. The requirements imposed by the IFTS on the mechanical design, software and electronics are also explained. The expression "image stabilizer" and ISPS will be used interchangeably in the following.

5.1. Literature Review

Remote sounding instruments for Earth observation and atmospheric measurements require a pointing device to point the instrument toward an area of interest. Usually this pointing device is a moving mirror with one or two degrees of freedom. As the science of remote sensing evolves, there is a high demand for more precise and high-resolution instruments. These new instruments require fast, precise, space-qualified and high-resolution, pointing devices.

Several technologies have been used in developing such pointing devices. Table 4 lists a few sample image stabilizer pointing system platforms. Microelectromechanical systems (MEMS) are one of these technologies. MEMS pointing mirrors use electromagnetic actuation to steer micromirrors built onto an electronics chip. This type of actuation is frictionless and a good option for space qualified instrumentation but, the MEMS sensor's optical surface is on the order of a few millimeters and not suitable for Earth observation instrumentation requiring a large aperture (refer

to entry 4 in Table 4) (Texas Instruments, 2018).

Piezoelectric stepping motor actuators are another technology used in the development of pointing mirrors. Piezo stepping motors are frictionless but, their travel range is usually on the order of micro meters (max 1mm) which gives a maximum travelled angle of ~2° (refer to entry 2 in Table 4). This angle is not enough for an Earth observation instrument on orbit to fully scan the area of interest. Usually piezoelectric drives cannot take a high load. For example, in entry 3 of Table 4, the maximum load is 0.5 kg which limits the type of mirror which can be used.

A widely used technology for steerable mirror platforms is employed in Stewart platforms. These platforms have six actuators and can cover a wide range of travel as well as heavy loads. These platforms come in a variety of sizes. Physik Instrumente (PI) company produces these platforms under the name of Hexapods and uses brushless DC motors to drive them (Physik Instrumente, 2018). These motors are not frictionless (refer to entry 1 in Table 4).

The image stabilizer pointing system presented in this chapter provides an alternative to commercially available platforms. It is a state-of-the-art image tracking and stabilization platform. It is light weight and compact and uses frictionless voice coil motors (VCM) with a maximum travel range of 8° and a maximum load of 5 kg which gives the freedom of choosing different types of mirrors for different applications (refer to entry 5 of Table 4).

Table 4: A comparison of select image stabilizer pointing mirror platforms.

	Instrument	Driver	Optical surface Ø	Max range	Max load	Weight	Volume
1	Miniature Hexapod (PI instruments H-810)	Brushless DC Motor	9 cm	±10°	5 kg	1.7 kg	11.8 x 10 x 10 cm
2	Miniature Piezo Hexapod (PI instruments P-911)	Piezoelectric stepping motor	8 cm	±1°	1.5 kg	N/A	10 x 10 x 9 cm
3	Q-motion SpaceFAB (PI instruments Q-845)	Piezoelectric Inertia	7 cm	±7°	0.5 kg	1.9 kg	18 x 18 x 8 cm
4	MEMS pointing mirror (Texas instruments TALP-1000B)	Electromag-netic actuation	3 mm	±5°	N/A	Light weight chip (<100 g)	13 x 22 x 8 mm sensor
5	Image Stabilizer Pointing System (ISPS)	Voice Coil Motors	10 cm	±4°	5 kg	2.5 kg including Mirror	15 x 15 x 13 cm including Mirror

5.2. Requirements

The image stabilizer acts as a fine pointing device to track the sun or an image on the ground. It is complimentary to the attitude control of a satellite or the tracking system of a balloon gondola platform. It is required to be operational in vacuum and at low temperatures as well as being small, lightweight and frictionless for space applications.

The IFTS instrument imposes other requirements on the image stabilizer. For a balloon demonstrator of this instrument, the image stabilizer should provide a 500 second dwell time on each spatial element (the duration of a scan of the interferometer). Several factors contribute to scene movement on a balloon platform. Wind speed is a key factor. Other factors are the gondola

pendulum oscillation, which consists of a uniaxial swing mode. The frequency of the uniaxial swing is on the order of 1 Hz. Payload-induced vibrations can also cause the scene viewed by the instrument to change. These vibrations can come from high frequency pointing jitters from other instrument tracking systems or the gondola tracking system.

Usually flights are done at turnaround time when the wind speeds at stratospheric levels are ~10 km/h. To account for that, the angular speed of the ISPS mirror should be 0.004 °/s. To account for other vibrations and oscillations of the gondola the refresh rate on the correction of the mirror should be on the order of 10 Hz. The pointing accuracy required to avoid blurring on the 30 μm pixels should be ~10^{-5} radians.

5.3. Development and Design

The image stabilizer was designed and developed at the Laboratory for Atmospheric Remote Sounding from Space (LARSS) at York University by the author of this thesis. The image stabilizer is a two-axis, precise tilt mirror, pointing system platform with a ± 4.0° travel range in the X and Y axes. It has dimensions of 15 cm x 15 cm x 13 cm and weighs 2.5 kg without its electronics. Figure 5-1 and Figure 5-2 show the image stabilizer with the different parts labelled. The mechanical CAD drawings of the ISPS can be found in appendix N.

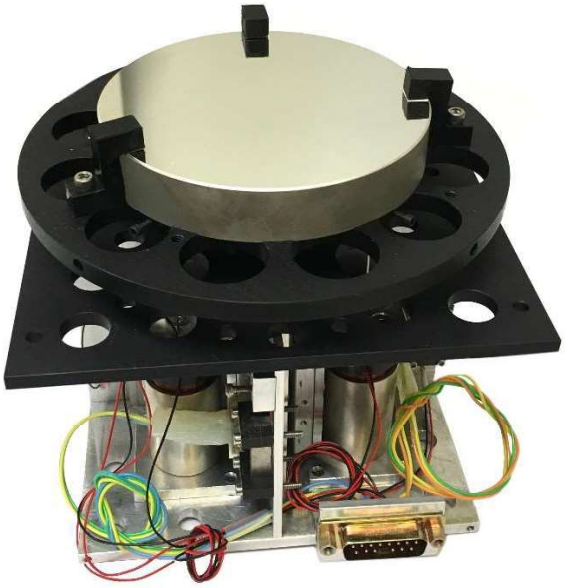

Figure 5-1: A linear two-axis tilt mirror image stabilizer pointing system.

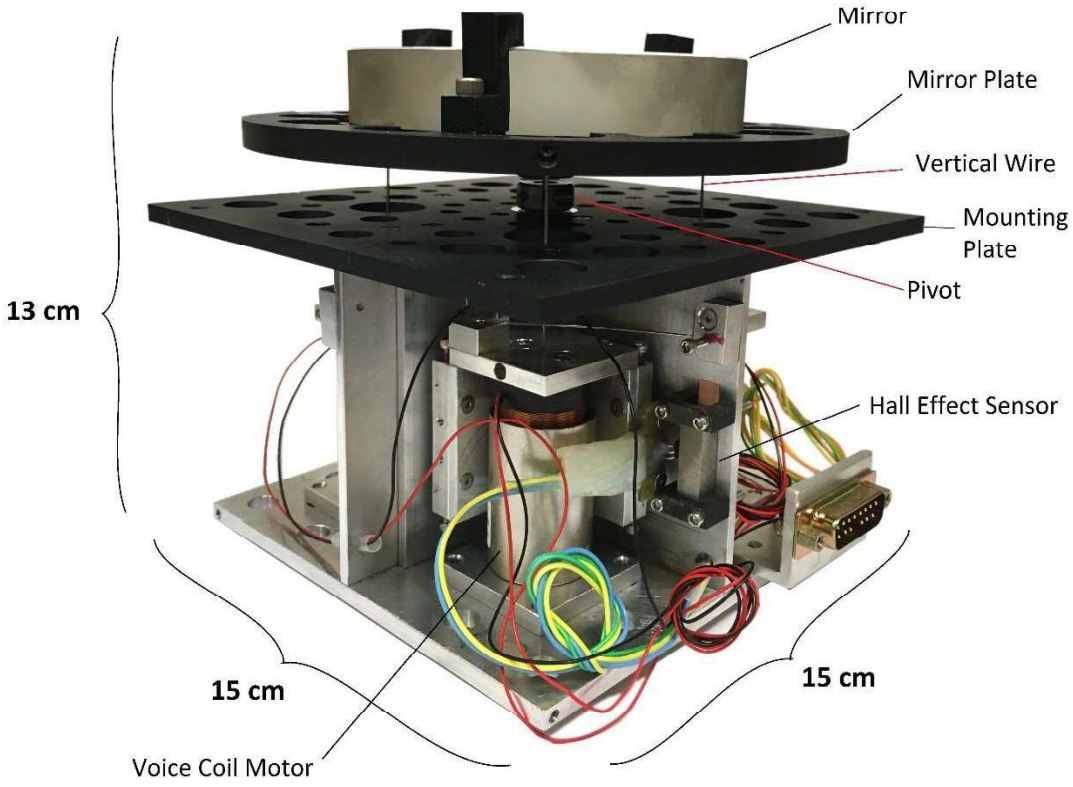

Figure 5-2: Image stabilizer pointing system with different parts labelled.

5.3.1. Mechanical

The two-axis motorized tilt mirror image stabilizer design is based on wire flexure pivots. It consists of four modules, two in each of the X and Y axis. The extra module in each axis is for redundancy. Each module contains a voice coil motor, a carriage and a base of its own. The motor magnet is fixed to the base angle and plate, whereas, the coil is fixed to the carriage angle. The carriage is connected to the base via two stainless steel wires called horizontal wires in each of the X' and Y' axis. A lateral wire also connects the carriage to the base to control rotational movement of the carriage. These wires are stainless steel wires with a diameter of 0.022 inch and a tensile strength of 205,000 psi. Each wire is clamped down with a set screw at each attachment point on the carriage and base angle. This design allows the motors to move up and down in a frictionless, linear motion. Figure 5-3 shows one module of the image stabilizer where the horizontal wires are marked in purple and the lateral wire is dark green. In this image the base plate is removed to show the details of the wire flexure design. Figure 5-4 shows all four modules integrated and mounted onto the base plate. All four modules are identical.

The magnet section of the voice coil motor is aligned with the coil very carefully so that while the motor is moving up and down the slight movement of the coil towards the origin of axis X and Y does not result in the coil touching the magnet. This alignment is done by hand and once alignment is achieved, four bolts that attach the magnet plate to the base plate are tightened.

From each carriage, a single wire (vertical wire) goes up to the mirror plate (refer to Figure 5-2) which pulls and pushes the mirror along the Z axis. The mirror plate is also connected from the centre to the mounting plate (refer to Figure 5-2) with a wire that acts as the pivot point for the X and Y axes. These wires are stainless steel wires with a thickness of 0.031 inch and a tensile strength of 205,000 psi. The carriage wires are clamped down with set screws at each point of

attachment. The pivot wire is clamped at each end with a D-profile, two-piece, shaft, collar clamp as seen in Figure 5-5. The use of this type of clamp instead of a set screw clamp allows even pressure to be applied to the pivot wire from all directions. The clamp design removes any hysteresis which would arise from a set-screw design.

The image stabilizer can be integrated into any instrument that is making solar or nadir measurements. In the case of the LARSS IFTS it is integrated with the IFTS instrument. Figure 5-6 shows how the image stabilizer is integrated with the IFTS instrument in Nadir mode. An angled mirror (in blue) directs the nadir image to the IFTS instrument. A small camera is placed at the aperture of the IFTS which sees the same image that the IFTS is seeing for feedback to the control software of the image stabilizer.

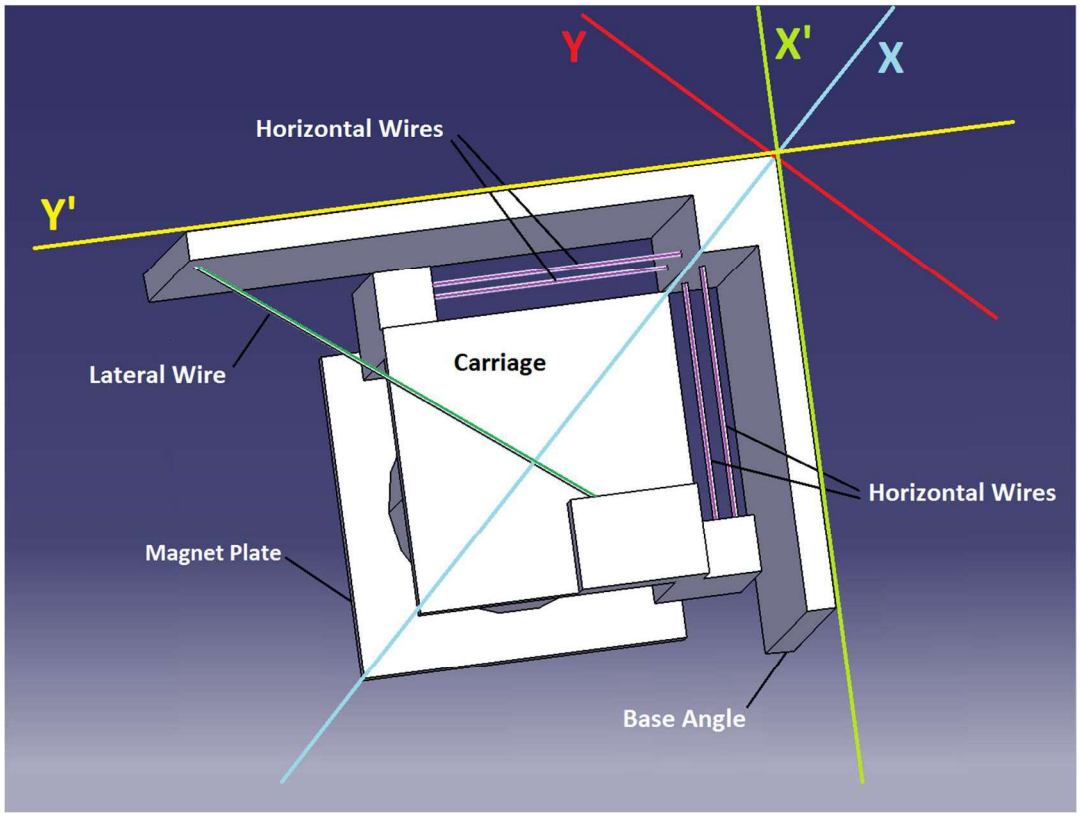

Figure 5-3: A single module of the image stabilizer is shown.

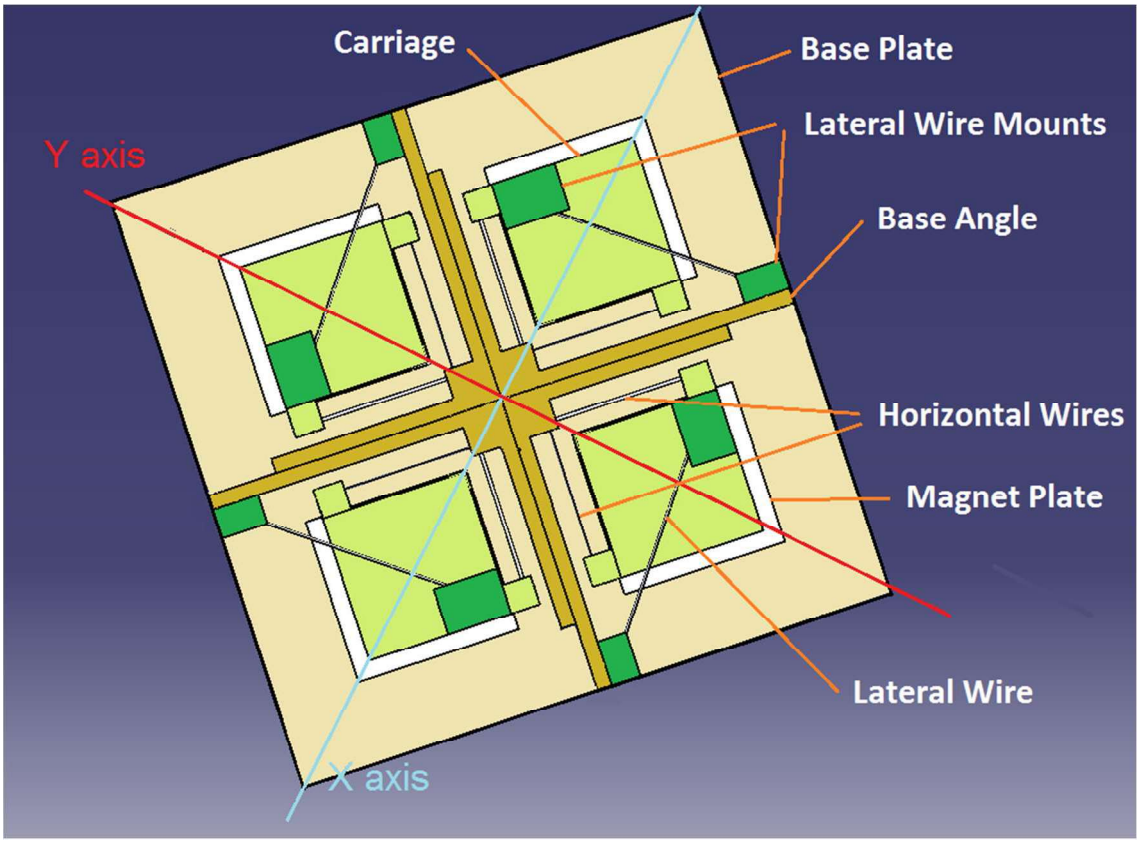

Figure 5-4: Four modules of the image stabilizer integrated onto the base plate are shown.

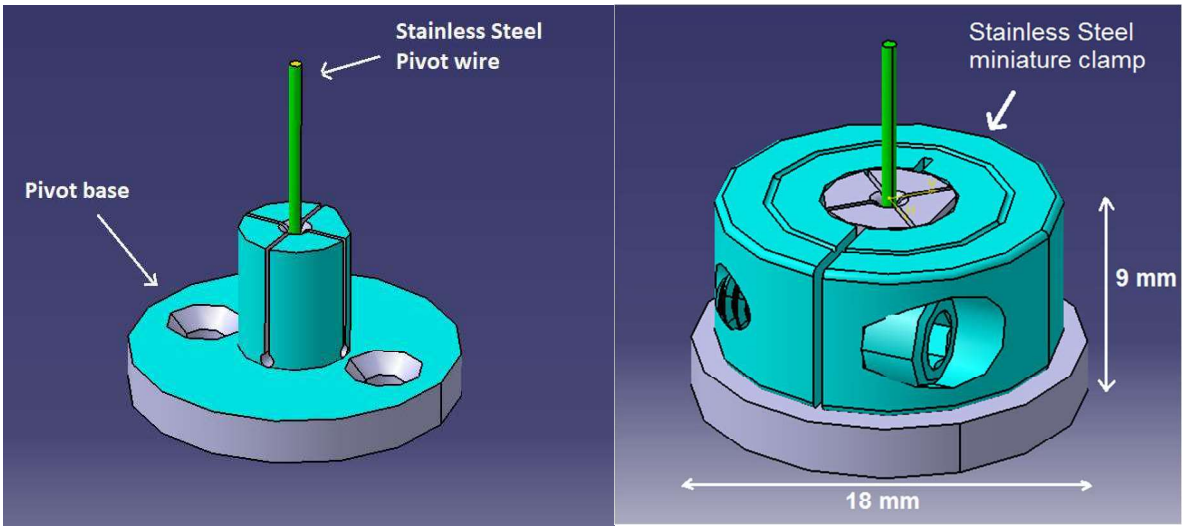

Figure 5-5: Pivot base design (left) and the miniature D-clamp (right) are shown.

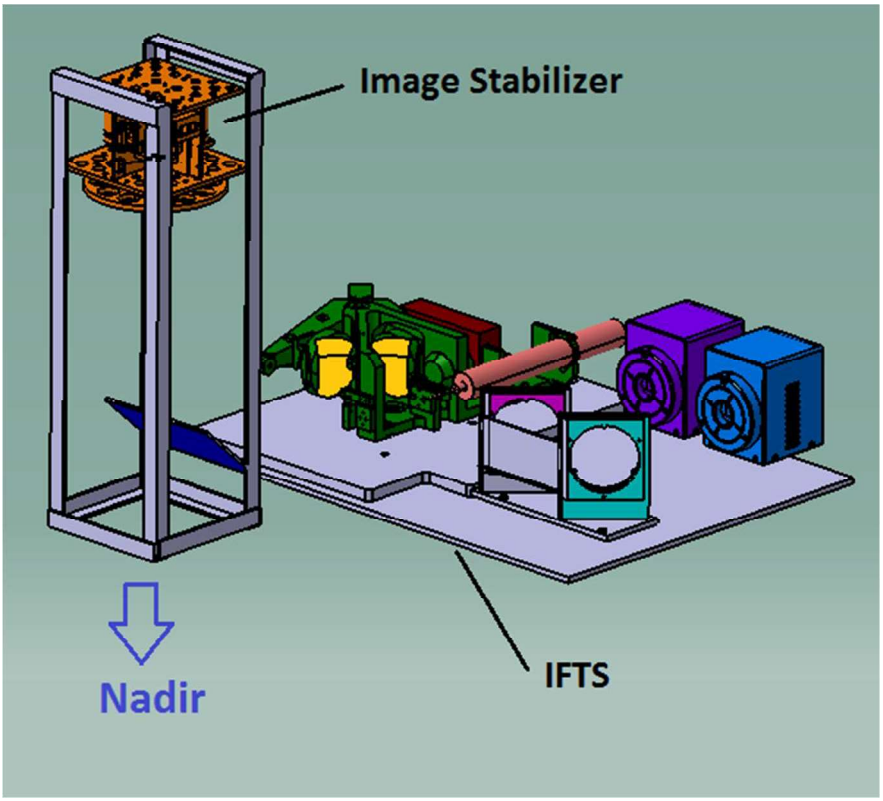

Figure 5-6: Image stabilizer integrated with the IFTs instrument in Nadir mode.

5.3.2. Software

The control software of the image stabilizer was written by Chen Zheng, a postdoctoral fellow working at the LARSS laboratory at York University under the direction of the author.

Two Hall effect sensors, one in each of the X and Y axes, provide accurate data on the position of the voice coil motor in each axis. This information is used in a feedback loop to allow the control software of the image stabilizer to determine whether the position of the mirror is correct.

The software is based on image processing. In the first step an image is acquired by a small camera placed at the aperture of the IFTS instrument. In this image 30 point-features are chosen by the software. The criteria for choosing these points are contrast and repeatability. As the image seen by the camera moves or changes, the software will find the 30 points again and will try to match

them with the initial image. After matching is done, the software calculates the angle through which the image stabilizer has to move in order to achieve the same orientation as the initial image. This process is done repeatedly until the image has moved far enough that the camera cannot detect a displacement of those 30 points. The key is to keep the measurement time of the instrument for a single scan to within the time the image stabilizer is able to track a single image. The image tracking software structure flow chart can be seen in Figure 5-7. At the initialization of the software, the camera settings, image and image processing settings and the RS232 communications settings are read from a setup file. Then the initial image is acquired, and the image matching routine begins. The correction angles are continuously sent to a microcontroller via an RS232 port. The microcontroller converts angles to voltages which drive the voice coil motors in each of the X and Y axes. The Hall effect sensors inform the microcontroller of the position of the mirror.

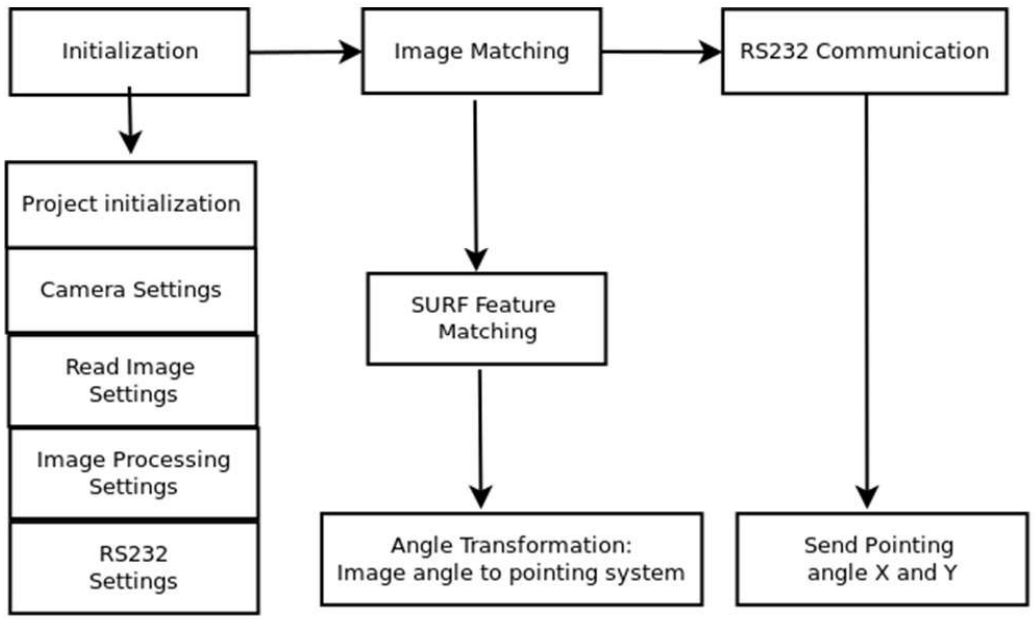

Figure 5-7: Image tracking software structure for the image stabilizer. (Personal communications, Zheng, 2015)

5.3.3. Electronics

The control electronics of the image stabilizer were designed and developed at the LARSS laboratory by a group of summer students (at the time), including Gurpreet Singh and Bobby Ngo, under the supervision of David Barton.

Figure 5-8 shows a flowchart of the control electronics for the image stabilizer. The protocol of operation of the control electronics is as follows:

- The camera provides a steady feedback (of images) to the control computer which applies the image processing software and determines the correction angles to the mirror of the image stabilizer.
- These correction angles are sent via RS232 ports to two Freescale microcontrollers, one for the X axis and one for the Y axis. The two Freescales calculate the correction voltages and apply them to the voice coil motors in each axis via a voltage driver.
- The Hall effect sensors read the position of the voice coil motors and report that information back to the Freescale microcontrollers.

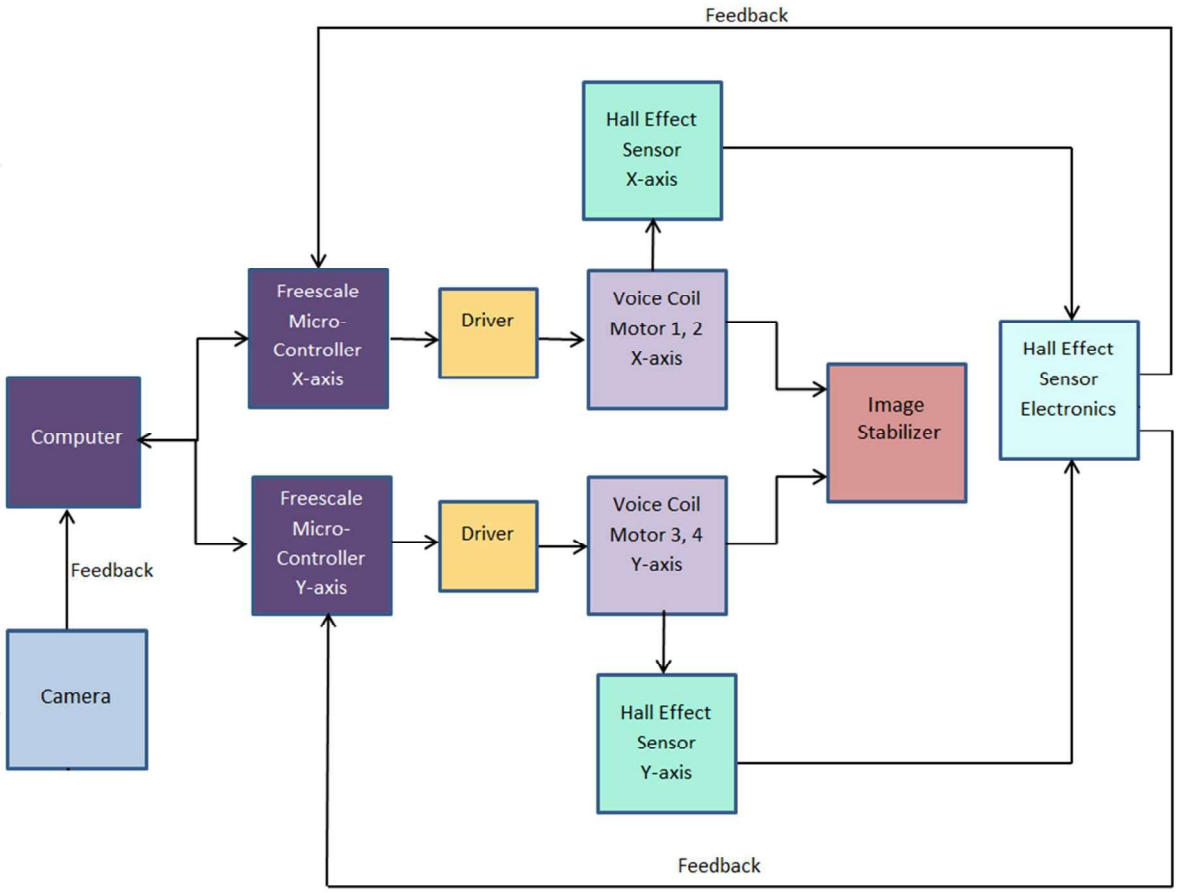

Figure 5-8: Image stabilizer control electronics flowchart.

5.4. Testing and Results

Several tests were done to verify the linearity, repeatability and operation of the image stabilizer. These tests were carried out at the LARSS laboratory as well as on a balloon flight which will be discussed later in this section.

The first test done was to determine the relation between the duty cycle of the VCM motors and the angle travelled by the ISPS. The duty cycle of the VCM refers to the ratio of the duration the motor is at high voltage to low voltage. Figure 5-9 shows this relation for the X axis. Two

directions for the movement of the VCM are defined, down and up, referring to the downward or upward motion of the VCM. The graph on the left shows this relation for the down direction and the graph on the right shows the same for the up direction. Figure 5-10 shows the same for the Y axis. In all cases the linearity of the system is evident. This linearity is important because it shows that the movement of the mirror of the ISPS in each axis is linear to the angle. The distance travelled by the mirror in each axis is determined by the voltage shown on the hall effect sensor mounted in each axis. Then the distance is converted into angle travelled.

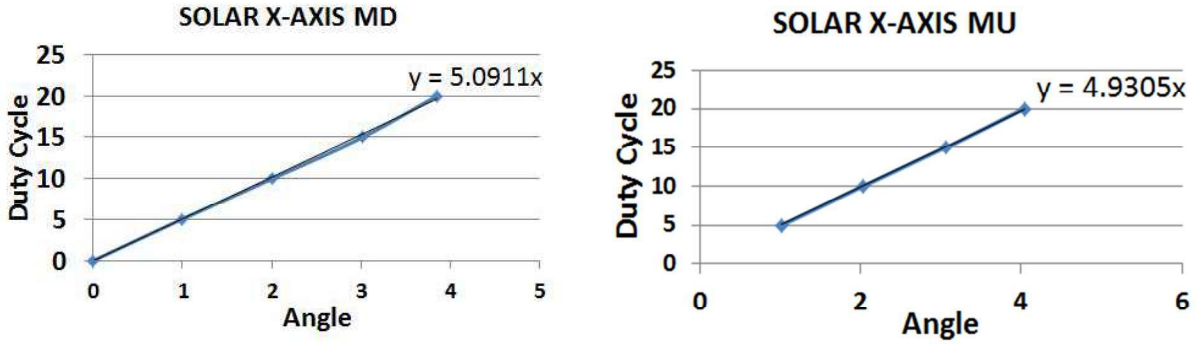

Figure 5-9: Duty cycle versus angle travelled by the mirror for the X axis in the down direction (left) and the up direction (right) of the VCM.

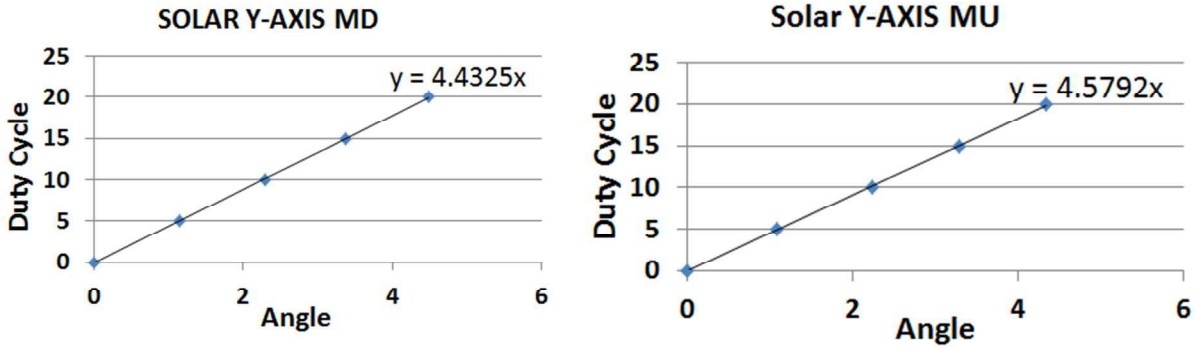

Figure 5-10: Duty cycle versus angle travelled by the mirror for the Y axis in the down direction (left) and the up direction (right) of the VCM.

The next test done on the image stabilizer was to mount it on a frame to look in the nadir direction and observe the linearity and repeatability of the system by means of a laser as the VCMs in each axis are commanded to move in the up and down directions repeatedly. The experimental setup used is shown in Figure 5-11. A ladder was used as a frame to mount the ISPS in the nadir direction. A laser was placed on the floor of the lab at a distance of 15 m from the base of the frame. The ISPS is mounted at a height of 3 m from the 45° mirror placed at the foot of the frame. The laser beam is reflected from the mirror to the ISPS which reflects it back to the floor onto a white board. The axes of the whiteboard are named X' and Y' so as to not be confused with the X and Y axis of the ISPS.

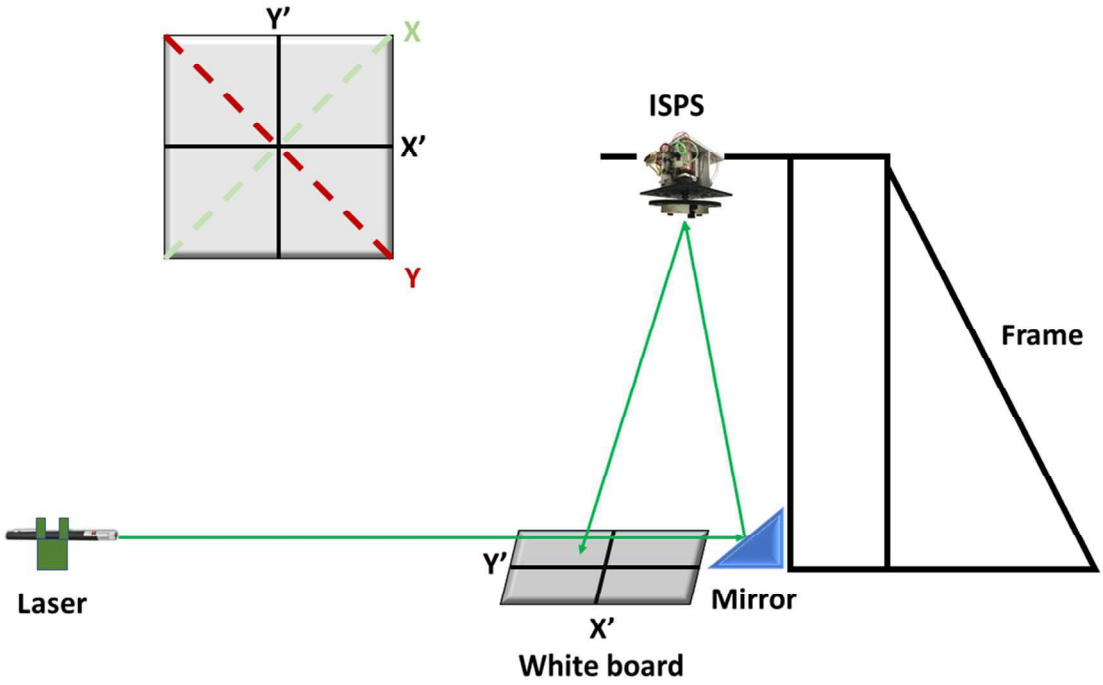

Figure 5-11: Experimental setup used to test the ISPS for linearity and repeatability.

As the ISPS is commanded to move up and down in each axis, the reflection of the laser beam is

recorded on the white board. Because the laser beam expands as it travels a long distance, the beam image on the whiteboard forms a circle with a diameter of about 1.5 cm. The position of the reflected laser beam was chosen to be the centre of this circle. Figure 5-12 shows the positions of the reflected laser beam with respect to the white board axis. These data points refer to a certain mirror position in the X and Y axes of the ISPS. The green dots show the X axis and the red dots show the Y axis in the up (positive) and the down (negative) directions. The error bars show the standard error.

The trend lines show that the image stabilizer acts linearly and there is no hysteresis present. The slope of the trendlines should be perpendicular to each other showing that the X and Y axis of the ISPS are perpendicular to each other. The intercept of the two trend lines shows the origin of the graph as well as the resting point of the ISPS. The average departure from linearity of the image stabilizer position is 1.4×10^{-5} radians, in accordance with the requirements imposed by the performance required for the IFTS. This number was calculated by averaging the distance of each point to the trendline and converting it to the angle.

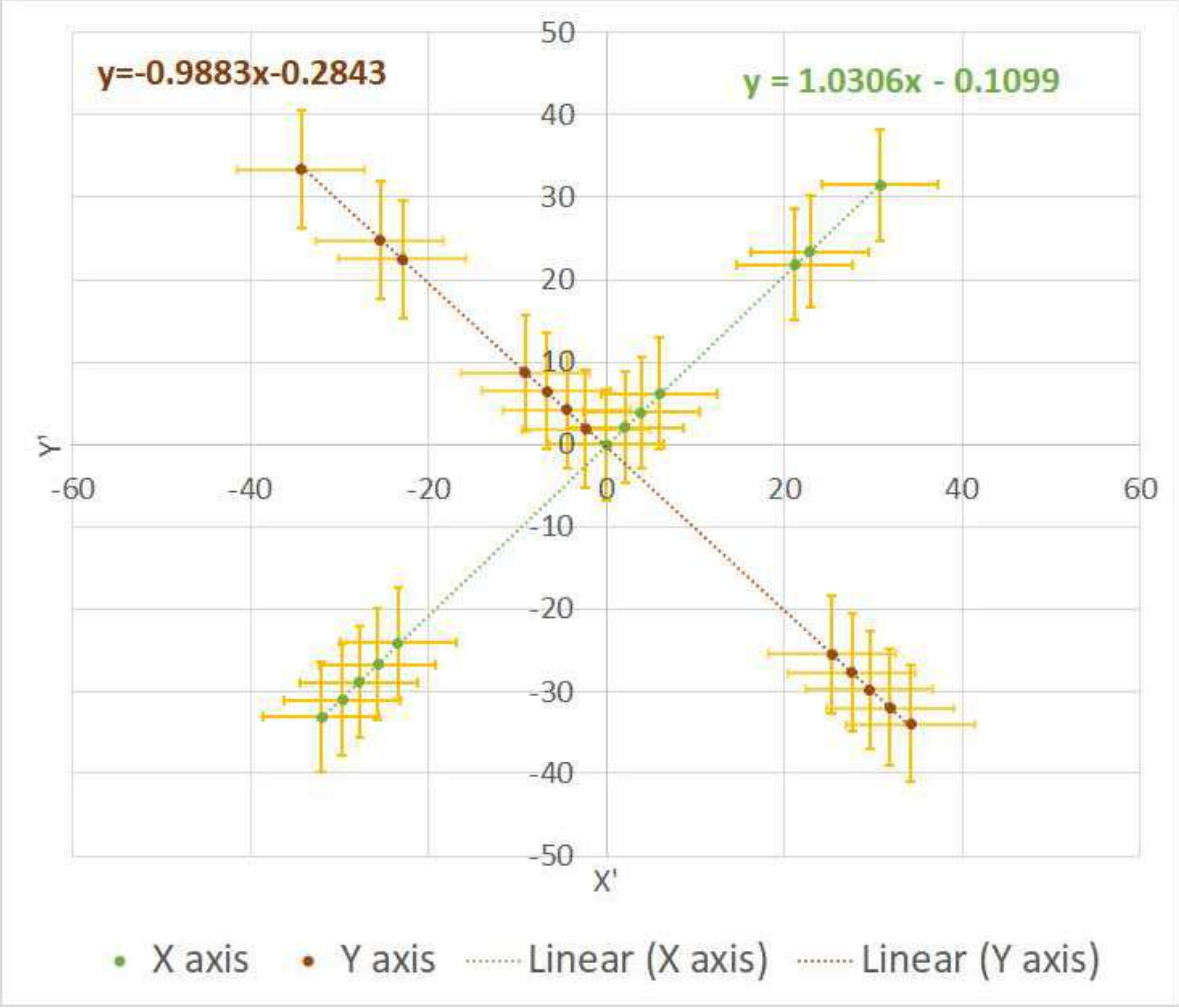

Figure 5-12: X (green) and Y (red) positions of the image stabilizer showing linearity in both axes. Error bars show the standard error.

The final test done on the image stabilizer was to fly it on a high-altitude stratospheric research balloon. This mission, named PARABLE (Payload for Remote sounding of the Atmosphere using Balloon Limb Experiments) is a training project that consists of the development and implementation of a balloon-based payload to make atmospheric observations in order to validate satellite data. The balloon flight was conducted by CNES (Centre national d'etudes spatiales) and CSA (Canadian Space Agency) at the Timmins Stratospheric Balloon base.

In this flight, the image stabilizer was used to track the sunrise and sunset from onboard the

balloon. It was integrated with the SPS (SunPhotoSpectrometer) instrument which is a heritage instrument for ACE-MAESTRO (Atmospheric Chemistry Experiment-Measurement of Aerosol Extinction in the Stratosphere and Troposphere Retrieved by Occultation). It has been going up to the Arctic every year since 2005 as part of the instrument suite that was deployed in Eureka for the ACE Arctic Validation Campaigns. The SPS instrument flew on the Shuttle as part of the STS-52 mission in 1992. It has been part of the NASA Upper Atmosphere Chemistry Research Program and has flown on the ER-2 aircraft from 1992 to 2000. It has also been flown on the MANTRA 1998, 2000, 2002 and 2004 balloon flights. SPS is a single concave holographic UV-Visible spectrometer with an effective spectral range of 375 to 775 nm and a spectral resolution of ~1 to 2.5 nm. It has a field of view of 0.1° by 10°. It is based on a 10-24 pixel, Reticon diode array detector and measures atmospheric species such as Aerosol, Nitrogen Dioxide and Ozone as well as absolute irradiance and radiance (C. T. McElroy, 1995).

On the PARABLE flight, SPS was appointed as the solar occultation instrument to measure during sunrise and sunset. The gondola tracking system tracks the sun in azimuth direction up to ±1° accuracy. The image stabilizer integrated with the SPS instrument tracked the sun in elevation. In order to detect the sun a PSD (Position Sensitive Device) sensor was mounted next to the aperture of the instrument. The field of view of the PSD sensor is ±4° (limited by the image stabilizer range), therefore it is limited to tracking the sun over a range of elevation angles of 8°. The details of the operation of a PSD sensor is described in appendix J.

During the PARABLE flight the solar image stabilizer tracked the sun successfully during sunset. Figure 5-13 shows the solar elevation angle recorded by the image stabilizer during sunset. These angles are with reference to the centre of the PSD sensor. The time axis is in time stamps because the actual time was not recorded by the ground station software.

Two other instruments from University of Toronto were also on-board the gondola and were taking measurements during sunset. These instruments are the PARIS (Portable Atmospheric Research Interferometric Spectrometer) instrument and the DA-2 instrument. Figure 5-14 and Figure 5-15 show solar elevation angles from the sun trackers of the DA-2 instrument and the PARIS instrument respectively. The DA-2 sun tracker shows a lot of noise in their tracking system. The PARIS sun tracker tracks the sun through the sunset smoothly. Small wiggles in the plot show oscillations of the gondola. At approximately zero degrees the SPS image stabilizer starts to have trouble tracking the sun and there is more noise and oscillation in the elevation angle data. This is because the feedback signal switched to the high-gain channel and there was an uncorrected offset relative to the original pointing signal.

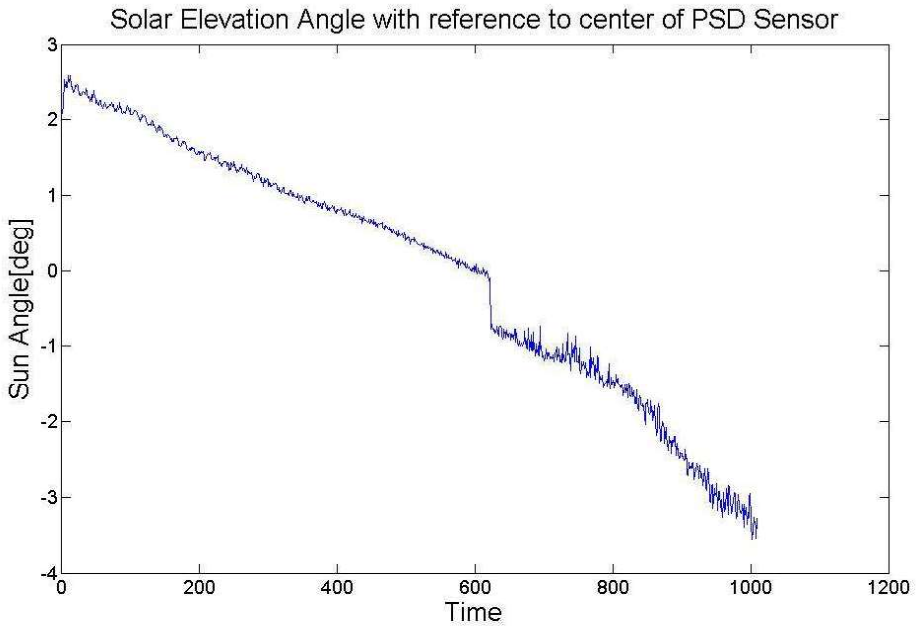

Figure 5-13: Solar elevation angles recorded by the solar SPS image stabilizer during sunset.

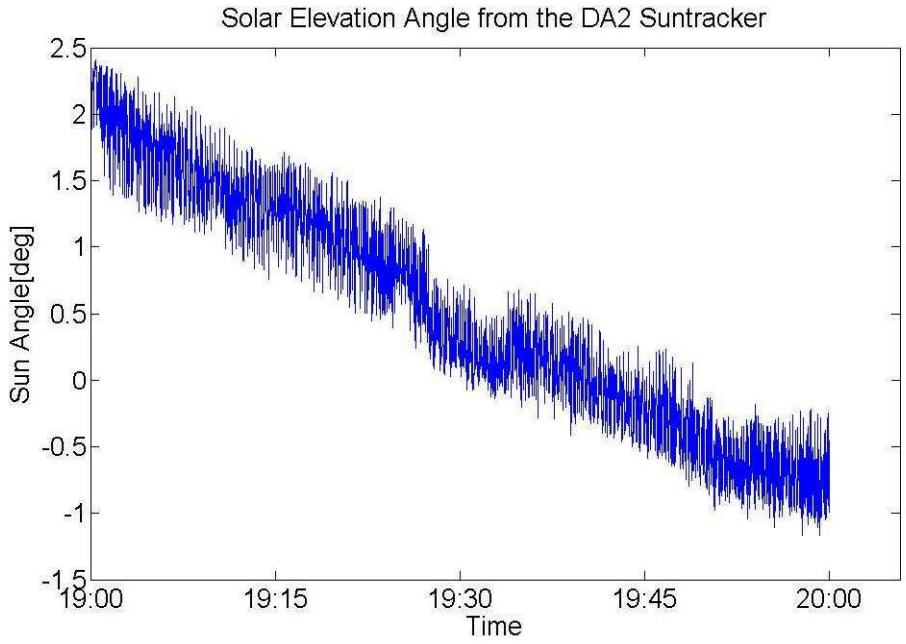

Figure 5-14: Solar elevation angles recorded by the sun tracker of the DA-2 instrument during sunset.

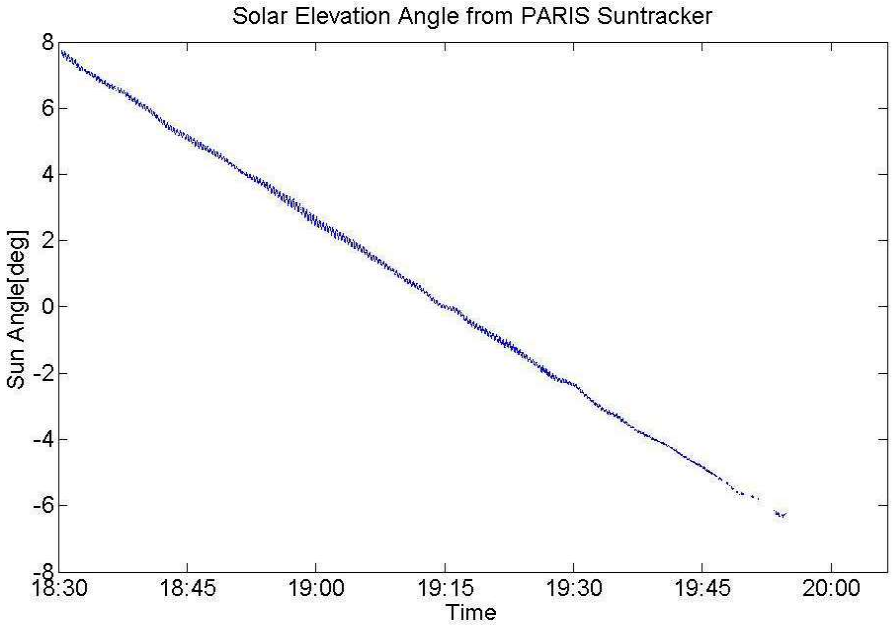

Figure 5-15: Solar elevation angles recorded by the sun tracker of the PARIS instrument during sunset.

To investigate the sudden drop and noise increase in the SPS image stabilizer elevation angle data, some plots of the gondola attitude where made. Figure 5-16 shows the Gondola altitude at sunset between 22:30 and 24:00 UTC. At time 23:40 the gondola altitude becomes unstable and there is an up/down wave-like motion that continues until 24:00 UTC when the sunset is over. Figure 5-17 shows the gondola azimuth pointing in degrees during the sunset which implies that the gondola was stable in the azimuth direction. Figure 5-18 shows the roll and pitch of the gondola. From approximately 19:40 (23:40 UTC) the change in roll and pitch angles start to increase and change rapidly showing an oscillation movement in the gondola which contributes to the sudden noisiness of the image stabilizer elevation angle data. The gondola attitude data were obtained from on-board sensors provided by the CSA and CNES.

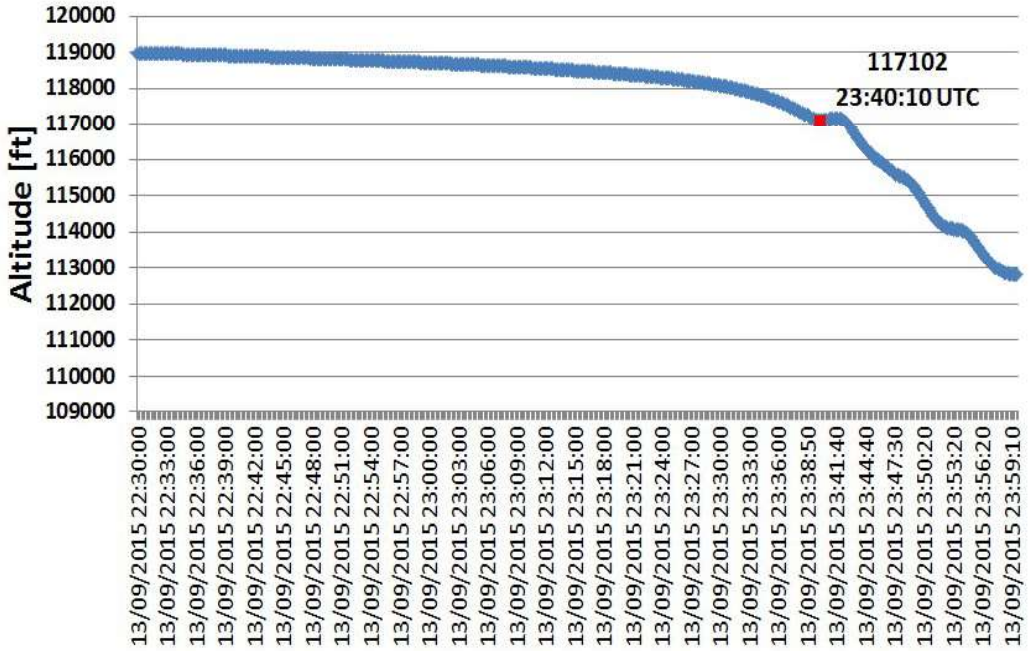

Figure 5-16: Altitude of the Gondola during sunset between 22:30 and 24:00 UTC (18:30 – 20:00 local time).

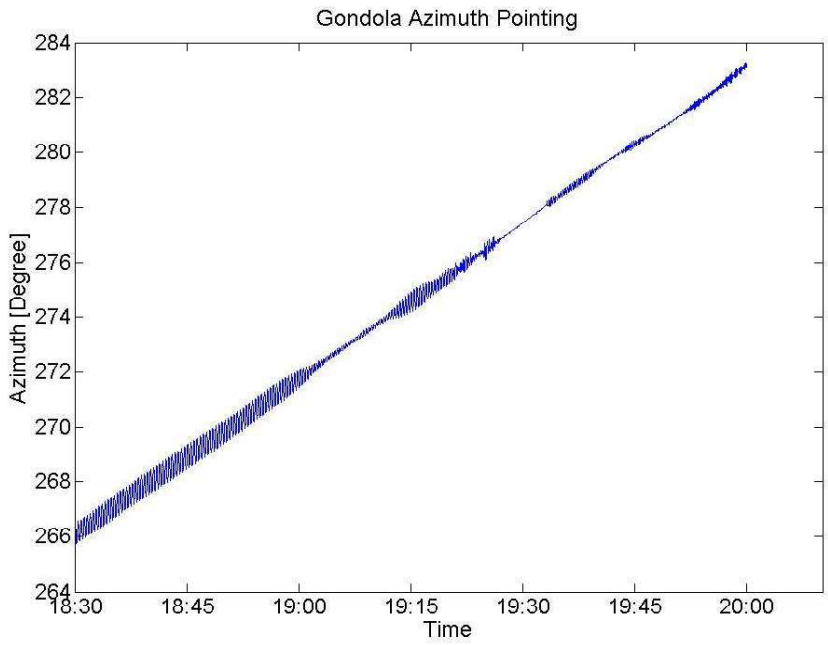

Figure 5-17: Gondola azimuth pointing data in degrees during sunset between 18:30 and 20:00 local time.

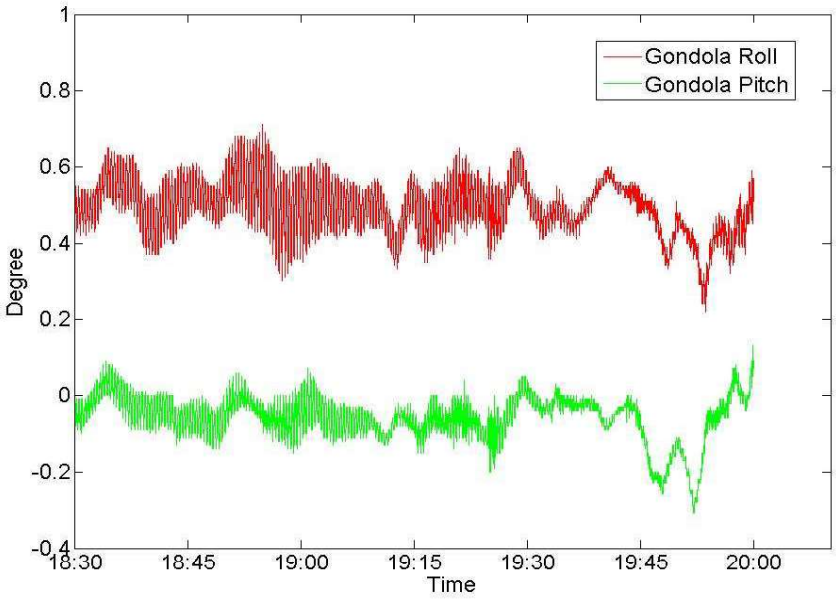

Figure 5-18: Gondola Roll (red) and Pitch (green) data in degrees during sunset between 18:30 and 20:00 local time.

5.5. Discussion

The image stabilizer, designed and developed in this chapter, is an essential part of the IFTS instrument, but could find application with any Earth observation instrument. This device can track a light source (e.g. the sun) or an image on the ground in azimuth and elevation up to ±4°. The image stabilizer is complementary to the attitude control of a satellite or balloon platform. While the balloon or satellite maintains its attitude, the image stabilizer can point to an area of interest within the field of view and maintain the image for the duration of measurements of the instrument it is integrated to.

It is superior to its counterparts in many ways such as:

- It has a large angular travel range,
- It is frictionless and could be qualified to operate in space,
- The control software is simple,
- The design and assembly are simple yet sophisticated,
- It can be assembled with different mirrors of maximum weight of 5 kg,
- It is compact and light weight.

The image stabilizer can also be used as a smart pointing device for atmospheric measurement instruments. By using a camera at the aperture of the instrument it is integrated with (e.g. the IFTS), the control software can detect areas with cloud cover and instruct the image stabilizer to point to a different section for maximizing the efficiency of measurements.

6. Conclusion

This thesis deals with some of the most important climate change factors. The ozone content of the atmosphere is discussed and a correction method for the effects of stray light in one of the most commonly used and most accurate instruments for ozone measurements around the world (Brewer Spectrophotometer) is presented. Other climate change factors such as the CO_2 and CH_4 content of the atmosphere were also discussed. These GHGs are studied widely with the use of satellite instruments, however, none are specifically designed to provide long-term observations of the Arctic atmosphere. The instrument presented in this thesis specifically focuses on measuring these species at higher latitudes and it is one of the first of its kind to be built. The fore-optics of this instrument are also designed and developed which is unique among its counterparts for being designed for atmospheric applications.

To conclude this thesis a summary of the conclusions and achievements of the projects will be discussed in the following.

6.1. Summary of Achievements

6.1.1. Brewer Spectrophotometer Stray Light Analysis

A common problem that exists with single and double Brewer Spectrophotometers is instrumental stray light. The effects of stray light are more prominent at large ozone slant paths as seen in the Arctic regions. The presence of stray light causes an underestimation of ozone total column amounts, especially in the single Brewer, which shows a difference of up to 10% compared to the double Brewer.

In chapter three of this thesis a mathematical model was presented that accounts for the departure

from linearity in Beer's law arising from the effects of instrumental stray light. This model which includes a non-linearity factor, a filter change factor and a deadtime factor successfully characterizes the effects of stray light and corrects the total ozone column amounts accordingly.

The results presented in chapter three show that the double Brewer suffers less from these effects and, therefore, is a more reliable instrument. Single Brewers around the world are being replaced by double Brewers and as a result, an increased ozone trend may be observed. This misconception is most dangerous as it may imply a false belief that the ozone layer is replenishing. Therefore, the importance of applying this method to historical ozone data to eliminate this problem is evident.

6.1.2. Design and Development of an Imaging Fourier Transform Spectrometer

The IFTS instrument designed and developed in this thesis is a breakthrough in terms of Arctic observations. It provides significant increase in spatial resolution if operated in a quasi-geostationary or HEO orbit. In this type of orbit the satellite is approximately 40,000 km away from the surface of Earth and with current instrumentation, there will be a need for heavy and complicated fore-optics to increase spatial resolution. The ground-based demonstrator IFTS eliminates this need by using imaging detectors.

The IFTS instrument not only provides an increase in spatial resolution but also increases ground coverage. As shown in Figure 4-8, the IFTS field of view covers an approximately 2,500 by 2,000 km rectangular element from a HEO orbit which is imaged during one scan of the IFTS which, is approximately 65 s. By pointing the instrument at different elements in a grid of 3 x 3, the field of regard of the instrument can be imaged every minute which, increases the temporal resolution in comparison to other instruments in LEO orbits.

The SNR, which depends on albedo and SZA, was calculated for the IFTS in chapter 4. It is based on a SZA of 0° and an albedo of 1. The SNR is comparable to the specifications outlined for the PCW-PHEOS instrument discussed earlier in chapter 4. The SNR specified by the PHEOS-FTS instrument is given in the table below. These numbers are for an albedo of 0.25 and a SZA of 60°.

Table 5: SNR for the 1600 nm and 762 nm channel of the PHEOS-FTS instrument compared to the IFTS instrument (ABB Inc, 2012)**.**

Spectral band	PHEOS-FTS	IFTS
1550 nm – 1680 nm	SNR > 122 for an albedo of 0.25 and a solar zenith angle of 60°	SNR ~ 92 for an albedo of 0.25
758 nm – 766 nm	SNR > 100 for an albedo of 0.25 and a solar zenith angle of 60°.	SNR ~ 80 for an albedo of 0.25

The IFTS instrument is currently at a Technology Readiness Level (TRL) of 4. TRL 4 refers to component and/or breadboard validation in laboratory environment. A complete list of TRL values and their meanings are provided in Appendix K.

This instrument is designed for running in a lab environment on an optical bench however with small modifications can be launched on a balloon platform. Advanced modifications need to be made to make this instrument space qualified. These modifications include:

- Designing a mechanical system to lock the instrument during launch to protect it from vibrations. This mechanism should be unlocked when instrument is in orbit and ready to start measurements.
- A conductive and radiative cooling path for the InGaAs imaging detectors needs to be

implemented.

- A complete stress analysis needs to be conducted on all the systems.
- The instrument plus its electronics must undergo thermal-vacuum tests as well as vibration tests.

6.1.3. Design and Development of an Image Stabilizer for Precise Image Tracking

The image stabilizer pointing system (ISPS) designed and developed in this thesis is a necessary fore-optics for the IFTS. It stabilizes the image being viewed on the ground for the duration of the scan of the IFTS. It can also point the instrument field of regard towards different surface elements in the 3 by 3 grid mentioned in section 6.1.2. It utilizes state-of-the-art software that performs image processing to track an image on the ground. This software identifies surface features on the initial image and tracks those features in the next image to command the ISPS to move in a way that the initial image is kept constant with respect to the point of view of the instrument. This tracking software is yet to be tested specially in the Arctic where the ground is covered in snow most of the year and it may be challenging to find enough surface features to be able to track.

The ISPS is unique among its counterparts in that it has a simple design, it is light weight and compact. Its design is frictionless which gives it the advantage of being able to become space qualified. It has already been qualified for balloon flights where it was tested to track the sun as a complementary tracking device to the gondola azimuth tracking of the PARABLE balloon. This instrument is at a TRL level 6 which refers to a prototype demonstration in a relevant environment.

6.2. Future Work

Brewer Stray Light Analysis

This research was aimed at developing a non-linear model approach to correct for the effects of stray light in the Brewer Spectrophotometer. This model can be applied independently on any Brewer instrument data to correct ozone total column amounts especially at high latitudes where the ozone slant path is large. The scope of this research was to develop the model and test it by applying it to a few days of Arctic data.

In the future, one can develop software from this model to correct historical ozone data measured by the Brewer spectrophotometer all over the world. This will be necessary as most of the older data is from single Brewer instruments and may show an underestimation of total ozone column amounts.

IFTS Instrument Development for Nadir Observations

This research encompassed the design and development of a demonstrator imaging Fourier transform spectrometer for nadir observations of CO_2, CH_4 and the O_2 A-band. This instrument is unique in that it can cover a large surface area with high spatial resolution if placed in a HEO or GEO orbit. This research covered the IFTS instrument's optical, mechanical, electrical and software design as well as the data analysis process and laboratory testing. The tests conducted confirm the spectral resolution, wavelength distribution across the detector and signal to noise ratio of the instrument.

In the future, with small modifications, one can fly the instrument on a high-altitude stratospheric research balloon to test it in Nadir mode. Certain measures must be taken to qualify it for flight in

near vacuum conditions such as the detectors' fans must be disabled, and a heating system must be put in place to keep the instrument at a constant temperature.

Image Stabilizer Pointing System for Precise Image Tracking

The research regarding the design and development of the ISPS focused on the mechanical, electrical and software design. The research also covered the testing of the image stabilizer to track a light source (e.g. The sun) on a high-altitude stratospheric research balloon. The next step in continuing this research would be to test the image stabilizer in nadir mode to track an image on the ground from a high-altitude stratospheric balloon. The challenge would be to test the image tracking software of the ISPS to see if it will track an image on a feature-less ground element such as in the Arctic or the desert.

References

ABB Inc: PHEMOS Science Payload Conceptual Design and Trade-off Document, 2012.

ABB Inc.: Laboratory Spectrometers, Retrieved from https://new.abb.com/ca 2018.

Aminou, D. M., Bézy, J.-L., Bensi, P., Stuhlmann, R., Tjemkes, S., and Rodriguez, A.: Meteosat third generation: Preliminary design of the imaging radiometers and sounding instruments, Sensors, Syst. Next-Generation Satell. VIII, 5570, 81–92, doi:10.1117/12.565585, 2004.

Andover Corp.: No Title, Retrieved from https://www.andovercorp.com 2018.

Antón, M., López, M., Costa, M. J., Serrano, A., Bortoli, D., Bañnón, M., Vilaplana, J. M., and Silva, A. M.: Influence of the ozone profile above Madrid (Spain) on Brewer estimation of ozone air mass factor, Ann. Geophys., 27(8), 3179–3183, doi:10.5194/angeo-27-3179-2009, 2009.

Bais, A. F., Zerefos, C. S., and McElroy, C. T.: Solar UVB measurements with the double- and single-monochromator Brewer ozone spectrophotometers, Geophys. Res. Lett., 23(8), 833–836, doi:10.1029/96GL00842, 1996.

BEI Kimco: Voice Coil Actuators, an Applications Guide, 1, 2002.

Bekki, S., Bodeker, G. E., Bais, A. F., Butchart, N., Eyring, V., Fahey, D. W., Kinnison, D. E., Langematz, U., Mayer, B., Protmann, R. W., and Rozanov, E.: Future Ozone and Its Impact on Surface UV, Sci. Assess. Ozone Deplet. 2010, Glob. Ozone Res. Monit. Proj. World Meteorol. Organ., Retrieved from http://ozone.unep.org/new_site/en/scientific_assessment_2010.php 2011.

Bernhard, G., Evans, R. D., Labow, G. J., and Oltmans, S. J.: Bias in Dobson total ozone measurements at high latitudes due to approximations in calculations of ozone absorption coefficients and air mass, J. Geophys. Res. D Atmos., 110(10), 1–10, doi:10.1029/2004JD005559, 2005.

Bloom, H.: The Cross-Track Infrared Sounder (CrIS): A sensor for operational meterological remote sensing, Opt. Soc. Am., 51, 2001.

BMVOPTICAL: BMV beamsplitter, 2017.

Bowman, K. P.: Global Trends in Total Ozone, Science (80-.)., 239(4835), 48–50, doi:10.1126/science.239.4835.48, 1988.

Brewer, A. W.: Evidence for a world circulation provided by the measurements of helium and water vapour distribution in the stratosphere, Q. J. R. Meteorol. Soc., 75(326), 351–363, doi:10.1002/qj.49707532603, 1949.

Brewer, A. W.: A replacement for the Dobson spectrophotometer?, Pure Appl. Geophys. PAGEOPH, 106–108(1), 919–927, doi:10.1007/BF00881042, 1973.

Buijs, H. L., and McKinnon, J.: Two-beam interferometer for fourier transform spectroscopy with double pivot scanning mechanism, doi:10.1126/science.Liquids, 2009.

Butchart, N.: The Brewer-Dobson circulation, Rev. Geophys., 52, 157–184, doi:10.1002/2013RG000448, 2014.

Butchart, N., Scaife, A. A., Bourqui, M., Grandpré, J., Hare, S. H. E., Kettleborough, J., Langematz, U., Manzini, E., Sassi, F., Shibata, K., Shindell, D., and Sigmond, M.: Simulations of anthropogenic change in the strength of the Brewer-Dobson circulation, Clim. Dyn., 27(7–8), 727–741, doi:10.1007/s00382-006-0162-4, 2006.

Chapman, S.: XXXV. On ozone and atomic oxygen in the upper atmosphere, London, Edinburgh, Dublin Philos. Mag. J. Sci. Ser. 7, 10(64), 369–383, doi:10.1080/14786443009461588, 1930.

Cubasch, U., Wuebbles, D., Chen, D., Facchini, M. C., Frame, D., Mahowald, N., and Winther, J.-G.: Introduction in Climate Change 2013, Intergov. Panel Clim. Chang. 2013 Phys. Sci. Basis. Contrib. Work. Gr. I to Fifth Assess. Rep. Intergov. Panel Clim. Chang., 119–158, doi:10.1017/CBO9781107415324.007, 2013.

Davis, S. P., Abrams, M. C., and Brault, J. W.: Fourier Transform Spectrometry, 2001.

Dobson, G. M. B.: A Photoelectric spectrophotometer for measuring the amount of atmospheric ozone, Proc. Phys. Soc., 43, 324–339, doi:10.1088/0959-5309/43/3/308, 1931.

Dobson, G. M. B.: Origin and Distribution of the Polyatomic Molecules in the Atmosphere, Proc. R. Soc. A Math. Phys. Eng. Sci., 236(1205), 187–193, doi:10.1098/rspa.1956.0127, 1956.

Dobson, G. M. B.: Forty years' research on atmospheric ozone at Oxford: a History, Appl. Opt., 7(3), 387–405, 1968.

Dobson, G. M. B., Harrison, D. N., and Lawrence, J.: Measurements of the Amount of Ozone in the Earth's Atmosphere and its Relation to other Geophysical Conditions. - Part III, Proc. R. Soc. London. Ser. A, Contain. Pap. a Math. Phys. Character, 110(1926), 456–486, doi:10.1098/rspa.1930.0165, 1929.

Fastie, W. G.: A Small Plane Grating Monochromator, J. Opt. Soc. Am., 42(9), 641, doi:10.1364/JOSA.42.000641, 1952.

Fioletov, V. E.: Ozone climatology, trends, and substances that control ozone, Atmos. - Ocean, 46(1), 39–67, doi:10.3137/ao.460103, 2008.

Fountoulakis, I., Redondas, A., Bais, A. F., Rodriguez-Franco, J. J., Fragkos, K., and Cede, A.: Dead time effect on the Brewer measurements: Correction and estimated uncertainties, Atmos. Meas. Tech., 9(4), 1799–1816, doi:10.5194/amt-9-1799-2016, 2016.

Grebenshchikov, S. Y., Qu, Z. W., Zhu, H., and Schinke, R.: New theoretical investigations of the photodissociation of ozone in the Hartley, Huggins, Chappuis, and Wulf bands, Phys. Chem. Chem. Phys., 9, 2044–2064, doi:10.1039/b701020f, 2007.

Griffiths, P. R., and Haseth, J. A. de: Fourier Transform Infrared Spectrometry, 2006.

Gröbner, J., Wardle, D. I., McElroy, C. T., and Kerr, J. B.: Investigation of the wavelength accuracy of brewer spectrophotometers., Appl. Opt., 37(36), 8352–60, Retrieved from http://www.ncbi.nlm.nih.gov/pubmed/18301659 1998.

Hassol, S. J.: Impacts of a Warming Arctic, Arct. Clim. Impact Assess., Retrieved from https://www.amap.no/arctic-climate-impact-assessment-acia 2004.

Herres, W., and Gronholz, J.: Understanding FT-IR Data Processing, J. Comput. Appl. Lab., 2, 216–220, 1984.

Holton, J. R., Haynes, P. H., McIntyre, M. E., Douglass, A. R., and Rood, R. B.: Stratosphere-Troposphere Exchange, Rev. Geophys., 33(4), 403–439, 1995.

Jacob, D. J.: Introduction to atmospheric chemistry, Princeton University press, Retrieved from http://science.kln.ac.lk/Chemistry/Teaching_Resources/Documents/Introduction to atmospheric chemistry.pdf 1999.

Karppinen, T., Redondas, A., García, R. D., Lakkala, K., McElroy, C. T., and Kyrö, E.:

Compensating for the effects of stray light in single-monochromator brewer spectrophotometer ozone retrieval, Atmos. - Ocean, 53(1), 66–73, doi:10.1080/07055900.2013.871499, 2015.

Kauppinen, J., and Partanen, J.: Fourier Transforms in Spectroscopy, 2001.

Kerr, J. B.: The Brewer Spectrophotometer, In W. Gao, D. L. Schmoldt, & J. R. Slusser (Eds.), UV Radiation in Global Climate Change, Tsinghua University Press, Beijing and Springer, 160–191, 2010.

Kerr, J. B., Evans, W. F. J., and Asbridge, I. A.: Recalibration of Dobson Field Spectrophotometers with a Travelling Brewer Spectrophotometer Standard, Proc. Quadrenn. Ozone Symp. Halkidiki, Greece, 1984., 381–386, 1985.

Kerr, J. B., McElroy, C. T., Wardle, D. I., Olafson, R. A., and Evans, W. F. J.: The automated Brewer spectrophotometer, In C. S. Zerefos & A. Ghazi (Eds.), Quadrennial Ozone Symposium, Halkidiki, Greece, 396–401, 396–401, 1984.

Kipp and Zonen: Brewer MKIII Operator's Manual, 2009.

Kuze, A., Suto, H., Nakajima, M., and Hamazaki, T.: Thermal and near infrared sensor for carbon observation Fourier-transform spectrometer on the Greenhouse Gases Observing Satellite for greenhouse gases monitoring, Appl. Opt., 48(35), 6716, doi:10.1364/AO.48.006716, 2009.

Lacis, A. A., and Hansen, J. E.: A Parameterization for Absorption of Solar Radiation in the Earth's Atmosphere, J. Atmos. Sci., 31(1), 118–133, doi:10.1175/1520-0469(1974)031<0118:APFTAO>2.0.CO;2, 1974.

Lagendijk, A., and van Tiggelen, B. A.: Resonant multiple scattering of light, Phys. Rep., 270(3), 143–215, doi:10.1016/0370-1573(95)00065-8, 1996.

Liou, K. N.: An Introduction to Atmospheric Radiation, International Geophysics Series, Vol. 84, doi:10.1016/S0074-6142(08)60682-8, 2002.

Mankins, J. C.: Technology Readiness Levels, A White Pap., 1995.

McConnell, J. C., and Jin, J. J.: Stratospheric ozone chemistry, Atmos. - Ocean, 46(1), 69–92, doi:10.3137/ao.460104, 2008.

McConnell, J. C., Mcelroy, C. T., Sioris, C., Neill, N. O., Nassar, R., Buijs, H., and Rahnama, P.:

PCW / PHEOS-WCA : Quasi-geostationary viewing of the Arctic and environs for weather, climate and air quality, Proc. ESA ATMOS-2012, 2012.

McElroy, C. T.: A spectroradiometer for the measurement of direct scattered solar irradiance from on-board the NASA ER-2 high-altitude research aircraft, Geophys. Res. Lett., 22(11), 1361–1364, 1995.

McElroy, C. T., McConnell, J. C., Sioris, C. E., Rahnama, P., and Team, S.: PCW / PHEOS UV-VIS spectrometer: Air quality from a quasi-geostationary orbit, Proc. ESA ATMOS-2012, 2012.

McElroy, M. B., Salawitch, R. J., Wofsy, S. C., and Logan, J. A.: Reductions of Antarctic ozone due to synergistic interactions of chlorine and bromine, Nature, 321(6072), 759–762, doi:10.1038/321759a0, 1986.

Minus K: No Title, Retrieved from https://www.minusk.com/content/technology/transmissibility_curves_vibration_isolation_isolators_tables.html#BM-4 2018.

Moeini, O., Vaziri, Z., Mcelroy, C. T., Tarasick, D. W., Evans, R. D., Petropavlovskikh, I., and Feng, K.: The Effect of Instrumental Stray Light on Brewer and Dobson Total Ozone Measurements, Atmos. Meas. Tech., 2018.

Montenbruck, O., and Gill, E.: Satellite Orbits: Models, Methods, Applications, 1st ed., 2000.

Nassar, R., Sioris, C. E., Jones, D. B. A., and McConnell, J. C.: Satellite observations of CO2 from a highly elliptical orbit for studies of the Arctic and boreal carbon cycle, J. Geophys. Res. Atmos., (119), 2654–2673, doi:10.1002/2014JD021914.Received, 2014.

National Research Council: Solar Influences on Global Change, National Academies Press, Retrieved from https://doi.org/10.17226/4778 1994.

NOAA, and NASA: U.S. Standard Atmosphere, 1976, 1976.

Physik Instrumente: Hexapods, Retrieved from https://www.physikinstrumente.com/en/products/parallel-kinematic-hexapods/ 2018.

PIXELTEQ: No Title, Retrieved from https://opticalfiltershop.com/ 2018.

Redondas, A., Evans, R., Stuebi, R., Köhler, U., and Weber, M.: Evaluation of the use of five laboratory-determined ozone absorption cross sections in Brewer and Dobson retrieval

algorithms, Atmos. Chem. Phys., 14(3), 1635–1648, doi:10.5194/acp-14-1635-2014, 2014.

Redondas, A., Carreño, V., León-Luis, S. F., Hernández-Cruz, B., López-Solano, J., Rodriguez-Franco, J. J., Vilaplana, J. M., Gröbner, J., Rimmer, J., Bais, A. F., Savastiouk, V., Moreta, J. R., Boulkelia, L., Jepsen, N., Wilson, K. M., Shirotov, V., and Karppinen, T.: EUBREWNET RBCC-E Huelva 2015 Ozone Brewer Intercomparison, Atmos. Chem. Phys., 18(13), 9441–9445, doi:10.5194/acp-18-9441-2018, 2018.

Rimmer, J. S., Redondas, A., and Karppinen, T.: EuBrewNet - A European Brewer network (COST Action ES1207), an overview, Atmos. Chem. Phys., 18(14), 10347–10353, doi:10.5194/acp-18-10347-2018, 2018.

Rodgers, C. D.: Inverse Methods for Atmospheric Sounding - Theory and Practice, doi:10.1142/9789812813718, 2000.

Royer, M., Lorans, D., Bischoff, I., Giotta, D., and Wolny, M.: IR detectors for the Infrared Atmospheric Sounding Interferometer (IASI) instrument payload for the METOP-1 ESA polar platform, Proc. SPIE, 2312, 251–261, doi:10.1117/12.197379, 1994.

Savastiouk, V.: Improvements To the Direct-Sun Ozone Observations Taken With the Brewer Spectrophotometer, York University, Retrieved from https://www.esrl.noaa.gov/gmd/grad/neubrew/docs/publications/VladimirSavastiouk_PhD_thesis.pdf 2006.

Savastiouk, V., and McElroy, C. T.: Brewer spectrophotometer total ozone measurements made during the 1998 Middle Atmosphere Nitrogen Trend Assessment (MANTRA) Campaign, Atmos. - Ocean, 43(4), 315–324, doi:10.3137/ao.430403, 2005.

Schuur, E. A. G., Bockheim, J. G., Canadell, J. G., Euskirchen, E., Field, C. B., Goryachkin, S. V, Hagemann, S., Kuhry, P., Lafleur, P. M., Lee, H., Mazhitova, G., Nelson, F. E., Rinke, A., Romanovsky, V. E., Shiklomanov, N., Tarnocai, C., Venevsky, S., Vogel, J. G., and Zimov, S. A. A.: Vulnerability of Permafrost Carbon to Climate Change: Implications for the Global Carbon Cycle, Bioscience, 58(8), 701–714, doi:10.1641/B580807, 2008.

Serreze, M. C., Walsh, J. E., Chapin, F. S. I., Osterkamp, T., Dyurgerov, M., Romanovsky, V., Oechel, W. C., Morison, J., Zhang, T., and Barry, R. G.: Observational evidence of recent change in the northern high- latitude environment, Clim. Change, 46(1–2), 159–207, doi:10.1023/A:1005504031923, 2000.

Shindell, D. T., Rind, D., and Lonergan, P.: Increased polar stratospheric ozone losses and delayed eventual recovery owing to increasing greenhouse-gas concentrations, Nature, 392(6676), 589–592, doi:10.1038/33385, 1998.

Silva, A. A., and Kirchhoff, V. W. J. H.: Aerosol optical thickness from Brewer spectrophotometers and an investigation into the stray-light effect, Appl. Opt., 43(12), 2484–2489, 2004.

Slavin, W.: Stray Light in Ultraviolet, Visible and Near-Infrared Spectrophotometry, Anal. Chem., 35(4), 561–566, 1963.

Smith, E., and Dent, G.: Modern Raman Spectroscopy - A Practical Approach, Journal of the American College of Surgeons, John Wiley & Sons Ltd., Chichester, West Sussex, Vol. 190, doi:10.1016/S1072-7515(99)00299-9, 2005.

Solomon, S: Stratospheric ozone depletion: A review of concepts and history, Rev. Geophys., 37(3), 275–316, doi:10.1029/1999RG900008, 1999.

Solomon, S., and Sanders, R. W.: On the Interpretation of Zenith Sky Absorption Measurements, J. Geophys. Res., 92, 8311–8319, 1987.

Tarnocai, C., Canadell, J. G., Schuur, E. A. G., Kuhry, P., Mazhitova, G., and Zimov, S.: Soil organic carbon pools in the northern circumpolar permafrost region, Global Biogeochem. Cycles, 23(2), 1–11, doi:10.1029/2008GB003327, 2009.

Texas Instruments: Dual-Axis Analog MEMS Pointing Mirror, Retrieved from http://www.ti.com/lit/ml/slbb089/slbb089.pdf 2018.

Thomason, L. W., Herman, B. M., and Reagan, J. A.: The Effect of Atmospheric Attenuators with Structured Vertical Distributions on Air Mass Determinations and Langley Plot Analyses, J. Atmos. Sci., doi:10.1175/1520-0469(1983)040<1851:TEOAAW>2.0.CO;2, 1983.

Trishchenko, A. P., Garand, L., and Trichtchenko, L. D.: Three-Apogee 16-h Highly Elliptical Orbit as Optimal Choice for Continuous Meteorological Imaging of Polar Regions, J. Atmos. Ocean. Technol., 28, 1407–1422, doi:10.1175/JTECH-D-11-00048.1, 2011.

Trishchenko, A. P., Garand, L., Trichtchenko, L. D., and Nikitina, L. V.: Multiple-apogee highly elliptical orbits for continuous meteorological imaging of polar regions, Bull. Am. Meteorol.

Soc., 97(1), 19–24, doi:10.1175/BAMS-D-14-00251.1, 2016.

WOUDC: No Title, Retrieved May 1, 2017, from http://www.woudc.org/data/instruments/ 2016.

Xenics, I. S.: Xeva-1.7-320 VisNIR Data Sheet, Retrieved from http://www.xenics.com/sites/default/files/leaflets/xb-080_01_xeva-1.7-320_visnir_scientific_lowres.pdf 2018.

A. Appendix

The reactions that produce active chlorine from inactive species in the presence of PSCs are as follows:

$HCl + ClONO_2 \longrightarrow HNO_3 + Cl_2$	A 1
$N_2O_5 + H_2O \longrightarrow 2HNO_3$	A 2
$ClONO_2 + H_2O \longrightarrow HNO_3 + HOCl$	A 3
$HCl + HOCl \longrightarrow H_2O + Cl_2$	A 4
$BrONO_2 + H_2O \longrightarrow HNO_3 + HOBr$	A 5
$HCl + BrONO_2 \longrightarrow HNO_3 + BrCl$	A 6
$HCl + HOBr \longrightarrow H_2O + BrCl$	A 7

B. Appendix

Jacobian Calculations of M_{ik}:

$$\mathbf{M_{ik}} = \frac{\partial(\mathbf{F_{mi}})}{\partial \mathbf{v_k}} \begin{cases} \mathbf{M_{i1}} = \dfrac{\partial(\mathbf{F_{mi}})}{\partial \mathbf{x}} = -\boldsymbol{\alpha} \cdot \boldsymbol{\mu} - 3\boldsymbol{\gamma} \cdot (\boldsymbol{\alpha} \cdot \boldsymbol{\mu})^3 \cdot (\mathbf{x})^2 \\ \mathbf{M_{i2}} = \dfrac{\partial(\mathbf{F_{mi}})}{\partial \boldsymbol{\gamma}} = -(\boldsymbol{\alpha} \cdot \boldsymbol{\mu} \cdot \mathbf{x})^3 \\ \mathbf{M_{i3}} = \dfrac{\partial(\mathbf{F_{mi}})}{\partial \mathbf{b_j}} = \mathbf{ND_j} \\ \mathbf{M_{i4}} = \dfrac{\partial(\mathbf{F_{mi}})}{\partial \mathbf{F_0}} = \mathbf{1} \\ \mathbf{M_{i5}} = \dfrac{\partial(\mathbf{F_{mi}})}{\partial \boldsymbol{\tau}} = -\mathbf{10^4} \cdot \mathbf{w} \cdot \mathbf{C_\lambda} \end{cases}$$

C. Appendix

In the following the development of the equations mentioned in chapter 4 section 4.3.3 is explained in more detail.

As a result of discretizing the interferogram, the interferogram will be sampled at discrete points ($x_j = j\Delta x$) with a sampling interval of Δx. The interferogram will be sampled in a finite region between -L and +L or sample points -N and N-1. Due to the interferogram being discrete, the integral signs will be replaced by sums and therefore, equation (4-11) becomes (Kauppinen and Partanen, 2001):

$$\mathbf{E_L^{\Delta x}(\nu) = \Delta x \sum_{j=-N}^{N-1} I_j e^{-i2\pi\nu j\Delta x}} \qquad \textbf{(C 1)}$$

If a continuous, truncated interferogram is considered:

$$\mathbf{I_L(x) = \Pi_{2L}(x) I(x)} \qquad \textbf{(C 2)}$$

where $\prod_{2L}$ is the boxcar function defined as:

$$\mathbf{\Pi_{2L}(x) = \begin{cases} 1, & |x| \le L \\ 0, & |x| > L \end{cases}} \qquad \textbf{(C 3)}$$

The spectrum of a continuous truncated interferogram becomes:

$$\begin{aligned} \mathbf{E_L(\nu)} &= \mathbf{\mathcal{F}^{-1}\{\Pi_{2L}(x) I(x)\} = \mathcal{F}^{-1}\{\Pi_{2L}(x)\} * \mathcal{F}^{-1}\{I(x)\}} \\ &= \mathbf{W_L(\nu) * E(\nu) = \int_{-\infty}^{\infty} W_L(u) * E(\nu - u) du} \end{aligned} \qquad \textbf{(C 4)}$$

where, W is the instrument function of a Fourier transform spectrometer:

$$\mathbf{W_L(\nu) = \mathcal{F}^{-1}\{\Pi_{2L}(x)\} = \int_{-\infty}^{\infty} \Pi_{2L}(x) e^{-i2\pi\nu x} dx = 2L\,sinc(2\pi\nu L)} \qquad \textbf{(C 5)}$$

The spectrum of a discrete interferogram is periodic with a period of $1/(\Delta x)$ where Δx is the sampling interval as mentioned before. Therefore:

$$\mathbf{E}^{\Delta x}\left(\boldsymbol{\nu}-\frac{\mathbf{k}}{\Delta \mathbf{x}}\right)=\mathbf{E}^{\Delta x}(\boldsymbol{\nu}) \tag{C 6}$$

The combination of truncation and discrete sampling results in the spectrum below:

$$\begin{aligned}\mathbf{E}_{\mathbf{L}}^{\Delta x} &= \sum_{\mathbf{k}=-\infty}^{\infty} \mathbf{E}_{\mathbf{L}}\left(\boldsymbol{\nu}-\frac{\mathbf{k}}{\Delta \mathbf{x}}\right) \\ &= \sum_{\mathbf{k}=-\infty}^{\infty} \boldsymbol{\delta}\left(\boldsymbol{\nu}-\frac{\mathbf{k}}{\Delta \mathbf{x}}\right) * \mathbf{E}_{\mathbf{L}}(\boldsymbol{\nu}) \\ &= \sum_{\mathbf{k}=-\infty}^{\infty} \boldsymbol{\delta}\left(\boldsymbol{\nu}-\frac{\mathbf{k}}{\Delta \mathbf{x}}\right) * \mathbf{2Lsinc}(\mathbf{2\pi\nu L}) * \mathbf{E}(\boldsymbol{\nu}) \\ &= \left\{\sum_{\mathbf{k}=-\infty}^{\infty} \mathbf{2Lsinc}\left[\mathbf{2\pi}\left(\boldsymbol{\nu}-\frac{\mathbf{k}}{\Delta \mathbf{x}}\right)\mathbf{L}\right]\right\} * \mathbf{E}(\boldsymbol{\nu}) = \mathbf{W}_{\mathbf{L}}^{\Delta \mathbf{x}} * \mathbf{E}(\boldsymbol{\nu})\end{aligned} \tag{C 7}$$

$W^{\Delta x}{}_L$ shows the effect of truncation and discrete sampling on the interferogram. For example if the spectrum consists of two spectral lines at $-\upsilon_0$ and $+\upsilon_0$ meaning, $E(\upsilon) = \delta(\upsilon- \upsilon_0) + \delta(\upsilon+ \upsilon_0)$, the interferogram will be: $I(x) = 2\cos(2\pi\upsilon_0 x)$. If this interferogram is truncated from -L to L, then the spectrum becomes: $E_L(\upsilon) = 2L\text{sinc}[2\pi(\upsilon -\upsilon_0)L] + 2L\text{sinc}[2\pi(\upsilon +\upsilon_0)L]$. This spectrum consists of two sinc functions centred at $-\upsilon_0$ and $+\upsilon_0$. If the interferogram is truncated and sampled discretely, the spectrum becomes:

$$\begin{aligned}\mathbf{E}_{\mathbf{L}}^{\Delta x} &= \sum_{\mathbf{k}=-\infty}^{\infty} \mathbf{2Lsinc}\left[\mathbf{2\pi}\left(\boldsymbol{\nu}+\boldsymbol{\nu}_{\mathbf{0}}-\frac{\mathbf{k}}{\Delta \mathbf{x}}\right)\mathbf{L}\right] \\ &+ \sum_{\mathbf{q}=-\infty}^{\infty} \mathbf{2Lsinc}\left[\mathbf{2\pi}\left(\boldsymbol{\nu}-\boldsymbol{\nu}_{\mathbf{0}}-\frac{\boldsymbol{q}}{\Delta \mathbf{x}}\right)\mathbf{L}\right]\end{aligned} \tag{C 8}$$

The truncated, discretized spectrum consists of two sets of periodic series of sinc functions with a period of $1/(\Delta x)$.

In the case of a wide-band spectrum, the maximum wavenumber in the spectrum is υ_{max}. If the sampling period is short, then the period of the discretized spectrum is larger than the spectral band, $2\,\upsilon_{max} \leq 1/(\Delta x)$. In this case, the spectrum is distinguished and aliasing does not occur (Kauppinen and Partanen, 2001). The Nyquist frequency determines that the sampling interval of an interferogram should be:

$$(\Delta x)_{Nyquist} = \frac{1}{2\nu_{max}} \qquad \textbf{(C 9)}$$

If $\Delta x > 1/(2\,\upsilon_{max})$, the spectrum becomes distorted due to aliasing, meaning that the period of the spectrum is smaller than the width of the spectrum and overlap with each other. Therefore, the critical sampling frequency or Nyquist frequency is:

$$f_N = \frac{1}{\Delta t} = 2f_{max} \qquad \textbf{(C 10)}$$

where, f_{max} is the maximum frequency of the true spectrum being measured.

The equations above deal with the interferogram and spectrum of a point source. In dealing with extended sources, the optical path difference of the rays that are in the optical axis of the IFTS is x = 2d, where d is the mechanical path difference of the rays. For rays that are off axis in the direction of α with respect to the optical axis gives (Kauppinen and Partanen, 2001):

$$x\cos(\alpha) \approx x\left(1 - \frac{\Omega'}{2\pi}\right) \qquad \textbf{(C 11)}$$

Where, Ω' is $\pi\alpha^2$ and varies between 0 and Ω which is the solid angle subtended by the source as seen from the aperture. Integrating over the source gives the interferogram (Kauppinen and Partanen, 2001):

$$\mathbf{I_\Omega(x) = \int_0^\Omega I\left[x\left(1-\frac{\Omega'}{2\pi}\right)\right]d\Omega'}$$

$$\mathbf{= \Omega\int_{-\infty}^{\infty} E(\nu)\,sinc\left(\frac{\nu x\Omega}{2}\right)e^{i2\pi\nu x\left(1-\frac{\Omega}{4\pi}\right)}d\nu} \qquad \textbf{(C 12)}$$

Equation (C 12) shows there is a shift of 1- Ω/(4π) in the measured wavenumber. In the case of a monochromatic spectrum (E(υ) = δ(υ- υ_0) + δ(υ+ υ_0)), the interferogram becomes:

$$\mathbf{I_\Omega(x) = \Omega\left\{sinc\left(\frac{\nu_0 x\Omega}{2}\right)e^{i2\pi\nu_0 x\left(1-\frac{\Omega}{4\pi}\right)}\right.}$$

$$\mathbf{\left. + sinc\left(\frac{\nu_0 x\Omega}{2}\right)e^{-i2\pi\nu_0 x\left(1-\frac{\Omega}{4\pi}\right)}\right\}} \qquad \textbf{(C 13)}$$

The spectrum of the interferogram becomes:

$$\mathbf{E_\Omega(\nu) = \mathcal{F}^{-1}\{I_\Omega(x)\}}$$

$$\mathbf{= \Pi_\Omega(\nu,\nu_0)}$$

$$\mathbf{* \left\{\delta\left(\nu+\nu_0\left(1-\frac{\Omega}{4\pi}\right)\right)+\delta\left(\nu-\nu_0\left(1-\frac{\Omega}{4\pi}\right)\right)\right\}} \qquad \textbf{(C 14)}$$

Where, ∏ is the boxcar function defined as:

$$\mathbf{\Pi_\Omega(\nu,\nu_0) = \begin{cases} \frac{2\pi}{\nu_0} & |\nu| \le \frac{\nu_0\Omega}{4\pi} \\ 0 & |\nu| > \frac{\nu_0\Omega}{4\pi} \end{cases}} \qquad \textbf{(C 15)}$$

Therefore, the peaks of the spectrum appear as boxes with the width of $\nu_0\Omega/(2\pi)$ and a height of $2\pi/\nu_0$. The broadening of the spectral lines is called aperture broadening and is due to the size of the source. Equation (C 14) can be further simplified and written as:

$$\mathbf{E_\Omega(\nu) = W_\Omega(\mp\nu_0,\nu) * \delta(\nu \pm \nu_0)} \qquad \textbf{(C 16)}$$

Where, δ ($\nu \pm \nu_0$) is E(ν) and W_Ω is:

$$\mathbf{W_{\Omega}}(\mp\boldsymbol{\nu_0},\boldsymbol{\nu}) = \boldsymbol{\Pi_{\Omega}}(\boldsymbol{\nu},\boldsymbol{\nu_0}) * \boldsymbol{\delta}\left(\boldsymbol{\nu} \mp \frac{\boldsymbol{\nu_0\Omega}}{\boldsymbol{4\pi}}\right) \tag{C 17}$$

Combining the effects of truncation, discretization and extended source on the spectrum gives:

$$\begin{aligned}\mathbf{E_{L,\Omega}^{\Delta x}}(\boldsymbol{\nu}) &= \mathbf{W_{\Omega}}(\mp\boldsymbol{\nu_0},\boldsymbol{\nu}) * \mathbf{E_L^{\Delta x}}(\boldsymbol{\nu}) = \mathbf{W_{\Omega}}(\mp\boldsymbol{\nu_0},\boldsymbol{\nu}) * \mathbf{W_L^{\Delta x}}(\boldsymbol{\nu}) * \mathbf{E}(\boldsymbol{\nu}) \\ &= \mathbf{W_{L,\Omega}^{\Delta x}}(\boldsymbol{\nu}) * \mathbf{E}(\boldsymbol{\nu})\end{aligned} \tag{C 18}$$

Where,

$$\mathbf{W_{L,\Omega}^{\Delta x}}(\boldsymbol{\nu}) = \mathbf{W_{\Omega}}(\mp\boldsymbol{\nu_0},\boldsymbol{\nu}) * \left\{\sum_{\mathbf{k}=-\infty}^{\infty} \mathbf{2Lsinc}\left[\boldsymbol{2\pi}\left(\boldsymbol{\nu} - \frac{\mathbf{k}}{\boldsymbol{\Delta x}}\right)\mathbf{L}\right]\right\} \tag{C 19}$$

And the spectrum becomes (Kauppinen and Partanen, 2001):

$$\begin{aligned}\mathbf{E_{L,\Omega}^{\Delta x}}(\boldsymbol{\nu}) = &\sum_{\mathbf{k}=-\infty}^{\infty} \mathbf{W_{\Omega}}(-\boldsymbol{\nu_0},\boldsymbol{\nu}) * \mathbf{2Lsinc}\left[\boldsymbol{2\pi}\left(\boldsymbol{\nu} + \boldsymbol{\nu_0} - \frac{\mathbf{k}}{\boldsymbol{\Delta x}}\right)\mathbf{L}\right] \\ &+ \sum_{\mathbf{l}=-\infty}^{\infty} \mathbf{W_{\Omega}}(\boldsymbol{\nu_0},\boldsymbol{\nu}) * \mathbf{2Lsinc}\left[\boldsymbol{2\pi}\left(\boldsymbol{\nu} - \boldsymbol{\nu_0} - \frac{\mathbf{l}}{\boldsymbol{\Delta x}}\right)\mathbf{L}\right]\end{aligned} \tag{C 20}$$

Where W_{Ω} is:

$$\mathbf{W_{\Omega}}(\mp\boldsymbol{\nu_0},\boldsymbol{\nu}) = \boldsymbol{\Pi_{\Omega}}(\boldsymbol{\nu},\boldsymbol{\nu_0}) * \boldsymbol{\delta}\left(\boldsymbol{\nu} \mp \frac{\boldsymbol{\nu_0\Omega}}{\boldsymbol{4\pi}}\right) \tag{C 21}$$

Where $\prod_{\Omega}$ is the boxcar function which is used to apodize the interferogram.

The instrument resolution depends on the size of the source and the length of the interferogram. If the source is large and the interferogram is long, the resolution will be full width at half maximum (FWHM) of W_{Ω} which is $\nu_0\Omega/(2\pi)$. If the source is small and the interferogram is short the resolution will be FWHM of the sinc function, 2Lsinc ($2\pi\nu L$), which is 1.21/(2L). In order to keep the signal to noise ratio (SNR) large it is ideal for these resolutions to be equal, $[\nu_0\Omega/(\ 2\pi\ )] = [1.21/(\ 2L\ )]$ (Kauppinen and Partanen, 2001).

D. Appendix

The performance curves of the Minus K vibration isolation table model 100 BM-4 are shown below.

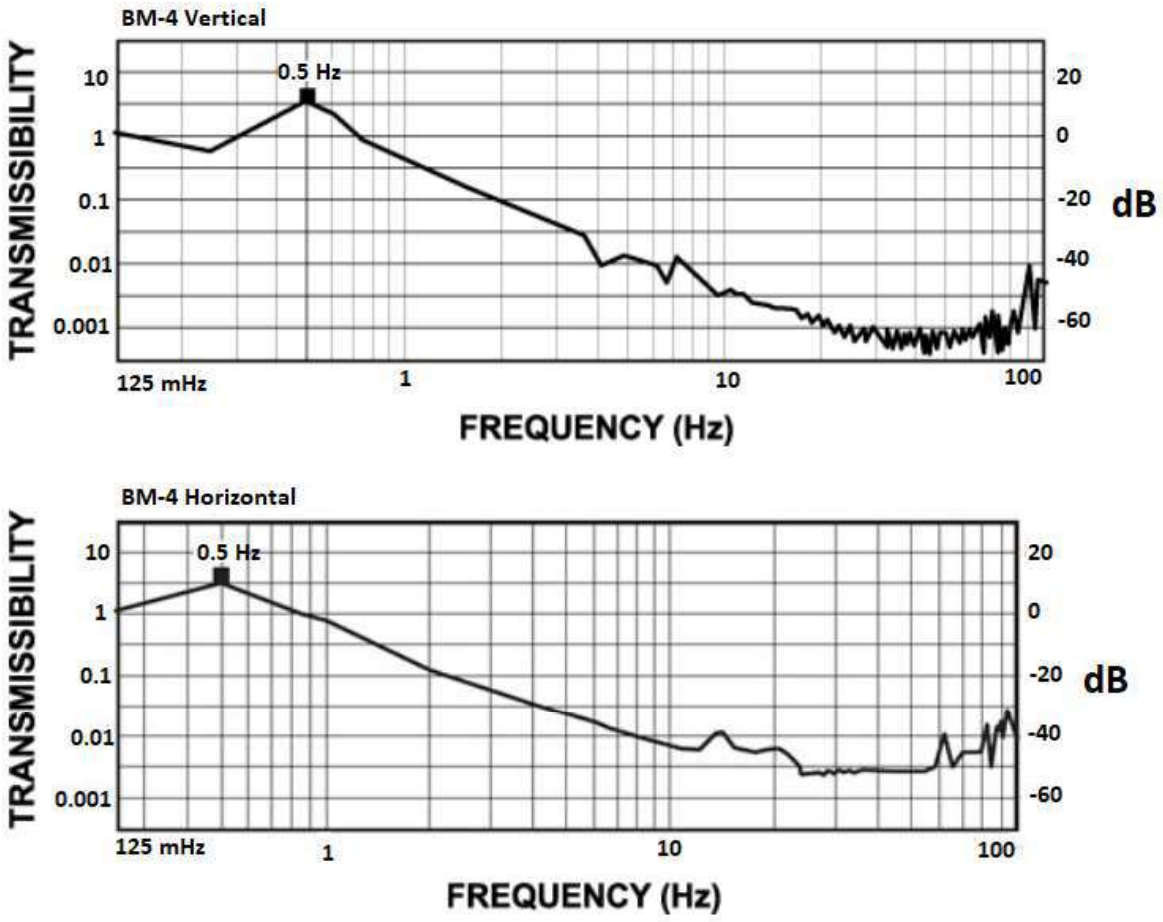

Figure D-1: Performance curves of the Minus k vibration isolation table model 100 BM-4 in the vertical (top) and horizontal (bottom). (Minus K, 2018)

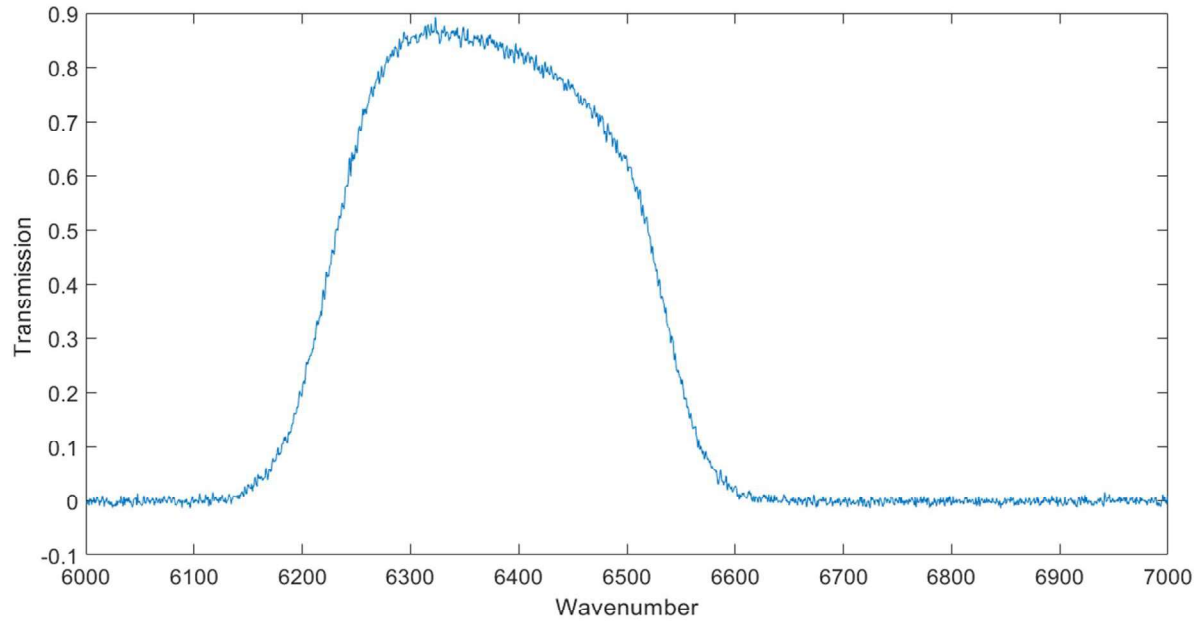

Figure D-2: Transmission curve for the 1.6 µm bandpass filter. (Andover Corp., 2018)

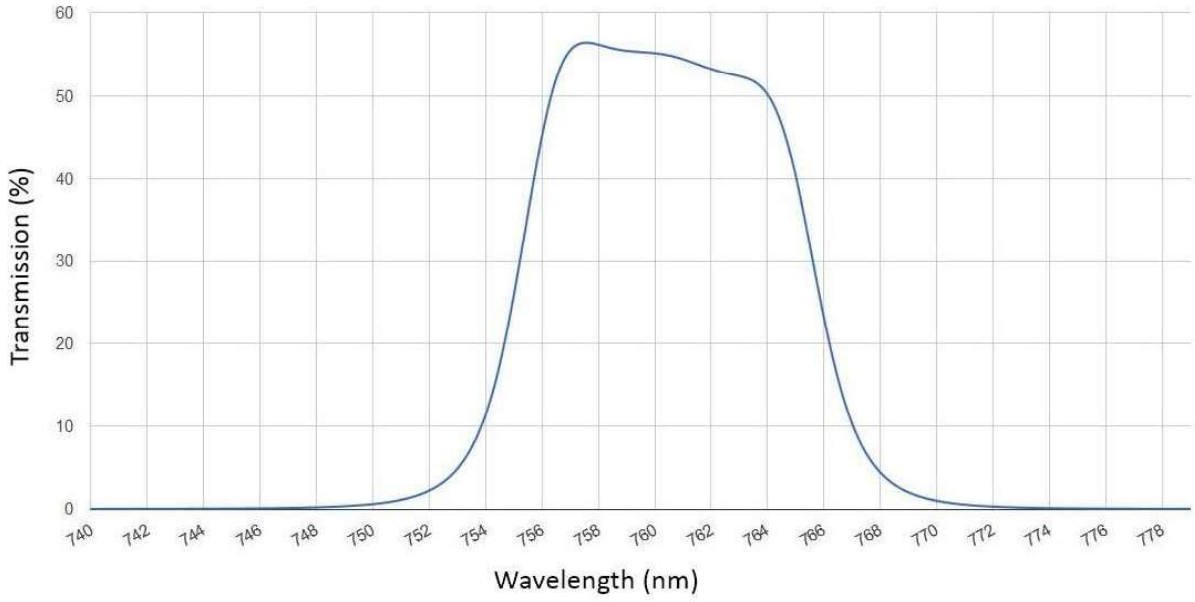

Figure D-3: Transmission curve of the 762 nm bandpass filter. (PIXELTEQ, 2018)

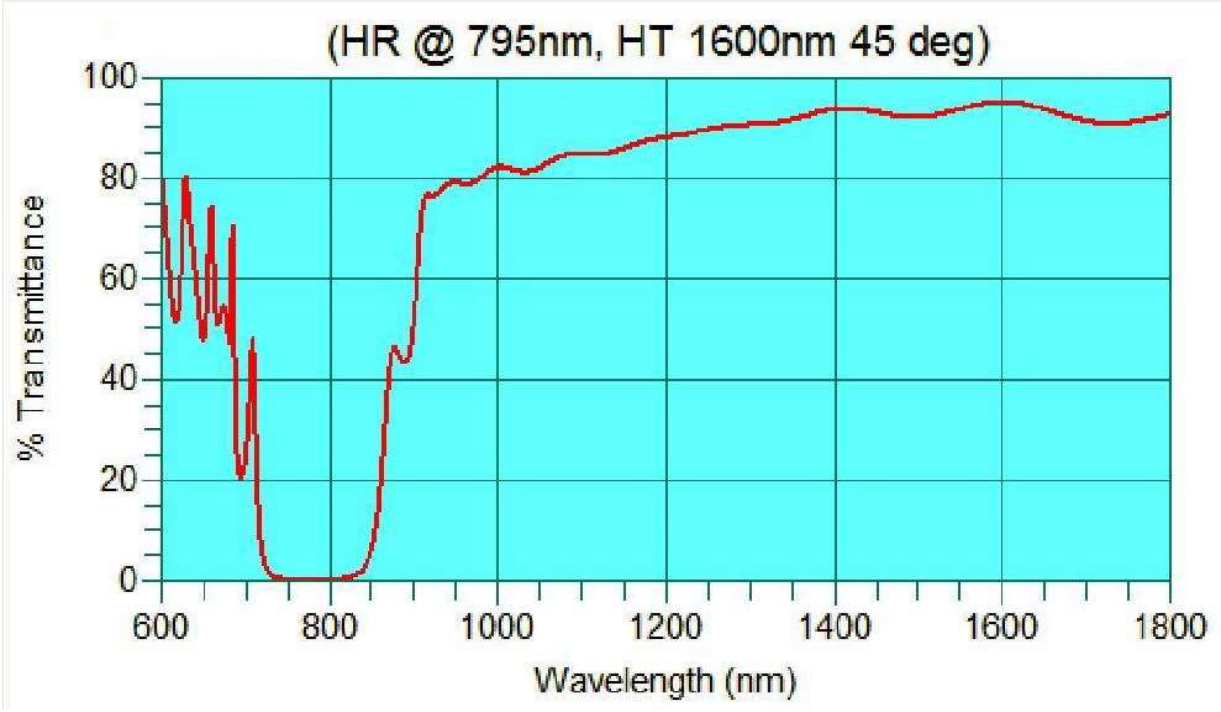

Figure D-4: Transmission curve of the second beam-splitter used in the IFTS. (BMVOPTICAL, 2017)

E. Appendix

A voice coil motor (VCM) consists of a permanent magnet as well as a coil that encloses the magnet, but, maintains an airgap to avoid friction. Figure E-1 depicts a conventional VCM and its cross section. The force that the VCM applies is directly proportional to the current that flows in the coil. The Lorentz force principal is used to determine the conversion of electromagnetic energy to mechanical force. This law states that if a total of N conductors with length L are placed in a magnetic field with density B and the current I flows through the conductors, the force acting upon the conductor will be obtained from equation (E 1), where, k is a constant (BEI Kimco, 2002).

$$\mathbf{F = kBLIN} \qquad \textbf{(E 1)}$$

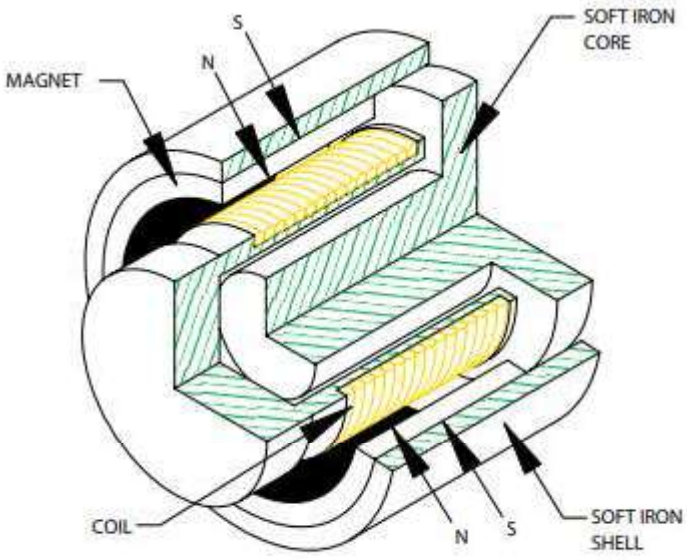

Figure E-1: Cross section of a conventional voice coil motor (VCM). (BEI Kimco, 2002)

F. Appendix

Signal to Noise Ratio Model (Personal Communications; McElroy, 2018)

The interferogram is sampled at the zero-crossing points of the metrology laser fringes at a rate of once per fringe in the 1.6 μm band and twice per fringe at 762 nm.

If the 1600 nm channel is considered, for a physical path difference scan of x, there will be $N_L = 2x/\lambda_L$ samples collected where λ_L is the laser wavelength. If the 762 nm channel is considered, the number of samples will be $N_L = 4x/\lambda_L$. If each sample is integrated for Δt = 500 μs, then the total integration time will be $t = N_L \Delta t$. However, the Fourier transform multiplies this signal by a cosine function at the frequency of interest. The signal itself is weighted by a cosine as well. If the cosine is integrated over a half cycle, the integral is 2. If the signal were integrated without the weighting the integral would be π. Therefore, the noise contribution will be weighted on average by 2/π. Since the signal at a single frequency detected is, necessarily, in phase with the cosine function, both the positive and negative half cycles will contribute. This means that the result of the FT will be the product of the signal, $S(\omega_s)\cos(\omega_s)$ and the cosine of the sampling frequency, $\cos(\omega_s)$. This results in:

$$\int_0^{\pi} \mathbf{S}(\omega_s)\mathbf{cos^2}(\omega_s \mathbf{t})\mathbf{dt} = \frac{\boldsymbol{\pi}}{\mathbf{2}}\mathbf{I} \qquad \textbf{(F 1)}$$

The actual amount of signal integrated will be less than the value of S times the total integration time because as shown in Figure F-1 the samples will be distributed evenly over the half cosine wave so that the contribution will be reduced in the ratio of π to the integral of $\cos^2$ over an angle of π. So the signal integrated up by the discrete samples taken by the IFTS will be reduced to $\frac{1}{2}\mathbf{S}(\omega_s)$.

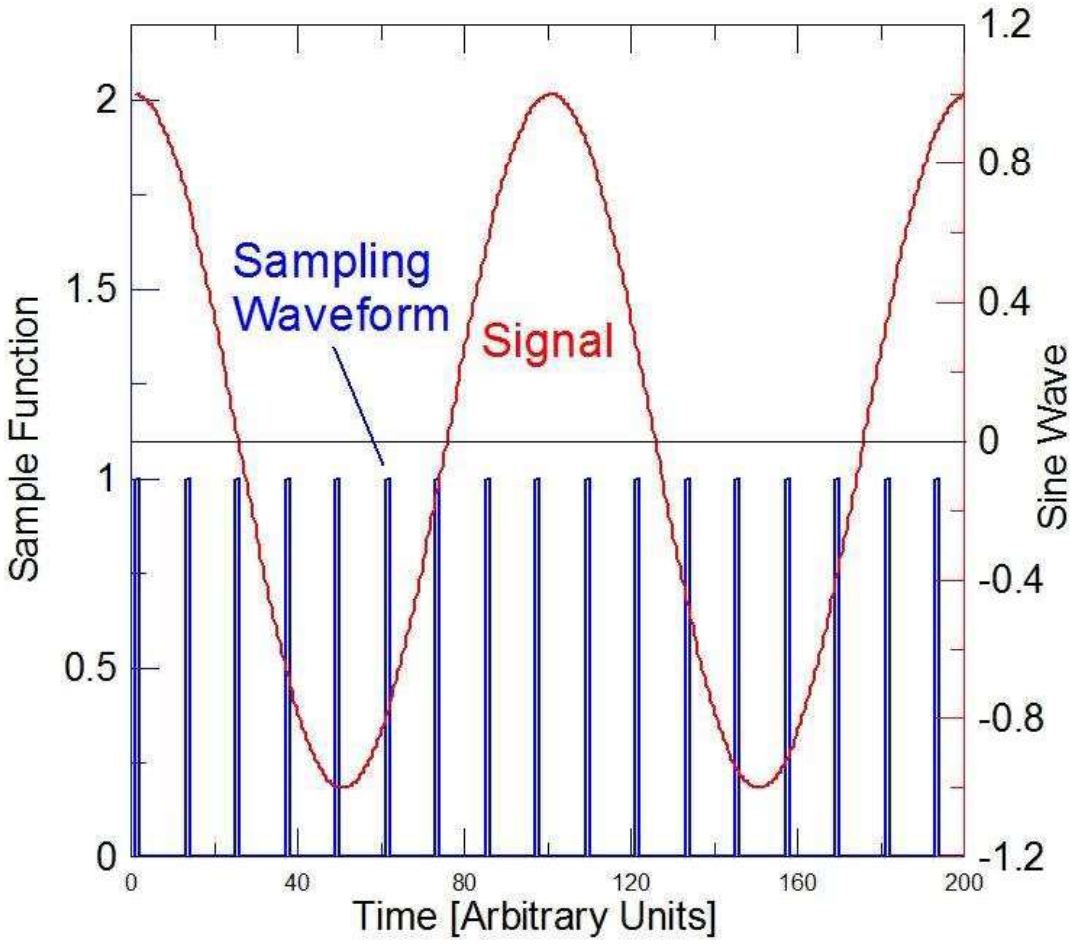

Figure F-1: Model of the sampling waveform (red) and the sample signal (blue). (Personal communications; McElroy, 2018)

The integrated signal is obtained from the equation below in Photons/s.

$$\mathbf{S_\nu = I' A\ \Omega\ \Delta\lambda\ \Delta t\ Q = \frac{1}{2}\ I\ A\ \Omega\ \Delta\lambda\ t\ Q} \qquad \textbf{(F 2)}$$

Where,

S is the signal [electrons],

I is the radiation intensity [photons/m^2/μm/sr/s],

A is the detection area of the instrument [m^2],

Ω is the solid angle subtended by the instrument optics of the instrument [sr],

$\Delta\lambda$ is the instrument resolution in wavelength space [μm],

t is the total integration time [s] which is equal to $N_L\ \Delta t$,

Q is the quantum efficiency of the detector [e/photon].

When the signal to noise ratio is calculated, it is recognized that the noise contribution from all the photons arriving in the passband of the bandpass filter ($\Delta\lambda_f$) must be considered. However, the average value of the signal will not be evident in the Fourier transform component of any particular frequency, but only the random component will.

Therefore, the noise contribution, S_N (equation (F **4**)), to the observations will be the square root of the total photon count arriving within the band pass filter, S_f (equation (F 3)).

$$\mathbf{S_f = \frac{2}{\pi}\ I\ A\ \Omega\ \Delta\lambda_f\ t\ Q} \qquad \textbf{(F 3)}$$

$$\mathbf{S_N = \sqrt{\frac{2}{\pi}\ I\ A\ \Omega\ \Delta\lambda_f\ t\ Q}} \qquad \textbf{(F 4)}$$

Therefore, the signal to noise ratio (SNR) is:

$$\mathbf{SNR = \frac{S_\nu}{S_N} = \frac{1}{2}\ \Delta\lambda \sqrt{\frac{\pi\ I\ A\ \Omega\ t\ Q}{2\ \Delta\lambda_f}}} \qquad \textbf{(F 5)}$$

G. Appendix

Efficiency of the Zinc Selenide Beam-Splitter (Personal communications; McElroy, 2018)

Figure G-1 shows the configuration of a conventional Michelson interferometer where flat mirrors have been used. Light from the source enters the instrument and is split at both surfaces of the beam-splitter (BS). The first reflection happens at the front surface of the beam-splitter and is reflected by Mirror 1 (M1). The remainder of that beam goes through the BS and part of it is reflected by the back surface of the BS and goes towards M1 and the other part goes through the BS to Mirror 2 (M2). Part of the reflected beam by M2 reflects from the front surface of the BS and goes towards the detector. The other part goes through the BS and is reflected by the back surface of the BS and goes to the detector.

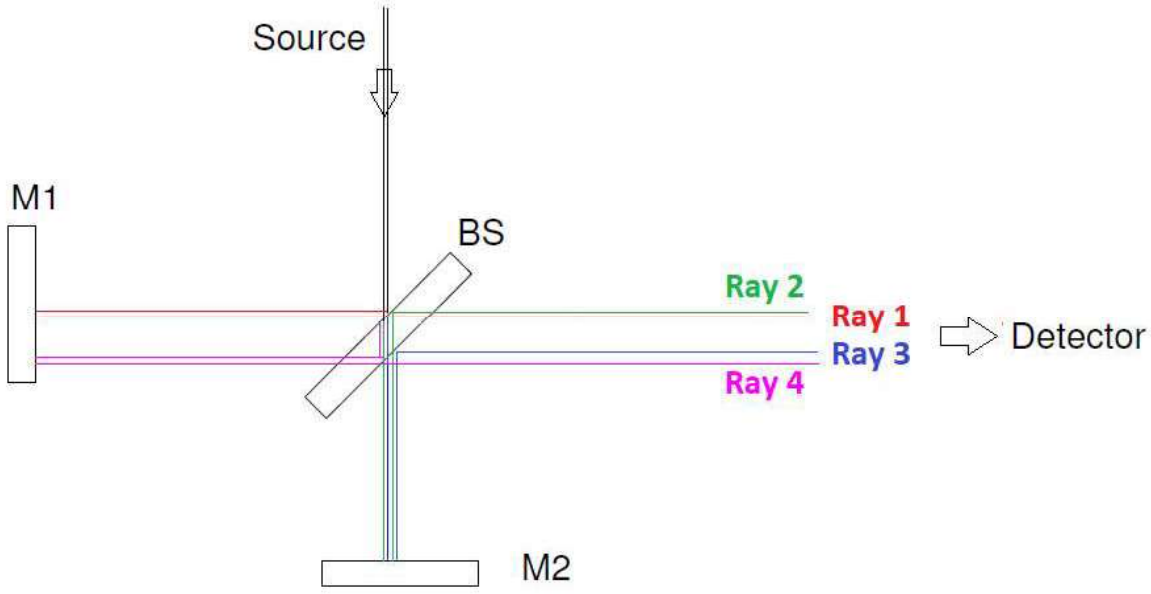

Figure G-1: Configuration of a conventional Michelson Interferometer. (Personal communications; McElroy, 2018)

To simplify this description the definitions below are used:

TBS: Transmit through the beam-splitter

M1: Mirror 1

M2: Mirror 2

FSR: Front surface reflection

BSR: Back surface reflection

L: Loss due to transmission through the beam-splitter

MR: Mirror reflection coefficient

S: Source

The path of the rays is described as below:

Ray 1: S➔ FSR➔ M1➔ TBS➔ Detector

Ray 2: S➔ TBS➔ M2➔ TBS➔ BSR➔ TBS➔ Detector

Ray 3: S➔ TBS➔ M2➔ FSR➔ Detector

Ray 4: S➔ TBS➔ BSR➔ TBS➔ M1➔ TBS➔ Detector

The transmission coefficient is complementary to the reflection coefficient (1-Reflection coefficient). In the IFTS instrument the flat mirrors are replaced with corner cubes which have three reflections, therefore the mirror reflection coefficient should be raised to the power of 3. The intensities of the rays are derived below:

$$\text{Ray } 1 = \mathrm{I} \times \mathrm{FSR} \times \mathrm{MR}^3 \times (1 - \mathrm{FSR}) \times \mathrm{L} \times (1 - \mathrm{BSR})$$

$$\text{Ray } 2 = \mathrm{I} \times (1 - \mathrm{FSR}) \times \mathrm{L} \times (1 - \mathrm{BSR}) \times \mathrm{MR}^3 \times (1 - \mathrm{FSR}) \times \mathrm{L} \times \mathrm{BSR} \times \mathrm{L} \times (1 - \mathrm{BSR})$$

$$\text{Ray } 3 = \mathrm{I} \times (1 - \mathrm{FSR}) \times \mathrm{L} \times (1 - \mathrm{BSR}) \times \mathrm{MR}^3 \times \mathrm{FSR}$$

$$\text{Ray } 4 = \mathrm{I} \times (1 - \mathrm{FSR}) \times \mathrm{L} \times \mathrm{BSR} \times \mathrm{L} \times (1 - \mathrm{BSR}) \times \mathrm{MR}^3 \times (1 - \mathrm{FSR}) \times \mathrm{L} \times (1 - \mathrm{BSR})$$

(G-1)

Rays 1 and 3 will have the same intensity and path difference and rays 2 and 4 will have the same intensity and path difference.

Loss through the beam-splitter due to transmission depends on the thickness and attenuation coefficient of the beam-splitter. The loss factor (L) determined by the data sheet for the ZnSe beam-splitter is negligible therefore is equal to 1. The mirror reflection coefficient (MR) is 0.98.

To find the FSR and BSR the Fresnel equations below are used:

For S-polarization (electric field normal to the plane of incident and reflected rays):

$$\mathbf{FSR_s} = \left|\frac{\mathbf{n_1 Cos(\theta_i) - n_2 Cos(\theta_t)}}{\mathbf{n_1 Cos(\theta_i) + n_2 Cos(\theta_t)}}\right|^2 \quad \textbf{(G-2)}$$

$$\mathbf{BSR_s} = \left|\frac{\mathbf{n_2 Cos(\theta_t) - n_1 Cos(\theta_i)}}{\mathbf{n_2 Cos(\theta_t) + n_1 Cos(\theta_i)}}\right|^2 \quad \textbf{(G-3)}$$

For P-polarization (electric field parallel to the plane of incident and reflected rays):

$$\mathbf{FSR_p} = \left|\frac{\mathbf{n_1 Cos(\theta_t) - n_2 Cos(\theta_i)}}{\mathbf{n_1 Cos(\theta_t) + n_2 Cos(\theta_i)}}\right|^2 \quad \textbf{(G-4)}$$

$$\mathbf{BSR_p} = \left|\frac{\mathbf{n_2 Cos(\theta_i) - n_1 Cos(\theta_t)}}{\mathbf{n_2 Cos(\theta_i) + n_1 Cos(\theta_t)}}\right|^2 \quad \textbf{(G-5)}$$

Where, n_1 is the refractive index of air and n_2 is the refractive index of ZnSe which is dependant on wavelength. θ_i is the incident angle and θ_t is the transmission angle.

The index of refraction for ZnSe at 1600 nm is 2.477 and for 762 nm is 2.496, θ_i is 45° and $n_1 = 1$.

To find θ_t Snell's law is used:

$$\mathbf{n_1 Sin(\theta_i) = n_2 Sin(\theta_t)} \quad \textbf{(G-6)}$$

Therefore, θ_t for 1600 nm is 16.587° and for 762 nm is 16.457°. Substituting these values in equation (G-2) to (G-5) for the 1600 nm wavelength results in:

$\mathbf{FSR_s = 0.2927}$ $\mathbf{BSR_s = 0.2927}$

$\mathbf{FSR_p = 0.0857}$ $\mathbf{BSR_s = 0.0857}$

And for the 762 nm wavelength results in:

$\mathbf{FSR_s = 0.2959}$ $\mathbf{BSR_s = 0.2959}$

$\mathbf{FSR_p = 0.0875}$ $\mathbf{BSR_s = 0.0875}$

Substituting these numbers into equation (G-1), the intensities of the s and p polarized rays be:

1600 nm	762 nm
$I_{1,3_s} = I_s \times 0.138$ $I_{1,3_p} = I_p \times 0.0674$ $I_{2.4_s} = I_s \times 0.069$ $I_{2.4_p} = I_p \times 0.0563$	$I_{1,3_s} = I_s \times 0.138$ $I_{1,3_p} = I_p \times 0.0686$ $I_{2.4_s} = I_s \times 0.0684$ $I_{2.4_p} = I_p \times 0.0571$

Where, $I_s = I_p = I/2$.

The difference between the 1600 nm wavelength and 762 nm wavelength is negligible.

The average s-polarized intensity will be 0.207 and the average p-polarized intensity will be 0.124 and results in a total of 0.331.

The intensities of rays 1 and 3 are equal and rays 2 and 4 are equal which results in a modulation efficiency of 100%.

H. Appendix

Calculations for the SNR of the 200 W lamp:

Intensity

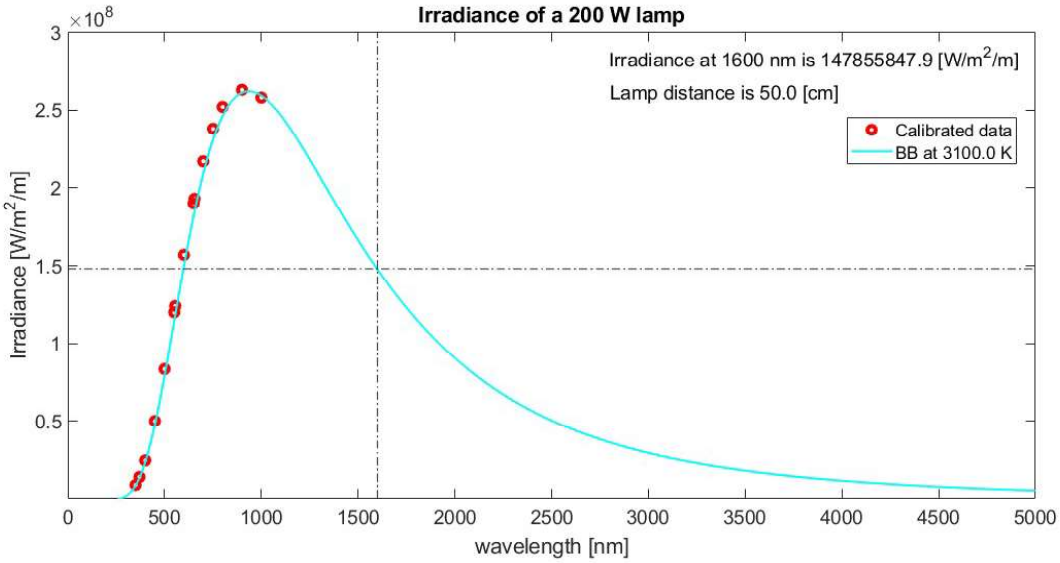

Figure H-1: Irradiance of the 200 W lamp using a black body curve at 3100 K fitted to the calibrated data.

$I = 1.48 \times 10^{8}$ W.m^{-2}.m^{-1}

A surface albedo of 1 and a diffuser set at 45°:

$I = (1/\pi) \times 1.48 \times 10^{8} \times \cos(45) = 3.33 \times 10^{7}$ [W.m^{-2}.m^{-1}.sr^{-1}]

$1\ \left[\frac{J}{s}\right] = \frac{1}{1.24 \times 10^{-19}} = 8.05 \times 10^{18}\ [\frac{Ph}{s.W}]$ Therfore:

$I = 3.33 \times 10^{7} \times 8.05 \times 10^{18} = 2.68 \times 10^{26}$ [Ph.m^{-2}.m^{-1}.sr^{-1}.s^{-1}]

For the 1600 nm channel the accumulated attenuation will be 26.24% and the estimated uncertainty in the lamp irradiance is 20% therefore:

$I = 2.68 \times 10^{26} \times 0.2624 \times 0.2 = 1.41 \times 10^{25}$ [Ph.m^{-2}.m^{-1}.sr^{-1}.s^{-1}]

Instrument Detection Area, A

The corner-cube mirror diameter is 50 mm, therefore, the instrument detection area (A) will be:

$$A = \pi r^2 = \pi(25\text{mm} \times 10^{-3})^2 = 1.9 \times 10^{-3}[\text{m}^2]$$

Instrument Solid Angle, Ω

The IFTS input lens has a focal length of 100 mm and the detector has a 30 μm square pixel. Therefore, the solid angle subtended by the instrument optics for one pixel will be:

$$\Omega = \frac{A}{r^2} = \frac{30 \times 30 \times 10^{-12}\ \text{m}^2}{(0.1\ \text{m})^2} = 9 \times 10^{-8}[\text{sr}]$$

Instrument Resolution, Δλ

The instrument resolution (Δν) is 0.5 cm^{-1} which in the wavelength space is:

$$\Delta\lambda = \frac{\Delta\nu \cdot \lambda}{\nu} = \frac{0.5 \times 1.6}{6250} = 1.3 \times 10^{-4}[\mu\text{m}] = 1.3 \times 10^{-10}[\text{m}]$$

Total Integration Time, t

There are 65,425 data points in the IFTS filter interferogram and at an integration time of 200 μs, The total integration time becomes:

$\Delta t = 65425 \times 200 \times 10^{-6} = 13.085$ s

Filter Bandpass, $\Delta\lambda_f$

If the band is limited to 6190 cm^{-1} to 6500 cm^{-1} by means of an optical filter (transmission curve provided in appendix D, Figure D-2) meaning $\Delta\lambda_f = 77.05$ [nm] $= 7.7 \times 10^{-8}$ [m].

Quantum Efficiency, Q

In the 1.6 μm band the energy of one photon is:

$$E = \frac{h \cdot c}{\lambda} = \frac{6.626 \times 10^{-34} \times 3 \times 10^{8}}{1.6 \times 10^{-6}} = 1.24 \times 10^{-19}\ [\text{J/Ph}]$$

Therefore 1 joule = $\frac{1}{1.24 \times 10^{-19}} = 8.05 \times 10^{18}$ [Ph] photons. Dividing both sides by 1 s results in 1 W = 8.05×10^{18} [Ph/s]. The sensitivity of the detector in this spectral region is 1 A/W where 1 A is 6.24 x 10^{18} electrons per second. Considering the above, the quantum efficiency will be:

$$Q = \frac{6.24 \times 10^{18}\ \mathrm{e/s}}{8.05 \times 10^{18}\ \mathrm{Ph/s}} = 0.78\ [\frac{\mathrm{e}}{\mathrm{ph}}]\ .$$

Lamp SNR

Quoting equation (4-24): $\mathbf{SNR} = \frac{\mathbf{1}}{\mathbf{2}}\ \Delta\boldsymbol{\lambda}\sqrt{\frac{\boldsymbol{\pi}\ \mathbf{I}\ \mathbf{A}\ \boldsymbol{\Omega}\ \mathbf{t}\ \mathbf{Q}}{\mathbf{2}\ \Delta\boldsymbol{\lambda}_{\mathbf{f}}}}$

$$\mathrm{SNR} = \frac{1}{2} \times (1.3 \times 10^{-10}) \sqrt{\frac{\pi \times 1.41 \times 10^{25} \times 1.9 \times 10^{-3} \times 9 \times 10^{-8} \times 13.085 \times 0.78}{2 \times 7.7 \times 10^{-8}}} = 46$$

I. Appendix

Data volume calculation for the IFTS:

A typical output file (interferogram) from each pixel of the detector is 385 Kilo bytes (Kb). The detector has 320 by 256 pixels therefore the volume of the data per one scan for all pixels will be:

$385 \times 320 \times 256 = 31539200$ Kb ~ 31.5 Gb

At a scan speed of 500 Hz and a sampling of twice per fringe, the time interval between two data points in the interferogram will be 0.001 s.

A typical scan contains ~ 65000 data points. Therefore, the total time for one scan is 65 s.

In one hour the IFTS can do ~ 50 scans therefore in one hour the data volume will be:

31.5 Gb × 50 scans ~ 1575 Gb ~ 1.5 Tb

J. Appendix

Description of a Position Sensitive Device (PSD):

The incident light on the PSD sensor cases a change in the local resistance. This change effects the current flowing in each of the four electrodes I_1, I_2, I_3 and I_4. The figure below shows the diagram of such a sensor.

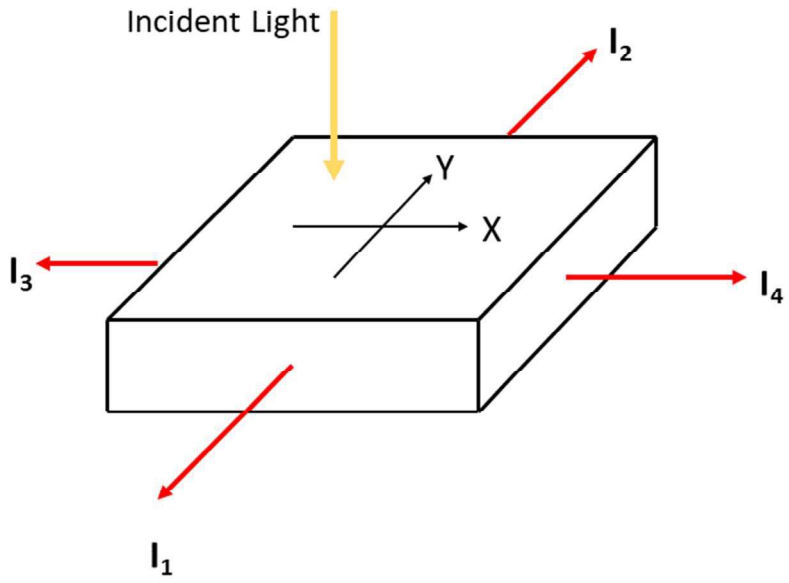

Figure J-1: Diagram of a PSD sensor.

The location of the incident light with respect to the reference frame of the sensor is calculated from the equations below where k_x and k_y are converting scaling factors.

$$x = k_x \frac{I_4 - I_3}{I_4 + I_3} \quad \textbf{J-1}$$

$$y = k_y \frac{I_2 - I_1}{I_2 + I_1} \quad \textbf{J-2}$$

K. Appendix

Technology Readiness Levels Overview (Mankins, 1995):

TRL 1	Basic principles observed and reported
TRL 2	Technology concept and/or application formulated
TRL 3	Analytical and experimental critical function and/or characteristic proof-of concept
TRL 4	Component and/or breadboard validation in laboratory environment
TRL 5	Component and/or breadboard validation in relevant environment
TRL 6	System/subsystem model or prototype demonstration in a relevant environment (ground or space)
TRL 7	System prototype demonstration in a space environment
TRL 8	Actual system completed and “flight qualified” through test and demonstration (ground or space)
TRL 9	Actual system “flight proven” through successful mission operations

L. Appendix

Curriculum Vitae

Personal information

First name, Surname	**Zahra, Vaziri Zanjani**
Telephone	+1-647-975-1405
E-mail	zvaziri@yorku.ca , zahra_vaziri@yahoo.com
Date of birth	14/05/1987

www.linkedin.com/in/zahra-vaziri-2627833b

Education

Ph.D. Earth and Space Science and Engineering
2012- 2018

Principal subjects: Remote sensing, Atmospheric space instrumentation, Satellite and balloon payload design

Name of organisation: York University

M.Sc. Space Science and Technology
2010-2012

Principal subjects: Spacecraft Dynamics, System Design, Space Environment, Space Physics, Astronomy, Atmospheric Science

Name of organisation: Lulea University of Technology

B.Sc. Physics
2005-2010

Principal subjects: Mechanics, Electronics, Astronomy, Atmospheric Science, Thermodynamics

Name of organisation: Amirkabir University of Technology (Tehran Polytechnic)

Work experience

Research Associate at University of Toronto
Dec 2018 - present

Main activities and responsibilities: MOPITT instrument flight operations and science

Employer: James Drummond, University of Toronto, James.Drummond@dal.ca

Teaching and Research Assistant at York University
2012- 2018

Main activities and responsibilities: Teaching courses and labs at undergraduate level, Conducting research in space instrumentation, satellite payload design and systems engineering

Employer: Tom McElroy, York University, 4700 Keele st., Toronto, Canada, c.t.mcelroy@gmail.com

Intern at the Swedish Institute for Space Physics (IRF)
Oct 2011-Jan 2012

Main activities and responsibilities: Data analysis for PRIMA (space-based mass electron analyser onboard the Swedish Prisma satellite)

Employer: Stas Barabash, IRF, Box 812, SE98128 Kiruna, SWEDEN, stas.barabash@irf.se

Research Work

Ph.D.	**Development and Improvement of Spectroscopic Techniques for Atmospheric Composition Measurements from Ground and Space**	**2012-2018**
M.Sc.	**Space Radiation Effects on Channel Electron Multipliers: Analysis, Modelling and Sensor Design.**	**2011–2012**
B.Sc.	**The Implications of Space Radiation on Space Crafts and Protection Design Methodologies.**	**2009-2010**

Publications

Vaziri Zanjani, Z., Moeini, O., McElroy, T., Barton, D., and Savastiouk, V.: A calibration procedure which accounts for non-linearity in single-monochromator Brewer ozone spectrophotometer measurements, Atmos. Meas. Tech., 12, 271–279, https://doi.org/10.5194/amt-12-271-2019, 2019.

Moeini, O., **Vaziri Zanjani, Z.**, McElroy, C. T., Tarasick, D. W., Evans, R. D., Petropavlovskikh, I., and Feng, K.-H.: The effect of instrumental stray light on Brewer and Dobson total ozone measurements, Atmos. Meas. Tech., 12, 327–343, https://doi.org/10.5194/amt-12-327-2019, 2019.

Vaziri Zanjani, Z, *Singh, G.,* McElroy, C. T., *Barton, D., Blair, G., Grandmont, F.:* An Imaging Fourier Transform Spectrometer for Remote Nadir Atmospheric Measurements of CO_2, CH_4 and O_2 A-band (In preparation)

Projects

YUiFTS (YorkU Imaging Fourier Transform Spectrometer) **2016-2018**

- Systems, mechanical, optical and electric engineer in the design and development of an Imaging Fourier Transform Spectrometer for nadir atmospheric measurements of CO_2, CH_4 and O_2

Balloon Payload Design **2015**

- Systems, mechanical and optical engineer in the payload design for atmospheric measurements with the use of an Image Stabilization Pointing System platform

Image Stabilization Pointing System (ISPS) **2013-2014**

- Mechanical and Systems Engineer in the design and development of ISPS for use along with YUiFTS to make nadir atmospheric measurements

Field work in the Arctic to measure Ozone **2014-2015-2016**

- Operations, repair and conducting intensive measurements of Ozone using 3 different spectrometers (Brewer, SPS-G and MAESTRO) mounted on sun trackers at the PEARL laboratory at Eureka weather station in the Canadian high Arctic for the spring Ozone validation campaign for the SCISAT Canadian satellite mission.

Selected Oral Presentations

Conference	**EGU (European Geoscience Union) General Assembly**	**AGU (American Geoscience Union) Fall Meeting**
Presentation Title	A New Calibration Procedure Which Accounts for Non-linearity in Single-monochromator Brewer Ozone Spectrophotometers.	Balloon Demonstrator Imaging Fourier Transform Spectrometer for the Measurement of Methane and Carbon Dioxide over the Arctic
Date and place	27/4/2014-2/5/2014, Vienna, Austria	15-19/12/2014, San Francisco, USA
Website	http://www.egu2014.eu/	http://fallmeeting.agu.org/2014/
Conference	**ArcticNet**	**CMOS**
Presentation Title	Measurements of O3 from the SunPhotoSpectrometer (SPS) in Eureka	An Imaging Fourier Transform Spectrometer and pointing system for Nadir Atmospheric Measurements from a Balloon or Satellite Platform
Date and place	7-11/12/2015	8/6/2017
Website	http://www.arcticnetmeetings.ca/asm2015/	http://www.cmos.ca

Personal skills and competences

Awards

- First place at the Space Vision and Advanced Robotics (SVAR) Workshop at MDA (MacDonald, Dettwiler and Associations) corporation **16/6/2016**

Language skills

- English (Full Proficiency)
- Farsi (Native language)
- Other: French (Elementary), German (Elementary)

Technical skills

- Systems Engineering in several space related projects.
- Mechanical workshop training; Machining complex parts using Milling and Lathe machines
- Electronic laboratory training; Designing, soldering and troubleshooting circuits
- Operating optical instruments and parts; telescopes, spectrometers
- Excellent laboratory skills; operating signal generators, oscilloscopes, optics and electronics
- Fast and professional learning skills

Computer skills

- Software: CATIA, SIMION, Zemax
- Programming: MATLAB, Python, familiar with C++ and Perl
- Other: Microsoft Office

Social skills

- Creative and a very quick learner
- Motivated and enthusiastic
- Excellent communications skills and ability to adapt to multicultural environments
- Excellent team player
- Significant experience in project and team management

Hobbies

- Piano
- Jewellery Making
- Painting
- Hiking

M. Appendix

List of Software used throughout thesis:

Stray Light Analysis (Chapter 3)

```
clear all;
clc;

fileslist = dir('./009/logs*.009');
for fname=1:1%numel(fileslist)
  %measurements taken every 00:03:20
  RE=6371;
  o3ht=22;
  airht=8;
  alpha=0.33779;%009
  %alpha=0.33919;%119
  display( fileslist(fname).name );
  filename = sprintf('./009/%s',fileslist(fname).name);
  Dataf=importfile(filename,' ',1);
  Nobs=length(Dataf);
  xo3=Dataf(:,9);
  Outlier=0;
  out=1;
  for nn =1: Nobs
      if xo3(nn,1)<130
          Outlier(out)=nn;
          out=out+1;
      end
  end
  if Outlier~=0
      for jj=length(Outlier):-1:1
           Dataf(Outlier(jj),:)=[];
      end
  end
  Nobs=length(Dataf);
  mu=Dataf(:,5);
  %L0 to L5 =L
  L=[Dataf(:,11), Dataf(:,12), Dataf(:,13), Dataf(:,14), Dataf(:,15),
Dataf(:,16)];
  for j=1:Nobs
     F(j,1)=([0.0, -1.0, 0.5, 2.2, -1.7]*(L(j,2:6))');
     Fmu(j,1)=F(j,1)*mu(j,1);
  end
  P=mu;
  ND=Dataf(:,7);
  xo3=Dataf(:,9);
  s=1;
  for q = 1:Nobs
    if mu(q,1) <=2
        x(s,1)=mu(q,1);
        y(s,1)=F(q,1);
```

```
        s=s+1;
    end
  end
  %-------------------------------------------------------------
  A=length(y);
  B=sum(x);
  C=sum(x);
  for r=1:length(x)
      Din(1,r)=x(r,1)^2;
      vin(1,r)=x(r,1)*y(r,1);
  end
  D=sum(Din);
  u=sum(y);
  v=sum(vin);
  a1=(v-C*inv(A)*u)./(D-C*inv(A)*B);
  a0=(u-B*a1)*inv(A);
  %plot-------------------------------------------------------
  figure;%linear model
  plot(mu,F,'.r');%data
  hold on;
  x=0:0.1:12;
  ym=a0+a1*x;
  plot(x,ym);%linear model
  xlabel('Ozone airmass', 'fontsize', 18);
  ylabel('Absorption Func.', 'fontsize', 18);
  hleg1=legend('Data','Linear model');
  set(hleg1,'fontsize',14)
  set(hleg1,'Location','SouthEast')
  text(1,12000,['Data File:',sscanf(filename,'%s')],'fontsize',14)
  text(1,11000,['F0=',num2str(a0)],'fontsize',14)
  %-------------------------------------------------------------
  %First I will apply the model without the filter change to detect outlies
  %which are the points where the difference between model and data peaks.
  F0(1,1)=a0;
  gamma(1,1)=1e-7;
  xo(1,1)=200;
  maxiter=50;
  for iter=1:maxiter
    for i=1:Nobs
        Fm(i,1)=alpha*10*(((mu(i,1))^2)*xo(iter,1)-gamma(iter,1)*(((mu(i,1)-
1)*xo(iter,1))^3)*P(i,1))+F0(iter,1)*P(i,1);
        deltaf(i,1)=(Fmu(i,1)-Fm(i,1))/Fmu(i,1);
    end
    for i=1:Nobs
        dsdgamma(i,1)=-alpha*10*(((mu(i,1)-1)*xo(iter,1))^3)*P(i,1);
        dsdF0(i,1)=P(i,1);
        dsdx(i,1)=alpha*10*(((mu(i,1))^2)-3*gamma(iter,1)*((mu(i,1)-
1)*((mu(i,1)-1)*xo(iter,1))^2)*P(i,1));
        M(i,1)=dsdgamma(i,1)*gamma(iter,1)/Fm(i,1);
        M(i,2)=dsdF0(i,1)*F0(iter,1)/Fm(i,1);
        M(i,3)=dsdx(i,1)*xo(iter,1)/Fm(i,1);
    end
    for m=1:3
        for n=1:3
            for i=1:Nobs
                Ktemp(m,n,i)=M(i,n)*M(i,m);
                Htemp(i,m)=deltaf(i,1)*M(i,m);
```

```
            end
            K(m,n,iter)=sum(Ktemp(m,n,:));
        end
        H(m,iter)=sum(Htemp(:,m));
    end
    deltav(iter,1:3)=inv(K(:,:,iter))*H(:,iter);
    gamma(iter+1,1)=gamma(iter,1)*(1+deltav(iter,1));
    F0(iter+1,1)=F0(iter,1)*(1+deltav(iter,2));
    xo(iter+1,1)=xo(iter,1)*(1+deltav(iter,3));
end
gammaf=gamma(maxiter,1);
F0f=F0(maxiter,1);
xof=xo(maxiter,1);
for w=1:Nobs
    Fmodel1(w,1)=alpha*10*(mu(w,1)*xof-gammaf*(((mu(w,1)-1)*xof)^3))+F0f;
    Diff1(w,1)=abs(F(w,1)-Fmodel1(w,1));
end

figure;%non lin model
plot(mu,F,'-g.');
hold on;
plot(mu,Fmodel1,'-b*');
hleg1 =legend('Observation','non-lin model');
set(hleg1,'Location','NorthWest')
set(hleg1,'fontsize',14)
xlabel('O3 Airmass', 'fontsize', 18);
ylabel('Absorption Func.', 'fontsize', 18);

Fold=F;
FmodelOld=Fmodel1;
save('Fold.mat','Fold','FmodelOld');
%%reseting the values
Fm=0;
deltaf=0;
dsdgamma=0;
dsdF0=0;
dsdx=0;
F0=0;
gamma=0;
xo=0;
deltav=0;
Ktemp=0;
Htemp=0;
H=0;
K=0;
xo3=0;
mu=0;
ND=0;
x=0;
y=0;
A=0;
B=0;
C=0;
Din=0;
vin=0;
F=0;
```

```
  Fmodel=0;
  Fmu=0;
  P=0;
  %-----------------------------------------------------------------
  %taking out the values with Diff1>85
  Outlier=0;
  out=1;
  for i=1:Nobs
    if Diff1(i,1)> 200
        Outlier(out)=i;
        out=out+1;
    end
  end
  if Outlier~=0
      for j=length(Outlier):-1:1
          Dataf(Outlier(j),:)=[];
      end
  end
  %-----------------------------------------------------------------
  Nobs=length(Dataf);
  mu=Dataf(:,5);
  %L0 to L5 =L
  L=[Dataf(:,11), Dataf(:,12), Dataf(:,13), Dataf(:,14), Dataf(:,15),
Dataf(:,16)];
  for i=1:Nobs
     F(i,1)=([0.0, -1.0, 0.5, 2.2, -1.7]*(L(i,2:6))');
     for cc=1:5
       Ppcount(i,cc)=(10^(L(i,cc)/10000));
     end
  end
  for i=1:Nobs
      Pcount(i,1)=sqrt(([0.0, -1.0, 0.5, 2.2, -1.7]*(Ppcount(i,:))')^2);
      Fmu(i,1)=F(i,1)*mu(i,1)/Pcount(i,1);
  end
  P=mu;
  ND=Dataf(:,7);
  xo3=Dataf(:,9);
  s=1;
  for q = 1:Nobs
    if mu(q,1) <=2
        x(s,1)=mu(q,1);
        y(s,1)=F(q,1);
        s=s+1;
    end
  end
  A=length(y);
  B=sum(x);
  C=sum(x);
  for r=1:length(x)
      Din(1,r)=x(r,1)^2;
      vin(1,r)=x(r,1)*y(r,1);
  end
  D=sum(Din);
  u=sum(y);
  v=sum(vin);
  a1=(v-C*inv(A)*u)./(D-C*inv(A)*B);
  a0=(u-B*a1)*inv(A);
```

```
  %----------- Filter change factor ----------------------------------
  Vind=zeros(7,Nobs);
  for i=1:Nobs
    if ND(i)==1
        Vind(ND(i),i)=1;
    end
    if ND(i)==2
        Vind(ND(i),i)=1;
    end
    if ND(i)==3
        Vind(ND(i),i)=1;
    end
    if ND(i)==4
        Vind(ND(i),i)=1;
    end
    if ND(i)==5
        Vind(ND(i),i)=1;
    end
    if ND(i)==6
        Vind(ND(i),i)=1;
    end
    if ND(i)==7
        Vind(ND(i),i)=1;
    end
  end
  [mV,nV]=size(Vind);
  for vv=mV:-1:1
      if Vind(vv,:)==0
          Vind(vv,:)=[];
      end
  end
  [mV,nV]=size(Vind);
  %-----------------------------------------------------------
  F0(1,1)=a0;
  gamma(1,1)=1e-100;
  xo(1,1)=200;
  maxiter=50;
  b((1:mV),1)=1e-100;
  %-----------------------------------------------------------
  for iter=1:maxiter
    for i=1:Nobs
        Fm(i,1)=(alpha*10*(((mu(i,1))^2)*xo(iter,1)-gamma(iter,1)*(((mu(i,1)-
1)*xo(iter,1))^3)*P(i,1))+F0(iter,1)*P(i,1))/Pcount(i,1);
        for j=1:mV
            Fm(i,1)=Fm(i,1)+b(j,iter)*Vind(j,i)*P(i,1)/Pcount(i,1);
        end
        deltaf(i,iter)=(Fmu(i,1)-Fm(i,1))/Fmu(i,1);
    end
    for i=1:Nobs
        dsdgamma(i,1)=-alpha*10*(((mu(i,1)-
1)*xo(iter,1))^3)*P(i,1)/Pcount(i,1);
        dsdF0(i,1)=P(i,1)/Pcount(i,1);
        dsdx(i,1)=alpha*10*(((mu(i,1))^2)-3*gamma(iter,1)*((mu(i,1)-
1)*((mu(i,1)-1)*xo(iter,1))^2)*P(i,1))/Pcount(i,1);
        for j=1:mV
            dsdb(j,i)=Vind(j,i)*P(i,1)/Pcount(i,1);
        end
```

```
        M(i,1)=dsdgamma(i,1)*gamma(iter,1)/Fm(i,1);
        M(i,2)=dsdF0(i,1)*F0(iter,1)/Fm(i,1);
        M(i,3)=dsdx(i,1)*xo(iter,1)/Fm(i,1);
        for k=1:mV
            M(i,k+3)=dsdb(k,i)*b(k,iter)/Fm(i,1);
        end
    end
    for m=1:3+mV
        for n=1:3+mV
            for i=1:Nobs
                Ktemp(m,n,i)=M(i,n)*M(i,m);
                Htemp(i,m)=deltaf(i,iter)*M(i,m);
            end
            K(m,n,iter)=sum(Ktemp(m,n,:));
        end
        H(m,iter)=sum(Htemp(:,m));
    end
    deltav(iter,1:(3+mV))=inv(K(:,:,iter))*H(:,iter);
    gamma(iter+1,1)=gamma(iter,1)*(1+deltav(iter,1));
    F0(iter+1,1)=F0(iter,1)*(1+deltav(iter,2));
    xo(iter+1,1)=xo(iter,1)*(1+deltav(iter,3));
    for w=1:mV
        b(w,iter+1)=b(w,iter)*(1+deltav(iter,w+3));
    end
  end
  %-------------------------------------------------------------
  gammaf=gamma(maxiter,1);
  F0f=F0(maxiter,1);
  xof=xo(maxiter,1);
  for ff=1:mV
      bf(ff)=b(ff,maxiter);
  end
  for mm=1:Nobs
      Fmodel(mm,1)=alpha*10*(mu(mm,1)*xof-gammaf*(((mu(mm,1)-1)*xof)^3))+F0f;
      for j=1:mV
              Fmodel(mm,1)=Fmodel(mm,1)+bf(j)*Vind(j,mm);
      end
      %Diff2(mm,1)=FOVERmu(mm,1)-Fmodel(mm,1);
  end
  %-------------------------------------------------------------
  figure;%non linear model
  plot(mu,F,'-r.');
  hold on;
  plot(mu,Fmodel,'-b*');
  hleg2 =legend('Observation','Non-lin Model + Filter');
  set(hleg2,'Location','NorthWest')
  set(hleg2,'fontsize',14)
  xlabel('Ozone Airmass', 'fontsize', 14);
  ylabel('Absorption Func.', 'fontsize', 14);
  text(3.5,5000,['Data File:',sscanf(filename,'%s')],'fontsize',14)
  text(3.5,4700,['Non-lin Factor=',num2str(gammaf)],'fontsize',14)
  text(3.5,4400,['Ozone amount=',num2str(xof)],'fontsize',14)
  text(3.5,4100,['F0=',num2str(F0f)],'fontsize',14)
  %-------------------------------------------------------------
end
```

IFTS Data Analysis (Chapter 4)

```
clear all;
clc;
%Import the Data
data = importdata('D:\Dropbox\PhD\IFTS_data\06092019\4.csv');

for i=1:length(data)
    data(i,2)=i;
end
point = data(:,2);  %data point number in the interferogram
Ilength = length(point);
Iunnorm = (data(:,1)-mean(data(:,1)));  %subtract dc level
Inorm = Iunnorm./max(Iunnorm); %normalize
Iint = Inorm;
%% plot interferogram
figure;
plot(point,Iint);
xlabel('Data points');
ylabel('Intensity');
title('Interferogram ');
%% find ZPD
[ZPD, ZPDpos] = max(abs(Iint));

%% make Apodization function
after = Ilength - ZPDpos;
if after >= ZPDpos
    apodend = ZPDpos +( ZPDpos-1);
    apodstart = 1;
else
    apodend = ZPDpos + after;%
    apodstart = ZPDpos - after;
end
apodlength = apodend - apodstart +1;
%% Triangular apodization
for k = 1:length(Iint)
    if point(k)<= apodstart
        apodfunc(k)=0;
    end
    if point(k)>apodstart && point(k)<ZPDpos
        apodfunc(k)=(1/(ZPDpos-apodstart))*(point(k)-apodstart);
    end
    if point(k)==ZPDpos
        apodfunc(k)=1;
    end
    if point(k)>ZPDpos && point(k)<apodend
        apodfunc(k)=(-1/(apodend-ZPDpos))*(point(k)-apodend);
    end
    if point(k)>=apodend
        apodfunc(k)=0;
    end
end

%% cos squared apodization
for kk = 1:length(Iint)
```

```
    if point(kk)<= apodstart
        apodfunc(kk)=0;
    end
    if point(kk)>apodstart && point(kk)<ZPDpos
        apodfunc(kk)=(cos(-(pi/2)*(ZPDpos-point(kk))/(apodlength/2)))^2;
    end
    if point(kk)==ZPDpos
        apodfunc(kk)=1;
    end
    if point(kk)>ZPDpos && point(kk)<apodend
        apodfunc(kk)=(cos((pi/2)*(point(kk)-ZPDpos)/(apodlength/2)))^2;
    end
    if point(kk)>=apodend
        apodfunc(kk)=0;
    end
end

%% apodize the interferogram
Iapod = Iint.*apodfunc';

%Rotate it so the centerburst is at zero
Iapodrot = [Iapod((ZPDpos+1):end);Iapod(1:ZPDpos)];

figure;
plot(point,Iapodrot);
xlabel('Data points');
ylabel('Intensity');
title('Apodized Rotated Interferogram ');
%% Fourier transform of interferogram
spectra = fft(Iapodrot);   %fft of the rotated and apodized interferogram to
get a spectrum

%Create frequency axis
frequency = 1/(length(point)*6.32816*10^(-5));    %631.5 nm is the wavelength
of the metrology laser. double sampled.
wavenumber = (1:length(point)).*frequency;
wavenumber = wavenumber';     %x-axis (wavenumber) of the transformed
spectrum

%spectra Real and Imaginary parts
for ss=1:length(spectra)
    spectrareal(ss) = real(spectra(ss));
    spectraimage(ss) = imag(spectra(ss));
    magspectra(ss) = sqrt((spectrareal(ss))^2+(spectraimage(ss))^2);
%magnitude spectra
end
%magnitude spectra
magspectra=magspectra(1:length(spectra)/2);
wavenumber=wavenumber(1:length(spectra)/2);
%% find max peak and FWHM
[maxpeak , maxpeakpos] = max(magspectra(30:length(magspectra)));
halfmax = 0.5*maxpeak;
maxpeakwavenumber = wavenumber(maxpeakpos);
%%
%Plot spectrum
figure;
```

```
plot(wavenumber(30:length(wavenumber)),magspectra(30:length(magspectra)));
xlabel('Wavenumber [cm^{-1}]');
ylabel('Intensity [arb units]');
title('Spectrum ');
%%
figure;
plot(wavenumber(maxpeakpos-1000:maxpeakpos+1000),magspectra(maxpeakpos-
1000:maxpeakpos+1000)); %for IR laser
% plot(wavenumber(maxpeakpos-300:length(wavenumber)),magspectra(maxpeakpos-
300:length(magspectra)));%for red laser
xlabel('Wavenumber [cm^{-1}]');
ylabel('Intensity [arb units]');
title('Spectrum zoomed in');
hold on;
xline(maxpeakwavenumber,'r',maxpeakwavenumber);

%% determine phase
phase = atan2(spectraimage, spectrareal);

figure;
plot(wavenumber,phase);
xlabel('Wavenumber [cm\^-1]');
ylabel('Phase');
title('Phase curve of spectrum ');

%Phase correction
phasecos = cos(phase);
phasesin = sin(phase);

%Phase correct
spectrarealcor = spectrareal.*phasecos;
spectraimagecor = spectraimage.*phasesin;
spectraphasecor = spectrarealcor + spectraimagecor;     %spectrum with phase
correction

figure;
plot(wavenumber,spectraphasecor);
xlabel('Wavenumber [cm-1]');
ylabel('Intensity [arb units]');
title('Spectrum with phase correction');
figure;
plot(wavenumber(32500:33000),spectraphasecor(32500:33000));
xlabel('Wavenumber [cm-1]');
ylabel('Intensity [arb units]');
title('Spectrum with phase correction zoomed in');
```

Filter Analysis (Chapter 4)

```
clear all;
clc;
%% Manufactureres filter data

manufac = importdata('D:\Dropbox\PhD\GGGGG\filter\filter.csv');
wavenumfac = manufac.data(:,3);
```

```
filternumfac = manufac.data(:,2);
[maxpeakfilter , maxpeakposfilter] = max(filternumfac);
maxpeakwavenumberfilter = wavenumfac(maxpeakposfilter);
%% Import the IFTS Data

data = importdata('D:\Dropbox\PhD\IFTS_data\06092019\4.csv');

for i=1:length(data)
    data(i,2)=i;

end
point = data(:,2);  %data point number in the interferogram
Ilength = length(point);
Iunnorm = (data(:,1)-mean(data(:,1)));  %subtract dc level
Inorm = Iunnorm./max(Iunnorm); %normalize interferogram
Iint = Inorm;

%% find ZPD
[ZPD, ZPDpos] = max(abs(Iint));

%% make Apodization function

after = Ilength - ZPDpos;
if after >= ZPDpos
    apodend = ZPDpos +( ZPDpos-1);
    apodstart = 1;
else
    apodend = ZPDpos + after;%
    apodstart = ZPDpos - after;
end
apodlength = apodend - apodstart +1;

%% cos squared apodization

for kk = 1:length(Iint)
    if point(kk)<= apodstart
        apodfunc(kk)=0;
    end
    if point(kk)>apodstart && point(kk)<ZPDpos
        apodfunc(kk)=(cos(-(pi/2)*(ZPDpos-point(kk))/(apodlength/2)))^2;
    end
    if point(kk)==ZPDpos
        apodfunc(kk)=1;
    end
    if point(kk)>ZPDpos && point(kk)<apodend
        apodfunc(kk)=(cos((pi/2)*(point(kk)-ZPDpos)/(apodlength/2)))^2;
    end
    if point(kk)>=apodend
        apodfunc(kk)=0;
    end
end

Iapod = Iint.*apodfunc';

%Rotate it so the centerburst is at zero
```

```
Iapodrot = [Iapod((ZPDpos+1):end);Iapod(1:ZPDpos)];
spectra = fft(Iapodrot);
%Create frequency axis
frequency = 1/(length(point)*0.5*6.32816*10^(-5));    %631.5 nm is the
wavelength of the metrology laser. double sampled.
wavenumber = (1:length(point)).*frequency;
wavenumber = wavenumber';     %x-axis (wavenumber) of the transformed
spectrum

%spectra Real and Imaginary parts
for ss=1:length(spectra)
    spectrareal(ss) = real(spectra(ss));
    spectraimage(ss) = imag(spectra(ss));
    magspectra(ss) = sqrt((spectrareal(ss))^2+(spectraimage(ss))^2);
%magnitude spectra

end

magspectra=magspectra(1:length(spectra)/2);
normmagspectra=magspectra./max(magspectra(30:length(magspectra)));
wavenumber=wavenumber(1:length(spectra)/2);
%% find max peak and FWHM
[maxpeak , maxpeakpos] = max(magspectra(30:length(magspectra)));
halfmax = 0.5*maxpeak;
maxpeakwavenumber = wavenumber(maxpeakpos);

%% fit line to IFTS data

x=wavenumber(maxpeakpos-200:maxpeakpos+325);
y=normmagspectra(maxpeakpos-200:maxpeakpos+325)';
p=polyfit(x,y,6);
line=polyval(p,x);
%%
figure;
plot(x,y,'b');
hold on;
plot(x,line,'r');
legend('IFTS spectrum','Line of best fit');
xlabel('Wavenumber [cm^{-1}]');
ylabel('Normalized Intensity');
%% mean square error
for i= 1:length(x)
    Noise(i)=(y(i)-line(i));
    SNR(i)=(y(i))/(Noise(i));
end
SNR=sqrt((1/length(x))*sum(SNR));
```

N. Appendix

CAD drawings of the IFTS and ISPS parts are attached.

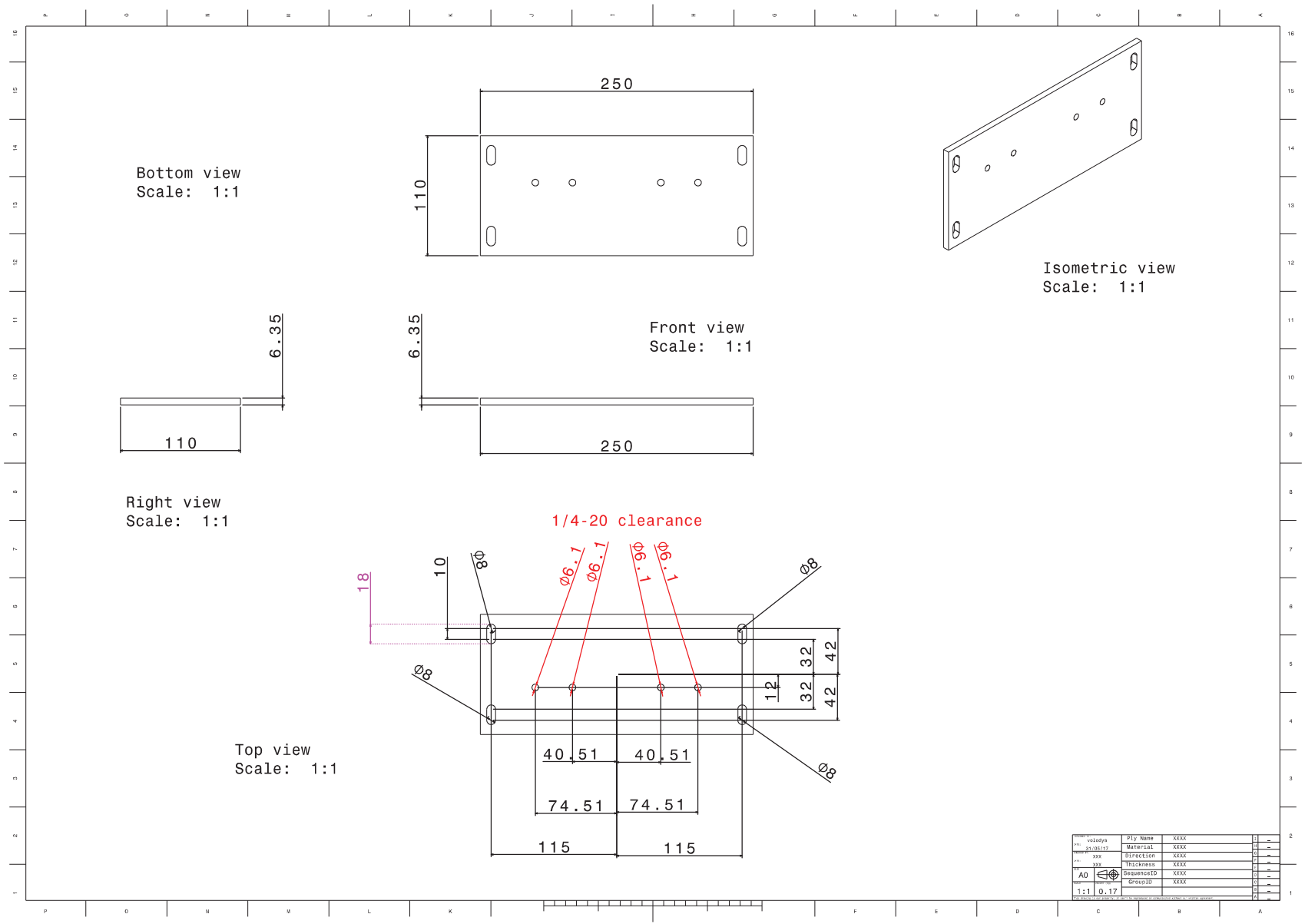
Bottom view
Scale: 1:1
250
110
Isometric view
Scale: 1:1
6.35
110
Right view
Scale: 1:1
6.35
250
Front view
Scale: 1:1
1/4-20 clearance
18
10
8Φ
Ø6.1
Ø6.1
Ø6.1
Ø6.1
Ø8
Ø8
Ø8
12
32
32
42
42
40.51
40.51
74.51
74.51
115
115
Top view
Scale: 1:1
voiodys
31/05/17
XXX
XXX
A0
1:1
0.17
Ply Name XXXX
Material XXXX
Direction XXXX
Thickness XXXX
SequenceID XXXX
GroupID XXXX

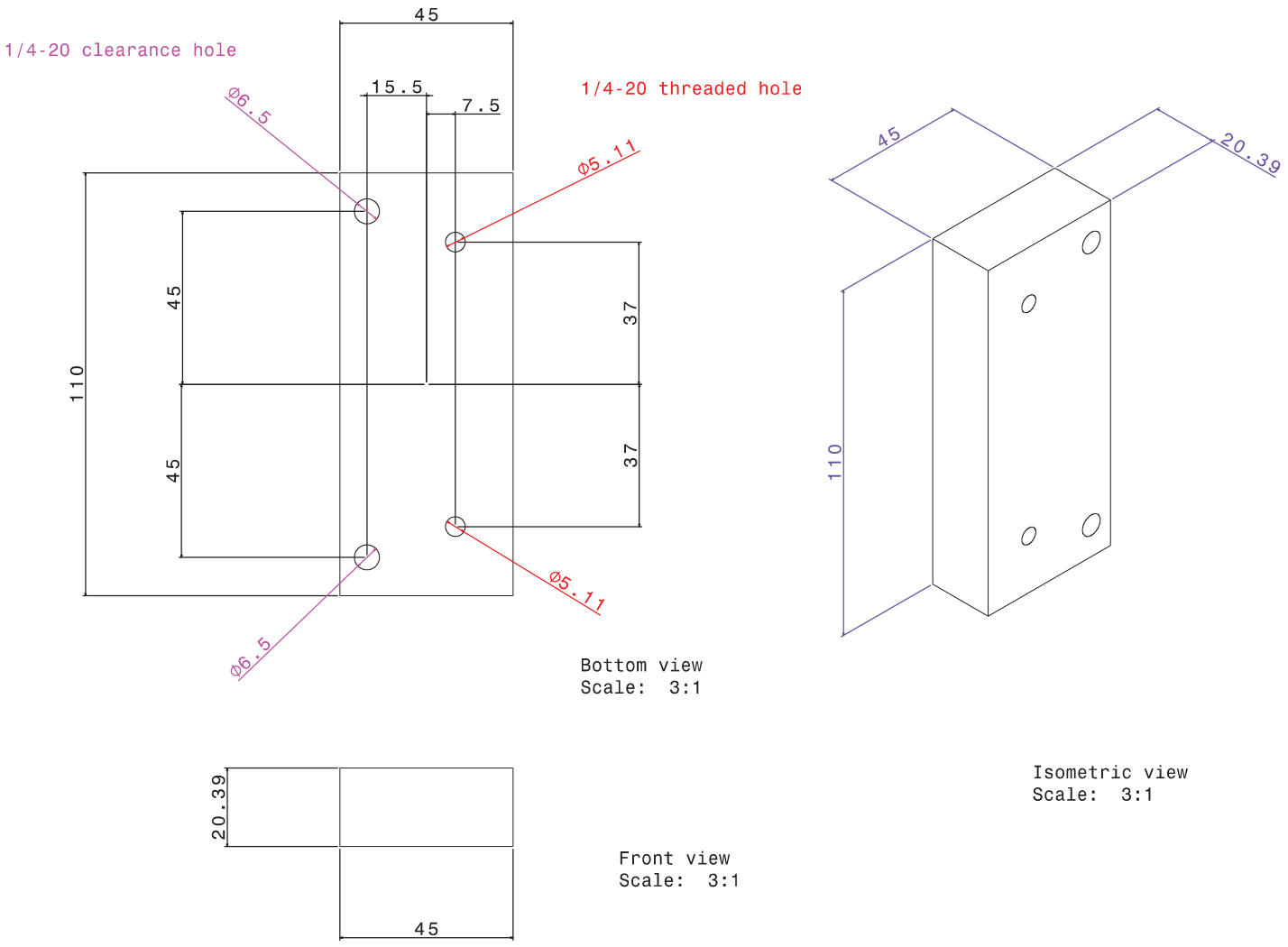
1/4-20 clearance hole
1/4-20 threaded hole
45
15.5
7.5
Ø6.5
Ø5.11
45
37
110
45
37
Ø5.11
Ø6.5
Bottom view
Scale: 3:1
45
20.39
110
Isometric view
Scale: 3:1
20.39
45
Front view
Scale: 3:1

0.5 inch thick plate

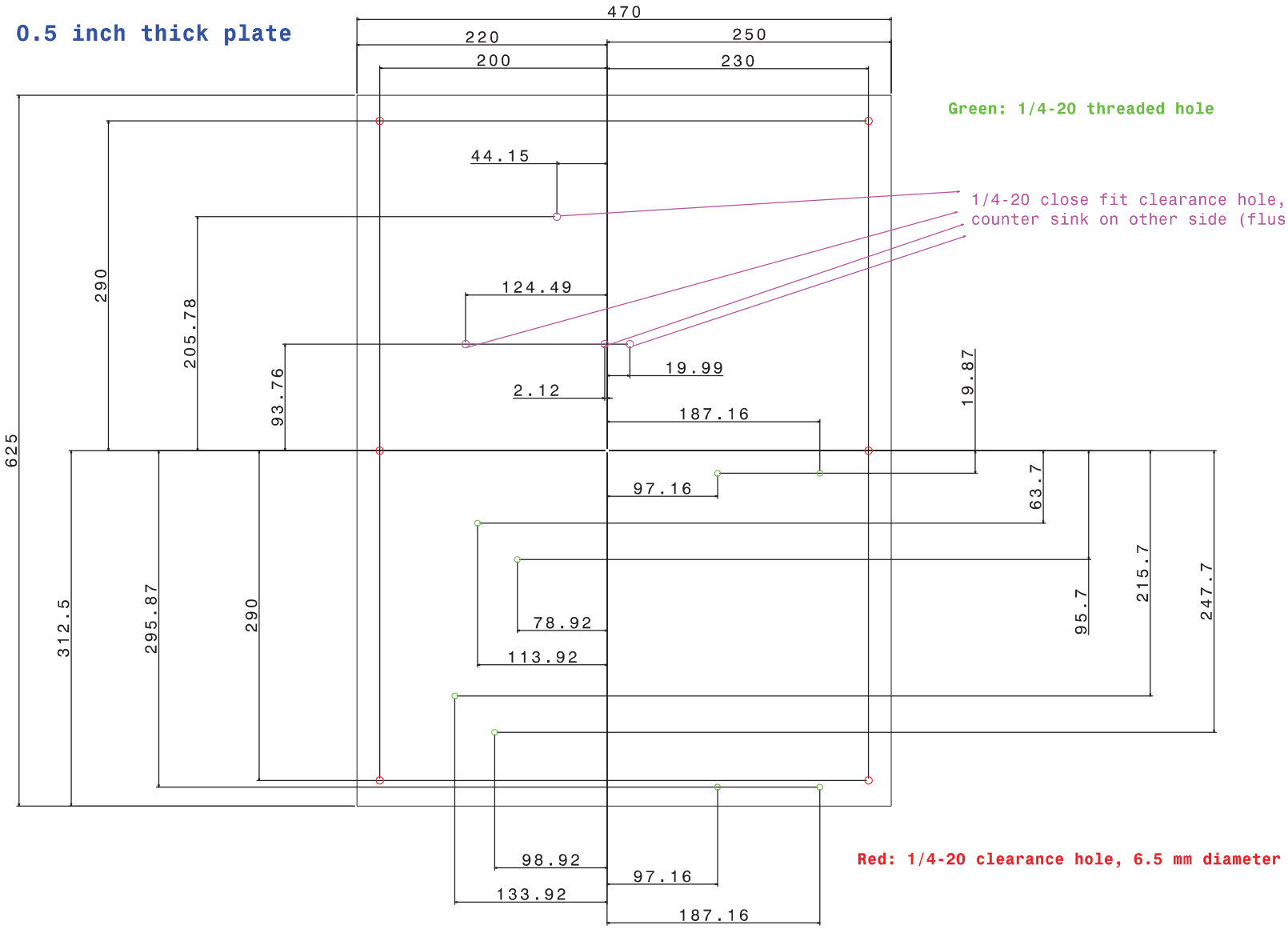

Green: 1/4-20 threaded hole

1/4-20 close fit clearance hole,
counter sink on other side (flush)

Red: 1/4-20 clearance hole, 6.5 mm diameter

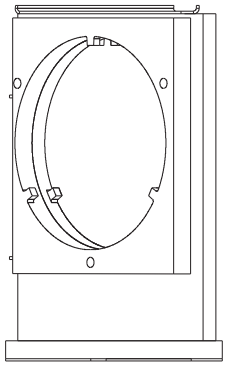

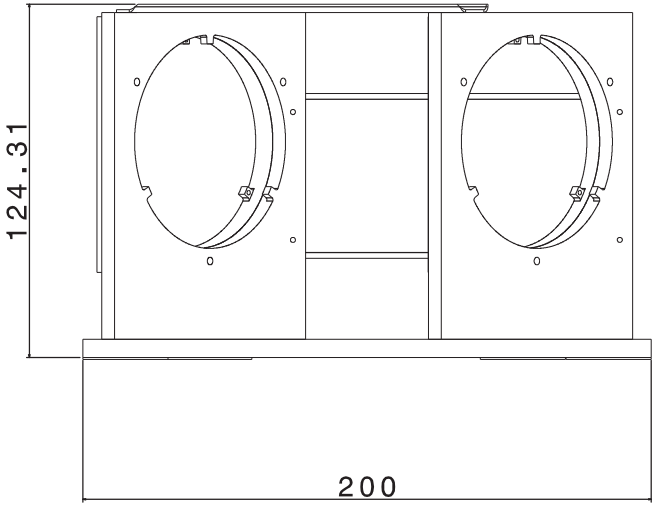

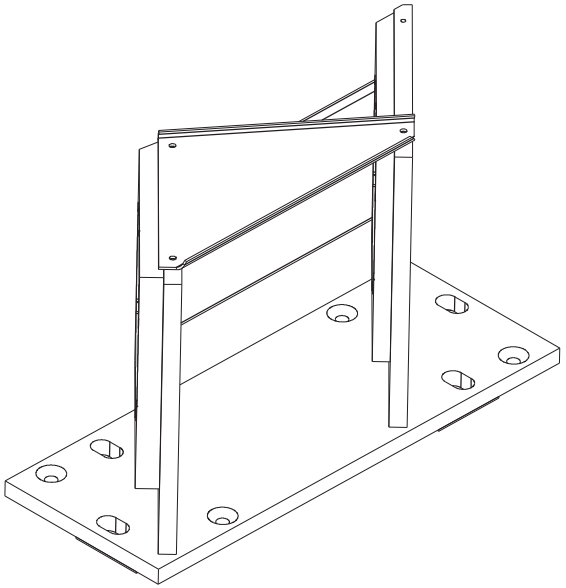

Isometric view
Scale: 2:1

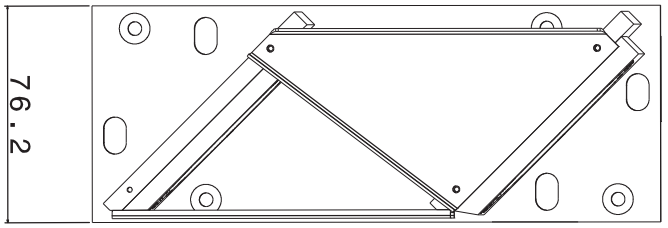

Front view
Scale: 2:1

1mm thick Al sheet metal

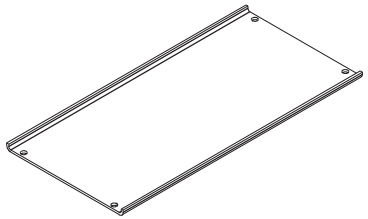

Isometric view
Scale: 2:1

Bottom view
Scale: 2:1

2-56 clearance holes

Right view
Scale: 2:1

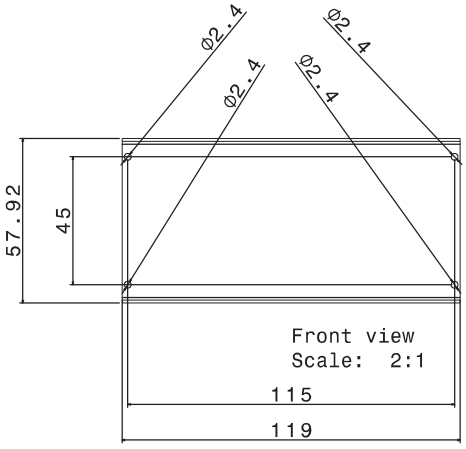

Front view
Scale: 2:1

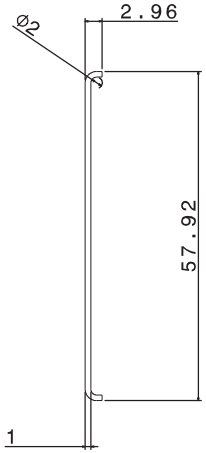

Left view
Scale: 4:1

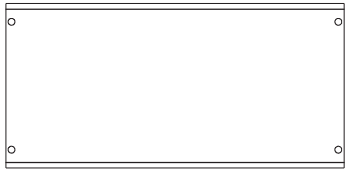

Rear view
Scale: 2:1

Top view
Scale: 2:1

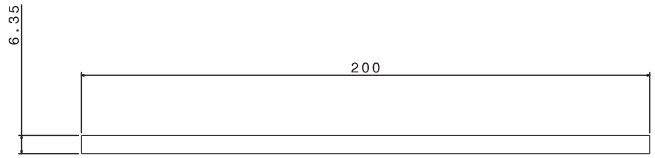

Bottom view
Scale: 2:1

Section view B-B
Scale: 2:1

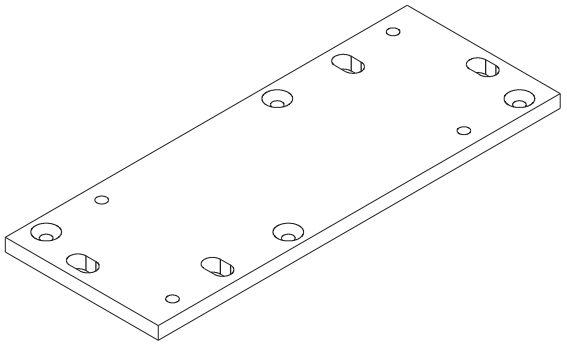

Isometric view
Scale: 2:1

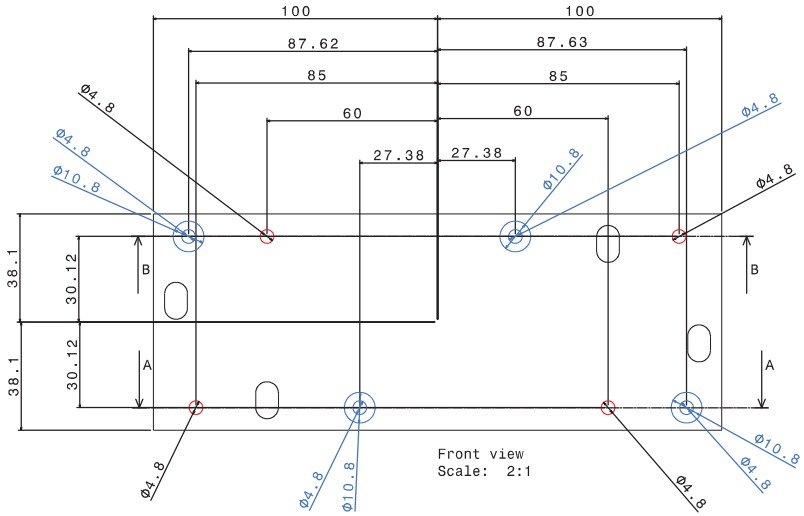

Front view
Scale: 2:1

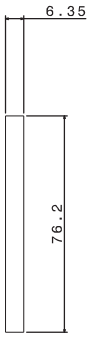

Left view
Scale: 2:1

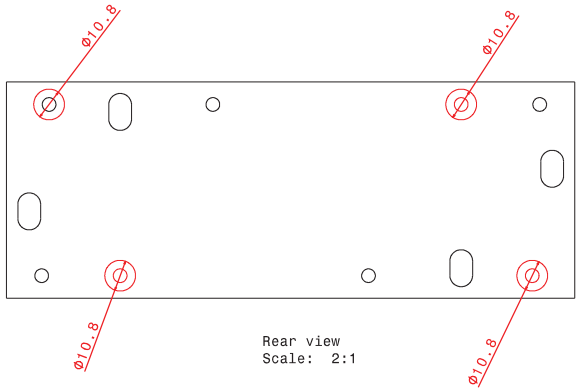

Rear view
Scale: 2:1

10-32 clearance hole
countersinc 82 degrees

10-32 clearance hole
countersinc 82 degrees

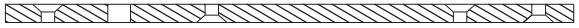

Section view A-A
Scale: 2:1

countersinc on opposite sides.
THE SIDES MUST BE EXACTLY AS SHOWN

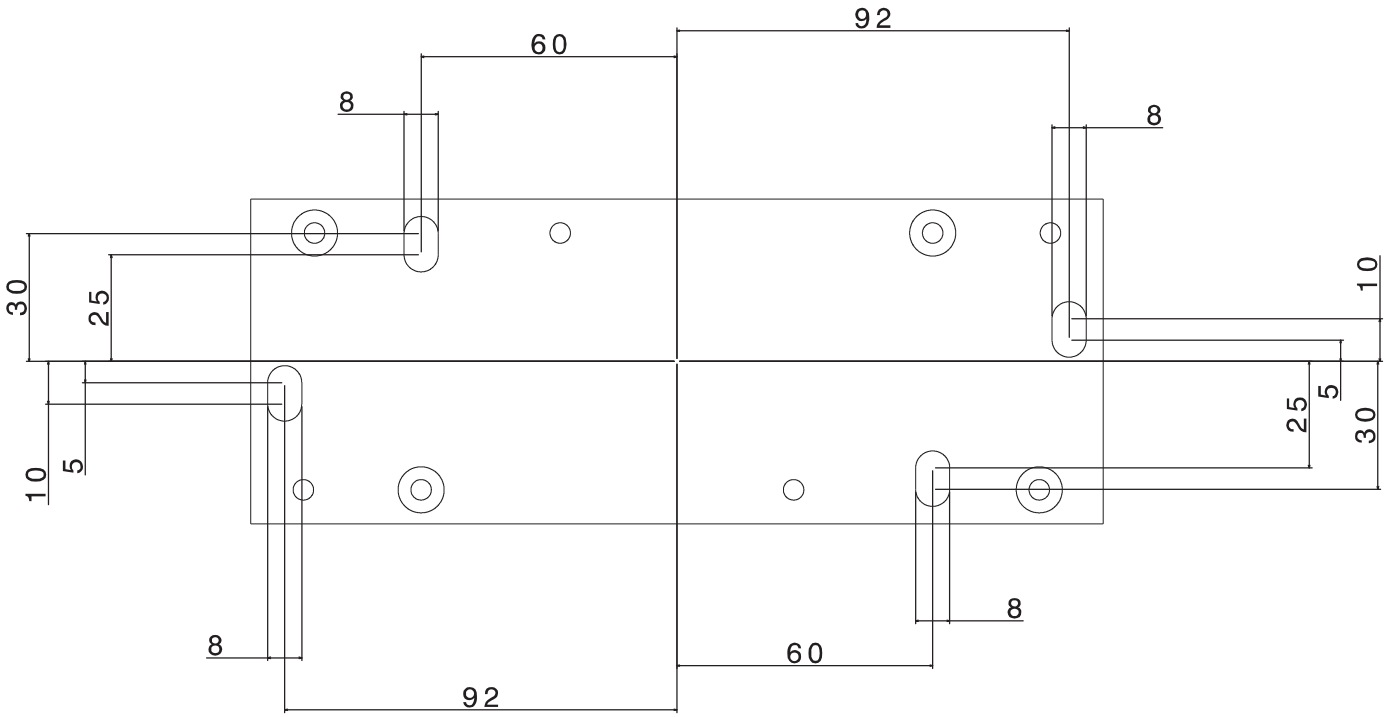

Rear view
Scale: 3:1

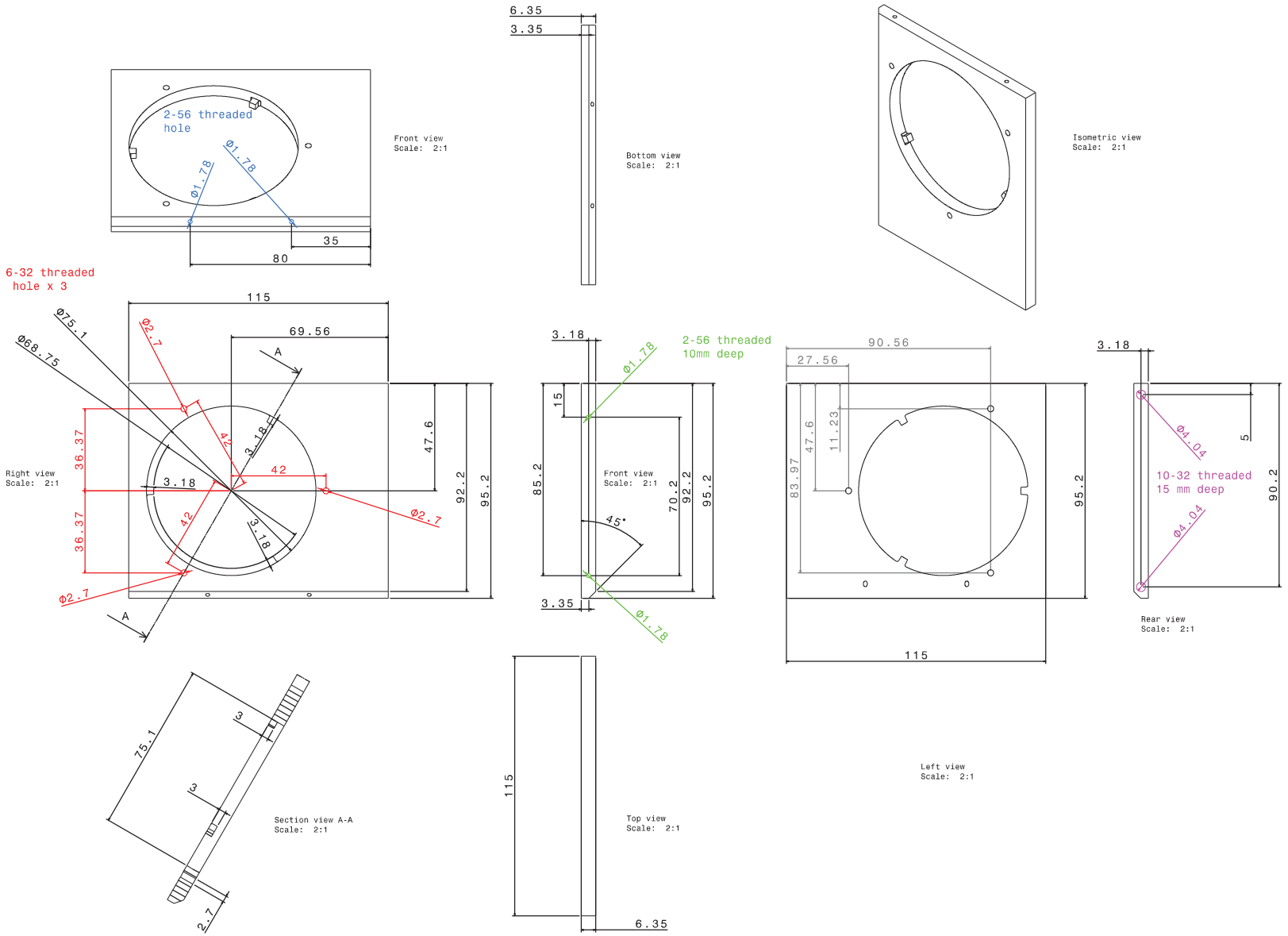
2-56 threaded hole
Ø1.78
Ø1.78
35
80
Front view
Scale: 2:1
6.35
3.35
Bottom view
Scale: 2:1
Isometric view
Scale: 2:1
6-32 threaded hole x 3
115
69.56
Ø75.1
Ø68.75
Ø2.7
A
47.6
92.2
95.2
36.37
36.37
3.18
42
42
3.18
3.18
Ø2.7
Ø2.7
A
Right view
Scale: 2:1
3.18
Ø1.78
2-56 threaded
10mm deep
15
85.2
70.2
92.2
95.2
45°
3.35
Ø1.78
Front view
Scale: 2:1
90.56
27.56
83.97
47.6
11.23
95.2
115
Left view
Scale: 2:1
3.18
Ø4.04
5
10-32 threaded
15 mm deep
Ø4.04
90.2
Rear view
Scale: 2:1
75.1
3
3
2.7
Section view A-A
Scale: 2:1
115
6.35
Top view
Scale: 2:1

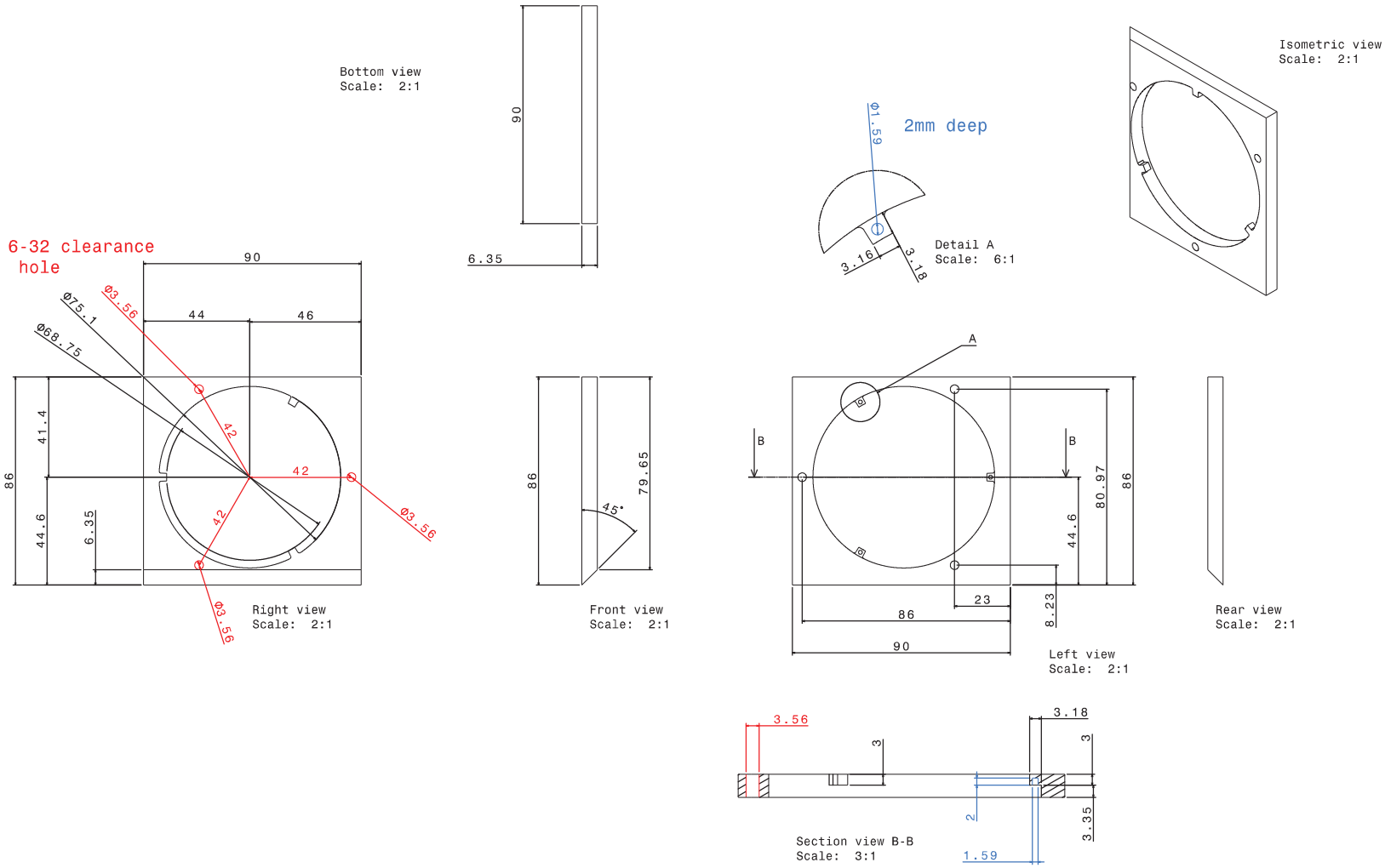
Bottom view
Scale: 2:1
90
6.35
Ø1.59
2mm deep
3.16
3.18
Detail A
Scale: 6:1
Isometric view
Scale: 2:1
6-32 clearance
hole
90
44
46
Ø3.56
Ø75.1
Ø68.75
41.4
86
44.6
6.35
42
42
42
Ø3.56
Ø3.56
Right view
Scale: 2:1
86
79.65
45°
Front view
Scale: 2:1
A
B
B
80.97
86
44.6
23
8.23
86
90
Left view
Scale: 2:1
Rear view
Scale: 2:1
3.56
3
3.18
3
2
3.35
1.59
Section view B-B
Scale: 3:1

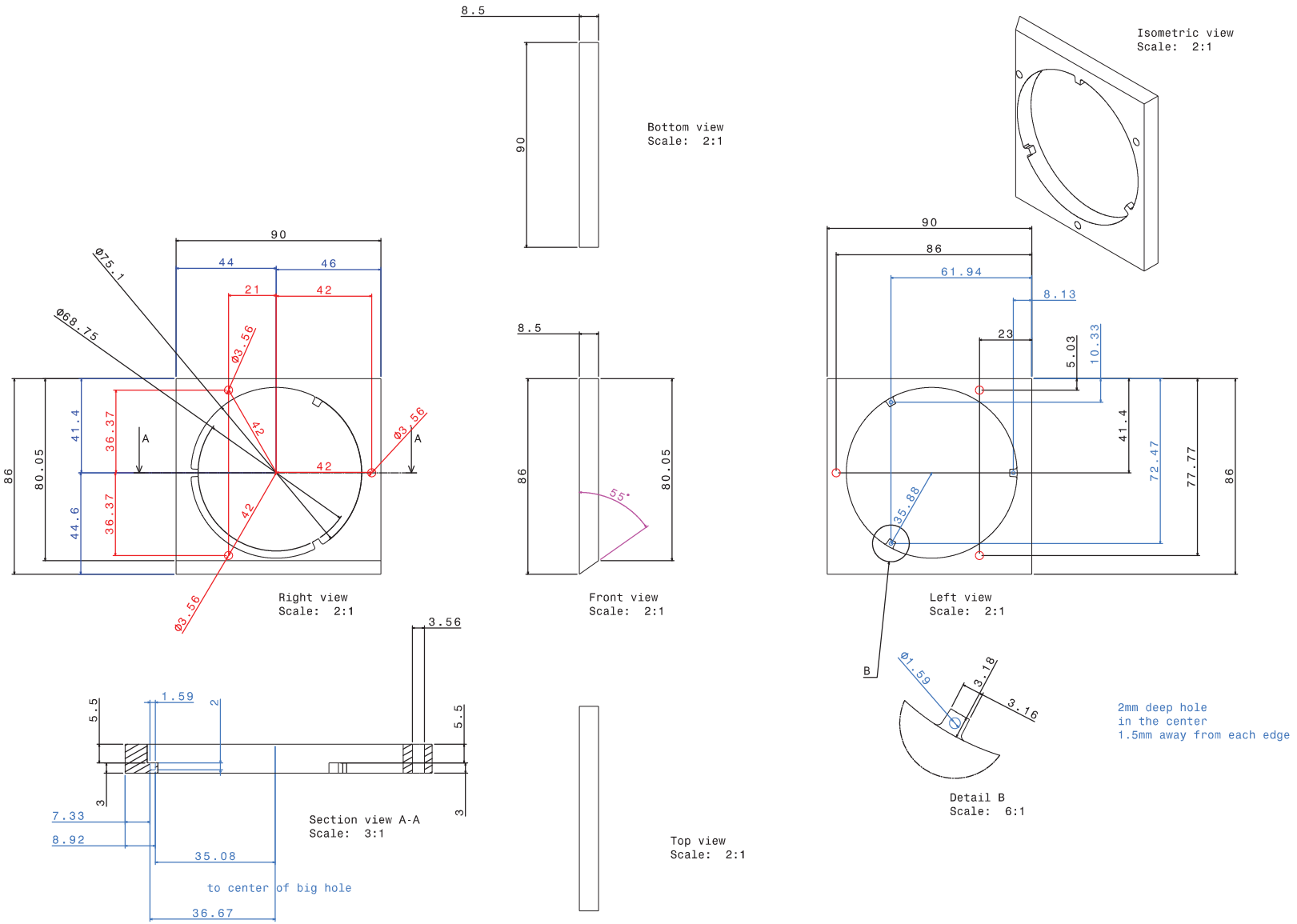
8.5
90
Bottom view
Scale: 2:1
Isometric view
Scale: 2:1
90
44
46
21
42
Ø75.1
Ø68.75
Ø3.56
42
Ø3.56
A
A
42
42
Ø3.56
86
80.05
41.4
36.37
44.6
36.37
Right view
Scale: 2:1
8.5
86
80.05
55°
Front view
Scale: 2:1
90
86
61.94
8.13
23
5.03
10.33
41.4
72.47
77.77
86
35.88
Left view
Scale: 2:1
B
Ø1.59
3.18
3.16
Detail B
Scale: 6:1
2mm deep hole
in the center
1.5mm away from each edge
3.56
5.5
1.59
2
5.5
3
3
7.33
8.92
35.08
to center of big hole
36.67
Section view A-A
Scale: 3:1
Top view
Scale: 2:1

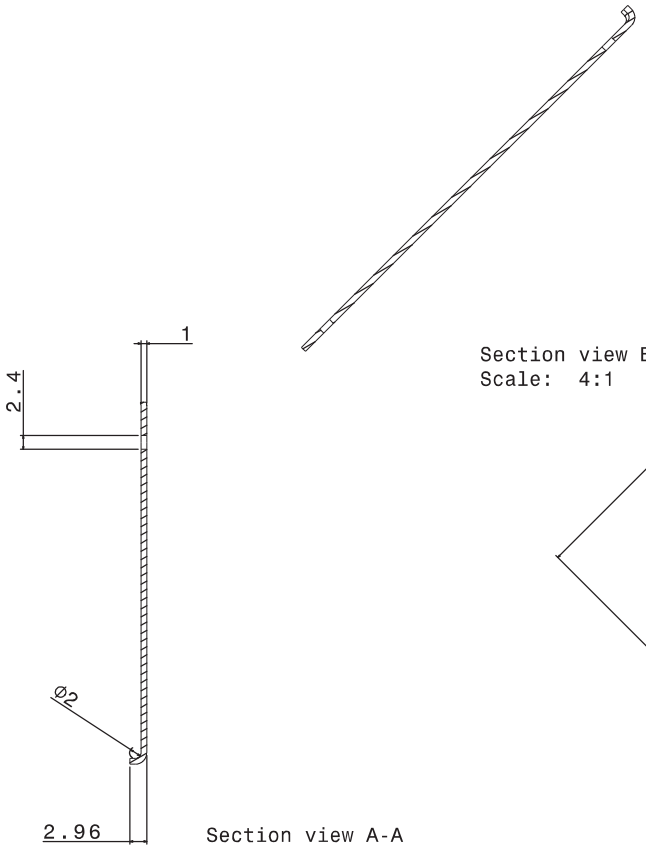

Section view A-A
Scale: 4:1

Section view B-B
Scale: 4:1

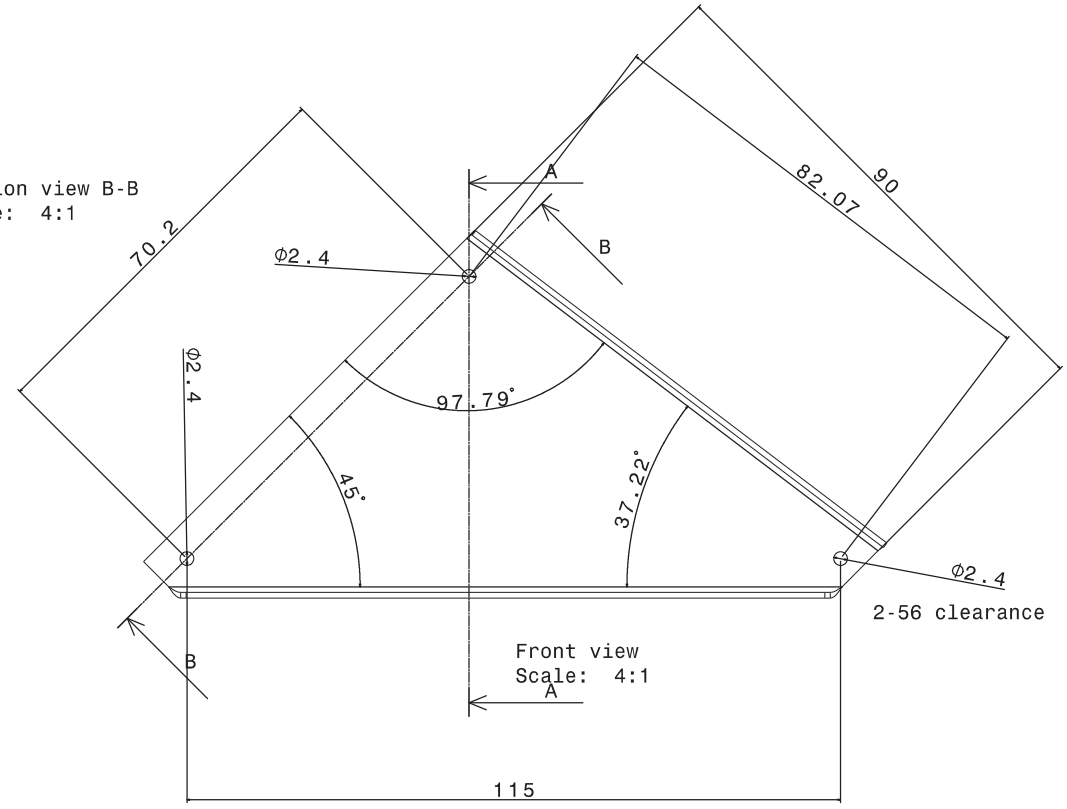

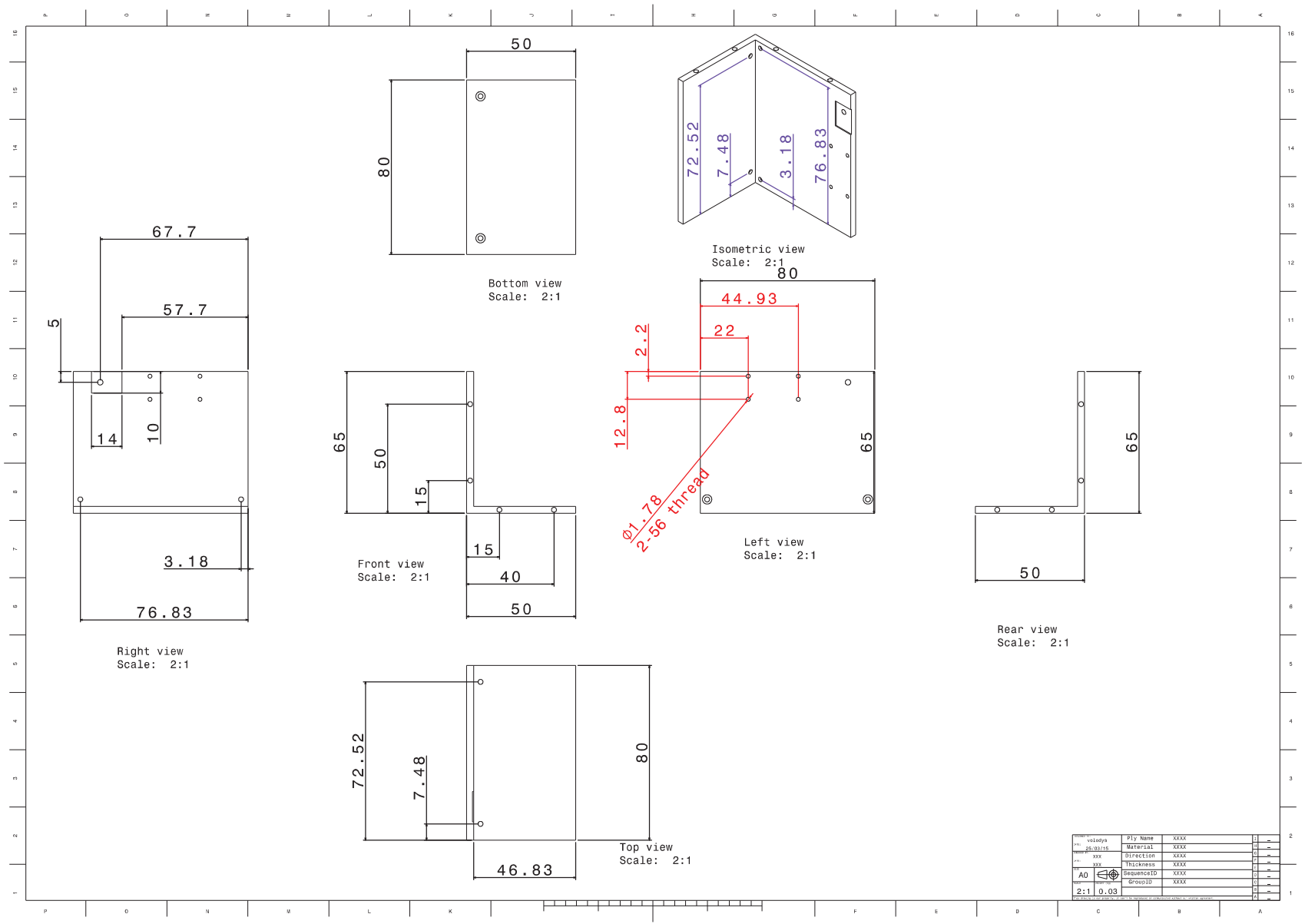
50
80
Bottom view
Scale: 2:1
72.52
7.48
3.18
76.83
Isometric view
Scale: 2:1
67.7
57.7
5
14
10
3.18
76.83
Right view
Scale: 2:1
65
50
15
15
40
50
Front view
Scale: 2:1
80
44.93
22
2.2
12.8
65
Ø1.78
2-56 thread
Left view
Scale: 2:1
65
50
Rear view
Scale: 2:1
72.52
7.48
80
46.83
Top view
Scale: 2:1
Ply Name
Material
Direction
Thickness
SequenceID
GroupID
XXXX
A0
2:1
0.03

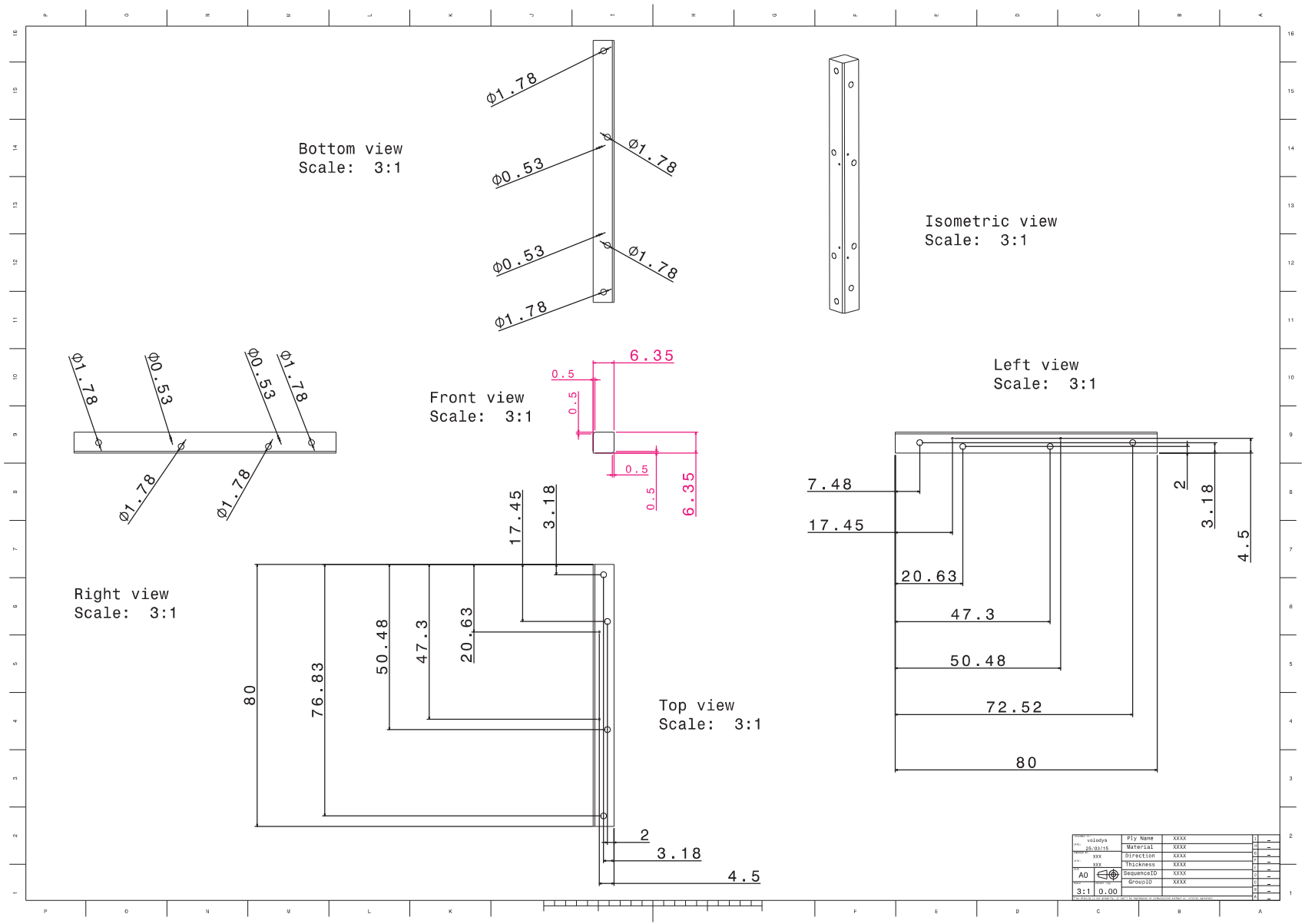
Bottom view
Scale: 3:1
Ø1.78
Ø0.53
Ø1.78
Ø0.53
Ø1.78
Ø1.78
Isometric view
Scale: 3:1
Front view
Scale: 3:1
6.35
0.5
0.5
0.5
0.5
6.35
Left view
Scale: 3:1
7.48
17.45
20.63
47.3
50.48
72.52
80
2
3.18
4.5
Right view
Scale: 3:1
Ø1.78
Ø0.53
Ø0.53
Ø1.78
Ø1.78
Ø1.78
Top view
Scale: 3:1
17.45
3.18
80
76.83
50.48
47.3
20.63
2
3.18
4.5
Ply Name
Material
Direction
Thickness
SequenceID
GroupID
XXXX
A0
3:1
0.00

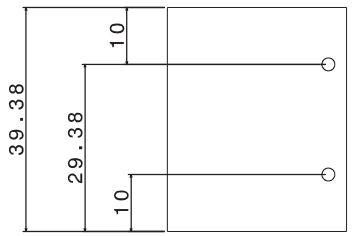

Bottom view
Scale: 4:1

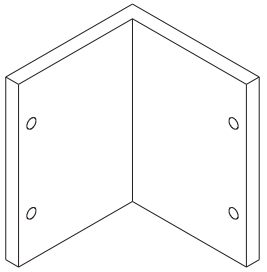

Isometric view
Scale: 4:1

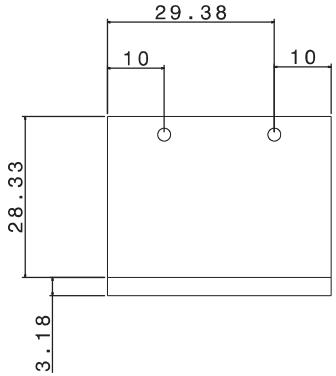

Right view
Scale: 4:1

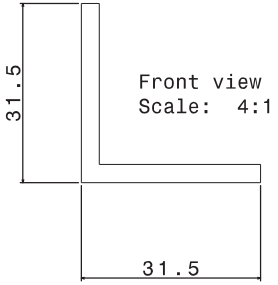

Front view
Scale: 4:1

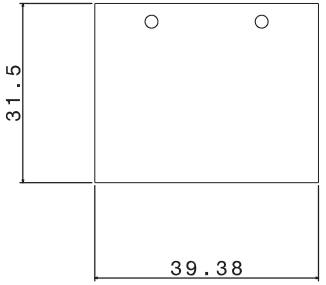

Left view
Scale: 4:1

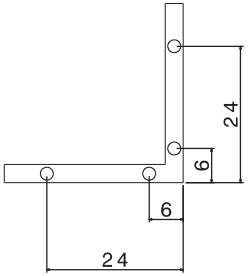

Rear view
Scale: 4:1

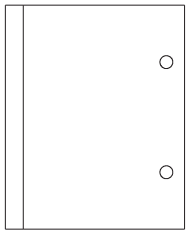

Top view
Scale: 4:1

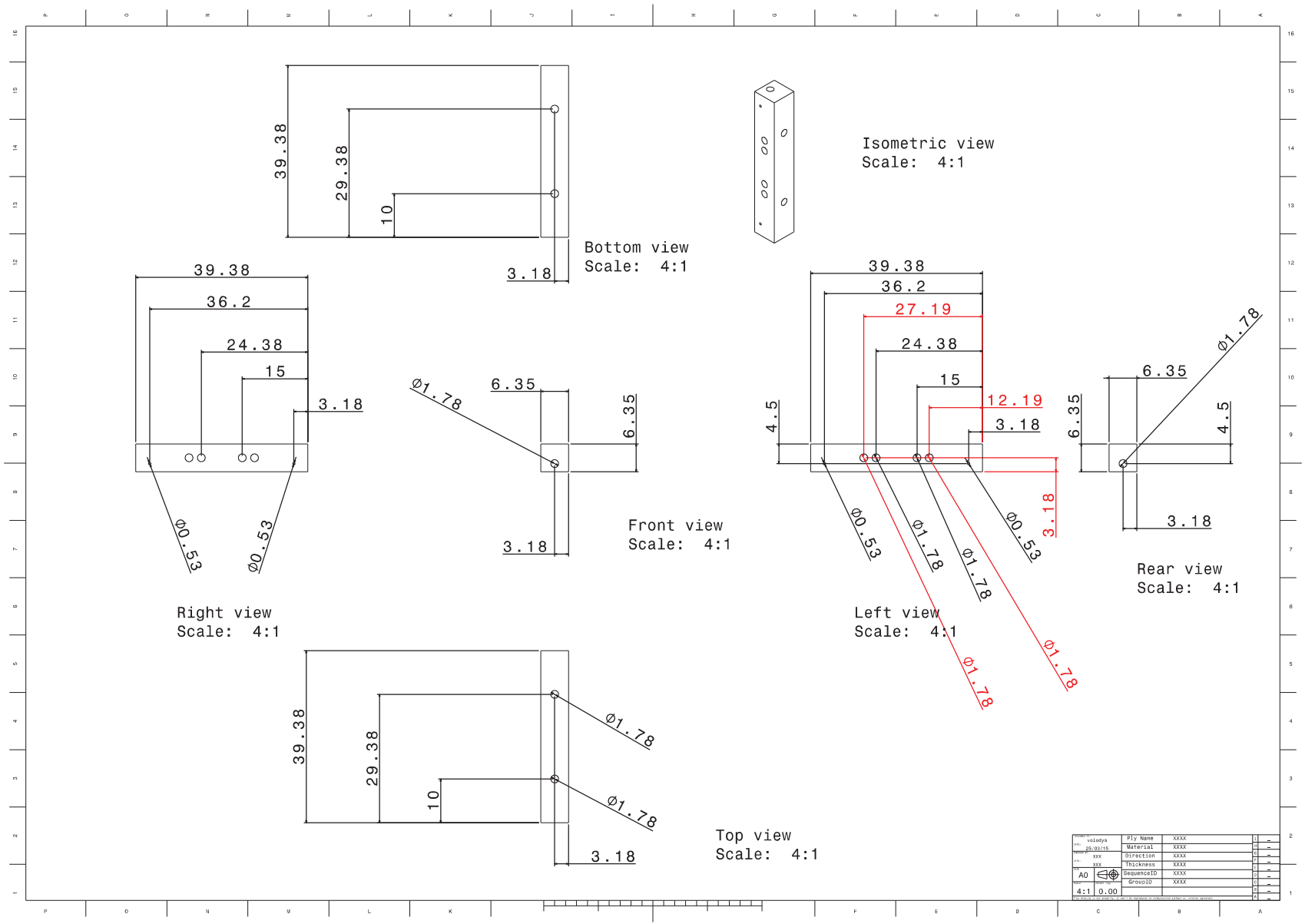
39.38
29.38
10
3.18
Bottom view
Scale: 4:1
Isometric view
Scale: 4:1
39.38
36.2
24.38
15
3.18
Ø0.53
Ø0.53
Right view
Scale: 4:1
Ø1.78
6.35
6.35
3.18
Front view
Scale: 4:1
39.38
36.2
27.19
24.38
15
12.19
3.18
4.5
3.18
Ø0.53
Ø1.78
Ø1.78
Ø0.53
Ø1.78
Ø1.78
Left view
Scale: 4:1
Ø1.78
6.35
6.35
4.5
3.18
Rear view
Scale: 4:1
39.38
29.38
10
Ø1.78
Ø1.78
3.18
Top view
Scale: 4:1
Ply Name
Material
Direction
Thickness
SequenceID
GroupID
XXXX
A0
4:1
0.00

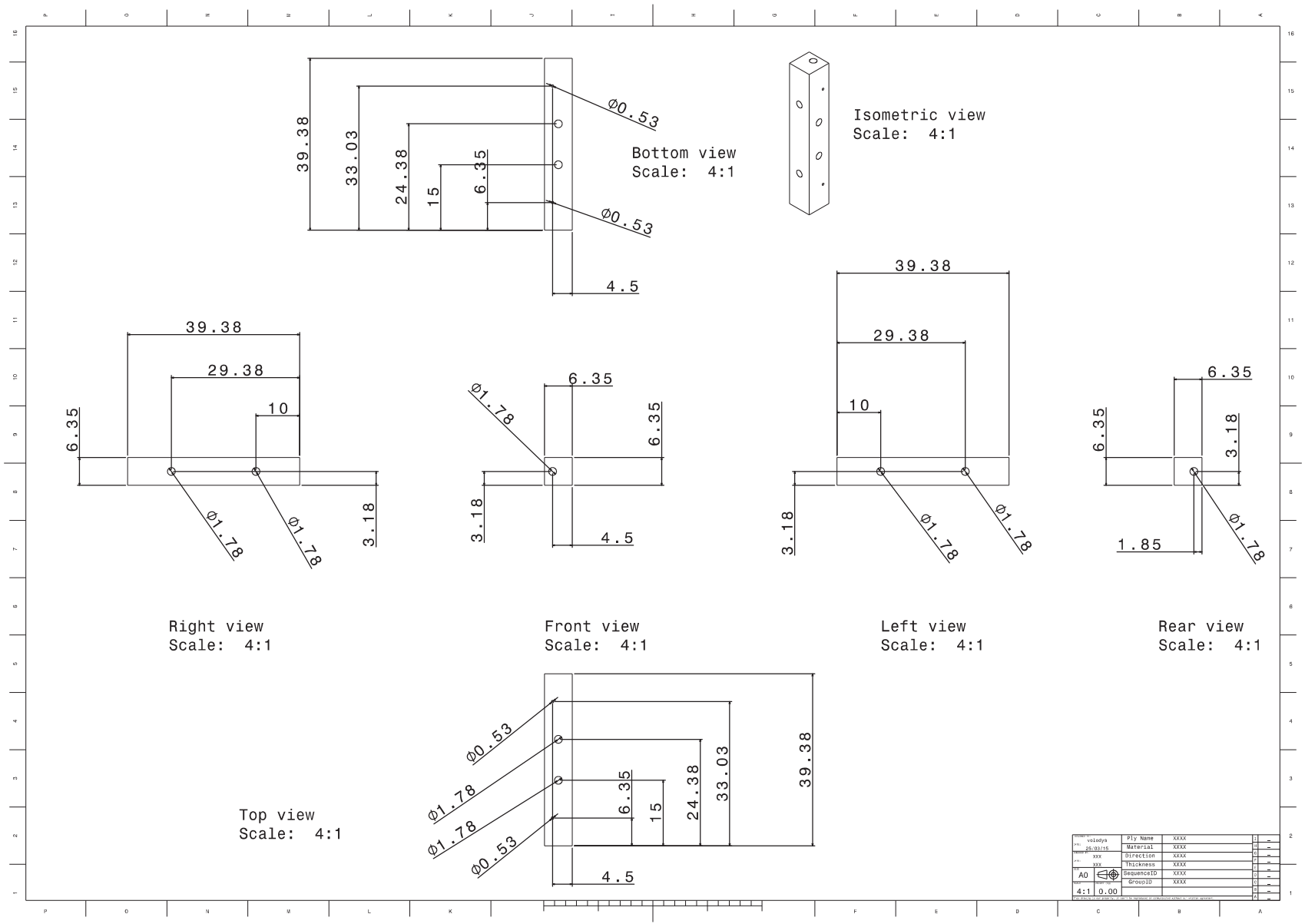
39.38
33.03
24.38
15
6.35
Ø0.53
Ø0.53
4.5
Bottom view
Scale: 4:1
Isometric view
Scale: 4:1
39.38
29.38
10
6.35
Ø1.78
Ø1.78
3.18
Right view
Scale: 4:1
6.35
Ø1.78
6.35
3.18
4.5
Front view
Scale: 4:1
39.38
29.38
10
3.18
Ø1.78
Ø1.78
Left view
Scale: 4:1
6.35
6.35
3.18
1.85
Ø1.78
Rear view
Scale: 4:1
Ø0.53
Ø1.78
Ø1.78
Ø0.53
6.35
15
24.38
33.03
39.38
4.5
Top view
Scale: 4:1
voloays
25/03/15
xxx
xxx
A0
4:1
0.00
Ply Name
Material
Direction
Thickness
SequenceID
GroupID
XXXX

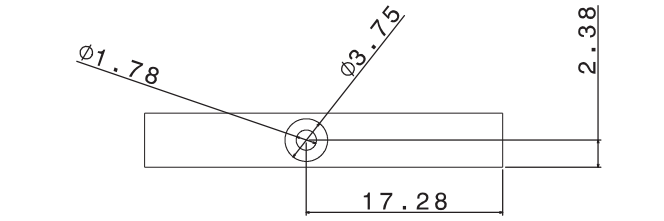

Side view
Scale: 8:1

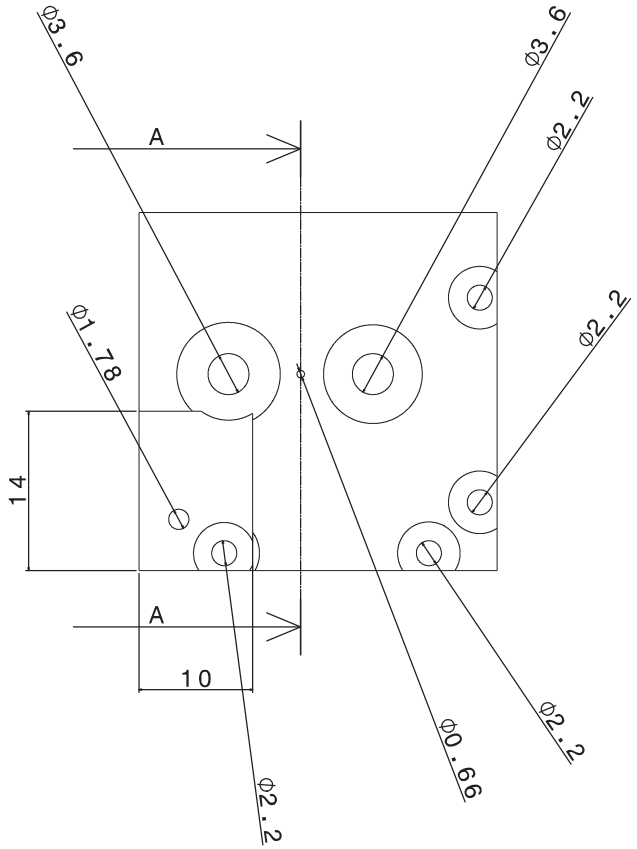

Front view
Scale: 8:1

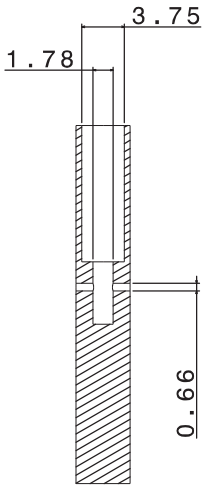

Section view A-A
Scale: 8:1

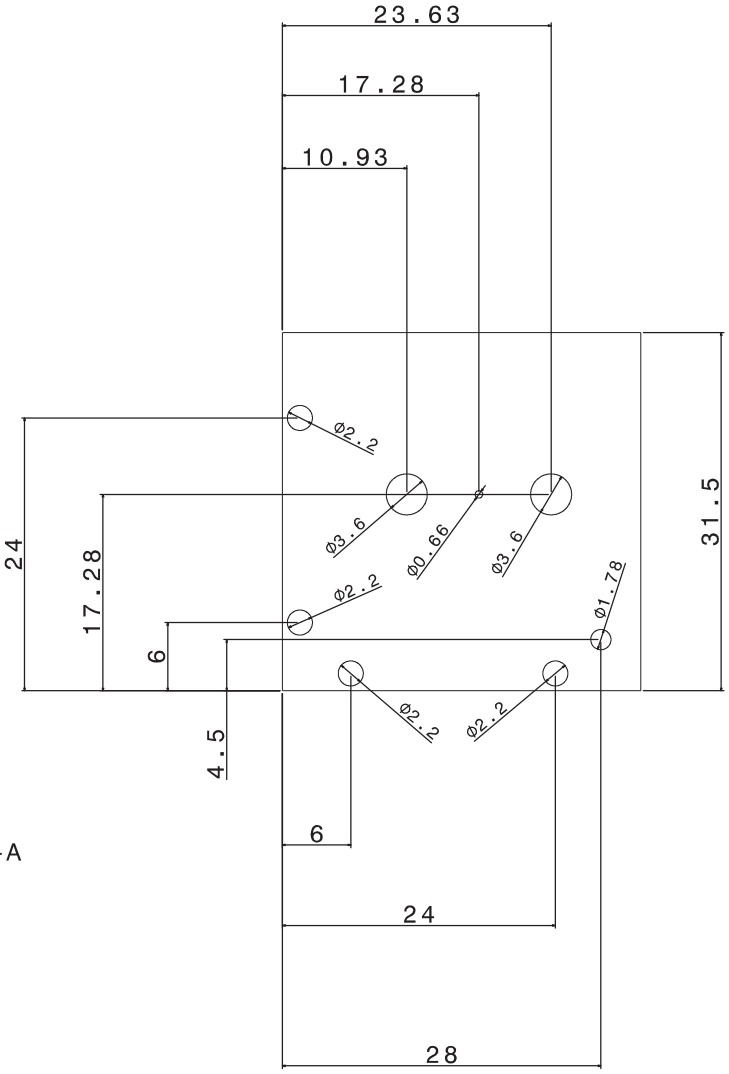

Back view
Scale: 8:1

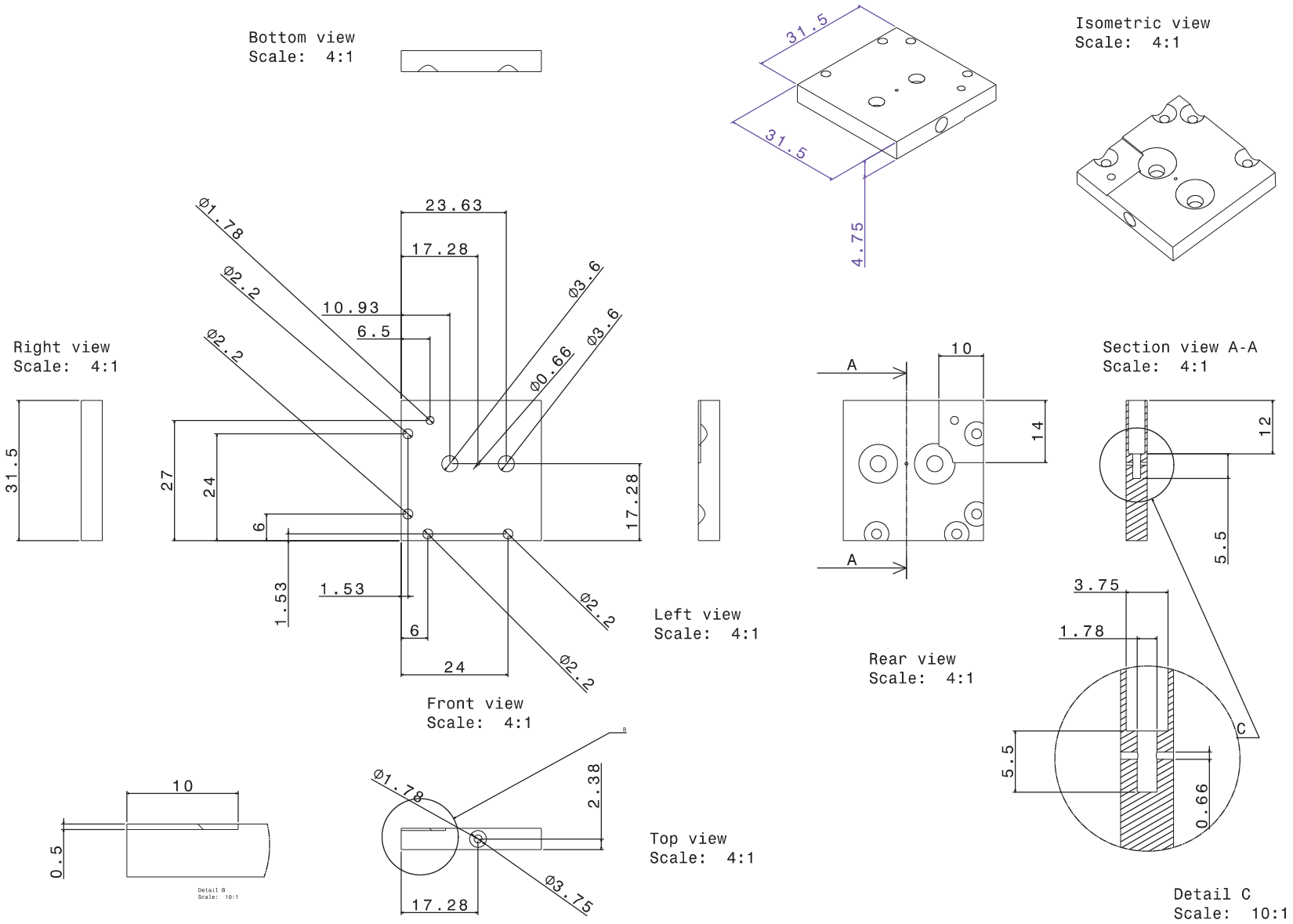
Bottom view
Scale: 4:1
31.5
31.5
4.75
Isometric view
Scale: 4:1
Right view
Scale: 4:1
31.5
Ø1.78
Ø2.2
Ø2.2
23.63
17.28
10.93
6.5
Ø3.6
Ø0.66
Ø3.6
27
24
6
17.28
1.53
1.53
6
24
Ø2.2
Ø2.2
Front view
Scale: 4:1
Left view
Scale: 4:1
A
10
14
A
Rear view
Scale: 4:1
Section view A-A
Scale: 4:1
12
5.5
3.75
1.78
C
5.5
0.66
Detail C
Scale: 10:1
10
0.5
Detail B
Scale: 10:1
Ø1.78
2.38
Ø3.75
17.28
Top view
Scale: 4:1

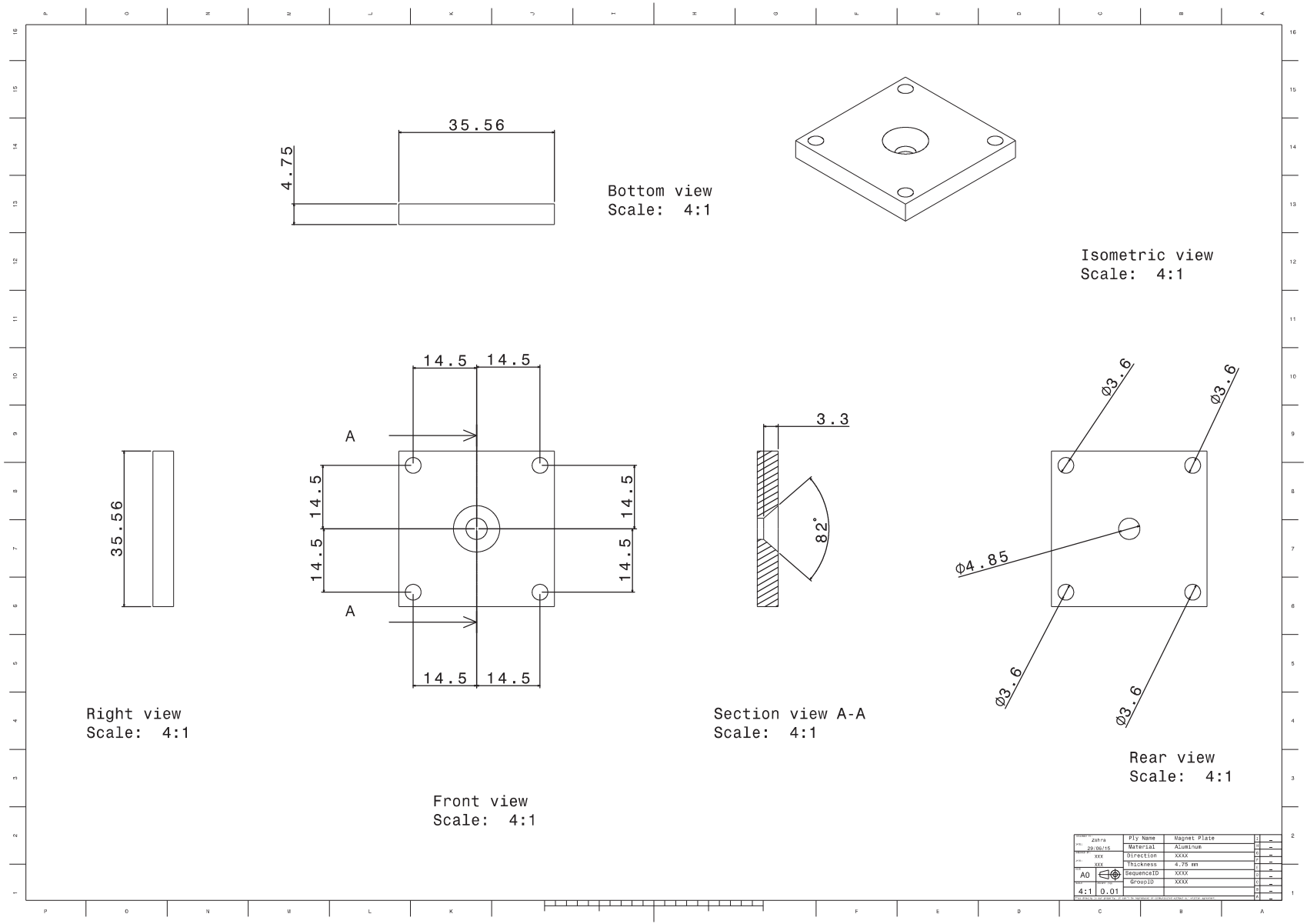
35.56
4.75
Bottom view
Scale: 4:1
Isometric view
Scale: 4:1
14.5 14.5
A
14.5
14.5
14.5
14.5
A
14.5 14.5
35.56
Right view
Scale: 4:1
Front view
Scale: 4:1
3.3
82°
Section view A-A
Scale: 4:1
Ø3.6
Ø3.6
Φ4.85
Ø3.6
Ø3.6
Rear view
Scale: 4:1
Zahra
29/06/15
XXX
XXX
A0
4:1
0.01
Ply Name
Magnet Plate
Material
Aluminum
Direction
XXXX
Thickness
4.75 mm
SequenceID
XXXX
GroupID
XXXX

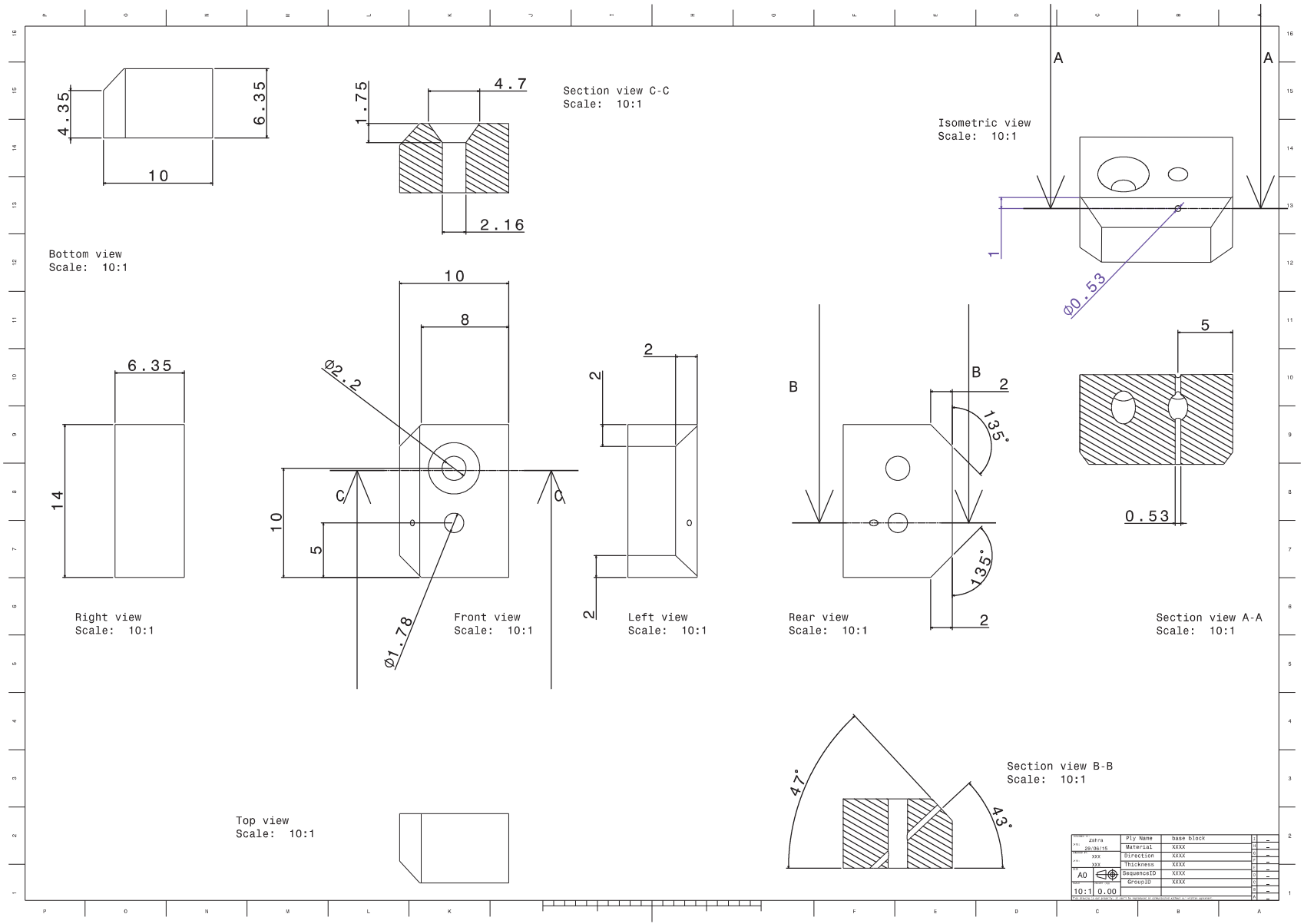
4.35
6.35
10
Bottom view
Scale: 10:1
1.75
4.7
2.16
Section view C-C
Scale: 10:1
A
A
Isometric view
Scale: 10:1
1
Ø0.53
6.35
14
Right view
Scale: 10:1
10
8
Ø2.2
C
C
10
5
Ø1.78
Front view
Scale: 10:1
2
2
2
Left view
Scale: 10:1
B
B
2
135°
135°
2
Rear view
Scale: 10:1
5
0.53
Section view A-A
Scale: 10:1
Top view
Scale: 10:1
47°
43°
Section view B-B
Scale: 10:1
Ply Name
base block
Material
XXXX
Direction
XXXX
Thickness
XXXX
SequenceID
XXXX
GroupID
XXXX
A0
10:1
0.00

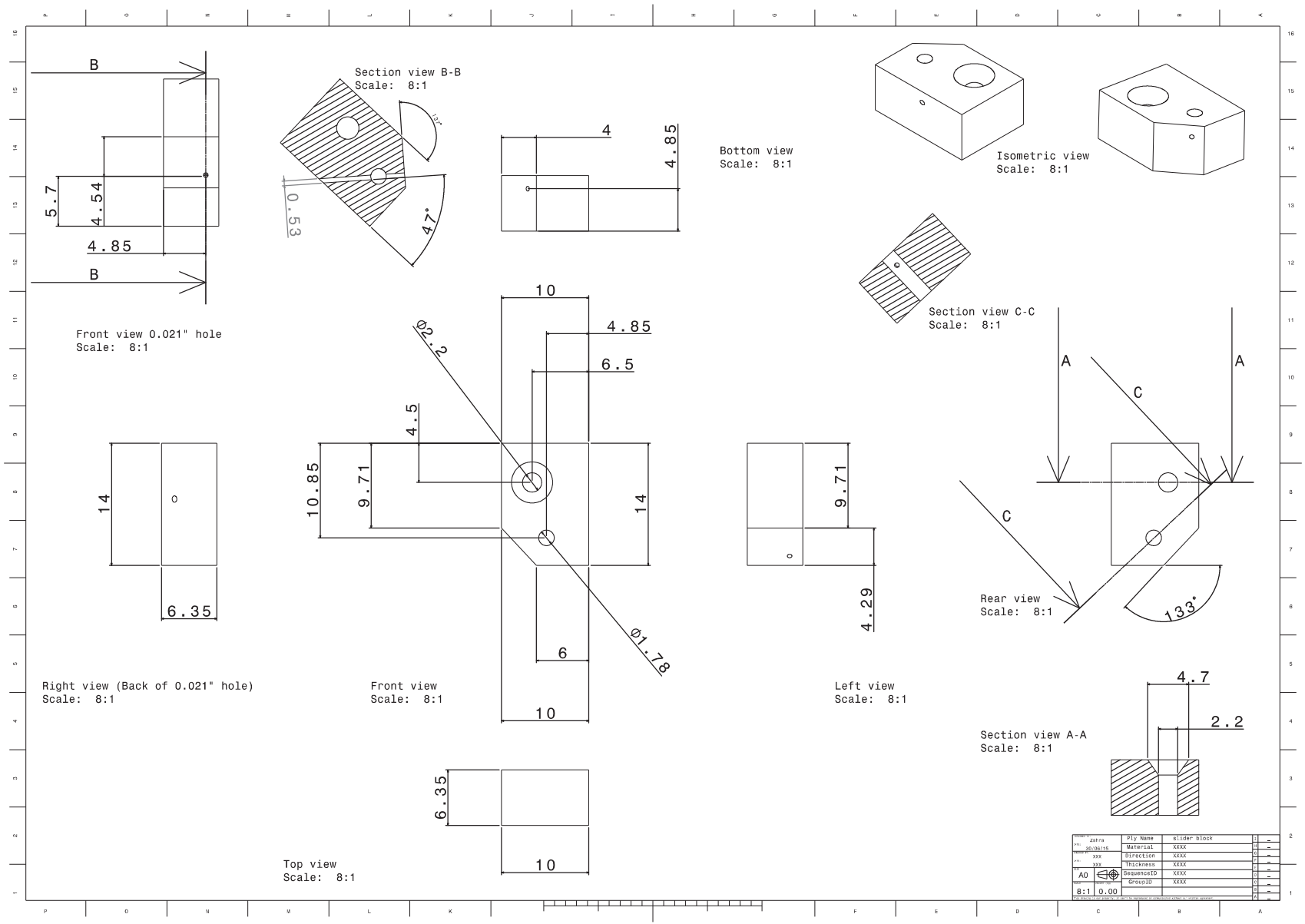
B
5.7
4.54
4.85
B
Front view 0.021" hole
Scale: 8:1
Section view B-B
Scale: 8:1
0.53
47°
4
4.85
Bottom view
Scale: 8:1
Isometric view
Scale: 8:1
Section view C-C
Scale: 8:1
A
C
A
C
Rear view
Scale: 8:1
133°
14
6.35
Right view (Back of 0.021" hole)
Scale: 8:1
10
4.85
6.5
Ø2.2
4.5
10.85
9.71
14
6
Ø1.78
10
Front view
Scale: 8:1
9.71
4.29
Left view
Scale: 8:1
4.7
2.2
Section view A-A
Scale: 8:1
6.35
10
Top view
Scale: 8:1
Ply Name
slider block
Material
XXXX
Direction
XXXX
Thickness
XXXX
SequenceID
XXXX
GroupID
XXXX
A0
8:1
0.00

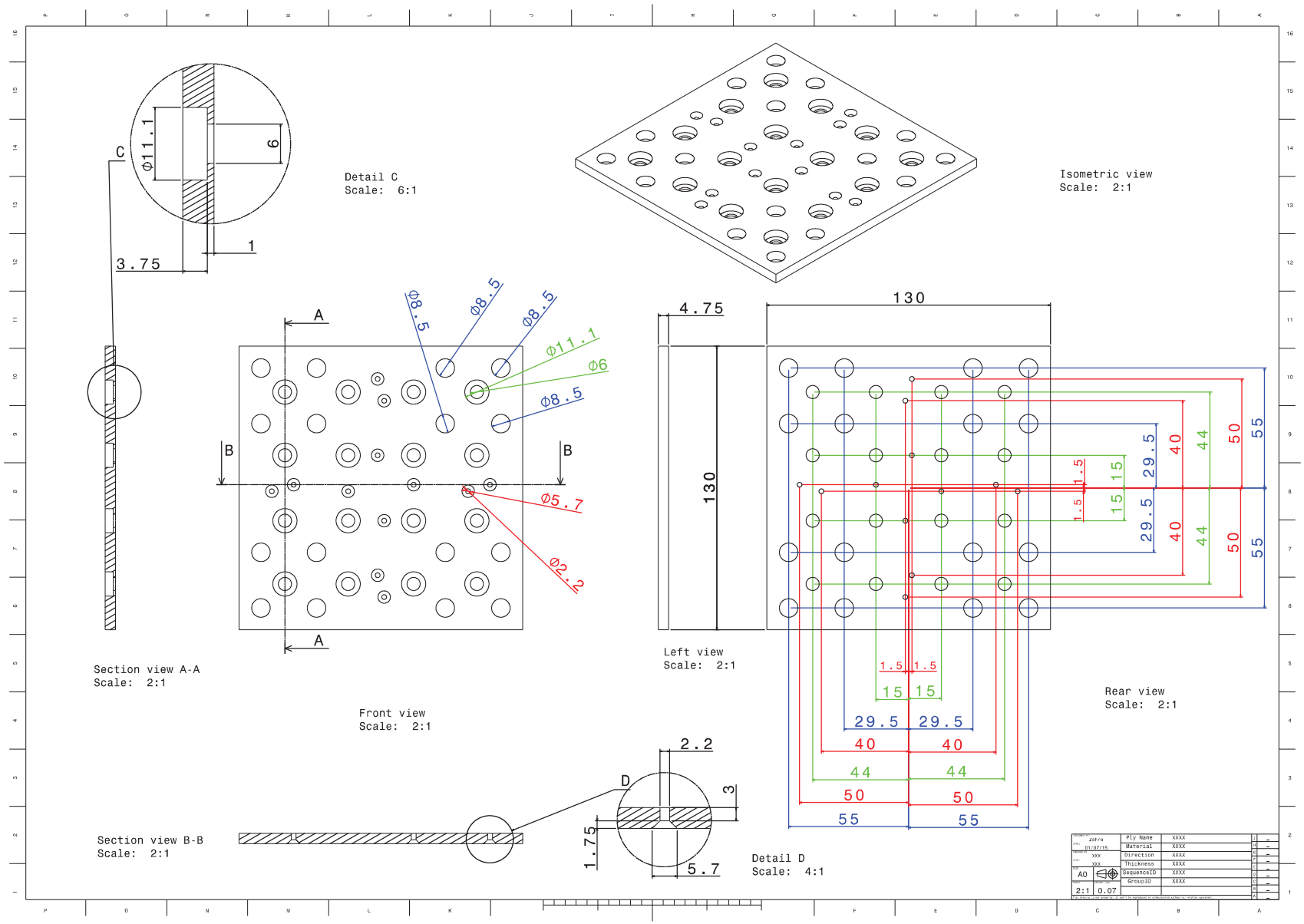
Detail C
Scale: 6:1
Isometric view
Scale: 2:1
Section view A-A
Scale: 2:1
Front view
Scale: 2:1
Left view
Scale: 2:1
Rear view
Scale: 2:1
Section view B-B
Scale: 2:1
Detail D
Scale: 4:1
130
4.75
3.75
2.2
1.75
5.7
Ply Name
Material
Direction
Thickness
SequenceID
GroupID
A0
2:1
0.07

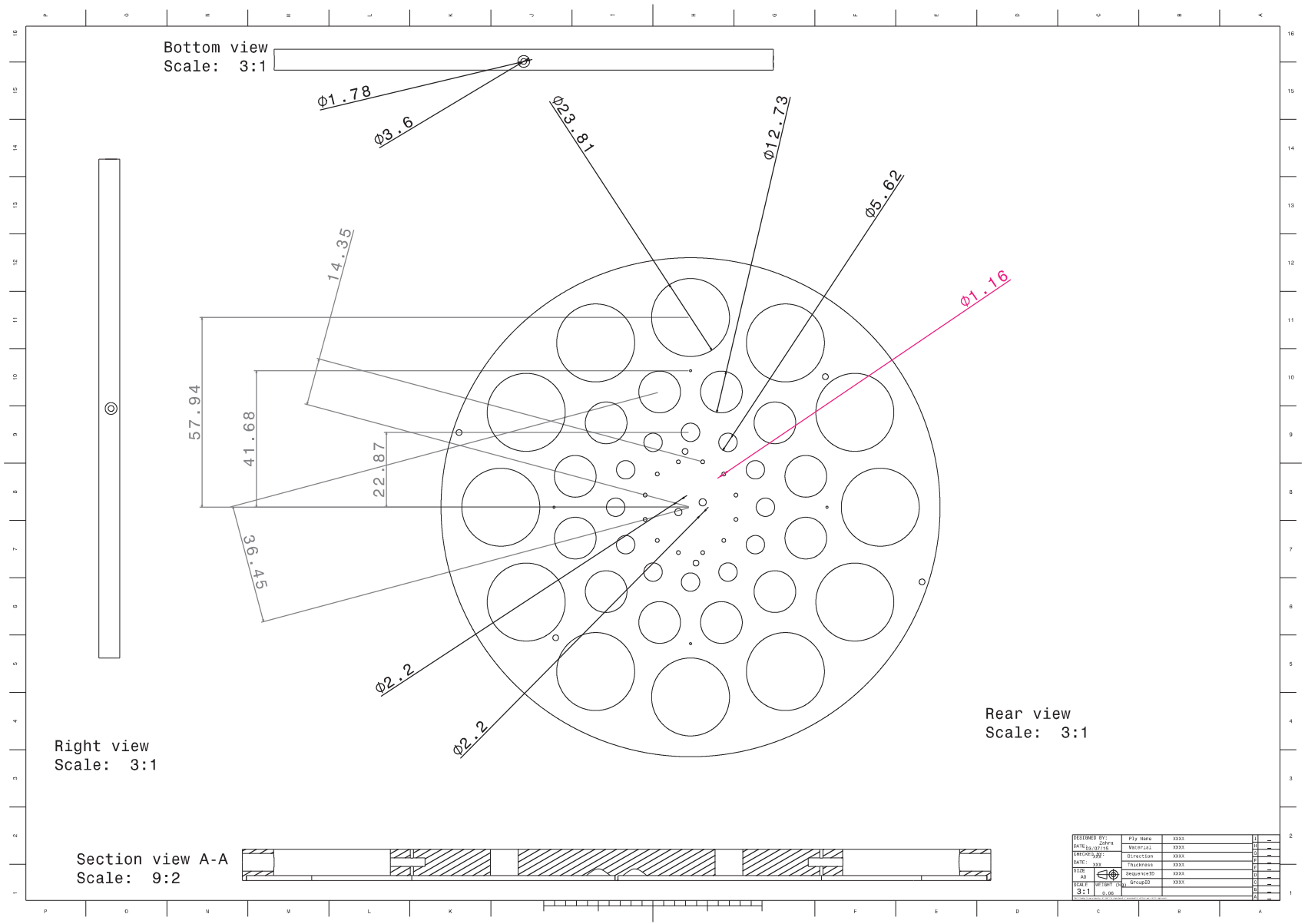
Bottom view
Scale: 3:1
Φ1.78
Φ3.6
Φ23.81
Φ12.73
Φ5.62
Φ1.16
14.35
57.94
41.68
22.87
3.45
Φ2.2
Φ2.2
Right view
Scale: 3:1
Rear view
Scale: 3:1
Section view A-A
Scale: 9:2
DESIGNED BY: Zohra
DATE: 03/07/15
CHECKED BY:
DATE: XXX
SIZE A0
SCALE 3:1
WEIGHT (kg) 0.06
Ply Name XXXX
Material XXXX
Direction XXXX
Thickness XXXX
SequenceID XXXX
GroupID XXXX

magnet clamp x 8

Delrin

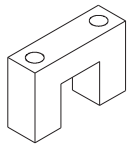

Isometric view
Scale: 6:1

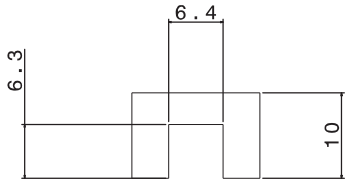

Bottom view
Scale: 6:1

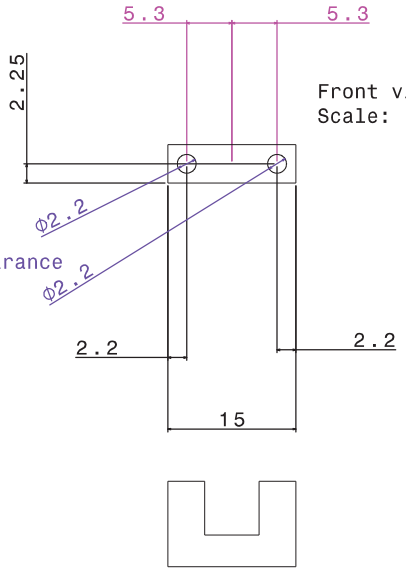

Front view
Scale: 6:1

Right view
Scale: 6:1

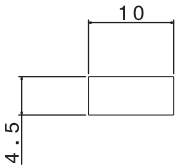

Left view
Scale: 6:1

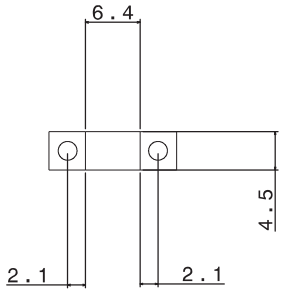

Rear view
Scale: 6:1

Top view
Scale: 6:1

Zahra	Ply Name	XXXX	
03/07/15	Material	XXXX	
XXX	Direction	XXXX	
XXX	Thickness	XXXX	
A0	SequenceID	XXXX	
	GroupID	XXXX	
6:1	0.00		

mirror clamp x 12 Delrin

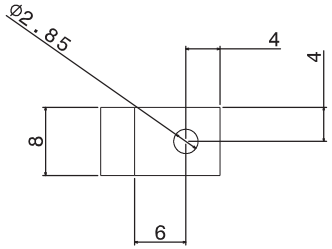

Bottom view
Scale: 6:1

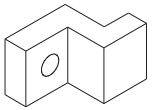

Isometric view
Scale: 6:1

Right view
Scale: 6:1

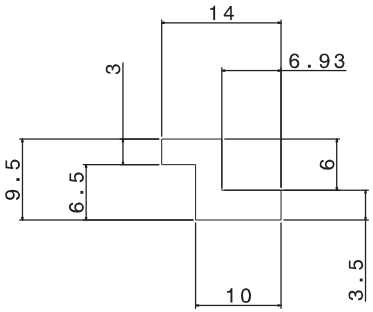

Front view
Scale: 6:1

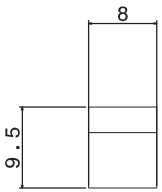

Left view
Scale: 6:1

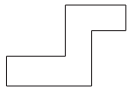

Rear view
Scale: 6:1

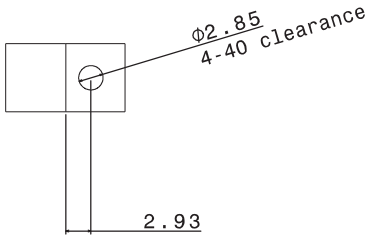

Top view
Scale: 6:1

Drawn by: velodys	Ply Name	XXXX	
Date: 30/07/15	Material	XXXX	
Drawing No: XXX	Direction	XXXX	
Rev: XXX	Thickness	XXXX	
Size: A0	SequenceID	XXXX	
Scale: 6:1	Drawing No: 0.00	GroupID	XXXX

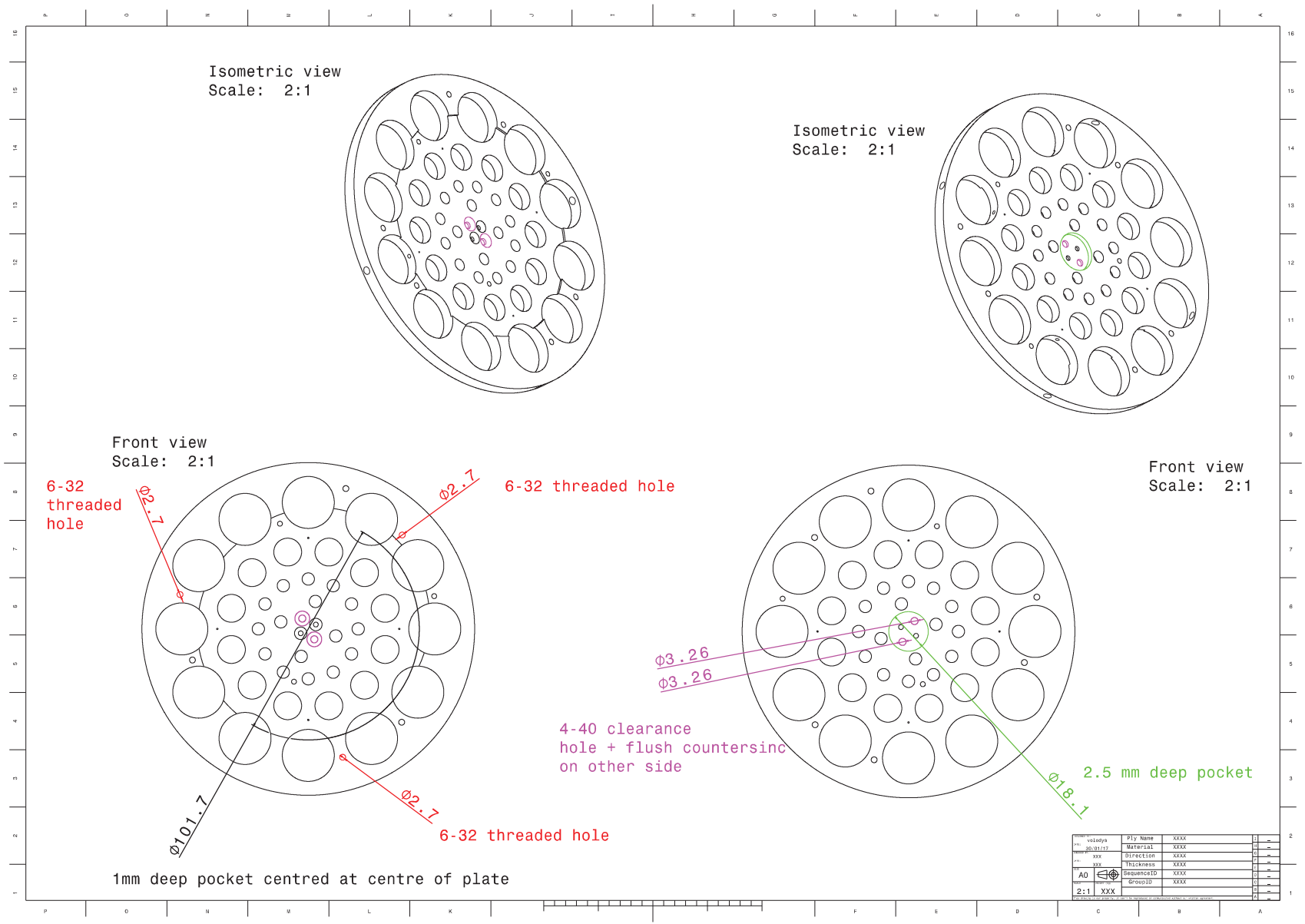
Isometric view
Scale: 2:1
Isometric view
Scale: 2:1
Front view
Scale: 2:1
6-32
threaded
hole
Ø2.7
Ø2.7
6-32 threaded hole
Ø101.7
Ø2.7
6-32 threaded hole
1mm deep pocket centred at centre of plate
Front view
Scale: 2:1
Ø3.26
Ø3.26
4-40 clearance
hole + flush countersinc
on other side
Ø18.1
2.5 mm deep pocket
Ply Name
Material
Direction
Thickness
SequenceID
GroupID
A0
2:1

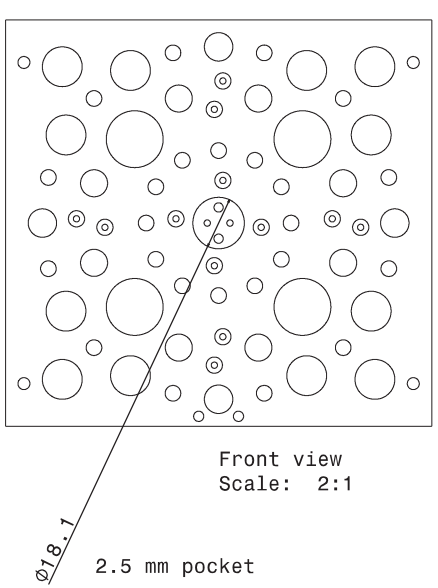

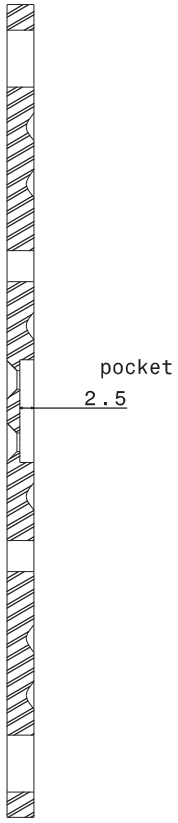

Section view A-A
Scale: 4:1

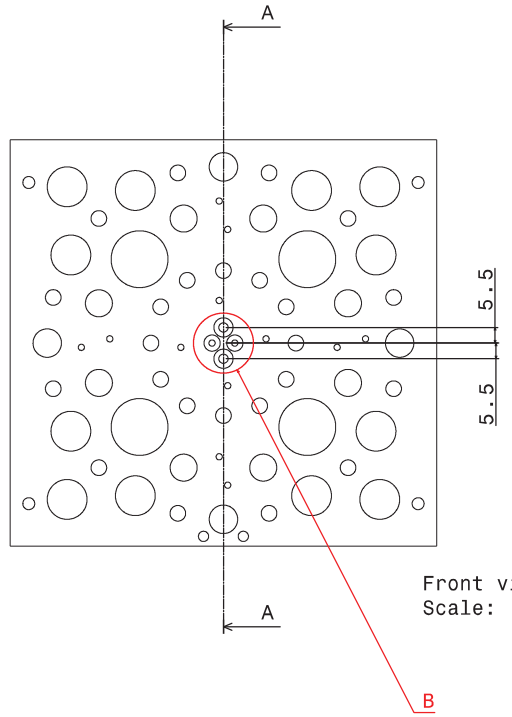

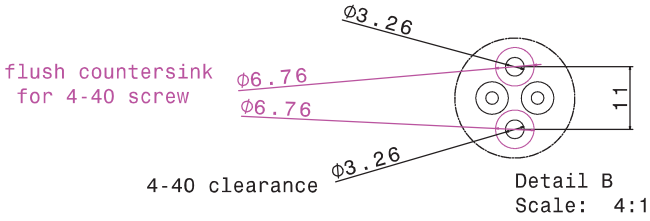

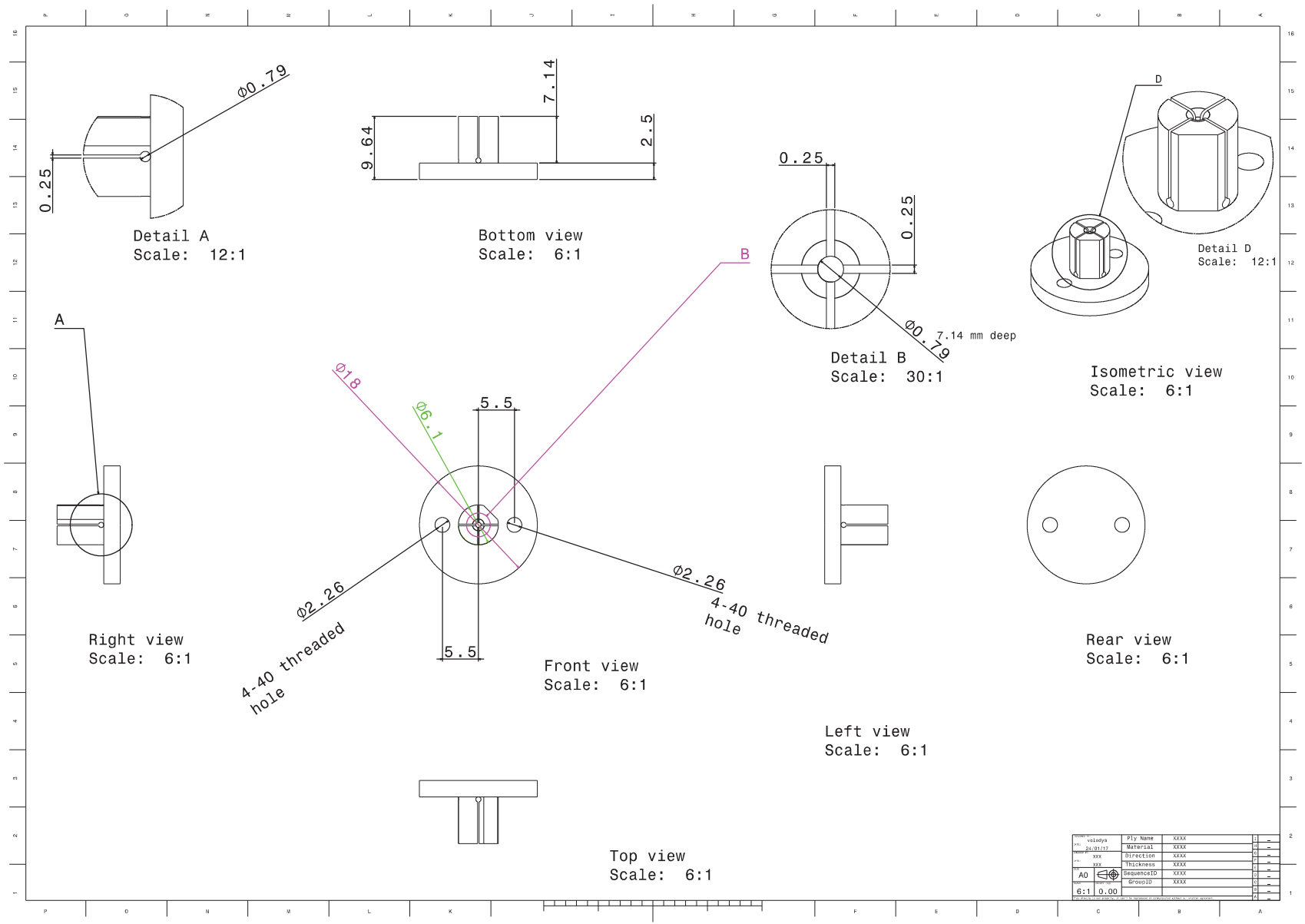
Ø0.79
0.25
Detail A
Scale: 12:1
7.14
9.64
2.5
Bottom view
Scale: 6:1
0.25
0.25
Ø0.79
7.14 mm deep
Detail B
Scale: 30:1
D
Detail D
Scale: 12:1
Isometric view
Scale: 6:1
A
Right view
Scale: 6:1
B
Ø18
Ø6.1
5.5
Ø2.26
4-40 threaded hole
Ø2.26
4-40 threaded hole
5.5
Front view
Scale: 6:1
Left view
Scale: 6:1
Rear view
Scale: 6:1
Top view
Scale: 6:1
Ply Name
Material
Direction
Thickness
SequenceID
GroupID
XXXX
A0
6:1
0.00

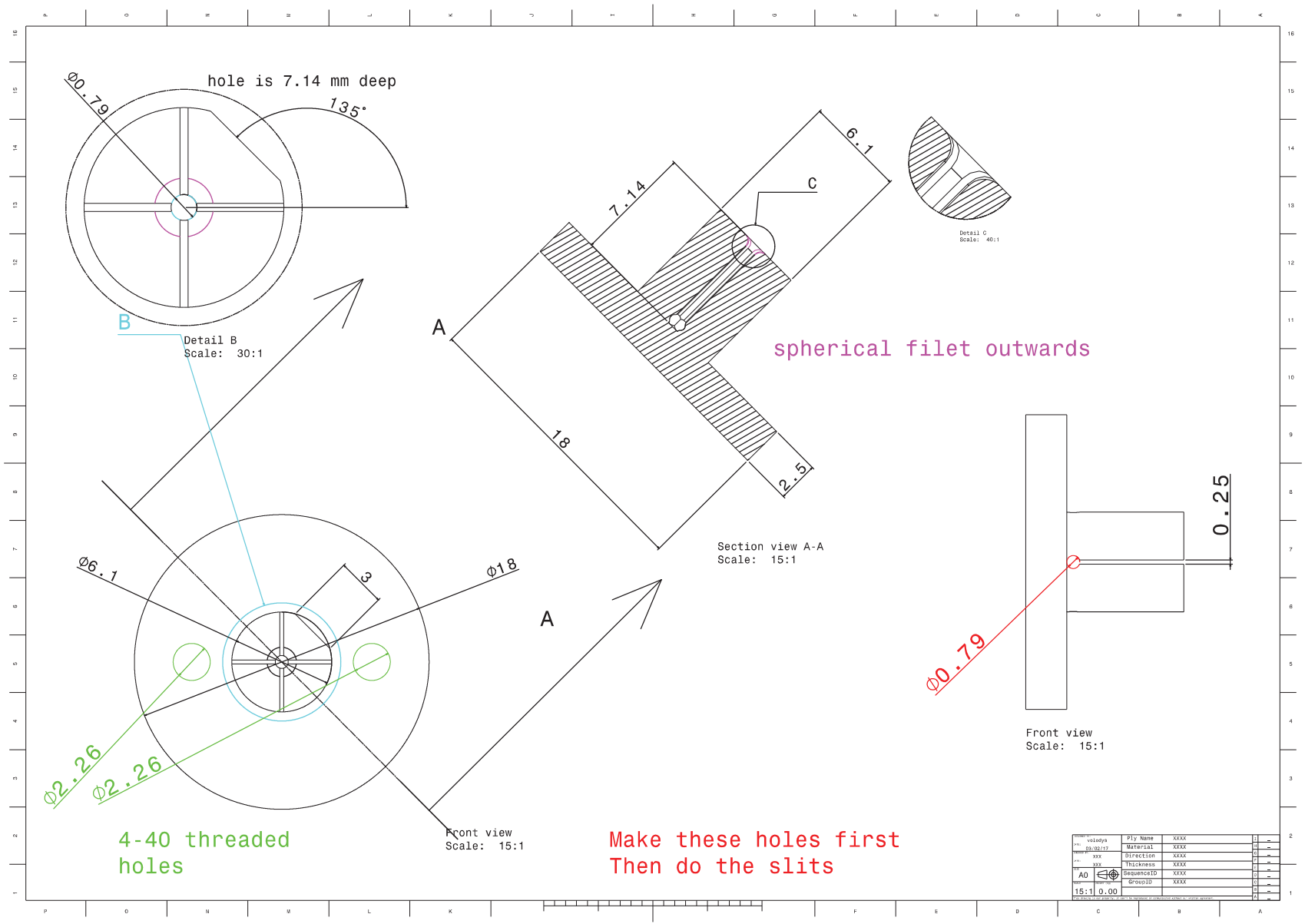
hole is 7.14 mm deep
Φ0.79
135°
B
Detail B
Scale: 30:1
A
7.14
6.1
C
18
2.5
Section view A-A
Scale: 15:1
Detail C
Scale: 40:1
spherical filet outwards
Φ6.1
3
Φ18
A
Φ2.26
Φ2.26
Front view
Scale: 15:1
4-40 threaded
holes
Make these holes first
Then do the slits
0.25
Φ0.79
Front view
Scale: 15:1
Ply Name
Material
Direction
Thickness
SequenceID
GroupID
A0
15:1
0.00